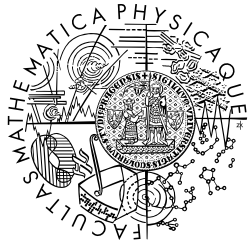

FACULTY
OF MATHEMATICS
AND PHYSICS
Charles University

MASTER THESIS

Marek Biroš

Study of the rare B-meson decays with the ATLAS experiment

Institute of Particle and Nuclear Physics

Supervisor of the master thesis:	RNDr. Pavel Řezníček, Ph.D.
Study programme:	Physics
Study branch:	Nuclear and Subnuclear Physics

Prague 2020

I declare that I carried out this master thesis independently, and only with the cited sources, literature and other professional sources.

I understand that my work relates to the rights and obligations under the Act No. 121/2000 Sb., the Copyright Act, as amended, in particular the fact that the Charles University has the right to conclude a license agreement on the use of this work as a school work pursuant to Section 60 subsection 1 of the Copyright Act.

In ..... date ..... signature of the author

Firstly, in the sense of a latin motto: “Ubi panis ibi patria” I have to say a huge Thank you! to the whole Institute of Particle and Nuclear Physics and especially to my supervisor Dr. Reznicek. The most I appreciate the fair and almost collegial spirit at the institute and opportunities to participate on international events and acquaint with international HEP community .

The rest of my dedication continues in my mother tongue – Slovak. Citujúc menej známe príslovie: “Raz máš hlavu hore, a raz dole” by som sa v neposlednej rade chcel poďakovať svojim blízkym, že ma aj v týchto neľahkých časoch podporovali a najmä v kritických chvíľach mi pomáhali držať “hlavu hore” a úspešne dobojovať začatý boj. Takže menovite, ďakujem Vám mami, oci, Matúš, babi a *dedo*. Zvlášť by som chcel poďakovať mojej Mimke za pomoc v hľadaní motivácie.

Title: Study of the rare B-meson decays with the ATLAS experiment

Author: Marek Biroš

Institute: Institute of Particle and Nuclear Physics

Supervisor: RNDr. Pavel Řezníček, Ph.D., Institute of Particle and Nuclear Physics

Abstract:

The rare $B_d^0 \to K^{*0}(892)\mu\mu$ decay is one of the B-physics channels sensitive to Beyond Standard Model effects. The potential deviation from Standard Model predictions could be observed in the angular distribution of this decay. The work compiles several sub-tasks at the initial stage of this complex analysis: decay angles fit validation and signal event preselection. The fit functions used in the analysis are verified on generated toy Monte Carlo data. Ranges of parameters, for which are these functions positive, are established and within this parametric space, the testing of possible intrinsic fit biases is evaluated. A dependence of the fit bias with respect to the collected number of events (expected in Run 2 as well as at HL-LHC) and to the different signal-to-background ratio is studied. The second part of the thesis deals with processing of raw reconstructed data from the detector into n-tuples resulting in a more compact dataset that would be used in the final analysis. Within the process,baseline cuts are applied in order to minimize size of final datasets by reducing majority of background events. The procedure is validated on full Monte Carlo simulated data, applying final event selection taken from the Run-1 analysis.

Keywords: ATLAS, LHC, rare B-meson decays, angular analysis, maximum likelihood fit validation, event selection

Názov práce: Štúdium vzácných rozpadov B-mezónov v experimente ATLAS

Autor: Marek Biroš

Ústav: Ústav částicové a jaderné fyziky

Vedúci diplomovej práce: RNDr. Pavel Řezníček, Ph.D, Ústav částicové a jaderné fyziky

Abstrakt:

Štúdium vzácneho rozpadu $B_d^0 \to K^{*0}(892)\mu\mu$ má veľký potenciál pozorovať prejavy fyziky za Štandardným modelom, ktoré by sa mohli prejaviť v uhlovom rozdelení jeho produktov. Táto práca je zameraná na prípravu rôznych medzičlánkov, potrebných v počiatočnom štádiu zložitej analýzy rozpadu $B_d^0 \to K^{*0}(892)\mu\mu$ a to konkrétne: validácia fitu uhlového rozdelenia a predvýber signálnych udalostí. Plánované fitovacie funkcie sú testované na generovaných toy Monte Carlo dátach. V rámci stanovených testovacích rozsahov, množine parametrov kde funkcia nadobúda iba kladné hodnoty pre všetky kombinácie uhlov, sú skúmané prejavy vnútorných skreslení, resp. vychýlení (tzv. biasov) fitu. Skúmaná bola najmä závislosť biasov na počte nameraných signálnych udalostí očakávaných v Rune 2 a v HL-LHC a na rôznom pomere signal-vs-pozadie. Ďalšou časťou bolo spolupodieľanie sa na rekonštrukcii predspracovaných dát z detektora do n-tuplov za účelom tvorby viac kompaktného datasetu, neskôr použitého v samotnej analýze. Pre efektívnejšiu redukciu veľkosti datasetu, boli aplikované základné výberové kritéria na potlačenie pozadia.Táto procedúra bola testovaná aplikáciou výsledných výberových kritérií z analýzy Runu 1 na plnej Monte Carlo simulácii rozpadu a jeho detekcie.

Klúčové slová: ATLAS, LHC, vzácne rozpady B-mezónov, validácia fitu maximálnej vierohodnosti, uhlová analýza, výberové kritéria

Contents

Introduction

This thesis presents initial stages of the Run 2 (data collected in years 2015–2018) analysis of the decay $B_d^0 \to K^{*0}(892)\ \mu^+\mu^-$ ($B_d^0 \to K^*\mu\mu$ from now on) with the ATLAS experiment. Decays including FCNC transition of b quark into s quark (as $B_d^0 \to K^*\mu\mu$) are forbidden at the tree level in the Standard Model (SM) and undergo through loops only. In extensions of the SM, new particles may occur inside the loops and manifest themselves in the matrix element that could be measured in the branching fraction of the decay or in the distribution of decay angles between momenta of the final-state particles. The most recent results of the angular distribution measurement was provided by the LHCb collaboration. Results from their analysis of Run 1 (2011–2012) are in a good agreement with SM predictions except of the local deviation in one of the observables ($P_5^{'}$, see definition later) with a significance at the level of 3 standard deviations. Recent update of the analysis with data collected in 2016 specifies the deviation at the similiar level and therefore more data are needed in order to confirm or disprove the discrepancy between the measurements and the theoretical predictions.

The thesis is organized as follows. The first chapter introduces CERN, LHC and the ATLAS detector. Realized and planned upgrades of ATLAS and principles of particle detection are described there as well. In the second chapter, a necessary theoretical background is introduced, and the $B_d^0 \to K^*\mu\mu$ decay peculiarities are discussed: description of the decay reconstruction and parametrization, the known background processes, observables of the decay angles analysis, and the recent results of the decay measurement. The rest of the thesis is devoted to author's results achieved within the thesis. The validation of the fit of the decay angles distribution using toy Monte Carlo (MC) simulations is presented in the third chapter. The chapter starts with detemination of valid fit-parameters range. Due to the complexity of the fit and relatively low number of expected signal events in real data, the fit suffers from intinsic biases. A dependence of the fit bias with respect to the collected number of events measured in Run 1, expected in Run 2 and at HL-LHC, and to the different signal-to-background ratio is studied with and without effects of the detector. The chapter focuses on the fit involving parameter $P_5^{'}$ where LHCb observed the deviation from SM prediction. However, the results with rest of the fit-parameters are collected in the appendix. The fourth chapter reports results from processing of raw reconstructed data from the detector into n-tuples used in the final analysis. This task was rather more technical, contributing to the analysis software development within the ATLAS $B \to K^*\mu\mu$ working group. The functionality of the n-tuple maker is demonstrated on processing of limited-size of fully simulated Monte Carlo samples (including full simulation and reconstruction chain of the ATLAS experiment). The tests are based on application of set of cuts from the analysis of the ATLAS Run-1 data [1]. The first appendix is devoted to a summary of useful technical details of CERN linux and batch service.

1. The ATLAS Experiment

The ATLAS experiment [2] is one of major particle experiments in CERN. To be more specific, ATLAS is the biggest general-purpose particle detector on the world with height of 25 m and length of 44 m. The acronym ATLAS stands for A Toroidal LHC ApparatuS. The ATLAS detector measures mainly proton-proton but also proton-lead and lead-lead collisions in the Large Hadron Collider. The main aims of the experiment were established to find Higgs boson, search for decays of supersymmetric particles, gravitons and the minimal supersymmetric extension of the SM Higgs mechanism. The first one was fulfilled in 2012, however measurements of the Higgs boson's properties still continue.

1.1 CERN

CERN is an acronym for its french name - Conseil européen pour la recherche nucléaire - the European Organization for Nuclear Research. It was established in 1954 in Geneva on the Franco–Swiss border, devoted to the study of atomic nuclei. Nowadays CERN has 23 member states (originally 12), and since our understanding of matter goes deeper than the nucleus, the CERN's main area of research moved to particle physics. CERN is one of the largest and most respected centers for scientific research in the world. It is a place where flavour changing neutral currents (more in section 2.2), W, Z and Higgs bosons were discovered, as well as direct CP violation was observed, number of neutrinos families were determined and the first antihydrogen atom was created.

The ATLAS experiment is collecting data from collisions at the CERN's largest accelerator: Large Hadron Collider. However, CERN hosts also number of other smaller experiments as the Antiproton Decelerator, CAST, nTOF, ISOLDE, NA61, NA62, etc. Except of direct scientific research, CERN is also a birthplace for many technologies, e.g. the World Wide Web.

1.2 Large Hadron Collider

The Large Hadron Collider (LHC) is the world's largest and most powerful particle accelerator. It is a 27-kilometre long synchrotron devoted to acceleration of protons and lead nuclei. Two beams travel in opposite directions in separate beam pipes with ultrahigh vacuum and are made to collide at four locations around the accelerator ring. Each interaction point is enveloped by one of four great particle detectors – ATLAS, CMS, ALICE and LHCb.

Detectors ATLAS, CMS and ALICE are built symmetrically around the interaction point. LHCb is a single arm forward detector. ATLAS and CMS, A Toroidal LHC ApparatuS and the Compact Muon Solenoid, respectively, are general purpose detectors, so called, discovery machines. A Large Ion Collider Experiment (ALICE) is a heavy-ion detector, focusing on lead lead collisions. It is designed to study the physics of quark-gluon plasma, a strongly interacting phase of matter at extreme energy densities. The LHC beauty (LHCb) is specialized in heavy flavour measurements, in particular involving b-hadrons, primarily

the measurement of CP violation parameters.

In addition, there are tree less known LHC-experiments: TOTEM, LHCf and MoEDAL. TOTal Elastic and diffractive cross section Measurement is designed to take precise measurements of protons emerging from collisions at small angles. Since TOTEM is placed in the CMS cavern, both collaborations coordinate the usage of their detectors to perform combined measurements. The LHC-forward experiment uses particles thrown forward by collisions in the ATLAS interaction point as a source to simulate cosmic rays in laboratory conditions. The LHCb cavern hosts the Monopole and Exotics Detector that searches directly the magnetic monopole – a hypothetical particle with a magnetic charge. MoEDAL also looks for Beyond Standard Model (BSM) physics, particularly highly ionizing Stable Massive Particles (SMPs).

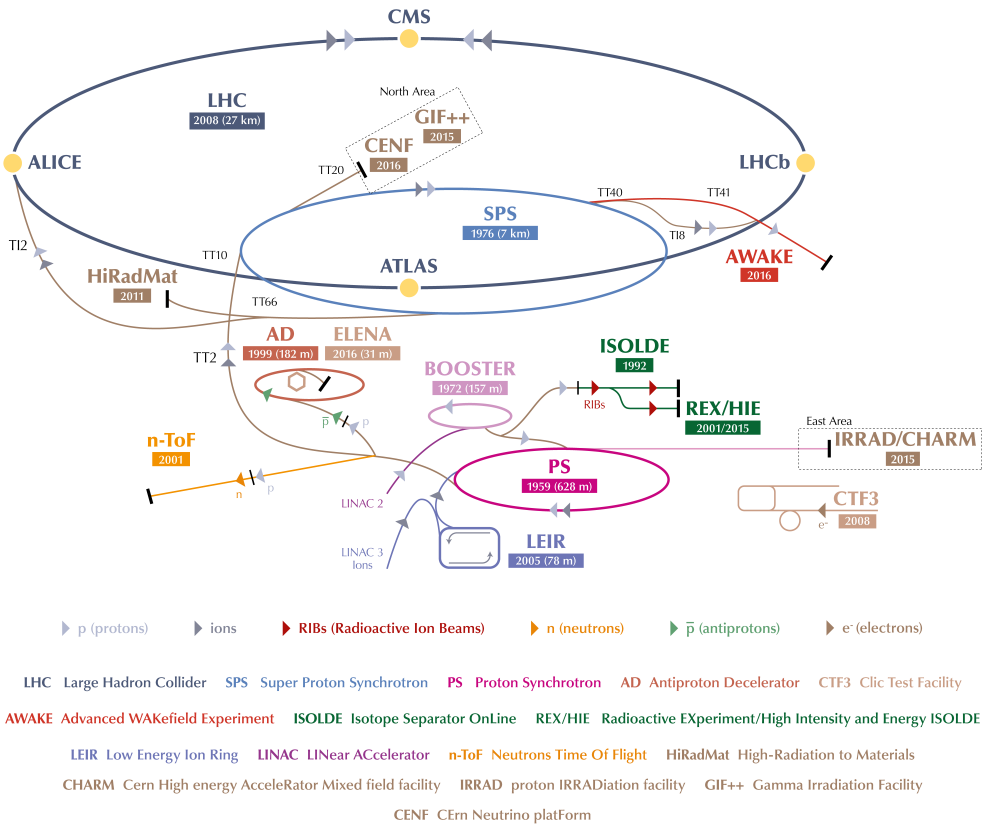

Figure 1.1: The CERN accelerator complex [3]. Protons are collected from the hydrogen bottle, ionized and accelerated to energy of 50 MeV in Linac 2. Then they are boosted to energy of 1.4 GeV in Booster, to 25 GeV in PS and finally to 450 GeV in SPS. After all, protons are injected inside of LHC where they reach the maximal energy of 13 TeV.

The accelerator ring consists of superconducting magnets with several accelerating structures to boost the energy of particles along the way. There are two types of magnet systems: dipole magnets which bend the beams, and quadrupole

magnets which focus the beams. Protons are injected into LHC from the pre-acceleration chain as is shown on Fig. 1.1.

1.3 The ATLAS Detector

The ATLAS detector consists from four main subsystems: inner detector, calorimetry, muon spectrometer and trigger.

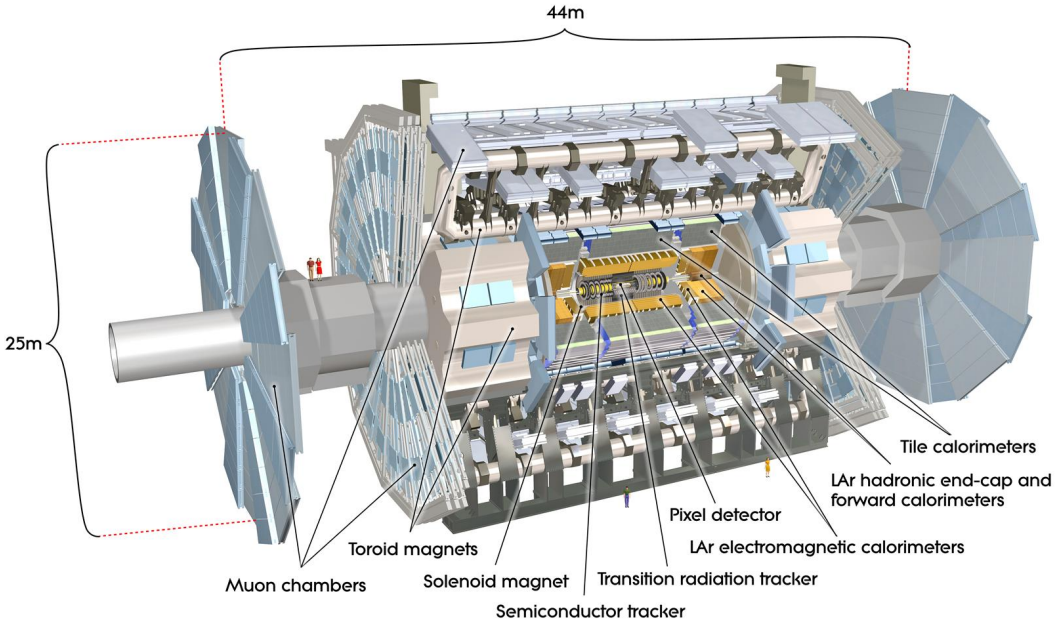

Figure 1.2: Scheme of the ATLAS detector [2].

Inner Detector (ID) measures tracks of charged particles. The system of calorimeters measures deposited energy of particles passing through it. The outermost layer of the detector is devoted for muon detection since most of particles stop in the calorimeters and only muons continue to the muon spectometer. The number of proton collisions is enormous, however recording possibilities are limited. Thus one has to reduce amount of data which will be saved to later analysis and that is a purpose of the trigger system. Individual parts of detector are here described according to their first construction in 2008 [2]. This is followed, in section 1.4, by the already placed and expected upgrade of the ATLAS experiment. Detection abilities are discused in general in section 1.5 and more specific with respect to the $B \to K^* \mu\mu$ analysis in section 2.3.1.

1.3.1 The ATLAS Coordinate System

"ATLAS uses a right-handed coordinate system with its origin at the nominal interaction point (IP) in the centre of the detector and the z-axis along the beam pipe. The x-axis points from the IP to the centre of the LHC ring, and the y-axis points upward. Cylindrical coordinates (r, ϕ) are used in the transverse plane, ϕ

being the azimuthal angle around the z-axis. The pseudorapidity is defined in terms of the polar angle θ as $\eta = -\ln\tan(\theta/2)$." [4]

1.3.2 Inner Detector

The ATLAS inner detector is the closest part of ATLAS to the beam. The beryllium beam pipe with radius less then 3.6 cm is surrounded by three cylindrical layers of the 80 cm long pixel detectors. The first layer is often refered as the "B-layer" because information from it is used to determine whether if particles came from primary vertex. If they were shifted from the pp interaction point, they most likely came from a decay of a secondary particle, usually b-hadron (but from others like τ as well), therefore the name "B". The pixel detectors are on the edges enclosed by the end-cap disks. Together they create the first layer of the ID, the pixel detector. The second layer, the semiconductor tracker (SCT), contains four double layers of barrel silicon-microstrip sensors and encircles the pixel layers and the pixel end-caps. The SCT's barrels' dimensions are: radius 0.5 m and length 1.5 m. The SCT edges are enclosed with the end-cap disks either. The third layer is the transition radiation tracker (TRT). It fences the both inner layers with final radius about 1 m and length of 6.2 m. The TRT is formed of the polyimide drift (straw) tubes of 4 mm diameter and length of 144 cm for the barrel and 37 cm for the end-caps. The straws are filled with gas mixture of Xe, CO_2 and O_2 and operated in an envelope of CO_2. The ID incorporates also a cooling system and a lot of read out electronics and power supplies.

The inner detector is placed in the solenoid magnetic field of 2 T.

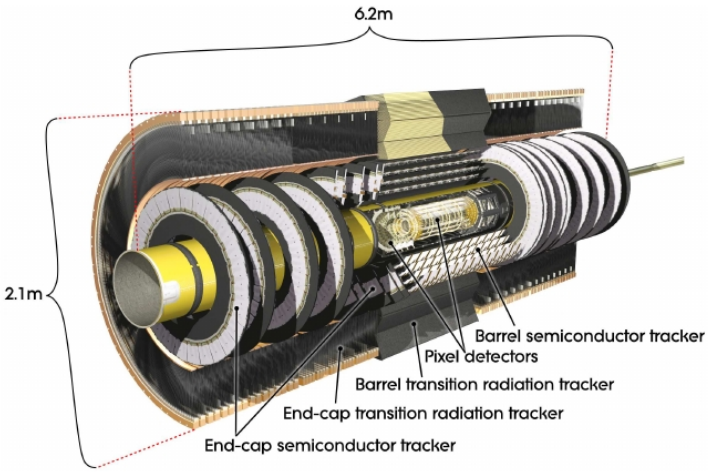

Figure 1.3: Cut-away view of the inner detector [2].

1.3.3 Calorimetry

The system of calorimeters encapsulates the inner detector. It consists of two parts: electromagnetic and hadronic calorimeter. The EM calorimeter is divided into a barrel part and end-caps. The hadronic calorimeters contains

three parts: tile calorimeter (TileCal), hadronic end-cap calorimeter (HEC) and forward calorimeter (FCal).

Measurements in the calorimeters are complementary to the ID. Measurements of low energetic particles would be more precise in the ID and vice versa high energetic particles in the calorimeter, since the ID's uncertainty of momentum is proportional to its magnitude and the uncertainty of a measurement in the calorimeters is inversely proportional to the square root of energy.The calorimeters, unlike the ID can measure also neutral particles.

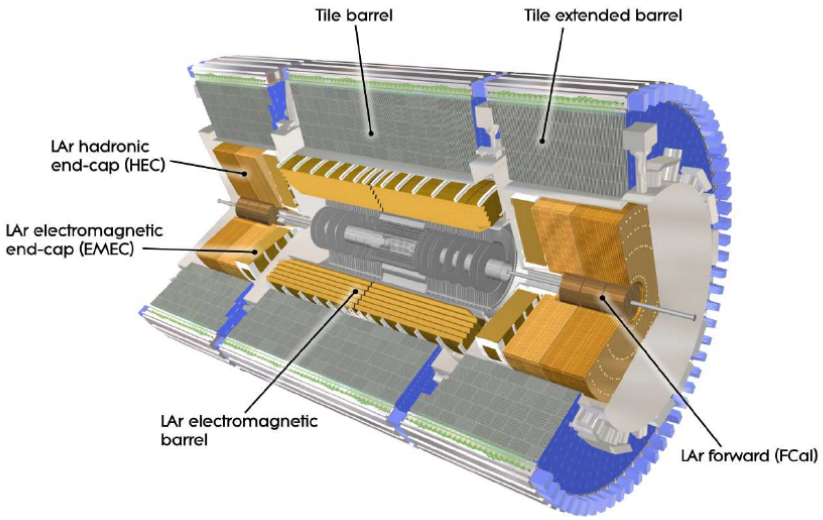

Figure 1.4: Cut-away view of the calorimeter system [2].

Both, the EM and the hadronic calorimeters, are sampling calorimeters; they use a high-density absorber, and except for the TileCal, liquid argon is used as the active detector medium. In order to prevent a dispersion of particles as well as minimize radiation background there is a tendency to reduce the construction material. The EM calorimeter is placed directly along the central solenoid (actually they share the vacuum vessel). The EM calorimeter has an accordion shape and uses lead absorbers. The tile calorimeter is placed immediately outside the EM calorimeter envelope with radius of 2.3 m and extends to outer radius of 4.3 m. The steel absorber and the active scintillating tiles are used. The HEC consists of two independent wheels per end-cap, located directly behind the end-caps of the electromagnetic calorimeter and sharing the same LAr cryostats. The innermost (outermost) wheels are made from 2.5 cm (5 cm, respectively) thick copper plates with radius in range from 47.5 to 203 cm. The plates are perforated with small LAr gaps. The Forward Calorimeter is integrated into the end-cap cryostats. As the depth of the FCal is limited, a high-density design is desired. The FCal is approximately 10 interaction lengths deep, and consists of three modules in each end-cap: the first, made of copper, is optimised for electromagnetic measurements, while the other two, made of tungsten, measure predominantly the energy of hadronic interactions.

1.3.4 Muon Spectrometer

Muon detectors are in general based on the principle of ionization chambers. Preference of gas detectors over pixel detectors is among other things caused by the price, since the muon spectrometer creates the outermost part of ATLAS, ergo it covers the largest area. The ATLAS muon spectrometer uses four types of technologies: Monitored Drift Tubes (MDT), Cathode Strip Chambers (CSC), Resistive Plate Chambers (RPCs) and Thin Gap Chambers (TGC), see Fig. 1.5. All of them are placed inside of the toroidal magnetic field.

A precision measurement of tracks are mostly provided by MDT except for the muons with a small angle θ between the particle three-momentum and the beam axis, which require using of CSC. RPCs and TGCs are used in the barrel and in the end-cap regions, respectively. Both are participated in triggering (muon p_T thresholds) and the determination of the second azimuthal coordinate to complement MDT's measurement of the bending (radial) direction.

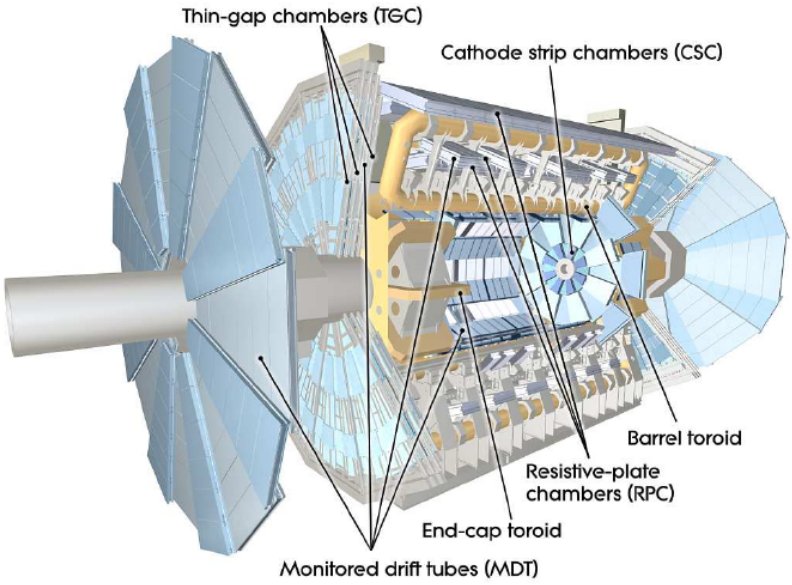

Figure 1.5: Cut-away view of the muon spectrometer [2].

The basic element of the MDT chambers is a pressurised drift tube with a tungsten-rhenium wire placed in the center. Contrariwise CSCs are multiwire proportional chambers with cathodes segmented into strips with higher granularity. They are used in the innermost end-caps to measure particles with higher pseudorapidities. RPC is a gaseous parallel electrode-plate detector with resistive plates made of phenolic-melaminic plastic laminate. TGC is a multiwire proportional chamber, specified by the wire-to-cathode distance smaller than the wire-to-wire distance.

The toroidal magnetic field is generated by three large air-core toroids placed symmetrically around the beam axis and two end-cap toroids. Resulting magnetic field has highly complicated structure, however mostly it is orthogonal to the muon trajectories.

1.3.5 Trigger System

Proton bunches collide approximately every 25 ns in ATLAS [1]; in terms of frequency, the rate of (bunch) collisions is 40 MHz. Since the event data recording is limited to roughly 200 Hz, the rejection factor of 2×10^5 is desired. This requires an overall elimination of uninteresting events in favour of maintaining potential candidates for new physics.

The first layer filter (L1 trigger) uses only information from a subset of detectors (the muon spectrometer and the calorimeter). An event passes through L1 trigger if it suited to one of implemented "trigger menus", made up of combinations of trigger selections. L1 searches for leptons[2]: e, μ and τ (decaying into hadrons), as well as photons, jets and large missing total transverse energy. For each passed event, L1 defines one or more Regions-of-Interest (RoI's), those regions within the detector where interesting features were identified. The RoI data include information on the type of feature identified and the criteria passed, e.g. a threshold; they usually represent 2 % of the total event data. The Level-1 trigger reduces the processed event rate to about 75 kHz, within time for a decision in less than 2.5 μs.

The RoI information serve as an input for Level-2 trigger. The L2 selections use full available information from detector within the RoI's and reduce the trigger rate to approximately 3.5 kHz during 40 ms in average.

The final stage of the event selection is carried out offline by the event filter. Its selections implement analysis procedures within an processing time of the order of seconds per event.

The events passing all trigger selection stages are stored in raw data format (RAW). These are then used to reconstruct physics objects and perform basic calibrations, resulting into reduced format Analysis Object Data (AOD). AODs are still too large for analysis purposes, so smaller files, Derived AODs (DAODs), are produced [7]. Derivation is done in two steps: data reduction and augmentation. Firstly the size of dataset is highly reduced by skimming, thinning and slimming. Skimming and thinning remove whole events and whole objects within remained events, respectively, based on pre-set criteria . Slimming remove of variables within objects uniformly across events without any dependence of any event/object properties; i.e. the same variables are removed for every event and object. Often it is useful to add new information into DAOD (augmentation) to avoid multiple calculations during analysis. Existing objects could be decorated with extra variables (e.g. truth variables for MC) or new reconstructed object containers could be added (e.g. B-vertices, refitted primary vertices).

1.4 The ATLAS Upgrades Summary

In order to achieve the best possible conditions for physics analysis the ATLAS detector is in continual development. Small improvements are performed during long shutdowns of LHC when the data-taking is stopped. The majority of changes are connected to the detector resolution and its radiation resistance. Especially

[1] One bunch collision included in average 20 pp collisions in Run 1 [5] and 32 pp-collisions in Run 2 [6].

[2] Leptons in a hadron collider always mark an inelastic collision.

the innermost parts of detector are highly sensitive to the radiation damage that increases with the increment of the LHC luminosity. The innovations are limited by accessible free space in the cavern for installation and by price.

The first considerable upgrade was implemented during first long shutdown (LS 1) in 2013-2014. The IBL (Insertable B-Layer) was installed as a new innermost layer for the pixel detector. It was inserted between the beam pipe and the current pixel B-layer [3] , back then the innermost pixel layer, at a radius of 3.2 cm. Thus an installation of a new beam pipe with a radius of 2.35 cm was necessary. The new layer consists of 14 staves [8] which are arranged in a turbine-like fashion. Each stave contains 12 double-chip sensors in planar technology and 8 single-chip sensors in 3D technology. The IBL provides a significant improvement to the vertexing, tracking and also b-tagging of the ATLAS detector.

For Run 2 the Level-2 trigger and the event filter were merged into new High-Level Trigger (HLT) that uses entire detector data but reads only minimal amount to reach decision. [9] The rate of saved events increased from 200 Hz to 1000 Hz.

Currently (LS 2 2018-2021) several accelerator updates are being undertaken in order to achieve higher luminosity. Integration of the Linac4 into the LHC injector complex, increment of the the PS Booster energy, reduction of the beam emittance, and upgrade of the collider collimation system are in progress. Thus the peak luminosity will increase to reach $(2-3) \times 10^{34}$ cm^{-2}s^{-1} corresponding to 55 to 80 interactions per pp crossing. [10] The integrated luminosity will be $300-400$ fb^{-1}. Higher number of events requires improvement of the present L1 trigger. This will be achieved by introducing a new tracking and trigger device in the inner layer of the forward muon spectrometer, and a new trigger readout boards and higher trigger granularity in the electromagnetic and forward calorimeters. This upgrade will improve among other things, the event selection (τ, b tagging) and enable ATLAS to establish limits on quartic gauge coupling $\gamma\gamma WW$.

Much more significant upgrades are planned during the LS 3 (2024-27) [11], preparing the ATLAS detector's cooperation with the expected conditions at HL-LHC (High Luminosity LHC). The instantaneous luminosity will be in range $(5-7) \times 10^{34}$ cm^{-2}s^{-1} which coresponds to $140-200$ pile-up events. Total integrated luminosity will reach $3,000$ fb^{-1}. The HL-upgrade would have the highest effect on the performance of ID (especially, the gas-based TRT) that would suffer from radiation damage and high occupancy. Therefore, the the whole ID will be replaced by a new, all-silicon Inner Tracker (ITk) [11]. Hence aging of the calorimetery system and the muon spectrometer (around 20 years of running), they will require restoration as well. The granularity of Tile Calorimeter will have to be increased. The performance of the existing MDT chambers together with the new small wheels, upgraded in LS 2, appears to be sufficient for operation at the HL-LHC. However, the MDT readout electronics will have to be adapted to the new trigger scheme and to the increased hit rates.

[3] Reference of the innermost layer as a B-layer comes from its ability to distinguish if particle came from the primary vertex or from a shifted secondary vertex (e.g. b-hadron decay) more precisely than other ATLAS parts.

1.5 Particle Detection with ATLAS

General purpose detectors, such as ATLAS, are devoted to the broadest examination of collisions in the interaction point; they should distinguish which particles have interacted and determine their properties (four-momenta, charge, lifetime, ...). That could be achieved by precise cooperation of all ATLAS parts.

Charged particles could interact with the inner detector by EM force and cause ionization or excitation of electrons in its material. This signal can be collected and allows to reconstruct a map of hits in the ID and build the particles tracks. Their momenta are established from measurements of the trajectories bending in the magnetic field. The orientation of the bending provides information about charge of particles. Since neutral particles do not interact electromagnetically, they fly through the ID unseen.

A better particle recognition stands on the way how particles deposit their energy in the calorimeters. Losses caused by bremsstrahlung are inversely proportional to particle mass square. The bremsstrahlung initiates and develops electromagnetic showers and therefore the lightest particles detected in ATLAS, electrons, stop in the calorimeter first. The electromagnetic cascades (showers) are composed from electrons, positrons and photons. The EM shower could be also created by photons, however photons and electrons could be easily distinguished because photons do not interact in the ID. Heavier partners of electrons, muons, have so small energy losses (without bremsstrahlung they do not initiate EM showers) that muons with higher energy (typically more than 2 GeV, but it depends on the muon direction) simply do not stop in the calorimeter volume but continue to the MS and out of the detector. The MS measures their tracks based on similar principle as the measurement in the ID and their momenta are established by combination of their tracks in the ID and in the MS. Hadrons interact with matter except of EM by strong interaction as well. That means that although they have higher masses than muons, so their bremsstrahlung is negligible and ionisation is similar to muons, they can loose energy by interaction with nuclei and create hadronic showers as well. ATLAS can use differences in particles ionisation for identification, however that works on the low energy level, $p_T < 0.5$ GeV and hence it can not be used in our study. This is more discussed in the section 2.3.1. The hadron collisions produce more often jets rather than isolated hadrons. Jets consist of many hadrons flying in the same direction. They are produced when a high-energy quark or gluon births in the primary collision and because partons can not stay alone in a state with non-zero colour, they hadronize and result in jets. Taons decay before they could interact with the detector and produce electrons, muons or jets, together with neutrinos. Neutrinos are undetectable for the ATLAS since they can interact by weak interaction only.

This chapter is summary illustrated in Fig. 1.6.

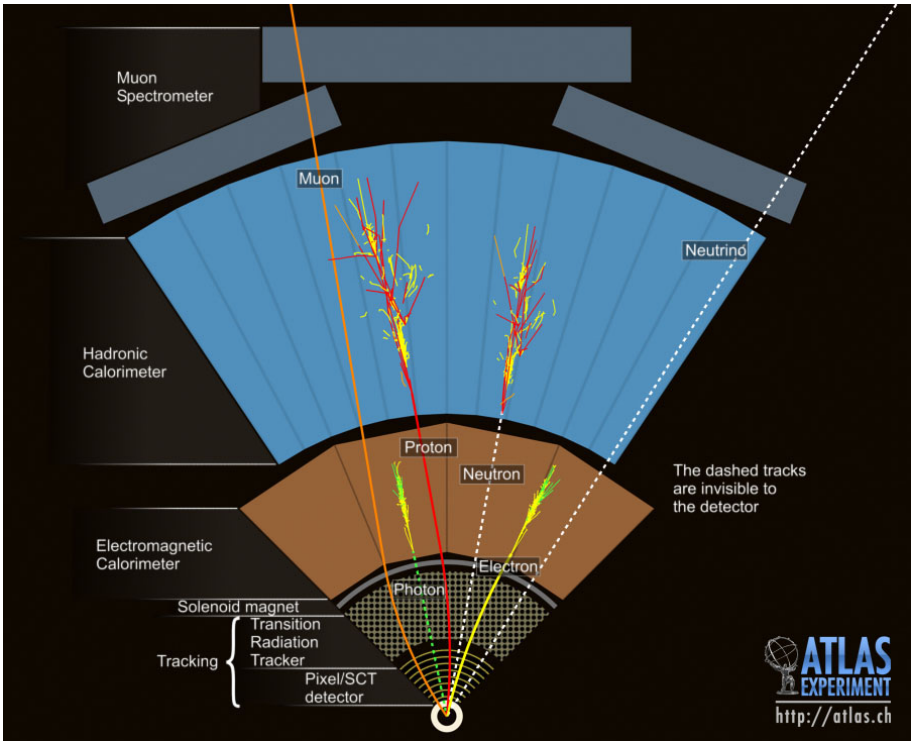

Figure 1.6: Scheme of the particle detection with ATLAS [12].

2. The Decay $B_d^0 \to K^* \mu^+ \mu^-$ in the ATLAS

One of indirect paths for searching a new physics beyond Standard Model is the precise measurement of higher order processes which is the task for flavour physics. New particles could occur in the loops and manifest themselves in the matrix element. The matrix element of decay can be measured only indirectly, e.g. can be extracted from a cross section or from an angular distribution of its products. The flavour physics mainly focuses on looking for flavour changing neutral currents and lepton flavour violation as they seem as the most promising physical channels that could potentially include a substantial trace to a new BSM physics. A big part of flavour physics, the B-physics, is observation of hadrons containing the bottom quark. Hadrons containing the b-quark are the most massive since the top quark decays before it could form a hadron. The large mass of b-quark might increase the coupling to new particles predicted by the BSM theories. B-hadrons are relatively stable so they could fly up to several milimeters in ATLAS before they decay. This distance is enough to distinguish their decay from the primary pp collisions.

This thesis is connected with one of the ATLAS B-physics analysis groups that is specialized in semileptonic rare decays.Our subgroup is focused on the angular distribution of $B_d^0 \to K^* \mu^+ \mu^-$. We also cooperate with an another subgroup trying to reveal a discrepancy of $K^* \mu\mu$ and $K^* ee$ branching ratios. Direct decays of B-meson into K^* and a pair of leptons are prohibited at the tree level therefore they are appropriate to a precise measurement of loop decays. The decays can be described by two types of loop diagrams – the penguin and the box one (shown in Fig. 2.1). The $B \to K^* \mu\mu$ decay rate is thus very low; the branching ratio is only $(9.4 \pm 0.5) \times 10^{-7}$ [13]. Although the $K^* \mu\mu$ decay is very rare, it is nowadays measurable thanks to the enormous LHC luminosity. The first ATLAS analysis of the decay in Run 1 found only slightly above 300 signal events [1].

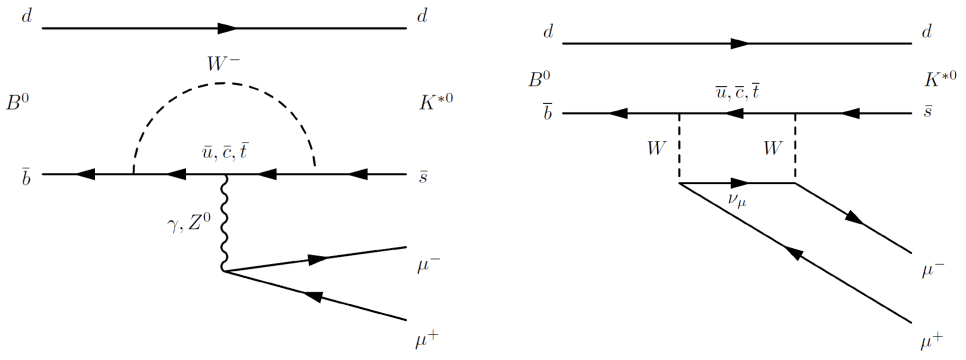

Figure 2.1: Loop Feyman diagrams of the $B_d^0 \to K^* \mu^+ \mu^-$ decay. The left one is usually refered as a penguin diagram, the right one as a box diagram.

2.1 The Standard Model of Particle Physics

The Standard Model of particle physics is a very successful theory describing fundamental particles and their phenomenology. It was formed and developed gradually during the 20th century. In the strict sense of the word, the SM refers to the Glashow-Weinberg-Salam standard model of electroweak interaction solely that was completed in the 70s. Later it was enriched with a description of strong interaction, the quantum chromodynamics (QCD), and now the SM in a broad sense refers to the combination of the GWS theory and QCD. Quarks, leptons and gauge bosons are considered as the most fundamental particles. Matter is composed from two first mentioned and gauge bosons serve as mediators of interactions between them. The present-day picture supposes 4 types of interactions in nature: electromagnetism, weak and strong interaction and gravity. Gravity does not have a proved particle interpretation yet but the remained are well described by particle carriers. EM force is carried by photons (γ), weak decays undergo through $W^{\pm}$ and Z^0 bosons and strong interaction is mediated by gluons carrying colour. The Higgs boson generates masses of leptons and quarks and explains why the photon has no mass, while the W and Z bosons are very heavy in the electroweak theory. The SM incorporates six types of leptons; naturally placed into three generations – electon, muon and tauon. Inside a generation, leptons differ by charge; e, μ and τ has charge -1 and their neighbors, called neutrinos, are chargeless. Similarly, there are six "flavours" of quarks organized in tree generations: (up, down), (strange, charm) and (bottom[1], top).

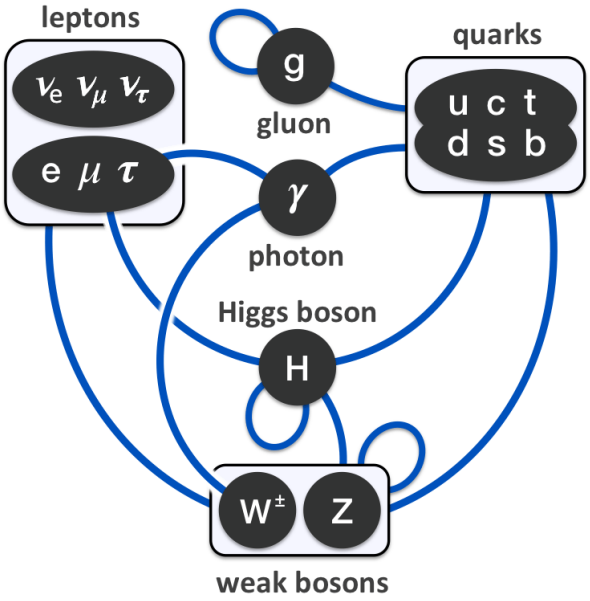

Figure 2.2: Schematic view of the fundamental particles and their interactions described by the Standard Model of particle physics [14].

The SM includes also corresponding antiparticles with the same mass as particles but with opposite quantum numbers (e.g. charge, flavour, lepton number,

[1]bottom quark is as well refered as beauty

colour). The antiparticles of neutral elemental particles without another quantum number, such as γ, Z^0 and H^0, are identical with the particles. Neutrinos and antineutrinos formally differ in the lepton number (neutrino ($L = -1$) births with an antilepton and antineutrino ($L = 1$) with a lepton, respectively); but an evidence, that they are not identical, is still missing.

Mathematically the SM could be described by the $SU(2) \times U(1) \times SU(3)$ group. Electromagnetic and weak interaction form together electroweak interaction described with the inner symmetry group $SU(2) \times U(1)$. It is spontaneously broken by the Higgs mechanism which generates one massless photon, three massive vector bosons ($W^{\pm}, Z$) and a spin-0 massive boson, the Higgs boson. Their electroweak unification is manifested in the relation of the weak coupling constant g and the elementary charge e (the EM coupling constant) bounded via the weak mixing angle θ_W:

$$g \sin \theta_W = e$$

The main quantum number for strong interaction is colour. Each quark carries one of 3 colours (or one of 3 anticolours) described by the $SU(3)$ group. Their colour state can be changed by an emittance or absorption of a gluon carring colour and anticolour simultaneously. Gluon as a strong interaction carrier can occur in 8 colour states since 1 combination is colourless and therefore can not mediate any interaction. Bounded states of quarks, hadrons, are colourless. The colourless state is mainly achieved by two ways: mesons consisting from quark and antiquark with a combination of colour and coresponding anticolour and baryons consisting from quarks with a combination of all three colours or all three anticolours. Leptons do not carry colour charge so they can not interact strongly.

The portion of information provided in this section is enormously summarized and reduced; an interested reader can consult the books [15] and [16].

2.2 Flavour Changing Neutral Currents

Flavour changing neutral currents (FCNCs) denote processes changing the flavour of a fermion current without altering its electric charge. In the Standard Model they can occur only on loop level so they are much more suppressed with compare to flavour changing charged current (FCCC) which can occur at tree level as well. The rarity of FCNCs is essential to their sensitivity to new physics. Suppresion of the SM contributions let us measure even very small BSM contributions that would be undetectable in the higher rate of FCCC processes. New particles may occur in the loops or can mediate FCNC at tree level with small couplings (their suppression is necessary for an agreement with observations).

A typical example for FCNC decay is the b to s transition included in the studied decay.

2.3 Angular Analysis of $B_d^0 \to K^* \mu^+ \mu^-$

Measurement of the $B_d^0 \to K^* \mu^+ \mu^-$ angular distribution is very attractive thanks to its very rich kinematical structure with many angular observables (in-

cluding direct CP asymmetries) [17]. This is more discussed at the end of the section while the beginning is devoted to the practical aspects of the analysis.

2.3.1 The Decay Reconstruction

The final state of the studied decay consists from a kaon, a pion and two muons. It was previously discussed in the Sec. 1.5 that muons are measued in the ID and in the MS and hadrons in the ID and in the calorimeters. As was suggested, the ATLAS particle identification is rather not very usable for hadrons within the kinematic range of the studied decay, so the output from ATLAS contains momenta of two oppositely charged hadrons without any information if K^* decayed into $K^+\pi^-$ or $\bar{K}^*$ into $K^-\pi^+$ or if it is some background composed of other hadronic tracks. This is solved by application of the mass hypothesis on the reconstructed mass of K^*. Firstly the reconstruction of both cases is evaluated; the invariant mass of kaon is assigned to the positive hadron and the pion mass to the negative (resp. vice versa) and the proper four-momenta and the invariant mass of the K^* (resp. $\bar{K}^*$) is computed. The mass distribution of the K^* is theoretically described by the Breit-Wigner distribution with mean 894 MeV and half-width of 50 MeV [13]. Finally both the reconstructed m_{K^*} and $m_{\bar{K}^*}$ are tested whether they fit in the interval 894 ± 50 MeV. In events with both masses or only one mass laying in the interval we choose the case with mass closer to the mean. If neither one mass fits in the interval, the event is excluded from the analysis.

According to the MC simulations, this approach leads to a 10% error of misidentication of the B_d^0 and $\bar{B}_d^0$ decays. This effect was in details investigated in Ref. [18].

2.3.2 Decay Parametrization

The usual parametrization of the angular distribution is shown in Fig. 2.3.

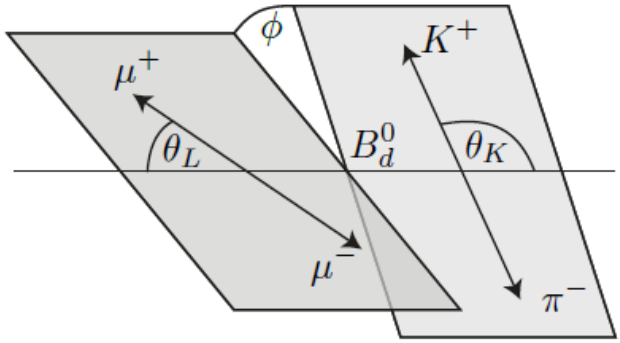

Figure 2.3: Scheme of the ATLAS angular parametrization of the decay [1].

The four kinematic variables are used: q^2, cos θ_K, cos θ_L and ϕ. q^2 stands for the squared invariant mass of the dimuon pair. The data are analyzed in a limited range of q^2: $0.04 - 6.0$ $(\mathrm{GeV/c^2})^2$ (from now on the thesis uses units notation where $c = 1$, as is usual in particle physics). The angle θ_L is defined as

the angle between the direction of the μ^+ (μ^-) and the direction opposite to that of the B_d^0 ($\bar{B}_d^0$) in the dimuon rest frame. The subscript L refers to a possibility of B-meson decaying into K^* and a pair of other leptons: e or τ. However decay into $K^*\tau\tau$ has not been detected yet because of pecularities of taon detection, there is no theoretical doubt for its existance. The angle θ_K is defined as the angle between the direction of the K^+ (K^-) and the direction opposite to that of the B_d^0 ($\bar{B}_d^0$) in the K^* ($\bar{K}^*$) rest frame. The angle ϕ is the angle between the plane containing the dimuon pair and the plane containing the kaon and pion from the K^{*0} in the B_d^0 rest frame. More detailed description can be found e.g. in the Sec. 1.4.1 of Ref. [19].

2.3.3 Background Processes

In this section, the known background processes that needs to be considered in the analysis are introduced. One can divide background events into three types: 1) other decay channels of B_d^0 with the same final state, 2) similar decays that seem like signal for the detector and 3) combinatorial background. The combinatorial background events are created when the detector reconstructed two muons and two hadrons into the a common vertex, however they originated from different decay vertices (a hadron and muon vertex or a partically reconstructed B-decay with an accidental hadron or muon track). This type of background would mostly vanish for the detector with the ideal spacial resolution. The second type of background would be suppressed with a good particle identification system.

The background studies in general are needed for the event selection and for the investigation of possible contributions of backgrounds decays to the measured angular distribution. Studies of 1) and 2) are typically accomplished using fully simulated MC data while 3) is naturally examined on the real data, out of the signal region, for the final event selection. However, still some of its componets could have non-trivial contribution to the angular distribution that must be considered in the analysis.

Decay channels of B_d^0 with the same final state particles (and reconstructed tracks) as the signal decay :

$$B_d^0 \to K^*(K\pi)J/\psi(\mu^+\mu^-)$$

$$B_d^0 \to K^*(K\pi)\psi(2S)(\mu^+\mu^-)$$
$$B_d^0 \to K^*(K\pi)\eta(\mu^+\mu^-)$$
$$B_d^0 \to K\pi J/\psi(\mu^+\mu^-)$$
$$B_d^0 \to K\pi\phi(2S)(\mu^+\mu^-)$$

Decays with similar final state particles, not distinguishable from signal due to missing hadron identification:

$$B_s^0 \to \phi(K^+K^-)\mu^+\mu^-$$

$$B_s^0 \to \phi(K^+K^-)\psi(2S)(\mu^+\mu^-)$$
$$B_s^0 \to \phi(K^+K^-)J/\psi(\mu^+\mu^-)$$
$$\Lambda_b \to \Lambda(1520)(p\pi^-)\mu^+\mu^-$$

$$\Lambda_b \to p\pi^-\mu^+\mu^-$$

Remarkable components of combinatorial background that could have non-trivial contribution to the angular analysis:

$$B^+ \to K^+\mu^+\mu^-$$

$$B^+ \to K^+\psi(2S)(\mu^+\mu^-)$$
$$B^+ \to K^+J/\psi(\mu^+\mu^-)$$
$$B^+ \to K^+\eta(\mu^+\mu^-)$$
$$B^+ \to \pi^+J/\psi(\mu^+\mu^-)$$
$$B^+ \to \pi^+\eta(\mu^+\mu^-)$$

Naturally, similar contributions are expected from the CP-conjugated states to those above (that could be formally achieved by exchanges of $B^0 \leftrightarrow \bar{B}^0$, $B^+ \leftrightarrow B^-$, $K^* \leftrightarrow \bar{K}^*$, ...). Finaly, the wrongly reconstructed events mentioned in Sec. 2.3.1 form a special type of background in this analysis as well.

Data are processed in three separete bins according to q^2 : $[0.04-2]$ GeV^2, $[2-4]$ GeV^2, $[4-6]$ GeV^2. In the analysis there are 3 more bins discussed: $[0.04-4]$ GeV^2 and $[1.1-6]$ GeV^2 serve for a comparison with the Belle and the CMS studies and $[0.04-6]$ GeV^2 that covers the whole range of the analysis. The lower edge is limited by muons mass while the upper is limited by a radiative tail from the $B^0_d \to K^*J/\psi$ events, significantly contributing for q^2 above 6.0 GeV^2. A veto of the range $[0.98-1.10]$ GeV^2 is applied, removing contribution from $\phi \to \mu\mu$ decays.

2.3.4 Angular observables

The angular differential decay rate as a function of q^2 and $\vec{\Omega} \equiv(\cos\theta_K\,, \cos\theta_L, \phi)$ can be written in many ways. In our analysis we used a form with coefficients representing the helicity or transversity amplitudes:

$$\begin{aligned}\frac{1}{\mathrm{d}\Gamma\mathrm{d}q^2}\frac{\mathrm{d}^4\Gamma}{\mathrm{d}\cos\theta_\mathrm{L}\mathrm{d}\cos\theta_\mathrm{K}\mathrm{d}\phi\mathrm{d}q^2} &= \frac{9}{32\pi}\Bigg[\frac{3(1-F_L)}{4}\sin^2\theta_K + F_L\cos^2\theta_K \\ &+\frac{1-F_L}{4}\sin^2\theta_K\cos 2\theta_L - F_L\cos^2\theta_K\cos 2\theta_L \\ &+S_3\sin^2\theta_K\sin^2\theta_L\cos 2\phi + S_4\sin 2\theta_K\sin 2\theta_L\cos\phi \\ &+S_5\sin 2\theta_K\sin\theta_L\cos\phi + S_6\sin^2\theta_K\cos\theta_L \\ &+S_7\sin 2\theta_K\sin\theta_L\sin\phi + S_8\sin 2\theta_K\sin 2\theta_L\sin\phi \\ &+S_9\sin^2\theta_K\sin^2\theta_L\sin 2\phi\Bigg]. \end{aligned} \quad (2.1)$$

Here F_L is the fraction of longitudinally polarised K^* mesons and the S_i are angular coefficients which are functions of the real and imaginary parts of the transversity amplitudes of the decay. The forward-backward asymmetry is given by $A_\mathrm{FB} = 3S_6/4$ [1]. The introduced parameters vary with q^2. Since the analysis is processed in bins, an average value for a given parameter in that bin is calculated.

Although the S_i parameters are used in the analysis, their transformation to P_i parameters is more useful for theoretical predictions. The P_i parameters are defined as fractions of the original parameters in order to eliminate a strong dependence on hadronic form factors which are the greatest source of theoretical uncertainties:

$$P_1 = \frac{2S_3}{1-F_L} \tag{2.2}$$

$$P_2 = \frac{1}{2}\frac{S_6}{1-F_L} \tag{2.3}$$

$$P_3 = -\frac{S_9}{1-F_L} \tag{2.4}$$

$$P'_{j=4,5,6,8} = \frac{S_{i=4,5,7,8}}{\sqrt{F_L(1-F_L)}}. \tag{2.5}$$

The full angular distribution $f(\theta_K, \theta_L, \phi; F_L, S_3, S_4, S_5, S_6, S_7, S_8, S_9)$ has 8 free fitted parameters. High number of free parameters leads to a fit instability, especially in a case with small number of events. Therefore our analysis restricts itself to 4 folded distributions with only 3 free parameters that could be obtained from 2.1 after an application of the following translations. This restriction puts also limits on angles θ_L and ϕ, so the new range of angular observables is listed below in Tab. 2.1.

$$f_{S_4}(\vec{\Omega}; F_L, S_3, S_4) : \begin{cases} \phi \to -\phi & \text{for } \phi < 0 \\ \phi \to \pi - \phi & \text{for } \theta_L > \frac{\pi}{2} \\ \theta_L \to \pi - \theta_L & \text{for } \theta_L > \frac{\pi}{2} \end{cases} \tag{2.6}$$

$$f_{S_5}(\vec{\Omega}; F_L, S_3, S_5) : \begin{cases} \phi \to -\phi & \text{for } \phi < 0 \\ \theta_L \to \pi - \theta_L & \text{for } \theta_L > \frac{\pi}{2} \end{cases} \tag{2.7}$$

$$f_{S_7}(\vec{\Omega}; F_L, S_3, S_7) : \begin{cases} \phi \to \pi - \phi & \text{for } \phi > \frac{\pi}{2} \\ \phi \to -\pi - \phi & \text{for } \phi < -\frac{\pi}{2} \\ \theta_L \to \pi - \theta_L & \text{for } \theta_L > \frac{\pi}{2} \end{cases} \tag{2.8}$$

$$f_{S_8}(\vec{\Omega}; F_L, S_3, S_8) : \begin{cases} \phi \to \pi - \phi & \text{for } \phi > \frac{\pi}{2} \\ \phi \to -\pi - \phi & \text{for } \phi < -\frac{\pi}{2} \\ \theta_L \to \pi - \theta_L & \text{for } \theta_L > \frac{\pi}{2} \\ \theta_K \to \pi - \theta_K & \text{for } \theta_L > \frac{\pi}{2} \end{cases} \tag{2.9}$$

Implementing Eq. (2.7) in Eq. (2.1) yields the distribution in terms of S_5:

$$\begin{aligned} f_{S_5}(\vec{\Omega}; F_L, S_3, S_4) = \frac{9}{8\pi}\Bigg[& \frac{3(1-F_L)}{4}\sin^2\theta_K + F_L\cos^2\theta_K + \frac{1-F_L}{4}\sin^2\theta_K\cos 2\theta_\ell \\ & -F_L\cos^2\theta_K\cos 2\theta_\ell + S_3\sin^2\theta_K\sin^2\theta_L\cos 2\phi \\ & +S_5\sin 2\theta_K\sin\theta_L\cos\phi\Bigg] \end{aligned} \tag{2.10}$$

	θ_L	θ_K	ϕ	$\cos(\theta_L)$	$\cos(\theta_K)$
f_{S_4}, f_{S_5}	$[0, \frac{\pi}{2}]$	$[0, \pi]$	$[0, \pi]$	$[0, 1]$	$[-1, 1]$
f_{S_7}, f_{S_8}	$[0, \frac{\pi}{2}]$	$[0, \pi]$	$[-\frac{\pi}{2}, \frac{\pi}{2}]$	$[0, 1]$	$[-1, 1]$

Table 2.1: The angular parameters range after application of the transformations.

Similarly the remaining transformations (2.6, 2.8 and 2.9) lead to differential decay rates in terms of S_4, S_7 and S_8 respectively. These functional forms can be found in the original paper [1].

2.4 Latest Overview of Measurements

The same angular analysis has been performed except of ATLAS by the BaBar, CMS, LHCb and Belle collaborations. All measurements agreed with the SM within uncertainties, except the $P_5^{'}$ parameter which shows a local discrepancy with predictions in some of the q^2 bins. The latest and most relevant results come from LHCb upgrade of Run 1 analysis with data from 2016. The measured deviations of 2.8 and 3.0 of the standard deviation in Run 1 for the q^2 bins [4,6] GeV^2 and [6,8] GeV^2, respectively, reduces a little to 2.5 and 2.9 σ after the addition of new data which could have two antipodal interpretations. The first approach is that with a higher statistics there is still a remarkable deviation from predictions and therefore some BSM physics can be revealed here. However a more conservative reader would interpret it rather contrariwise that the measurement rejoins the theory (the absolute difference between theory and experiment went down with the new 2016 data). Because of these ambiguous interpretations there is still a huge space for studying this decay in order to confirm one of these hypotheses.

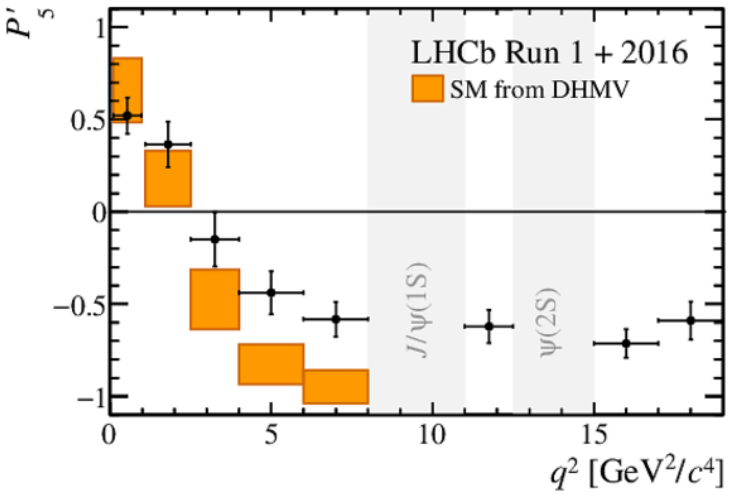

Figure 2.4: Results for the measurement of the $P_5^{'}$ parameter compared to SM predictions [20].

3. Toy Monte Carlo Studies of the Angular Fit

A very important, however sometimes overlooked part of data analysis is a validation of functions used in the fit. It is a process of generating and fitting MC data in order to establish the stability of the fit and to study possible intrinsic biases of fitted functions. Instead of a full generation of decays coming from the *pp* collisions and their propagation through the detector, only toy MC samples of angular (and mass) distribution according to the fitted functions are generated for each studied combination of the initial parameters. These samples are fitted and results of the fit are compared with the initial parameters and are averaged for N_{MC} samples. The number of generated signal and background events was based on results of Run 1 for each bin, and the impact of changing number of events (predictions for Run 2 and HL-LHC) and signal-to-background ratio was studied. The validation was processed twice: ignoring effects of the detector and taking into account the acceptance (affecting the angular shapes) from Run 1.

Before the validation it is necessary to introduce values of theoretical predictions for the SM (sec. 3.1) and to establish parameters' space where the functions are positive ($p.d.f. > 0$, see sec. 3.2). The validation strategy and studied variables are presented in sec. 3.3. In the main body of the thesis, results of the validation are presented only for the parameters F_L and S_5 and the acceptance from Run 1 in Sec. 3.4 since F_L and S_5 are connected with P_5', the parameter where LHCb observed deviation from SM prediction. Plots for all parameters and both acceptances are placed in the appendix.

3.1 Expected SM Values

In order to test the feasibility of measurement of deviation from the SM, it is necessary to well know the SM prediction. Therefore many theoretical publications analyze properties of $B_d^0 \to K^*\ell\ell$ decays. The predicted values of tested parameters are also needed for the fit validation since every test (generating and fitting) varies with only one variable while the rest is fixed for the SM values. This approach is based on the expectation that deviations from the SM should be small and simplifies studying of the evolution of multiparametric functions.

The predicted values from the paper [17](Tab. IV) are listed in Tab. 3.1 after transformation of theoretical P-parameters into S-parameters used in the analysis, using Eq. 2.2–2.5. The paper works with two times softer binning and therefore the P-values are firstly weighted-averaged according to the branching ratio into corresponding bins and then transformed from P to S.

3.2 Positive Range of Fitted Functions

Ranges of parameters F_L, S_3 and S_i, where the fitted functions f_i are positive, are established for each q^2 bin. A function passes the positivity criterion for a

	q^2 bin		
	[0.04 – 2.0] GeV^2	[2.0 – 4.0] GeV^2	[4.0 – 6.0] GeV^2
F_L	0.380	0.780	0.698
S_3	7.98×10^{-3}	-1.73×10^{-3}	-9.32×10^{-3}
S_4	0.061	-0.119	-0.214
S_5	0.227	-0.125	-0.343
S_6	-0.341	-0.220	0.292
S_7	2.05×10^{-2}	2.27×10^{-2}	6.70×10^{-2}
S_8	1.33×10^{-3}	5.59×10^{-3}	4.79×10^{-3}
S_9	-3.80×10^{-6}	-6.60×10^{-6}	-4.28×10^{-6}

Table 3.1: Predicted values of parameters in the SM [13].

specific parameter when it had positive values for the whole parametric space of $\vec{\Omega} = (\theta_K, \theta_L, \phi)$ (can be found in Tab. 2.1) while the rest of parameters are kept on SM values.

Taking into account non-zero effects of the detection process, the fitted functions are multiplied by the detector acceptance (product of polynoms for each angle). The acceptance for Run 2 has not been determined yet, thus the acceptance from Run 1 is used.

In order to cross-check the acceptance is not including any negative shapes in the angular space, the positivity tests were processed both with and without the acceptance. Nevertheless, as expected, both have the same results that are presented in the tab. 3.2.

		q^2 bin		
		[0.04 – 2.0] GeV^2	[2.0 – 4.0] GeV^2	[4.0 – 6.0] GeV^2
f_{S_4}	F_L	0.000 – 0.984	0.020 – 0.970	0.088 – 0.904
	S_3	-0.310 – 0.310	-0.110 – 0.110	-0.150 – 0.150
	S_4	-0.348 – 0.348	-0.295 – 0.295	-0.327 – 0.327
f_{S_5}	F_L	0.056 – 0.960	0.018 – 0.979	0.137 – 0.844
	S_3	-0.240 – 0.310	-0.098 – 0.110	-0.067 – 0.150
	S_5	-0.491 – 0.491	-0.411 – 0.411	-0.443 – 0.443
f_{S_7}	F_L	0.000 – 0.983	0.000 – 0.996	0.004 – 0.981
	S_3	-0.310 – 0.309	-0.110 – 0.110	-0.150 – 0.146
	S_7	-0.479 – 0.479	-0.417 – 0.417	-0.472 – 0.472
f_{S_8}	F_L	0.000 – 0.984	0.000 – 0.996	0.000 – 0.981
	S_3	-0.310 – 0.310	-0.110 – 0.110	-0.150 – 0.150
	S_8	-0.348 – 0.348	-0.295 – 0.295	-0.327 – 0.327

Table 3.2: Range of tested parameters, where the fit functions are positive for the whole angular space of $\vec{\Omega}$.

3.3 Used Methodology

As was mentioned before, the fit behaviour with respect to the number of events and different signal to background ratios was studied. In general, the fit quality should improve for higher number of data, so number of events from Run 1 analysis ($n = 1$) was compared with a rough expectations for Run 2 ($10\times$ more events, $n = 10$) and for High Luminosity LHC update ($n = 100$) [21]. Based on the similiar analysis of $B_s \to J/\psi\phi$, no significant changes in signal to background ratios are expected (difference of Run 1 and Run 2 is only a few percent). Nevertheless, rather more extrem values were tested: $2\times$ more background than signal and vice versa respectively: $r = 0.5, r = 2$, which would better demonstrate effects of different ratios on the fit. The more extreme values or r can also better represent possible updates in the event selection procedure, which is likely to happen in the Run 2 and beyond analyses: using multivariete techniques as Boosted Decision Trees (BDT) instead of simple cuts.

Number of measured signal and background events in Run 1:

q^2 bin	n_{sig}	n_{bck}
$[0.04, 2.0]$ GeV^2	128^{+22}_{-22}	122^{+22}_{-21}
$[2.0, 4.0]$ GeV^2	106^{+23}_{-22}	113^{+23}_{-22}
$[4.0, 6.0]$ GeV^2	114^{+24}_{-23}	204^{+26}_{-25}

Table 3.3: Signal and background yields from the Run 1 analysis [1].

The tests were performed for all q^2 bins separately; together 3195 combinations were tested for both cases: with and without detector acceptance. The tested range of parameters were chosen based on Tab. 3.2:

- $F_L \in [0.1, 0.9]$, with step 0.09; ([0.2,0.8] for 4-6 GeV^2 bin of f_{S_5})
- $S_3 \in [-0.1, 0.1]$, with step 0.02; ([-0.06,0.1] for 4-6 GeV^2 and [-0.08,0.1] for 2-4 GeV^2 bin of f_{S_5})
- $S_4 \in [-0.272, 0.272]$, with step 0.068
- $S_5 \in [-0.4, 0.4]$, with step 0.08
- $S_7 \in [-0.4, 0.4]$, with step 0.08
- $S_8 \in [-0.3, 0.3]$, with step 0.06

$N_{\text{MC}} = 100$ toy MC samples were generated and fitted for each combination. The most important parameters describing the fit stability are number of successfully fitted samples N_{pass} and the fit uncertainty σ_{fit}. Since the very complicated funcions were fitted with a very low statistics, the fit did not pass always successfully ($N_{\text{pass}} \leq N_{\text{MC}}$). The following parameters were computed only from the successfully passed events. The fit error σ_{fit} should scale with $1/\sqrt{n_{\text{ev}}}$; where n_{ev} is a number of signal events ($n_{\text{ev}} \approx n \times r \times n_{\text{Run1}}$). The measured signal yields in Run 1 can be found in Tab. 3.3.

The fit biases are tested by comparison of parameters obtained from the fit with the initial parameters for toy-MC generation, and described by a variable *pull*, defined as:

$$p = \frac{Y_i - Y_{init}}{\sigma_i} \tag{3.1}$$

In the ideal case, the pull distribution should correspond to Gaussian distribution with zero mean and sigma (RMS) equal to unity. A non-zero mean indicates intrinsic bias on the result of a fit-parameter, while non-unity RMS indicates bias on the fit-parameter uncertainty. The mean and RMS of the pull distribution are thus studied below.

3.4 Results

Graphs are plotted in a rather compact way where x-axis represents the q^2 bins used in the analysis, y-axis initial values of the parameter (that was used in generation of the MC samples), and z-axis value of fitted quantity. Two green bands on both sides represent the range of F_L or S_5 values where f_5 is positive in the full decay-angles phase space. For each q^2 bin there are 3 more bins on the right side, from the top, the maximal, mean and minimal values of a given q^2 bin. In addition, on the σ_{fit} plots another bin is added with value of $\sigma_{\text{fit}}^{\text{mean}}/\sqrt{n}$. This value should be same for all n in the q^2 bin. The z-axis range and scale is customarily chosen with its middle corresponding to the ideal value, naturally with the exception of N_{pass}, where 100% of passed fits is the ideal case. There in no expected ideal value of σ_{fit} (theoretically value of $\sigma_{\text{fit}}^{\text{Run1}}/\sqrt{n}$ with statistical uncertainty from Run 1 could be used but it varies with q^2), and therefore medium of the z-scale was phenomenologically chosen as $1/\sqrt{n \times r \times 114}$.

Results presented in this chapter take into account the detector acceptance from Run 1.

3.4.1 Plots of Number of Succesfully Passed Fits and the Fit Error for F_L with the Run 1 acceptance

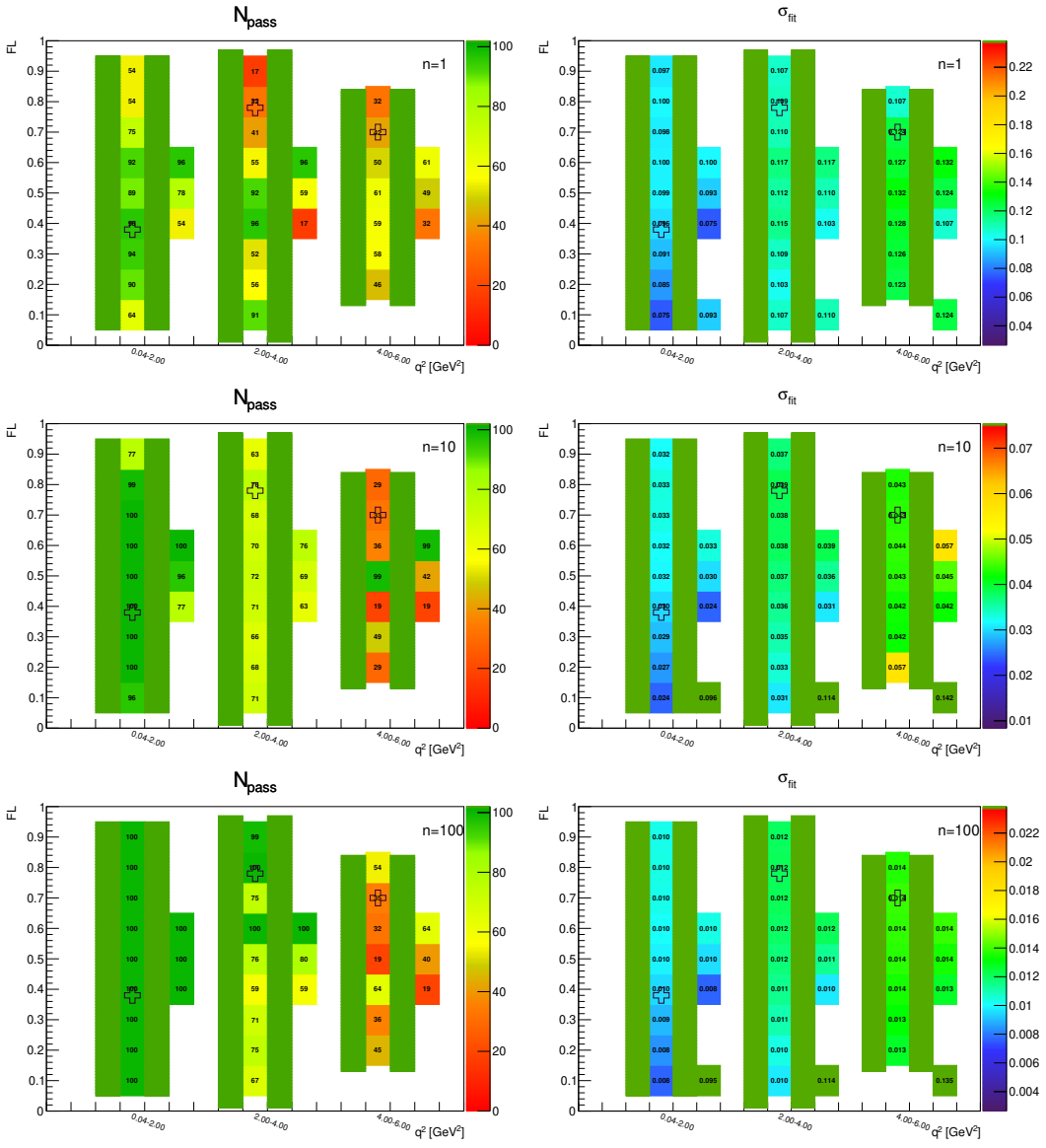

Figure 3.1: Toy-MC studies of the S_5-fold, with r = 0.5. Figures show the number of successfully passed fits on the toy-MC data (left) and average statistical errors on the parameter F_L (right). The green bands represent fit-p.d.f. positivity range. The top figures correspond to the Run-1 like number of events (n = 1), while the middle and the bottom to 10× and 100× larger simulated samples.

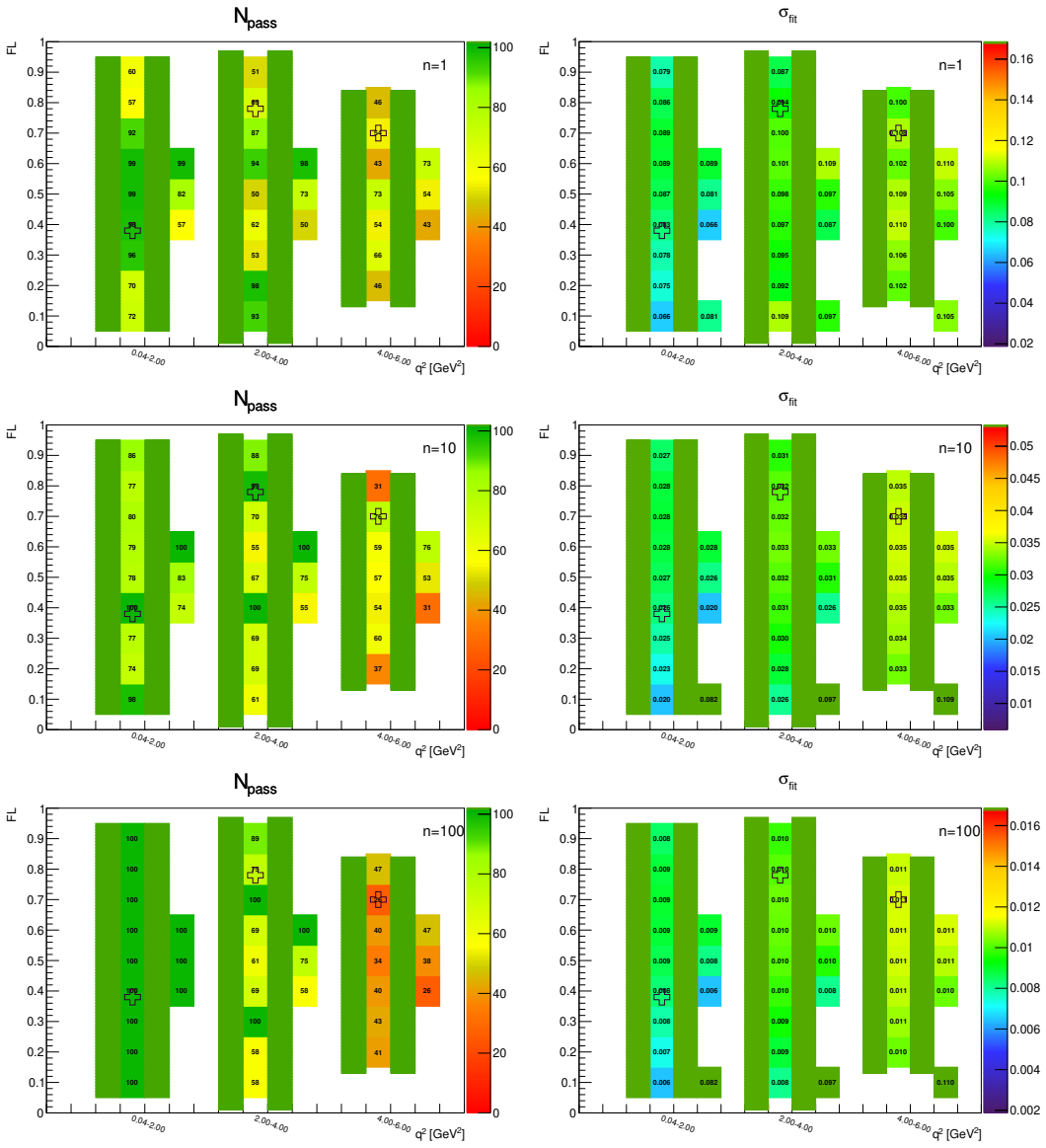

Figure 3.2: Toy-MC studies of the S_5-fold, with r = 1. Figures show the number of successfully passed fits on the toy-MC data (left) and average statistical errors on the parameter F_L (right). The green bands represent fit-p.d.f. positivity range. The top figures correspond to the Run-1 like number of events (n = 1), while the middle and the bottom to 10× and 100× larger simulated samples.

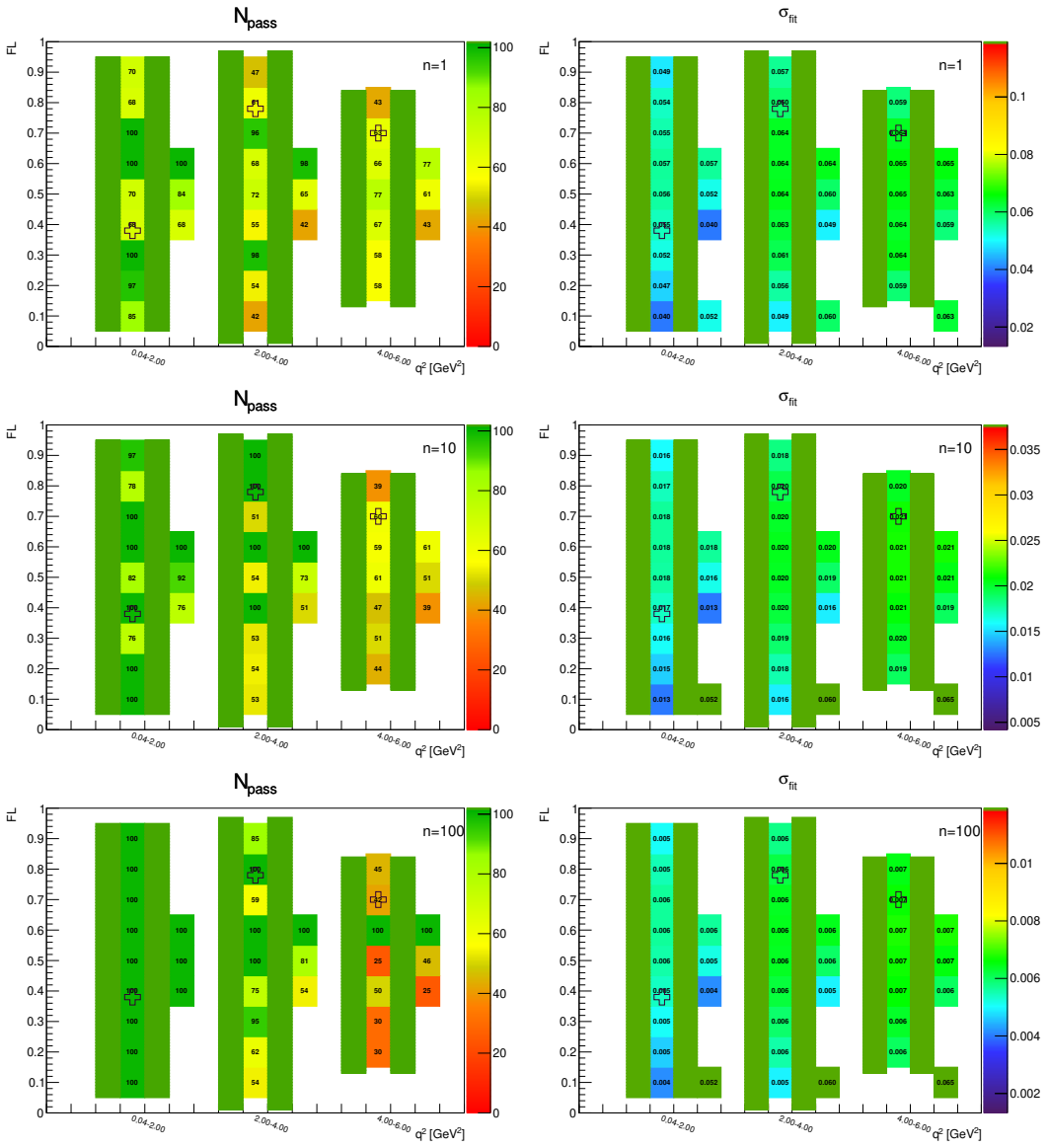

Figure 3.3: Toy-MC studies of the S_5-fold, with r = 2. Figures show the number of successfully passed fits on the toy-MC data (left) and average statistical errors on the parameter F_L (right). The green bands represent fit-p.d.f. positivity range. The top figures correspond to the Run-1 like number of events (n = 1), while the middle and the bottom to 10× and 100× larger simulated samples.

3.4.2 Plots of Number of Succesfully Passed Fits and the Fit Error for S_5 with the Run 1 acceptance

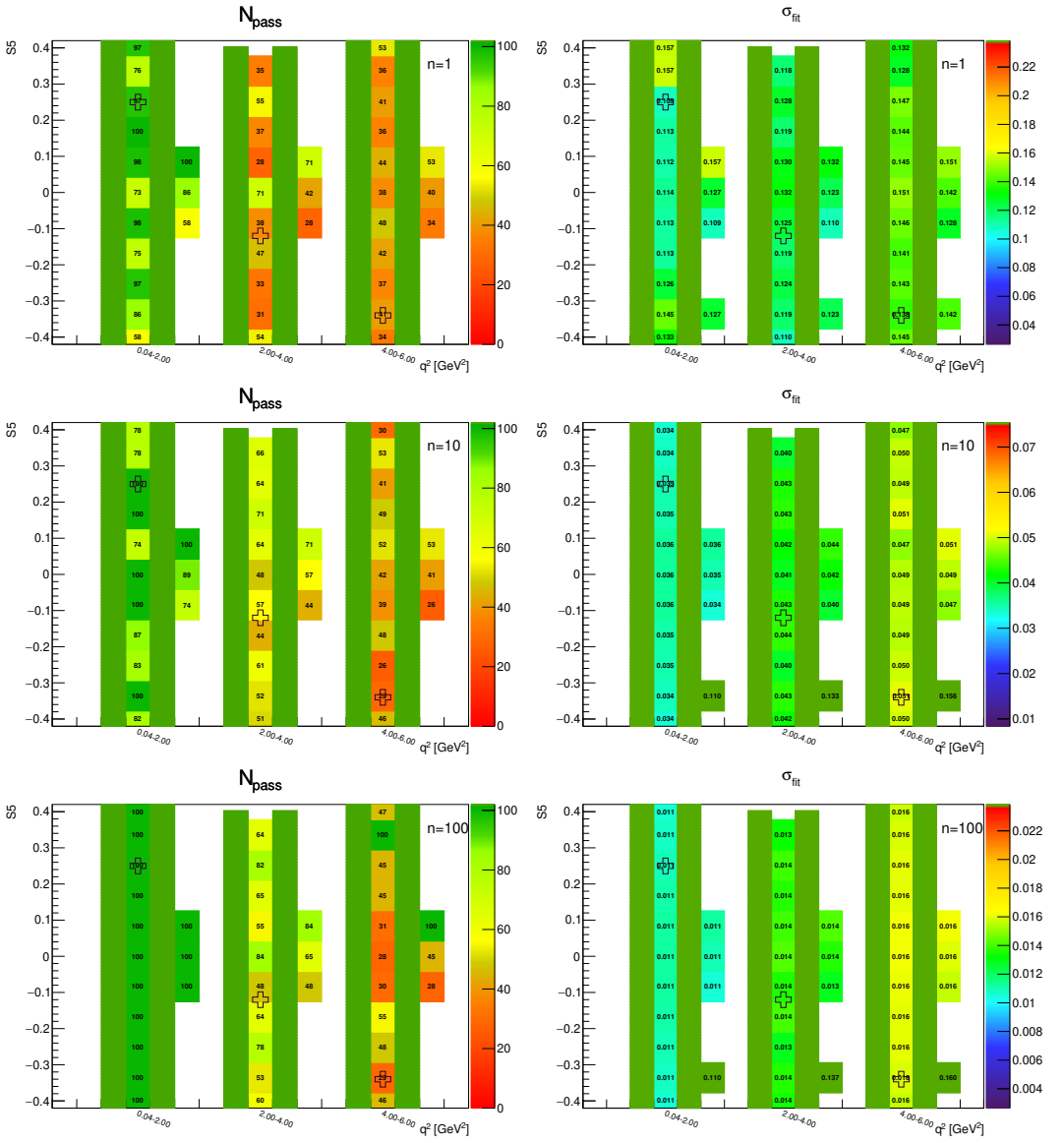

Figure 3.4: Toy-MC studies of the S_5-fold, with r = 0.5. Figures show the number of successfully passed fits on the toy-MC data (left) and average statistical errors on the parameter S_5 (right). The green bands represent fit-p.d.f. positivity range. The top figures correspond to the Run-1 like number of events (n = 1), while the middle and the bottom to 10× and 100× larger simulated samples.

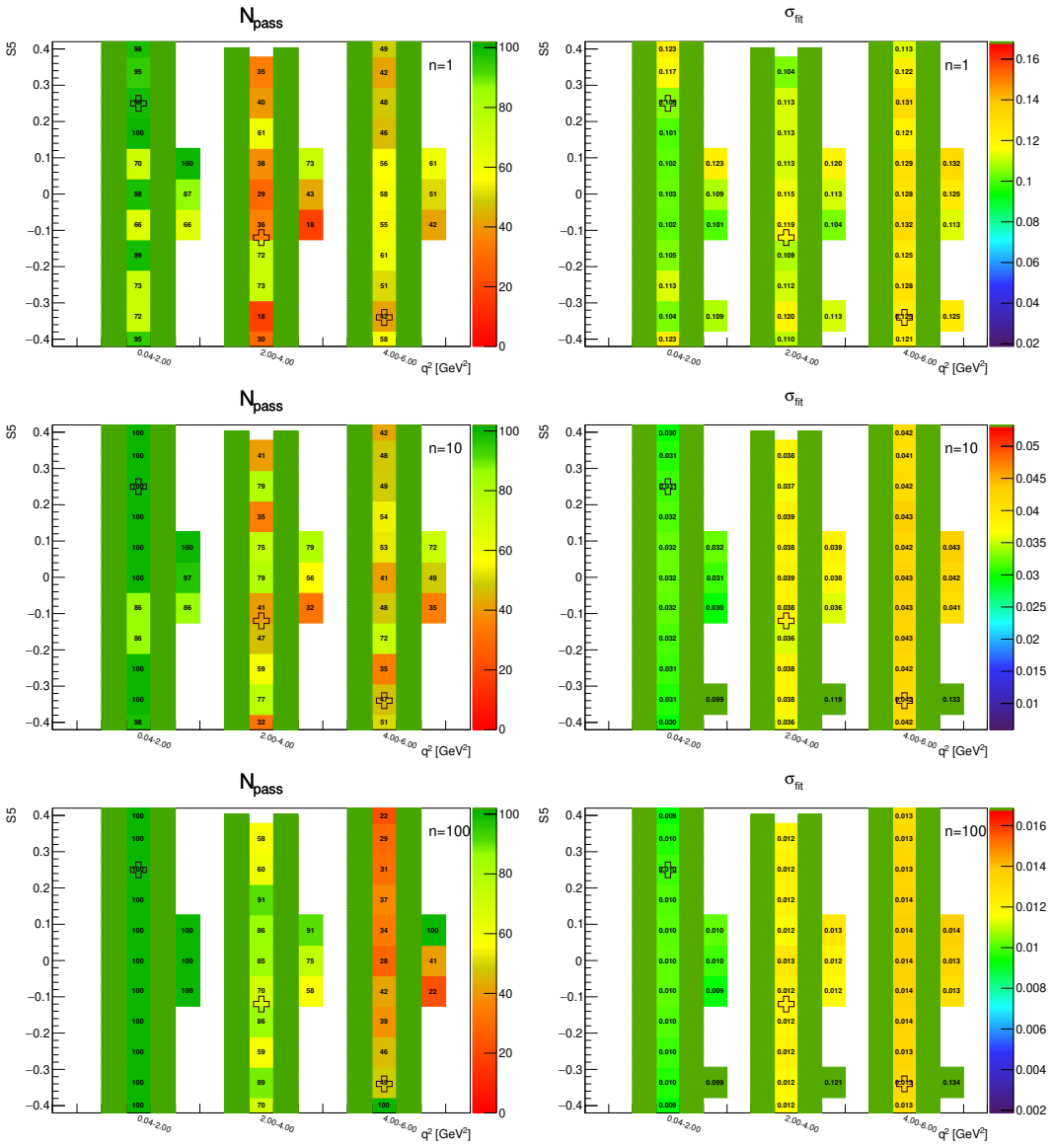

Figure 3.5: Toy-MC studies of the S_5-fold, with r = 1. Figures show the number of successfully passed fits on the toy-MC data (left) and average statistical errors on the parameter S_5 (right). The green bands represent fit-p.d.f. positivity range. The top figures correspond to the Run-1 like number of events (n = 1), while the middle and the bottom to 10× and 100× larger simulated samples.

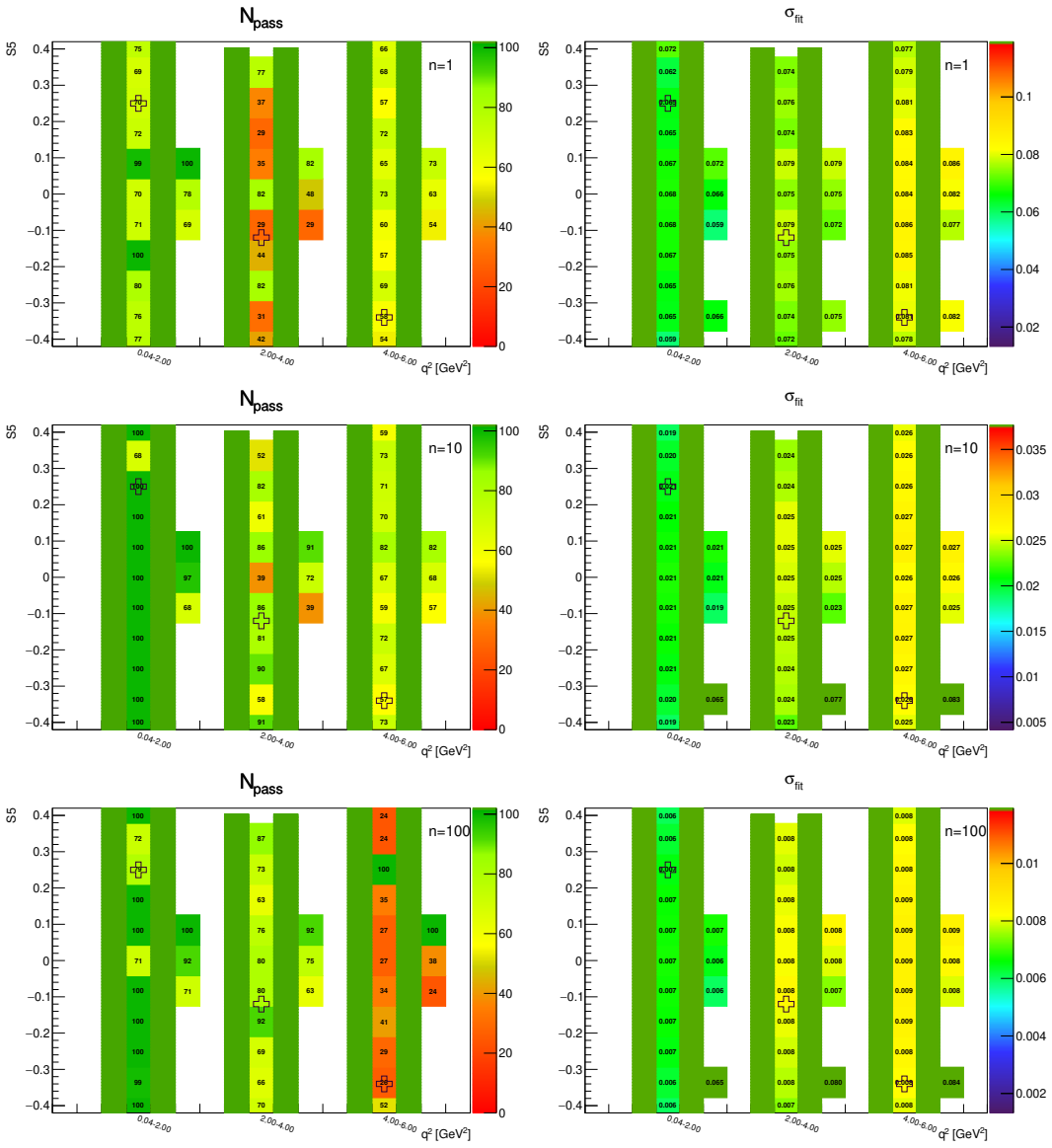

Figure 3.6: Toy-MC studies of the S_5-fold, with r = 2. Figures show the number of successfully passed fits on the toy-MC data (left) and average statistical errors on the parameter S_5 (right). The green bands represent fit-p.d.f. positivity range. The top figures correspond to the Run-1 like number of events (n = 1), while the middle and the bottom to 10× and 100× larger simulated samples.

3.4.3 Pull Plots for F_L with the Run 1 acceptance

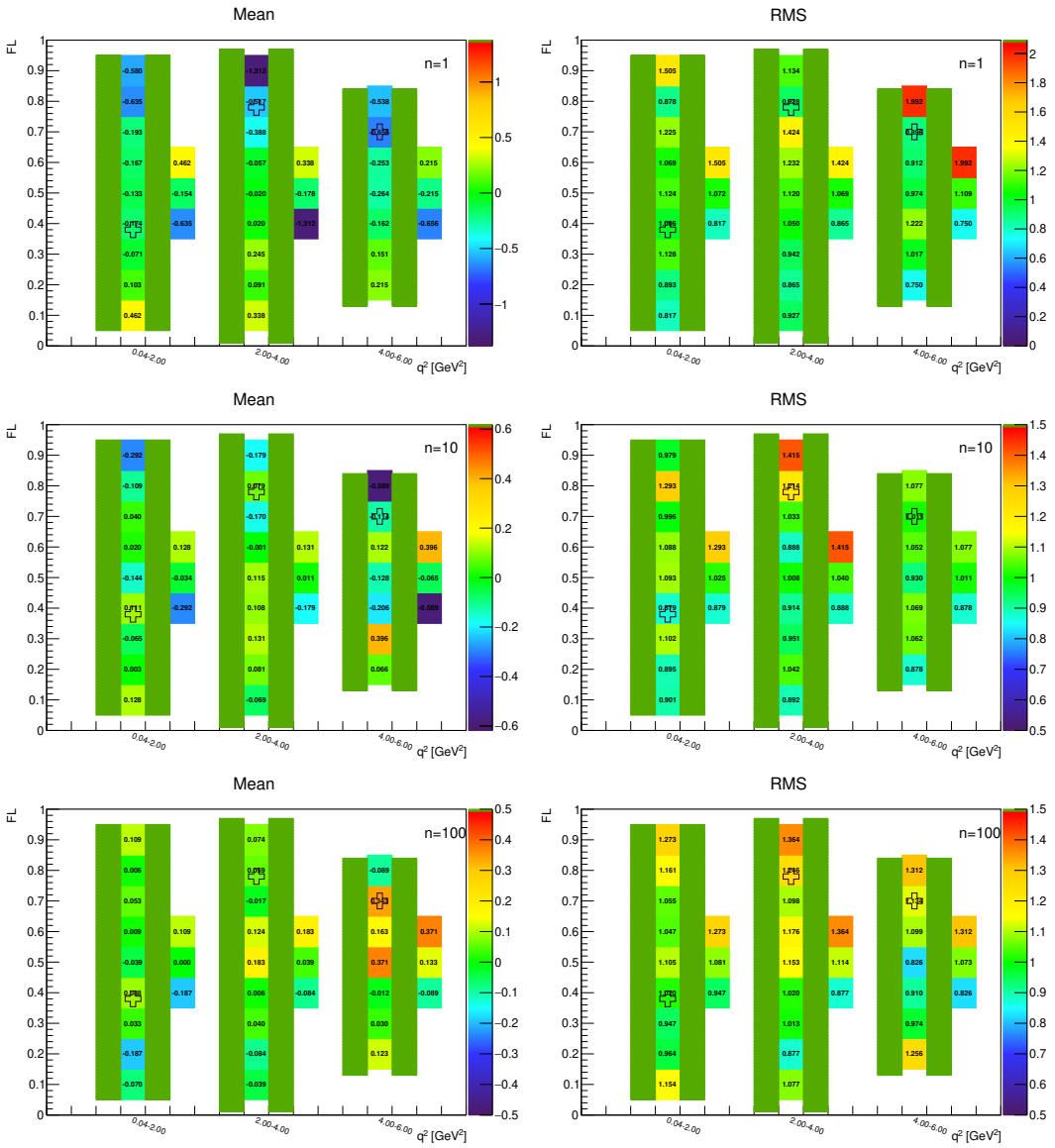

Figure 3.7: Toy-MC studies of the S_5-fold, with r = 0.5. Figures show the gaussian mean (left) and RMS (right) of pull on the parameter F_L. The green bands represent fit-p.d.f. positivity range. The top figures correspond to the Run-1 like number of events (n = 1), while the middle and the bottom to 10× and 100× larger simulated samples.

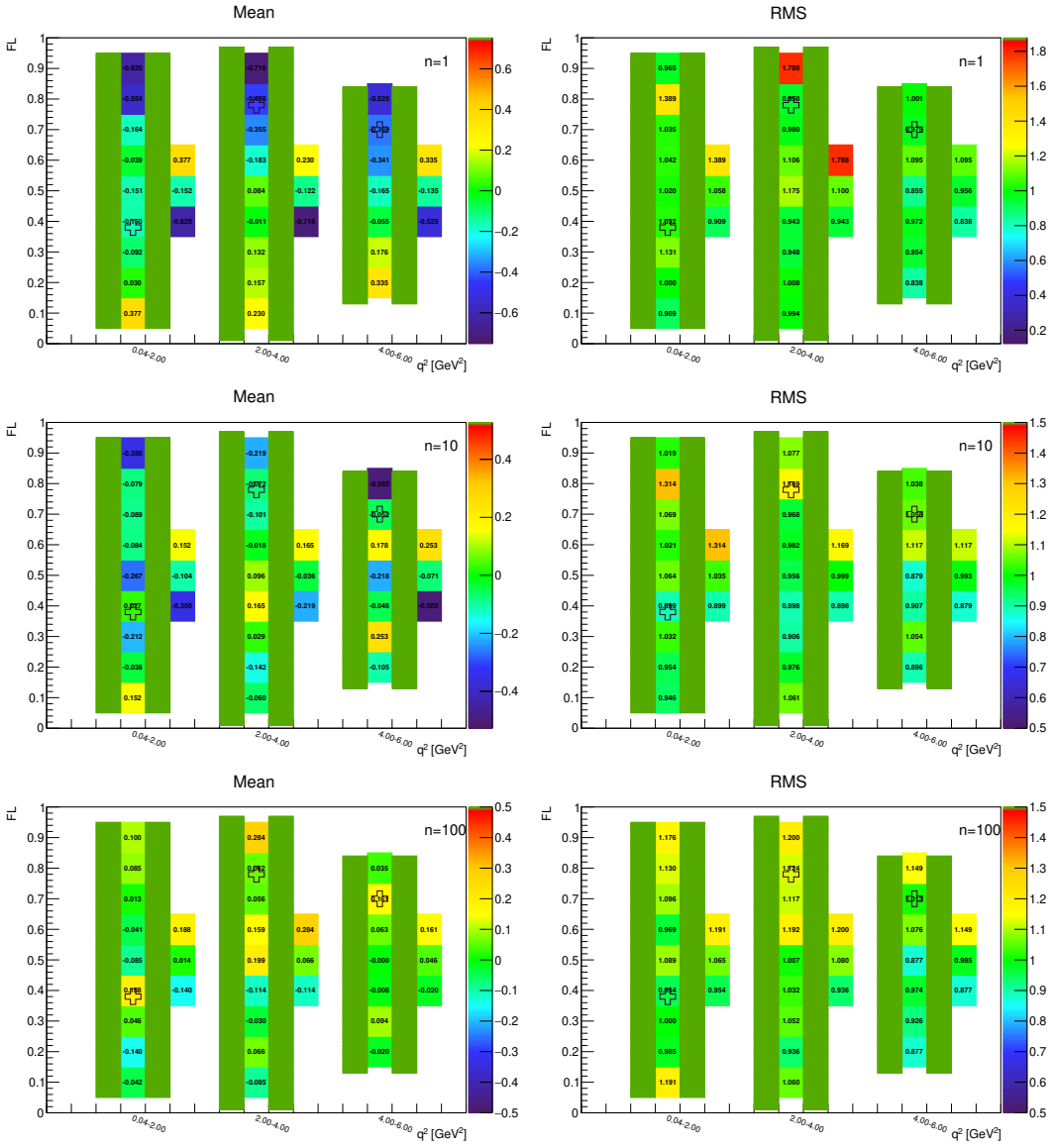

Figure 3.8: Toy-MC studies of the S_5-fold, with r = 1. Figures show the gaussian mean (left) and RMS (right) of pull on the parameter F_L. The green bands represent fit-p.d.f. positivity range. The top figures correspond to the Run-1 like number of events (n = 1), while the middle and the bottom to 10× and 100× larger simulated samples.

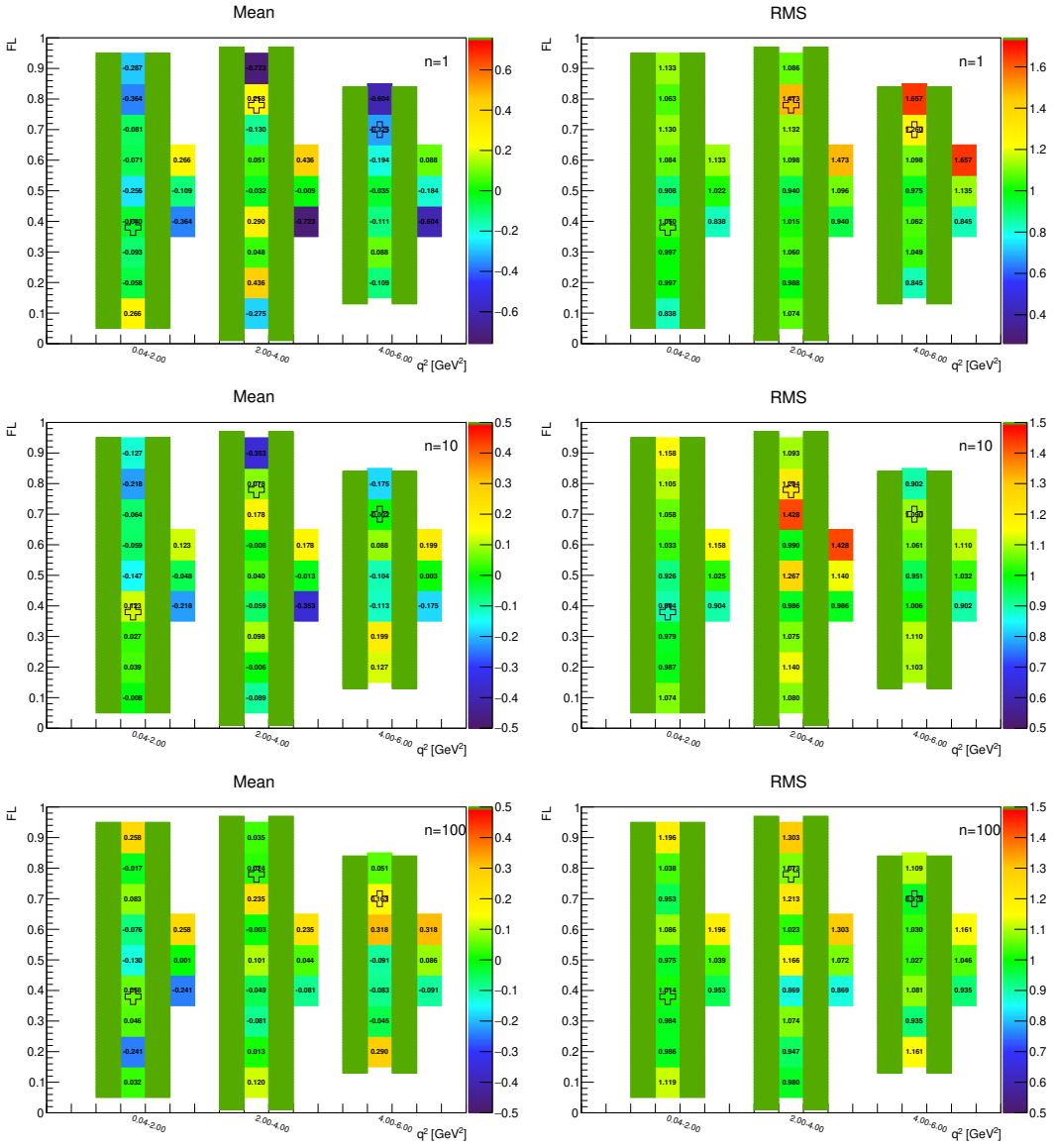

Figure 3.9: Toy-MC studies of the S_5-fold, with r = 2. Figures show the gaussian mean (left) and RMS (right) of pull on the parameter F_L. The green bands represent fit-p.d.f. positivity range. The top figures correspond to the Run-1 like number of events (n = 1), while the middle and the bottom to 10× and 100× larger simulated samples.

3.4.4 Pull Plots for S_5 with the Run 1 acceptance

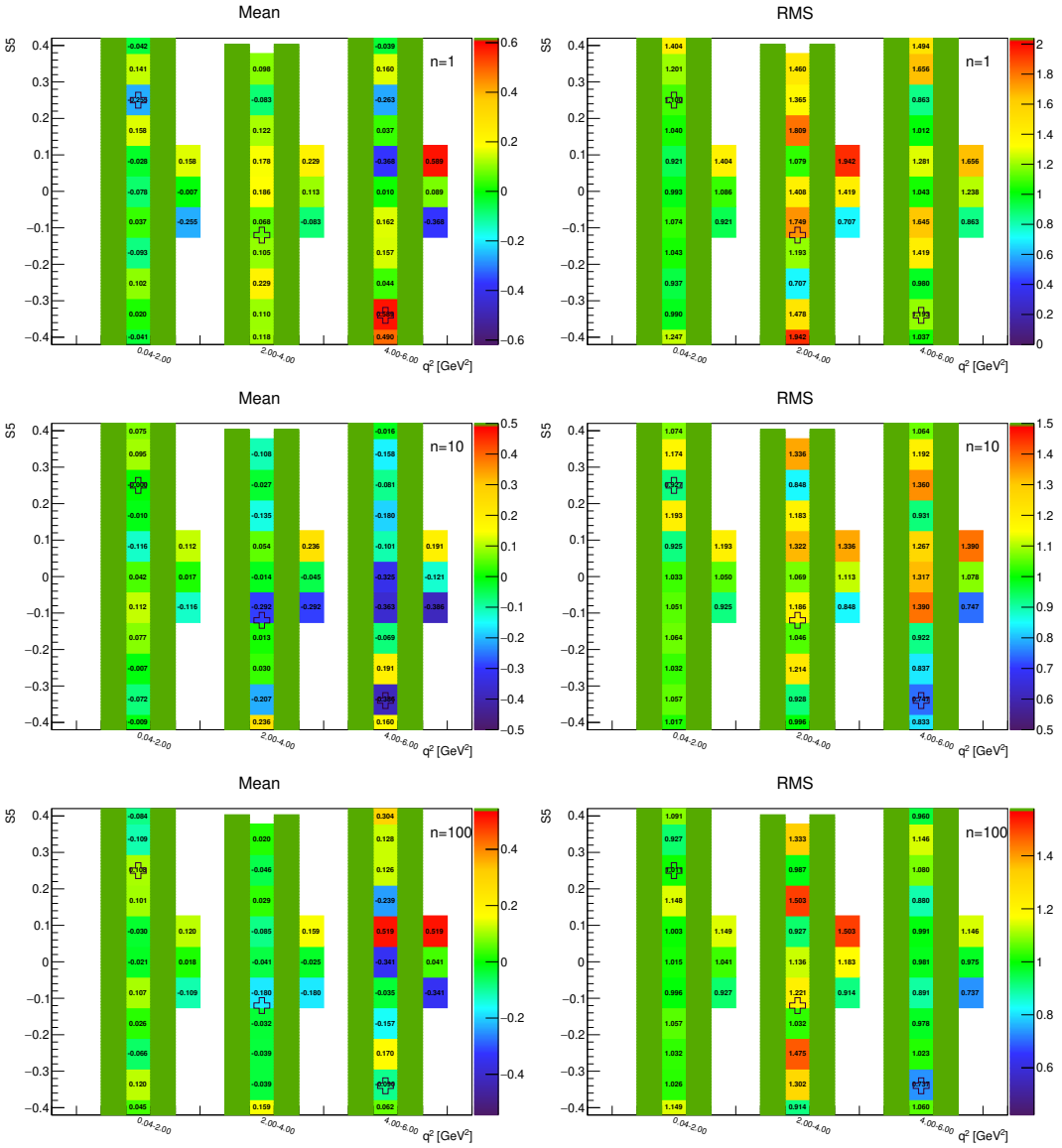

Figure 3.10: Toy-MC studies of the S_5-fold, with r = 0.5. Figures show the gaussian mean (left) and RMS (right) of pull on the parameter S_5. The green bands represent fit-p.d.f. positivity range. The top figures correspond to the Run-1 like number of events (n = 1), while the middle and the bottom to 10× and 100× larger simulated samples.

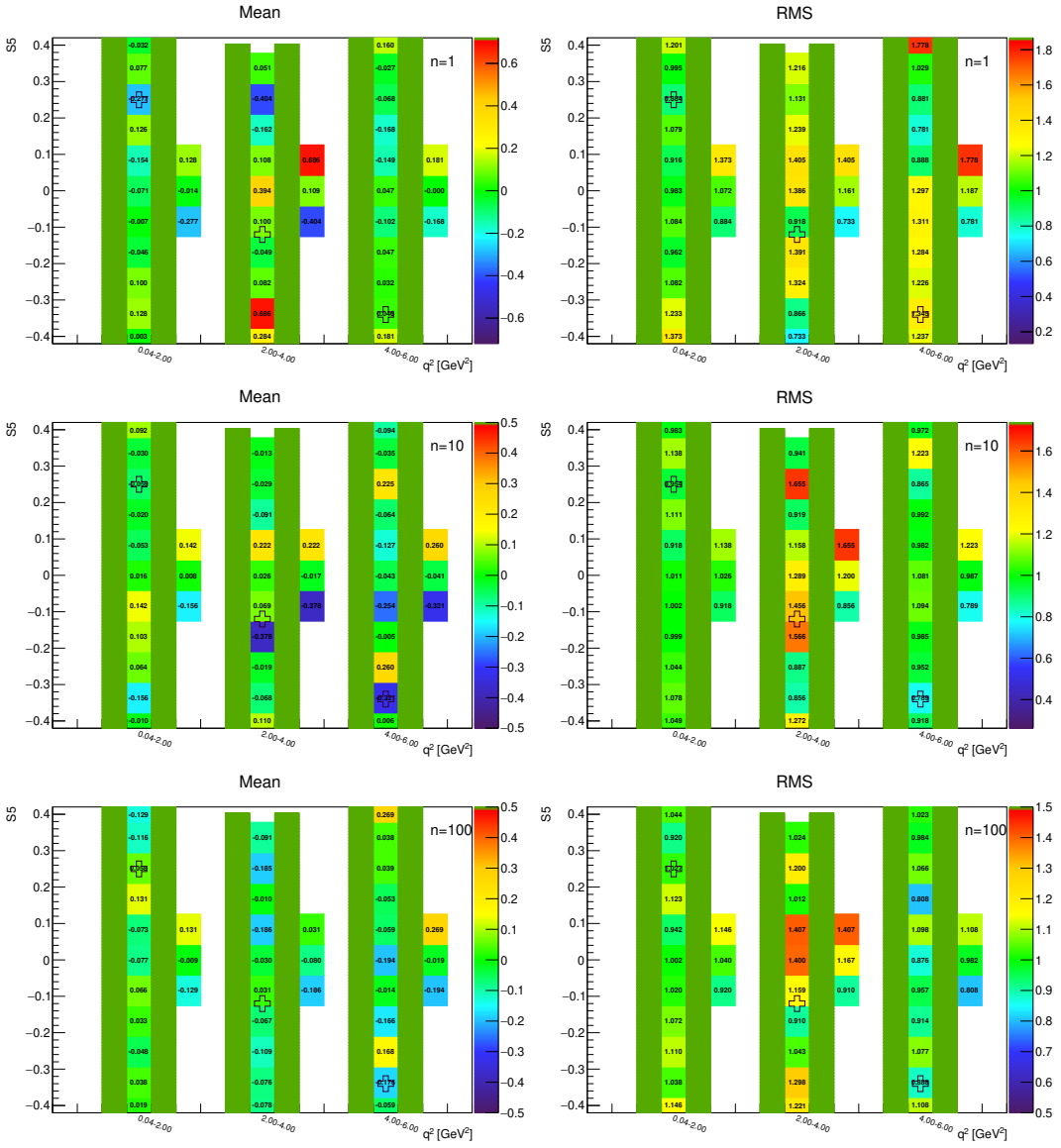

Figure 3.11: Toy-MC studies of the S_5-fold, with r = 1. Figures show the gaussian mean (left) and RMS (right) of pull on the parameter S_5. The green bands represent fit-p.d.f. positivity range. The top figures correspond to the Run-1 like number of events (n = 1), while the middle and the bottom to 10× and 100× larger simulated samples.

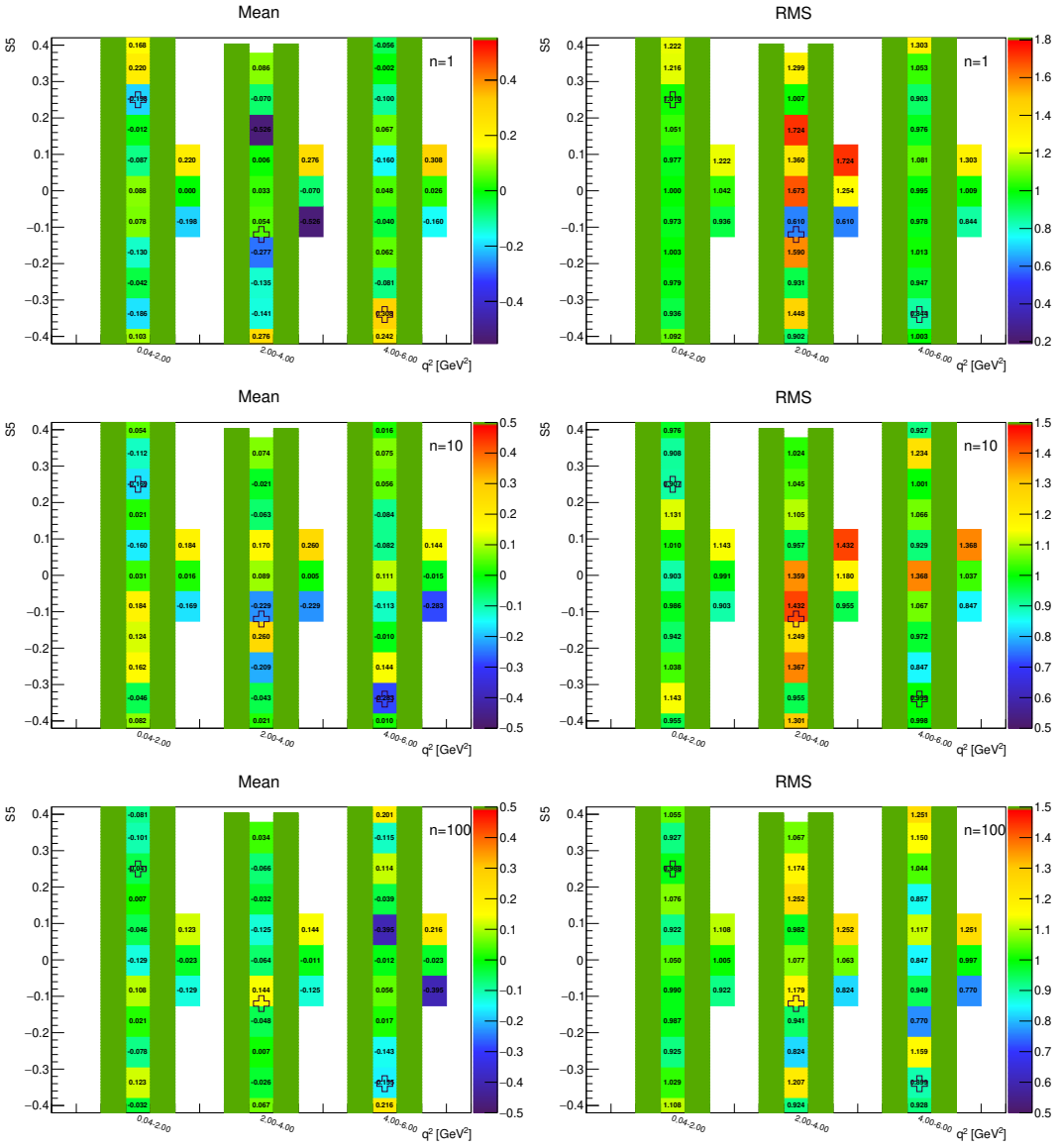

Figure 3.12: Toy-MC studies of the S_5-fold, with r = 2. Figures show the gaussian mean (left) and RMS (right) of pull on the parameter S_5. The green bands represent fit-p.d.f. positivity range. The top figures correspond to the Run-1 like number of events (n = 1), while the middle and the bottom to 10× and 100× larger simulated samples.

3.5 Summary of the Toy-MC Studies

This analysis was performed with 100 generated toy MC samples for each tested combination. These samples were fitted and results of the fits were compared with the initial parameters. Four variables were studied in order to examine stability and intrinsic biases of the fit: number of successfully passed fits, paramaters fit errors, gaussian mean and RMS of pulls of each of the parameters.

N_{MC}=100 was chosen as the best compromise between the relevance of results and the computational time consumed. This contributed to rather large fluctuations (uncertainties) of the results. We expect that sufficient suppression of statistical fluctuations could be achieved by 10 × increasement of N_{MC}. Despite of the fluctuations, there are some visible trends of the fit behaviour for different signal and background yields discussed below. We studied 9 combinations of n and r in order to establish properties of the fit for possible signal and background yields of Run 2 and HL-LHC. In the following steps of the Run 2 analysis after establishing the yields, the tool-kit developed can be used in a new study focused only on the established yields. Without testing other n-r combination, it would be possible to use N_{MC}=1000 with only small increasement of total computational demands.

The analysis of the number of successfully passed fits has the most straightforward interpretation of results, the fit is more stable for regions with higher N_{pass}. Expected increase of N_{pass} with higher number of events was observed in the [0.04, 2] and [2,4] GeV^2 q^2 bins while N_{pass} decreases in the [4,6] GeV^2 bin. This behavior is typical for all parameters F_L, S_3 and S_i for all f_i with acceptance from Run 1. The unstability in the most interesting bin could imply very undesirable consequences for the angular analysis investigating discrepancy between the fit and theory hidden there. The third bin is specific by 2× more background (see tab. 3.3), however, we suppose that different signal and background yields did not caused the unstability, since in the first two bins N_{pass} increases for each r, even for 2× more background (r=0.5) and results for the [4,6] GeV^2 bin does not improve even for r=2 (n_{sig}=n_{bck}). When we compare results with and without the acceptance, in the results without acceptance (see attachment) the opposite behaviour was observed, not so unambiguous growth or a small decline for the first two bins and expected increase in the third bin. Therefore we conclude that the unstability in the [4,6] GeV^2 bin was affected by coefficients of the polynomials describing acceptance (coefficients are specific for combinations of the q^2 bins and functions fitted). This was not deeper investigated yet because of planned modification of the acceptance description in Run 2. Instead of uncorrelated product of polynomials, separated for each angle, three-dimensional spherical harmonical functions will be used.

Values of the fit error are very similar without any significant fluctuations for the whole q^2 bin with more extreme values placed on the edges of tested ranges, where the fit can not estimate its error properly since negative values of functions do not have any probability interpretation and are forced to zero. Values are for the studied parameters F_L and S_5 smallest for the first q^2 bin and highest for the third bin as was established in the Run 1 analysis (Tab. 2 in Ref. [1]). The fit error scales with the number of events as was expected that is demostrated by the same ratio of $\sigma_{\mathrm{fit}}^{\mathrm{mean}}/\sqrt{n}$ for all n within the q^2 bin.

The ideal values that pull mean and pull RMS would achieve with the infinite statistics are 0 and 1, respectively. Results have rather fluctuating character, but the values do not indicate any major problems. Average values in the q^2 bins vary around the expected values. The bias on the pull mean is not exceeding value of 1 (i.e. the fit-parameter bias is well below statistical statistical uncertainty). The bias on the pull RMS (i.e. the bias of the fit-parameter statistical error), is typically at the order of 10%, although there are few cases suggesting almost factor of 2 $\times$ underestimation of the fit-parameters error, which should be investigated further. Reduction of the biases with increased number of events (n) is not observed, suggesting that even the 100 $\times$ larger data sample from Run 1 is still too small for the complex mass-angular fit to reach the expected zero-bias with infinite statistics.

4. Events Preselection

The final output from the ATLAS detector are analysis object data (AOD) saving all information about events intended for physics analyses. An individual analysis (or more likely a working group, counting more analyses) choose which data (from the AOD) will be studied, and saves them into derived analysis object data (DAOD). Events are typically selected according to triggers passed or a specific decay signature. Derivation, in addition to preselect events, discards unused information for the analysis (e. g. B-physics analyses normally do not use outputs from the calorimetry and therefore they are removed) and reconstructs physical quantities specific for the analysis (fitting of 4-particle vertex $K\pi\mu\mu$, reconstruction of m_B, m_{K^*}, etc.). DAOD represents an intermediate stage of the events preselection and still contains majority of information that would never be used in the following analysis after the event preselection. Therefore DAOD is again reduced and converted into a ROOT n-tuple, maintaining only physical quantities required for the analysis. Within the process of n-tuple creation, baseline selection criteria are applied in order to suppress majority of background and to ensure a sufficient quality of the measurement.

This chapter is focused on the last step of the events preselection, transformation of the DAOD into the final n-tuple. The software developed is tested on Monte Carlo data which passed the whole reconstruction process as the real data and were saved in the DAOD format. The MC samples of signal and most of background decays (and CP-conjugated antidecays) were used. A next stage of the analysis after the preselection would be the final event selection. In Run 1, simple selection criteria (cuts on chosen variables) were used, in Run 2 there is a plan to use more advanced multivariete techniques (e.g. BDT). However an optimization of selection criteria or BDTs requires the inclusive background taken from the real data (out of the region of interest) which are not available by the time of finishing this thesis. Therefore, the demonstration of the functionality of the developed n-tuple maker software is performed applying optimized criteria from the Run 1 analysis.

The chapter is organized as follows: technical aspects of the work are discussed in Sec. 4.1, baseline and optimized selection criteria of Run 1 are introduced in Sec. 4.2, branching ratios of studied background decays are listed in Sec. 4.3, and Sec. 4.4 is focused on a presentation of results of the selection criteria application. Detailed examination how the cuts effect the number of passed events of the signal decay and antidecay is described in Sec. 4.4.1. Sec. 4.4.2 indicates a rough estimation of expected proportion of background decays to 1 signal event.

4.1 Used Software

AOD and DAOD data are saved in a special data format xAOD [7] that is a new ROOT-readable data format [1]. xAOD includes information about the event (event number, luminosity block, run number, etc.) and about reconstructed objects within each event (tracks, muons, jets, etc.). Information conserved in

[1] In Run 1, AODs could not be read by ROOT directly.

the xAOD is split into the object itself and the auxiliary store, containing the numerical values of the object properties (m, p_T, etc.). This enables reading of a given variable across many objects/events with no necessity to load the full event. As all particle objects are stored in containers, it is possible to iterate over particles of the same type in a given event.

All ATLAS production workflows as event generation, detector simulation, reconstruction and derivation production as well as ATLAS High Level Trigger are handled with Athena [22], the ALAS software framework . Measured RAW data or generated MC samples are preprocessed into ESD (Event Summary Data), ESD is processed and saved into AOD from which DAOD is derived. An analysis can be also performed at the Athena level but more often the ROOT-based frameworks are involved. In the second case, instead of using derivated dataset (DAOD, which can be be read with ROOT on lxplus after launching AnalysisBase [23]) it is a good practise (or rather a necessity) to create ROOT n-tuple with only these information that will be used in the analysis.

For this purpose, software from the $\tau \to \mu\mu\mu$ analysis [24], based on ELBrain [25] and the PyAnalysisTools [26], was used as a model and was rebuilt into a new class $ELKstarMuMu$ within this framework, according to requirements of the $K^*\mu\mu$ and K^*ee analyses. The class is still in progress, however tasks within the scope of this thesis were successfully accomplished. After adaption to connection of different parts of the framework through the Python environment, the class $ELKstarMuMu$ was formally prepared beside the original $ELTau3Mu$ and reading and saving of following variables was ensured:

- event information (event number, luminosity block, run number),
- variables prepared during derivation (reconstructed masses, B life time, vertex fit quality, refitted primary vertex (PV) position),
- variables computed from them (p_T, η),
- "true variables" for MC samples (flag marking whether the reconstructed decay comes from the real signal decay, "true" positions of PVs).

The AOD contains list of particle tracks and their association primary pp collision vertices. Secondary (B-)vertices are not searched for. Therefore during the derivation, muon pairs with opposite charge and dimuon invariant mass lower than 5500 MeV are firstly refitted into dimuon candidates requiring vertex fit quality: $\chi^2/n.d.f. < 20$. Then B-vertices are formed from the dimuon candidates and two other oppositely-charged tracks not identified as muons. Finally all primary vertices are refitted excluding the 4-candidate tracks [19].

There are more possible approaches to assign a primary vertex from which the B-candidate is expected to originate. The following 3 are typically used: *minimal* a_0, *minimal* z_0 and *maximal* $\Sigma_i\ |p_{T_i}|$ where i runs through all tracks comming from the PV, a_0 stands for 3-dimensional impact parameter (distance between line in B-momentum direction pointing from the B-vertex) and z_0 represents distance in the longitudinal direction z along the beam. Maximal $\Sigma\ |p_T|$ chooses a vertex with the highest energy in the transversal direction that has the highest probability of an "interesting" decay. B-physics adopts the minimal a_0 approach since b-quark production is quite common in pp collisions so B-mesons do not

necessary have to origin in potentially the most interesting pp interaction vertex. Fortunatelly, the τ_B measurement is rather insensitive to the choice of PV, because the PVs are placed along the z-axis with minimal spread in the transverse (xy) plane, while the B-meson lifetime is calculated using the projections into the transverse plane.

4.2 Selection Criteria

In this section the baseline and optimized selection criteria that were used in ATLAS Run 1 data analysis are introduced.

4.2.1 Baseline Cuts

A set of baseline cuts is applied to ensure sufficient quality of the measurement. They are applied at the "n-tuple creation level" so only events passed through these selection criteria are saved. This set is taken from the ATLAS 2011 $B_d^0 \to K^{*0}J/\psi$ analysis as it has the same final state:

- to account for detector acceptance effects, all four tracks as well as K^*, di-muon and B candidates are required to have rapidity $|\eta| < 2.5$,
- m_{K^*} lays in the interval mean $\pm$ halfwidth: [846, 946] MeV,
- m_B lays in [5150, 5700] MeV,
- trigger requirement: $p_{T\mu} > 3500$ MeV,
- to reduce inaccuracies of the ID: $p_{Tmesons} > 500$ MeV (this cut was applied during the derivation and therefore we do not consider it in the thesis),
- the fit quality of dimuon vertex: $\chi^2/n.d.f. < 10$.

4.2.2 Run 1 Cuts

The selection criteria used in the Run 1 were optimised according to the efficiency defined as $\mathcal{P}(N_{sig}, N_{bckg}) = N_{sig}/\sqrt{N_{sig} + N_{bckg}}$. The specific values of cuts were obtained by the optimization but cutting variables were mostly chosen with respect to the physical motivation:

- $\tau_B/\Delta\tau_B > 12.75$ (The lifetime cut prefers the long-lived B-mesons and suppresses some short-lived hadrons. The cut is applied on lifetime significance to impose quality requirements on the lifetime measurement.)
- $\cos\theta > 0.999$; θ is defined as the angle between the reconstructed direction of flight of B-candidate and its 3-momentum (The cut on the 3D pointing angle θ is used to suppress hadronic background. Ideally, this angle should be equal to zero, but the limited detector resolution is accounted for. Due to technical reasons on the input derivation data, the $\cos\theta$ variable was not available and thus cut was not applied.)
- $p_{TK^*} > 3000$ MeV (comes from optimization).

- The quality of the four track (B-vertex) fit: $\chi^2/n.d.f. < 2$.
- $\Delta m \equiv |(m(B)_{rec} - m(B)_{PDG}) - (m(\mu^+\mu^-)_{rec} - m(c\bar{c})_{PDG})| > 130$ MeV; where $c\bar{c}$ represents J/ψ and $\psi(2S)$ (The last cut on a correlation of mass-shifting of B-candidate and dimuon candidate is required to remove radiative charmonium decays from corresponding B-decays as $B_d^0 \to K^{*0}J/\psi$ followed by $J/\psi \to \gamma\mu\mu$. The correlation is a consequence of the detector resolution affecting the masses of the B-meson and the charmonium.)

4.3 Branching Ratios of Processed Decays

The Tab. 4.1 and Tab. 4.2 are listing branching ratios of the studied B-meson decays and the branching ratios of the subsequent decays of the daughter particles in the decay tree. Fragmentation fractions of b-quarks into weakly-decaying b-hadrons are presented in Tab. 4.3. The fractions do not have strong dependence on the collision energy (see Ref. [27] and [28]) thus the values established in $p\bar{p}$ collisions at $\sqrt{s} = 1.96$ TeV can be used in pp collisions at higher energy of LHC as well.

decay chanel	BR
$B_d^0 \to K^*(K\pi)\mu^+\mu^-$	$(9.4 \pm 0.5) \times 10^{-7}$
$B_d^0 \to K^*(K\pi)J/\psi(\mu^+\mu^-)$	$(1.27 \pm 0.05) \times 10^{-3}$
$B_d^0 \to K^*(K\pi)\psi(2s)(\mu^+\mu^-)$	$(5.9 \pm 0.4) \times 10^{-4}$
$B_d^0 \to K\pi J/\psi(\mu^+\mu^-)$	$(1.15 \pm 0.05) \times 10^{-3}$
$B_d^0 \to K\pi\psi(2s)(\mu^+\mu^-)$	$(5.8 \pm 0.4) \times 10^{-4}$
$B_d^0 \to K^*(K\pi)\eta(\mu^+\mu^-)$	$(1.59 \pm 0.10) \times 10^{-5}$
$B_s^0 \to \phi(K^+K^-)\mu^+\mu^-$	$(8.2 \pm 1.2) \times 10^{-7}$
$B_s^0 \to \phi(K^+K^-)J/\psi(\mu^+\mu^-)$	$(1.08 \pm 0.08) \times 10^{-3}$
$B_s^0 \to \phi(K^+K^-)\psi(2s)(\mu^+\mu^-)$	$(5.4 \pm 0.6) \times 10^{-4}$
$B^+ \to K^+\mu^+\mu^-$	$(4.41 \pm 0.23) \times 10^{-7}$
$B^+ \to K^+J/\psi(\mu^+\mu^-)$	$(1.010 \pm 0.029) \times 10^{-3}$
$B^+ \to K^+\psi(2s)(\mu^+\mu^-)$	$(6.21 \pm 0.23) \times 10^{-4}$
$B^+ \to \pi^+J/\psi(\mu^+\mu^-)$	$(3.88 \pm 0.12) \times 10^{-5}$
$B^+ \to \pi^+\eta(\mu^+\mu^-)$	$(4.02 \pm 0.27) \times 10^{-6}$
$B^+ \to K^+\eta(\mu^+\mu^-)$	$(2.4 \pm 0.4) \times 10^{-6}$

Table 4.1: Branching ratios of the studied decays [13] (the $\bar{B}$ meson decays are simulated as well, the later calculations use the same branching ratios).

BR_h		BR_μ	
$K^* \to K\pi$	$2/3$	$J/\psi \to \mu^+\mu^-$	0.0596 ± 0.0003
$\phi \to K^+K^-$	0.492 ± 0.005	$\psi(2s) \to \mu^+\mu^-$	$(8.0 \pm 0.6) \times 10^{-3}$
		$\eta \to \mu^+\mu^-$	$(5.8 \pm 0.8) \times 10^{-6}$

Table 4.2: Branching ratios of following hadronic and muonic decays [13].

b-hadron	fraction
B^+,B^0	$34.3 \pm 2.1\%$
B_s^0	$11.5 \pm 1.3\%$

Table 4.3: The b-quarks fragmentation fractions in $p\bar{p}$ collisions at $\sqrt{s}$= 1.96 TeV [13].

4.4 Results

4.4.1 Application of Selection Criteria

DAOD full-MC samples of the signal decay and antidecay were generated with N_{GEN} events. Each event includes a "true" decay of B_d^0 ($\bar{B}_d^0$) into K^* ($\bar{K}^*$) $\mu\mu$ (as well as forcing K^* into charged $K\pi$ decay). Events pass the same reconstruction as the real data in the detector and N_{TOT} decays are reconstructed in $N_{\mathrm{GEN}}^{\mathrm{REC}}$ events. Most of them (N_{B}) do not correspond to the "true" decay and create, so called, self-background (a subset of combinatorial background inside of the signal events). In this section we omit that at this stage there are multiple candidates per event and focus solely on efficiency of the selection criteria. The Tab. 4.4 and 4.5 present:

- N_{S} (N_{B}) – the number of reconstructed signal (self-background) decays
- N_{PASS} – the number of all reconstructed decays passed the corresponding cut and the cuts listed above,
- N_{S} / N_{PASS} – the ratio of the signal to the all reconstructed decays ("the cut efficiency"),
- $N_{\mathrm{PASS}}/N_{\mathrm{TOT}}$ – the number of reconstructed decays passed the cut to the number of all reconstructed decays.

In the first line "raw data" are shown all reconstructed decays without application of any selection crietria ($N_{\mathrm{PASS}}^{\mathrm{RAW}} = N_{\mathrm{TOT}}$).

name	N_{S}	N_{B}	N_{PASS}	N_{S} / N_{PASS}	$N_{\mathrm{PASS}}/N_{\mathrm{TOT}}$:
raw data	8645	66798	75443	0.11	100.00%
$\|\eta\|_{4Btracks}$	8546	64644	73190	0.12	97.01%
dimuon vertex	5319	7052	12371	0.43	16.40%
$p_{T\mu}$	5240	6687	11927	0.44	15.81%
m_{K^*}	4102	2402	6504	0.63	8.62%
m_B	3767	637	4404	0.86	5.84%
τ_B/σ_{τ_B}	1132	454	1586	0.71	2.10%
p_{TK^*}	576	42	618	0.93	0.82%
B vertex	517	22	539	0.96	0.71%
$\Delta m_{radiative}$	374	15	389	0.96	0.52%

Table 4.4: Signal and self-background yield after the application of selection criteria for decay $B_d^0 \to K^*(K\pi)\mu^+\mu^-$.

name	N_{S}	N_{B}	N_{PASS}	N_{S} / N_{PASS}	$N_{\mathrm{PASS}}/N_{\mathrm{TOT}}$:
raw data	8433	64221	72654	0.12	100.00%
$\|\eta\|_{4Btracks}$	8362	62121	70483	0.12	97.01%
dimuon vertex	5313	7065	12378	0.43	17.04%
$p_{T\mu}$	5246	6719	11965	0.44	16.47%
m_{K^*}	4164	2443	6607	0.63	9.09%
m_B	3317	683	4000	0.83	5.51%
τ_B/σ_{τ_B}	998	478	1476	0.68	2.03%
p_{TK^*}	379	29	408	0.93	0.56%
B vertex	350	22	372	0.94	0.51%
$\Delta m_{radiative}$	265	13	278	0.95	0.38%

Table 4.5: Signal and self-background yield after the application of selection criteria for decay $\bar{B}_d^0 \to \bar{K}^*(K\pi)\mu^+\mu^-$.

4.4.2 Background Yield Estimation

The same approach as in the previous section with small modifications is used for the background decays introduced in Tab. 4.1. For background decays, there is no reasonable interpretation of N_{S} and N_{B} and therefore only N_{PASS} is used. A next modification for sake of brevity is replacement of partial results for a separate cut by results after application of the whole set of cuts, i.e.:

- $\frac{N_{\mathrm{PASS}}^{\mathrm{baseline}}}{N_{\mathrm{TOT}}}$ – efficiency of the decay reconstruction after application of the baseline cuts during the n-tuple creation,
- $\frac{N_{\mathrm{PASS}}^{\mathrm{Run1}}}{N_{\mathrm{TOT}}}$ – final efficiency of the decay reconstruction after application of the baseline cuts and the cuts from the Run 1 analysis.

To consider efficiency of the decay reconstruction, a new variable is introduced:

- $\eta^{\mathrm{REC}} \equiv \frac{N_{\mathrm{GEN}}^{\mathrm{REC}}}{N_{\mathrm{GEN}}}$, where $N_{\mathrm{GEN}}^{\mathrm{REC}}$ is the number of events with at least 1 reconstructed event.

In order to estimate expected background yields proportional to 1 signal event $\frac{N_{\mathrm{PASS}}^{\mathrm{Run1}}}{N_{\mathrm{TOT}}}$ is multiplied by the factor f defined as follows:

$$f \equiv \frac{f_{B_x} \times BR_{B_x \to h\mu\mu} \times BR_h \times BR_\mu}{f_{B_d} \times BR_{B_d \to K^*\mu\mu} \times 2/3 \times 1} \times \mathcal{N} \times \eta^{\mathrm{REC}}; \text{where}$$

$$\mathcal{N} \equiv \frac{1}{(\frac{N_{\mathrm{PASS}}^{\mathrm{Run1}}}{N_{\mathrm{TOT}}} \times \eta^{\mathrm{REC}})_{B_d \to K^*\mu\mu} + (\frac{N_{\mathrm{PASS}}^{\mathrm{Run1}}}{N_{\mathrm{TOT}}} \times \eta^{\mathrm{REC}})_{\bar{B}_d \to \bar{K}^*\mu\mu}}$$

The first part normalizes the probability of the processed decay to the signal decay, $\mathcal{N}$ factor makes the final expectation to be proportional to 1 signal event (decay or antidecay) and η^{REC} takes into account the reconstruction efficiency. The used branching ratios (BR) and fragmentation factors f_{B_x} are listed in Sec. 4.3.

decay chanel	η^{REC}	N_{TOT}	$\frac{N^{\mathrm{baseline}}_{\mathrm{PASS}}}{N_{\mathrm{TOT}}}$	$\frac{N^{\mathrm{Run1}}_{\mathrm{PASS}}}{N_{\mathrm{TOT}}}$	yield
$B^0_d \to K^*(K\pi)\mu^+\mu^-$	75.81%	75443	5.84%	0.516%	0.57
$\bar{B}^0_d \to \bar{K}^*(K\pi)\mu^+\mu^-$	75.81%	72654	5.51%	0.383%	0.43
$B^0_d \to K^*(K\pi)J/\psi(\mu^+\mu^-)$	74.76%	63052	6.12%	0.021%	1.8
$\bar{B}^0_d \to \bar{K}^*(K\pi)J/\psi(\mu^+\mu^-)$	74.61%	63719	5.44%	0.129%	11
$B^0_d \to K^*(K\pi)\psi(2s)(\mu^+\mu^-)$	74.93%	40605	7.46%	0.030%	0.16
$\bar{B}^0_d \to \bar{K}^*(K\pi)\psi(2s)(\mu^+\mu^-)$	75.45%	42770	6.35%	0.154%	0.86
$B^0_d \to K^*(K\pi)\eta(\mu^+\mu^-)$	79.25%	174749	0.95%	0.106%	$\sim 10^{-5}$
$\bar{B}^0_d \to \bar{K}^*(K\pi)\eta(\mu^+\mu^-)$	80.63%	90586	1.14%	0.106%	$\sim 10^{-5}$
$B^0_d \to K\pi J/\psi(\mu^+\mu^-)$	58.37%	83092	1.64%	0.019%	1.8
$\bar{B}^0_d \to K\pi J/\psi(\mu^+\mu^-)$	58.53%	40658	1.55%	0.030%	2.8
$B^0_d \to K\pi\psi(2s)(\mu^+\mu^-)$	66.23%	39387	2.80%	0.030%	0.22
$\bar{B}^0_d \to K\pi\psi(2s)(\mu^+\mu^-)$	64.68%	40164	2.28%	0.070%	0.49
$B^0_s \to \phi(K^+K^-)\mu^+\mu^-$	78.13%	152231	1.09%	0.055%	0.014
$\bar{B}^0_s \to \phi(K^+K^-)\mu^+\mu^-$	78.05%	50643	1.03%	0.041%	0.01
$B^0_s \to \phi(K^+K^-)J/\psi(\mu^+\mu^-)$	76.73%	47357	1.06%	0.011%	0.2
$\bar{B}^0_s \to \phi(K^+K^-)J/\psi(\mu^+\mu^-)$	77.25%	45732	1.08%	0.015%	0.29
$B^0_s \to \phi(K^+K^-)\psi(2s)(\mu^+\mu^-)$	77.10%	42756	1.27%	0.014%	0.018
$\bar{B}^0_s \to \phi(K^+K^-)\psi(2s)(\mu^+\mu^-)$	78.05%	43623	1.31%	0.011%	0.015
$B^+ \to K^+\mu^+\mu^-$	46.25%	68788	1.40%	0.064%	0.031
$B^- \to K^-\mu^+\mu^-$	47.05%	33213	1.16%	0.006%	0.0029
$B^+ \to K^+J/\psi(\mu^+\mu^-)$	45.49%	66466	1.32%	0.092%	5.9
$B^- \to K^-J/\psi(\mu^+\mu^-)$	45.67%	33183	0.95%	0.012%	0.78
$B^+ \to K^+\psi(2s)(\mu^+\mu^-)$	45.26%	58200	1.91%	0.084%	0.44
$B^- \to K^-\psi(2s)(\mu^+\mu^-)$	45.38%	27965	1.51%	0.018%	0.094
$B^+ \to \pi^+J/\psi(\mu^+\mu^-)$	45.94%	32698	1.02%	0.031%	0.076
$B^- \to \pi^-J/\psi(\mu^+\mu^-)$	44.86%	31941	0.83%	0.003%	0.0076
$B^+ \to \pi^+\eta(\mu^+\mu^-)$	65.93%	77825	0.55%	0.024%	$\sim 10^{-7}$
$B^- \to \pi^-\eta(\mu^+\mu^-)$	66.86%	79060	0.55%	0.009%	$\sim 10^{-7}$
$B^+ \to K^+\eta(\mu^+\mu^-)$	66.22%	79143	0.61%	0.025%	$\sim 10^{-7}$
$B^- \to K^-\eta(\mu^+\mu^-)$	66.13%	77576	0.58%	0.008%	$\sim 10^{-7}$

Table 4.6: The efficiency of reconstruction, baseline and Run 1 cuts on the signal and background samples. The last row presents the expected number of observed events from the given B-decay per single signal event.

Our very naive estimation results into 27 background events corresponding to one signal event if the Run 1 cuts would be processed. It is not the final number since the cut on $\cos\theta$ and ϕ-veto on di-muon mass were not applied yet.

The highest contributions come from decays: $B_d^0 \to K^* J/\psi(\mu\mu)$, $B_d^0 \to K^* J/\psi(\mu\mu)$, $B_d^0 \to K^*\psi(2S)(\mu\mu)$ and $B_d^0 \to K^*\psi(2S)(\mu\mu)$ since their structure is identical with the signal decay. However, an additional veto can be applied on di-muon mass around $c\bar{c}$ resonant peaks J/ψ and $\psi(2S)$ which suppresses them more significantly. This would also reduce higher contributions from $B^\pm \to K^\pm J/\psi$ (and $B^\pm \to K^\pm\psi(2S)$). On the other hand decays containing η are naturally suppressed by its branching ratio of the following decay into muons.

An unexpected result is the asymmetry observed between the estimated background yields for charged decays and their CP-conjugated antidecays. The detailed view on separate cuts showed that the asymmetry appears after cutting on p_{TK^*}. This would be studied deeper in the following analysis.

Conclusion

Two major tasks connected with the $B_d^0 \to K^* \mu\mu$ analysis were carried out within this thesis: toy-MC studies of possible intrinsic biases of the B_d-mass and decay-angles fit and development of the framework for creation of reduced dataset (ROOT n-tuple) from initial ATLAS analysis data format (derivation).

The first part examines the fit behaviour for 3×3 combinations of number of expected events and signal-to-background ratio representing possible signal and background yields of the Run 2 and HL-LHC analysis. An emphasis was put on the fit functions involving parameter P_5' connected with measured deviations from Standard Model by the LHCb experiment. Results for the remaining parameters with and without including the effect of detector acceptance are presented in the appendix. Expected improvement of the fit stability with higher statistics was observed in the $[0.04, 2.0]$ GeV^2 and $[2.0, 4.0]$ GeV^2 q^2 bins. The inverse behavior in the $[4.0, 6.0]$ GeV^2 bin is explained as the result of the acceptance effects. This is a new reason in favour of the planned modification of the acceptance description in Run 2. The fit biases did not decrease with increasing number of events that suggests that even the $100\times$ larger dataset after the HL-LHC update would be still too small to suppress the fit bias. On the other hand, the fit bias remains below the statistical precision and thus the study demonstrated that the systematic uncertainty connected with the fit bias remains under control.

The second part was focused on DAOD transformation into n-tuple containing event information and basic kinematic variables used in the analysis. Functionality of the developed software was demonstrated on transformation of the signal and most important background MC samples (simulated with the full detection process and saved as DAOD) and within that applying the baseline and Run-1 optimized selection criteria. Prediction of the background yields normalized to 1 signal event was estimated according to the Run 1 selection criteria efficiency and corresponding branching ratios of all tested B-decays.

Bibliography

[1] ATLAS Collaboration, *Angular Analysis of $B_d^0 \to K^{*}\mu^+\mu^-$ Decays in pp Collisions at $\sqrt{s} = 8$ TeV with the ATLAS Detector*, arXiv:1805.04000 [hep-ex].

[2] T. A. Collaboration, *The ATLAS Experiment at the CERN Large Hadron Collider*, Journal of Instrumentation **3** (2008) no. 08, S08003. https://doi.org/10.1088%2F1748-0221%2F3%2F08%2Fs08003.

[3] E. Mobs, *The CERN Accelerator Complex. Complexe des accélérateurs du CERN*, . https://cds.cern.ch/record/2197559.

[4] C. ATLAS, *The ATLAS Coordinate System Footnote*, https://twiki.cern.ch/twiki/bin/view/AtlasProtected/CcordinateSystemFootnote. online: 5. 5. 2020.

[5] ATLAS Collaboration, *Luminosity Public Results* , https://twiki.cern.ch/twiki/bin/view/AtlasPublic/LuminosityPublicResults. online: 4. 5. 2020.

[6] C. ATLAS, *Luminosity Public Results Run 2*, https://twiki.cern.ch/twiki/bin/view/AtlasPublic/LuminosityPublicResultsRun2. online: 4. 5. 2020.

[7] J. Catmore, *The ATLAS Data Processing Chain: from Collisions to Papers*, https://indico.cern.ch/event/472469/contributions/1982677/attachments/1220934/1785823/intro_slides.pdf. online: 22. 2. 2020.

[8] M. Kocian, *ATLAS Pixel, Phase 0 (IBL)*, Tech. Rep. ATL-COM-INDET-2012-107, CERN, Geneva, Dec, 2012. https://cds.cern.ch/record/1498241.

[9] L. Heinrich, *ATLAS Software Tutorial - Trigger Data and how to Analyze it*, https://indico.cern.ch/event/403126/contributions/956172/attachments/1153704/1657569/SoftwareTutorialTrigger-2015-09-14.pdf. online: 22. 2. 2020.

[10] C. ATLAS, *Letter of Intent for the Phase-I Upgrade of the ATLAS Experiment*, Tech. Rep. CERN-LHCC-2011-012. LHCC-I-020, CERN, Geneva, Nov, 2011. https://cds.cern.ch/record/1402470.

[11] C. ATLAS, *Letter of Intent for the Phase-II Upgrade of the ATLAS Experiment*, Tech. Rep. CERN-LHCC-2012-022. LHCC-I-023, CERN, Geneva, Dec, 2012. https://cds.cern.ch/record/1502664.

[12] *Brief ATLAS Informaton*, https://stanford.edu/group/stanford_atlas/4Particle%20Collision%20and%20Detection. online: 31. 10. 2019.

[13] Particle Data Group Collaboration, C. Patrignani et al., *Review of Particle Physics*, Chin. Phys. **C40** (2016) no. 10, 100001.

[14] *Standard Model*, https://en.wikipedia.org/wiki/Standard_Model. online: 16. 3. 2020.

[15] J. Horejsi and U. Karlova, *Fundamentals of Electroweak Theory*. Karolinum Press, 2002. https://books.google.sk/books?id=JGkFAQAACAAJ.

[16] J. Chýla, *Quarks, Partons and Quantum Chromodynamics*, https://www.fzu.cz/~chyla/lectures/text.pdf.

[17] S. Jäger and J. Martin Camalich, *Reassessing the Discovery Potential of the $B \to K^* \ell^+ \ell$ Decays in the Large-recoil Region: SM Challenges and BSM Opportunities*, Physical Review D **93** (2016) no. 1, . http://dx.doi.org/10.1103/PhysRevD.93.014028.

[18] M. Biros, *Bachelor thesis, Study of the Rare B-meson Decay with the ATLAS Experiment*, https://dspace.cuni.cz/bitstream/handle/20.500.11956/99922/130231775.pdf?sequence=1&isAllowed=y.

[19] I. Carli, *PhD thesis, Angular Analysis of the $B^0 \to K^* \mu^+ \mu^-$ Decay with the ATLAS Experiment*, http://cds.cern.ch/record/2696422/files/CERN-THESIS-2018-449.pdf.

[20] LHCb Collaboration, *Measurement of CP-averaged observables in the $B^0 \to K^{*0} \mu^+ \mu^-$ decay*, arXiv:2003.04831 [hep-ex].

[21] ATLAS Collaboration Collaboration, *$B_d^0 \to K^{*0} \mu\mu$ Angular Analysis Prospects with the Upgraded ATLAS Detector at the HL-LHC*, Tech. Rep. ATL-PHYS-PUB-2019-003, CERN, Geneva, Jan, 2019. https://cds.cern.ch/record/2654519.

[22] *ATLAS Athena Guide*, https://atlassoftwaredocs.web.cern.ch/athena/. online: 23. 5. 2020.

[23] *ATLAS Manual - Browsing the xAOD in ROOT* , https://twiki.cern.ch/twiki/bin/viewauth/AtlasComputing/SoftwareTutorialxAODEDM. online: 23. 5. 2020.

[24] *RK* Analysis Code*, https://gitlab.cern.ch/RKstar/run2analysis. online: 6. 5. 2020.

[25] *ELBrain*, https://elbraindocs.web.cern.ch. online: 6. 5. 2020.

[26] *PyAnalysisTools*, http://cern.ch/PyAnalysisToolsDocs. online: 6. 5. 2020.

[27] R. Aaij, C. Abellan Beteta, A. Adametz, B. Adeva, M. Adinolfi, C. Adrover, A. Affolder, Z. Ajaltouni, J. Albrecht, and et al., *Measurement of the Fragmentation Fraction Ratio f_s/f_d and its Dependence on B-meson Kinematics*, Journal of High Energy Physics **2013** (Apr, 2013) . http://dx.doi.org/10.1007/JHEP04(2013)001.

[28] G. Aad, B. Abbott, J. Abdallah, O. Abdinov, R. Aben, M. Abolins, O. AbouZeid, H. Abramowicz, H. Abreu, R. Abreu, and et al., *Determination of the Ratio of b-Quark Fragmentation Fractions f_s/f_d in pp Collisions at $\sqrt{s}$=7 TeV with the ATLAS Detector*, Physical Review Letters **115** (Dec, 2015) . http://dx.doi.org/10.1103/PhysRevLett.115.262001.

List of Abbreviations

BDT – Boosted Decision Trees
BSM – beyond Standard Model (physics)
CP – charge and parity (usually connected with conservation, violation)
CSC – cathode strip chambers
FCNC – flavour changing neutral current
IBL – insertable B layer
ID – inner detector
L1, L2 – Level-1, Level-2 trigger
LS – long shutdown
MC – Monte Carlo
MDT – monitored drift tubes
MS – muon spectrometer
PV – primary vertex
RPC – resistive plate chambers
SCT – semiconductor tracker
SM – standard model of particle physics
TGC – thin gap chambers
TRT – transition radiation tracker

A. Appendices

A.1 CERN Linux and Batch Service

This appendix is devoted to describe some technical capabilities that were required for successful accomplishment of the thesis. Hopefully, it can also help other younger students that starting to work on ATLAS which can use it as a kind of a introductory manual. However, a large piece of information provided here can have a short expiration period, especially technical limits, since CERN tries its best to improve technical background for researchers and enlarge computational capacities.

Every CERN's user gets in addition to CERN's mail also access to many useful software packages that could be accessible through the LXPLUS (Linux Public Login User Service). It is the interactive service to Linux for all CERN's users [`https://lxplusdoc.web.cern.ch/`]. Users can log on to *lxplus.cern.ch* through *secure shell connection* (*ssh*) in terminal:

```
ssh username@lxplus.cern.ch
```

A new user automatically obtains a home directory in the Andrew file system (AFS) structure of which size can be gradually increased to 10 GB. Available is also a workspace directory that can be activated, able to contain up to 100 GB. The directory structure is as follows:

```
/afs/cern.ch/home(or work)/first_letter_of_username/username
```

The cluster LXPLUS consists of public machines running CC7 (CERN CentOS 7) Linux in 64 bit mode. Users can log on the concrete machine (with a number XXX):

```
ssh username@lxplusXXX.cern.ch
```

However it is not recommended since they get automatically connected to the machine with the best response (the lowest CPU load and least number of login sessions) and LXPLUS does not guarantee that individual machines are available at any given time. The maximal computional time per user is limited freely – 40 CPU hours for the last 4 hours. This is enough for using more lxplus machines simultaneously (a couple of tens for our scripts generating and fitting MC samples, but in general it depends on the complexity of problem) in more terminals or through the *screen* command. A user crossing over this limit is warned by e-mail and if he or she keeps running the computations, they will be killed (cca after 30 minutes).

LXPLUS is devoted to interactive work and hence more computional demanding work should be processed on the CERN batch system. LXPLUS works *interactively* and distributes its computional capacity between all connected users *fairly*, while the batch system reserves some amount of computional capacity *only for one user*. The system is based on queues and users have to *wait* to get assigned computational capacity.

A.1.1 Technical Manual

One of very useful things, when one works on remote PC, is using of the *screen* command [`https://www.gnu.org/software/screen/`] that allows to continue running programs after disconnection.

Running *screen* on LXPLUS is a little complicated due to the usage of kerberos authentication, that requires a valid token in order to keep read/write rights on the AFS system. The token expires after user's logout and running program is then not capable writing output files. Keeping the token valid for 24 hours after user log out can be ensured with program *kinit*. A good, although a bit odd, practice for running *screen* on LXPLUS is:

```
ssh user_name@lxplus.cern.ch    #log in lxplus
screen                          #starting screen
                                #remember the lxplus machine id
                                #(lxplusXXX)
ctrl+a+d                        #detach screen
exit                            #log out
ssh username@lxplus.cern.ch     #log in to any lxplus
ssh username@lxplusXXX.cern.ch  #log in to the concrete lxplusXXX
screen -r                       #refresh screen
kinit                           #provide  token (requires password)
.\script_name                   #start a script
ctrl+a+d                        #detach screen
```

Setting a shortcut for the host name:

```
ssh lxplus, resp. ssh lxplusXXX
```

is possible by creation of the config file $\sim$ /*.ssh/config* including:

```
Host lxplus*
  user username
  Hostname lxplus.cern.ch
  ForwardX11 yes
  ForwardX11Trusted yes
```

The program Kerberos (*krb*5) allows a user to log in to LXPLUS without entering the password each time, the password is provided only once after restarting the computer. More about *screen* (more tabs, *kinit* without entering the password) can be found at [`https://hsf-training.github.io/analysis-essentials/shell-extras/screen.html`].

The older batch system on LXPLUS was replaced by HTCondor [`http://batchdocs.web.cern.ch/batchdocs/index.html`] that is controlled through the terminal by following (and many others) commands:

- *condor_submit job.sub* – asking for a computational capacities assignment for running a script specified in the config file *job.sub*
- *condor_q* – show the running state of the jobs (DONE/RUN/IDLE/HELD)
- *condor_wait out/job.log* – warn you after finishing all running jobs
- *condor_hold n* – hold (pause) job(s), they stay in the queue without running
- *condor_release n* – release held job(s) for running
- *condor_rm n* – remove job(s) from the queue

n - can represent the job id, the cluster id or username (removing all jobs from this user). An alternative to *condor_wait* is using of the bash command *watch*, that regularly update change: *watch -n timeperiod_in_seconds condor_q*.

The structure of config file *job.sub* is typically as follows:

```
executable = /totalpath/script_name.sh
arguments  = $(ClusterId) $(ProcId)
output = logfiles/batchDetail/script_name.$(ClusterId).$(ProcId).out
error  = logfiles/batchDetail/script_name.$(ClusterId).$(ProcId).err
log    = logfiles/script_name.$(ClusterId).log
...

queue
```

Users can also set their requirements:

```
+JobFlavour = "espresso"  # maximal time tag
+MaxRuntime = maximal running time of job in seconds
RequestCpus = required number of CPU
...
```

The lines *output* and *error* set output for *stdout* and *stderr* for each job and *log* saves a total preview of all jobs. The output files rewrite the older version.

Uses tags for maximal running time, after which is job automatically terminated, helps the batch system with planning to reserve the needed computional capacities (shorter running time means shorter waiting time as well):

```
espresso     = 20 minutes        tomorrow     = 1 day
microcentury = 1 hour            testmatch    = 3 days
longlunch    = 2 hours           nextweek     = 1 week
workday      = 8 hours
```

The default settings is *espresso* with 1 slot of CPU, 2 GB of RAM and 20 GB of free space.

The *queue* command pushes the *executable* script into queue to run. There are more ways of using it:

- *queue (without argument)* - push the script once
- *queue N* - push the same script N times
- *queue arguments from input_file.txt* - push the script with arguments from input file (separated in columns) as many times as the number of lines the file has

Jobs pushed with a different *queue* have specific $ClusterId$ while multiple jobs pushed with the same *queue* are numbered with $ProcId$ beginning from 0.

A.2 Fit Validation – Plots of Number of Succesfully Passed Fits

A.2.1 S_4-fold – parameter F_L

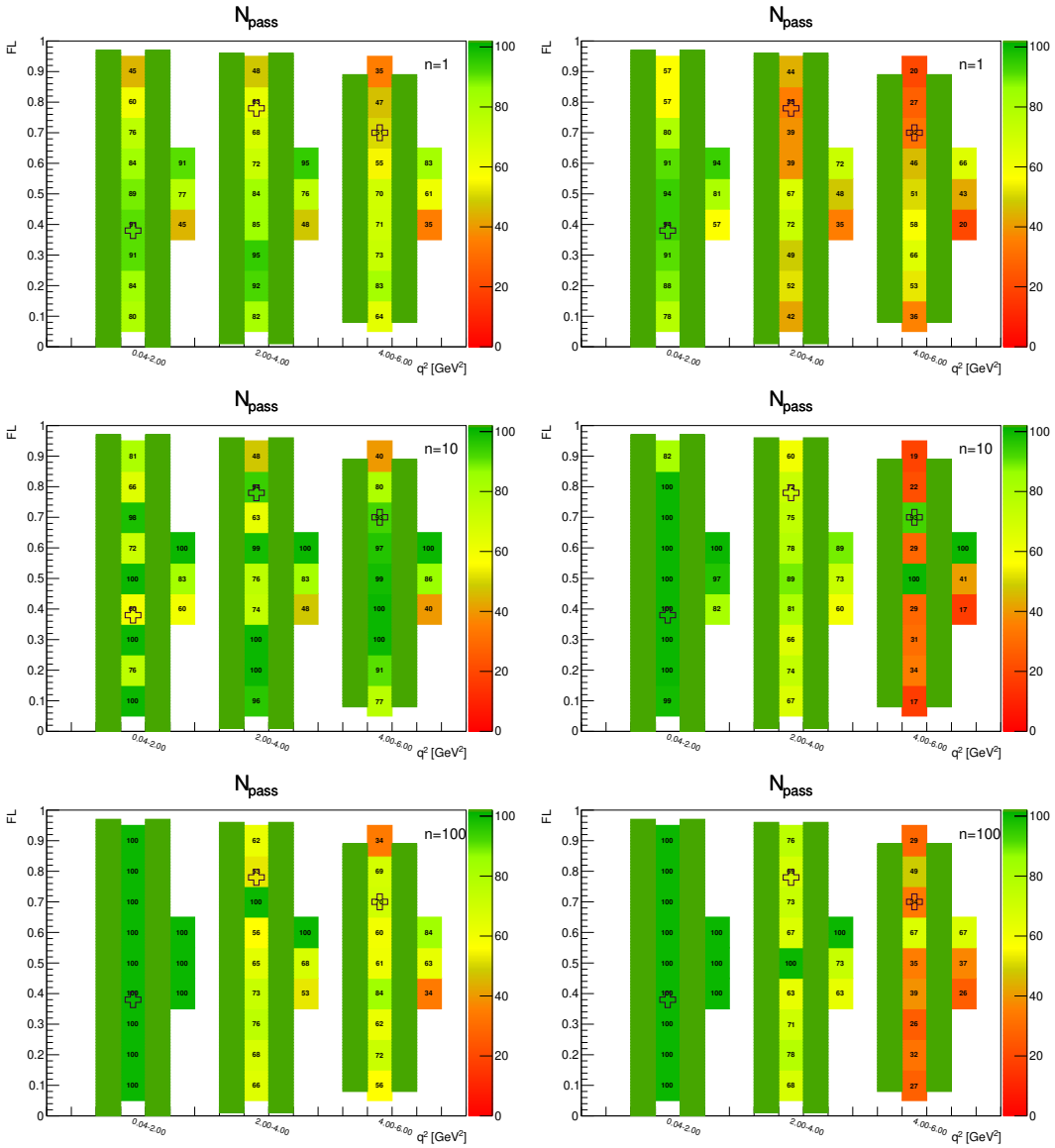

Figure A.1: Toy-MC studies of the S_4-fold, with r=0.5. Figures show the number of successfully passed fits without (left) and with acceptance (right) on the parameter F_L. The green bands represent fit-p.d.f. positivity range. The top figures correspond to the Run-1 like number of events (n = 1), while the middle and the bottom to 10× and 100× larger simulated samples.

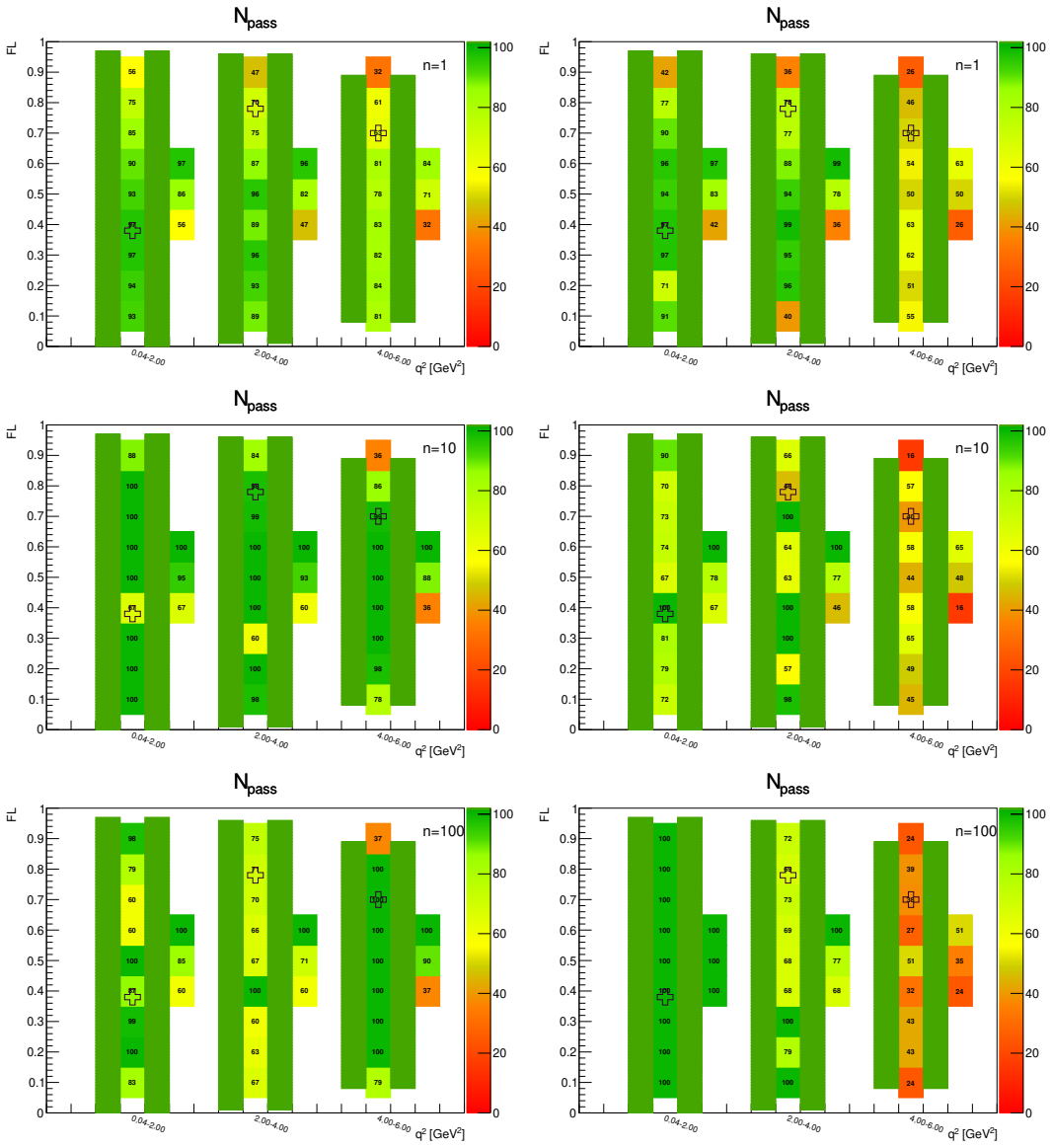

Figure A.2: Toy-MC studies of the S_4-fold, with r=1. Figures show the number of successfully passed fits on the toy-MC data without (left) and with acceptance (right) on the parameter F_L. The green bands represent fit-p.d.f. positivity range. The top figures correspond to the Run-1 like number of events (n = 1), while the middle and the bottom to 10× and 100× larger simulated samples.

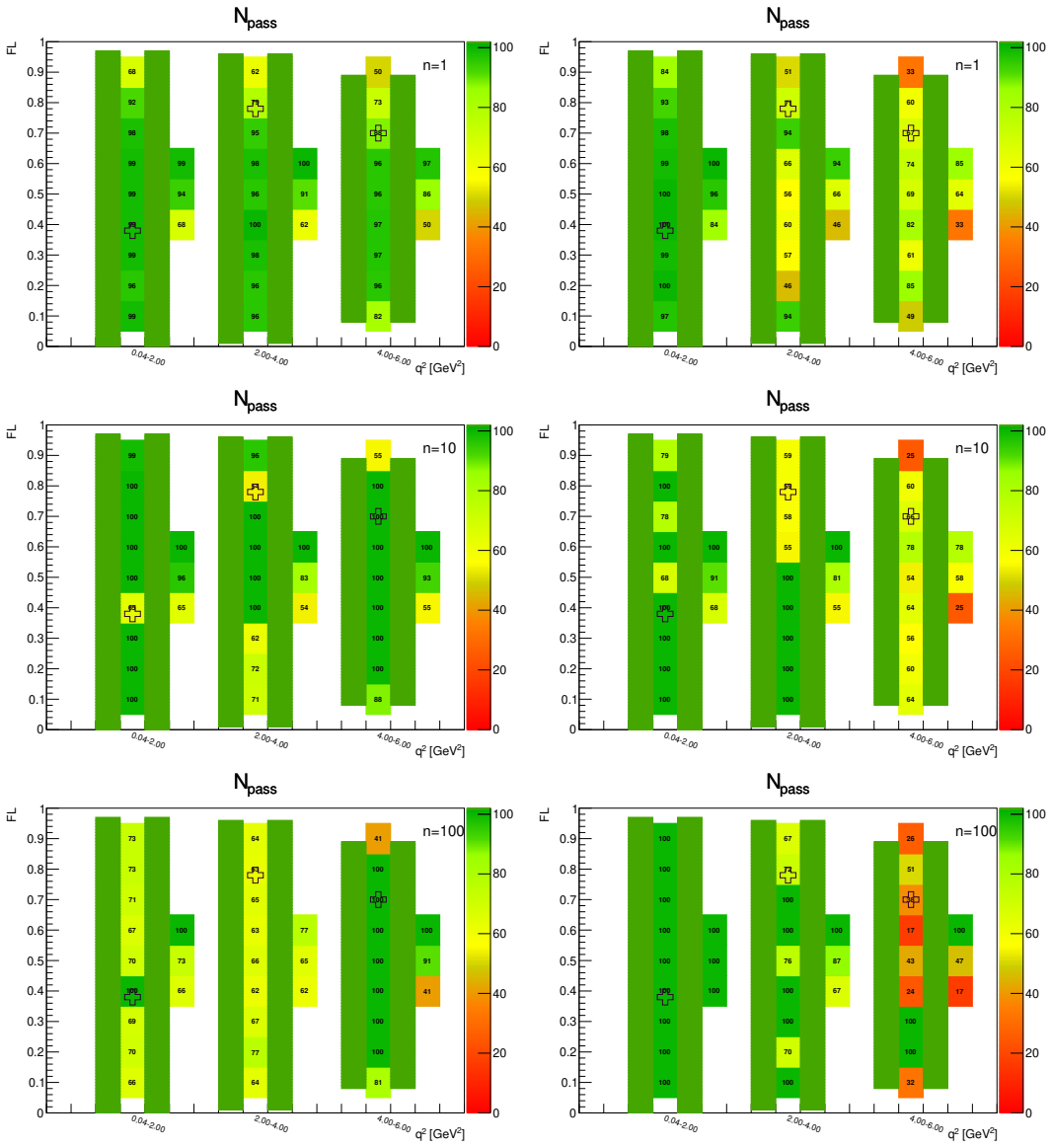

Figure A.3: Toy-MC studies of the S_4-fold, with r=2. Figures show the number of successfully passed fits on the toy-MC data without (left) and with acceptance (right) on the parameter F_L. The green bands represent fit-p.d.f. positivity range. The top figures correspond to the Run-1 like number of events (n = 1), while the middle and the bottom to 10× and 100× larger simulated samples.

A.2.2 S_4-fold – parameter S_3

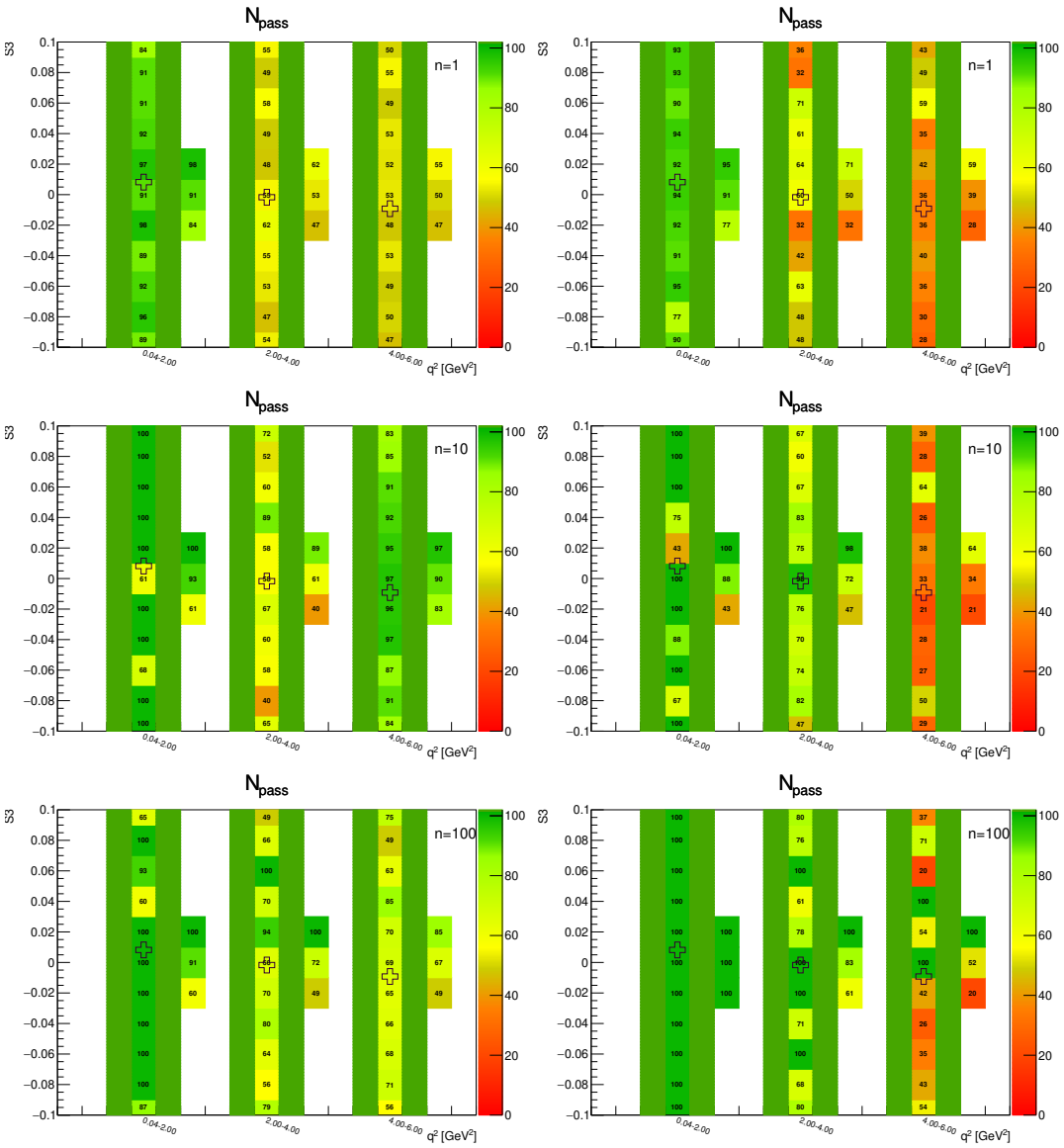

Figure A.4: Toy-MC studies of the S_4-fold, with r=0.5. Figures show the number of successfully passed fits on the toy-MC data without (left) and with acceptance (right) on the parameter S_3. The green bands represent fit-p.d.f. positivity range. The top figures correspond to the Run-1 like number of events (n = 1), while the middle and the bottom to 10× and 100× larger simulated samples.

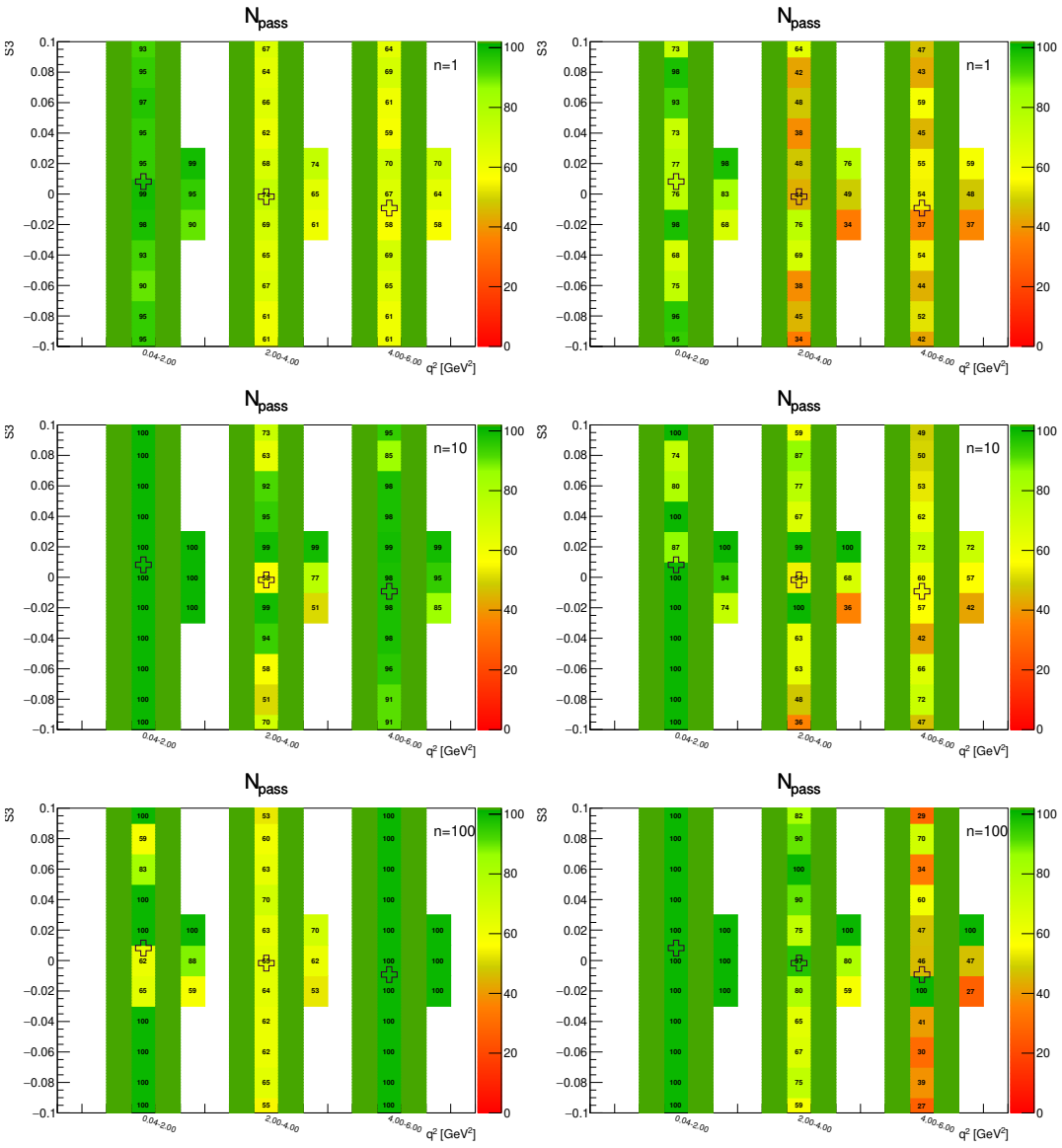

Figure A.5: Toy-MC studies of the S_4-fold, with r=1. Figures show the number of successfully passed fits on the toy-MC data without (left) and with acceptance (right) on the parameter S_3. The green bands represent fit-p.d.f. positivity range. The top figures correspond to the Run-1 like number of events (n = 1), while the middle and the bottom to 10× and 100× larger simulated samples.

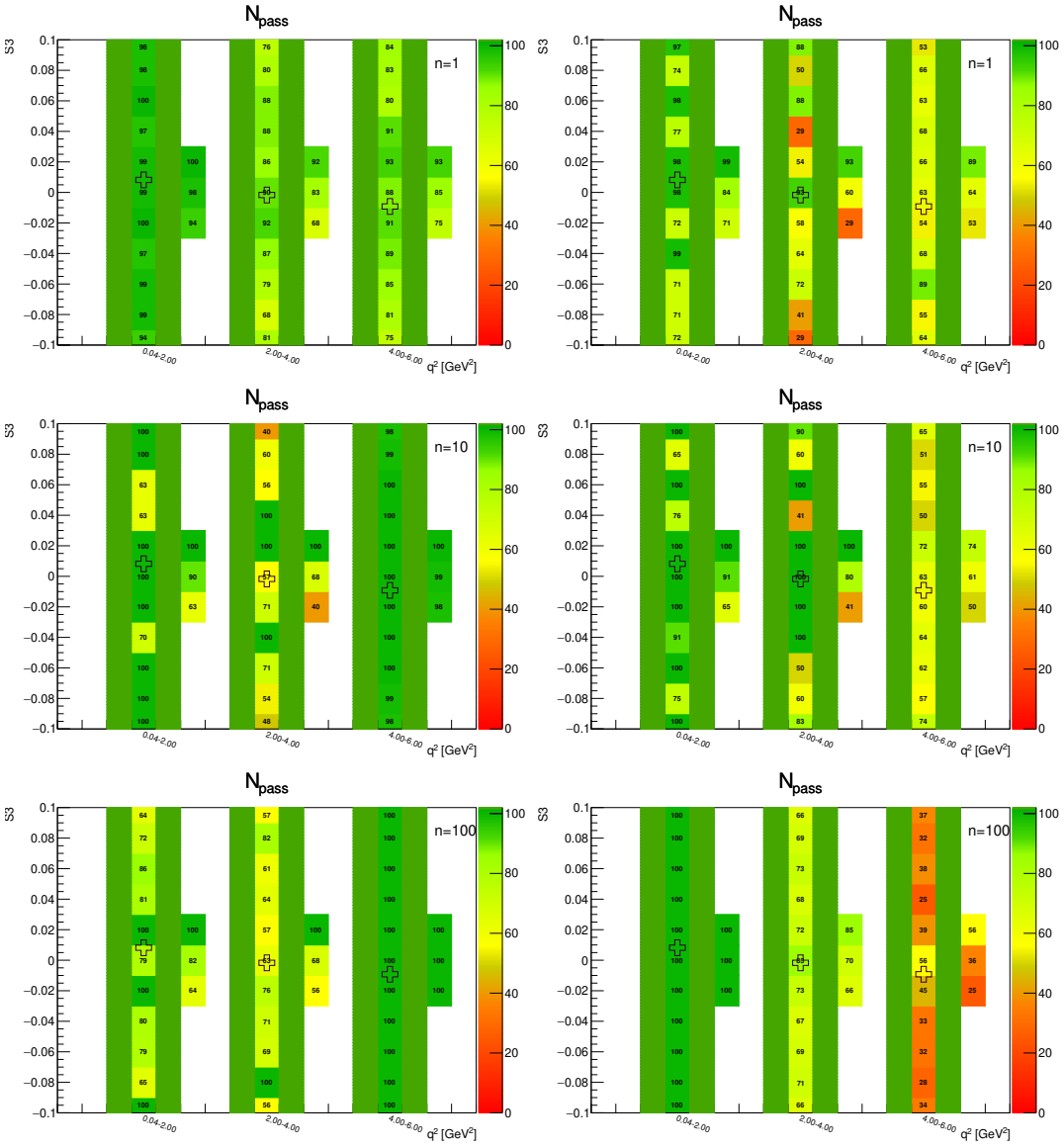

Figure A.6: Toy-MC studies of the S_4-fold, with r=2. Figures show the number of successfully passed fits on the toy-MC data without (left) and with acceptance (right) on the parameter S_3. The green bands represent fit-p.d.f. positivity range. The top figures correspond to the Run-1 like number of events (n = 1), while the middle and the bottom to 10× and 100× larger simulated samples.

A.2.3 S_4-fold – parameter S_4

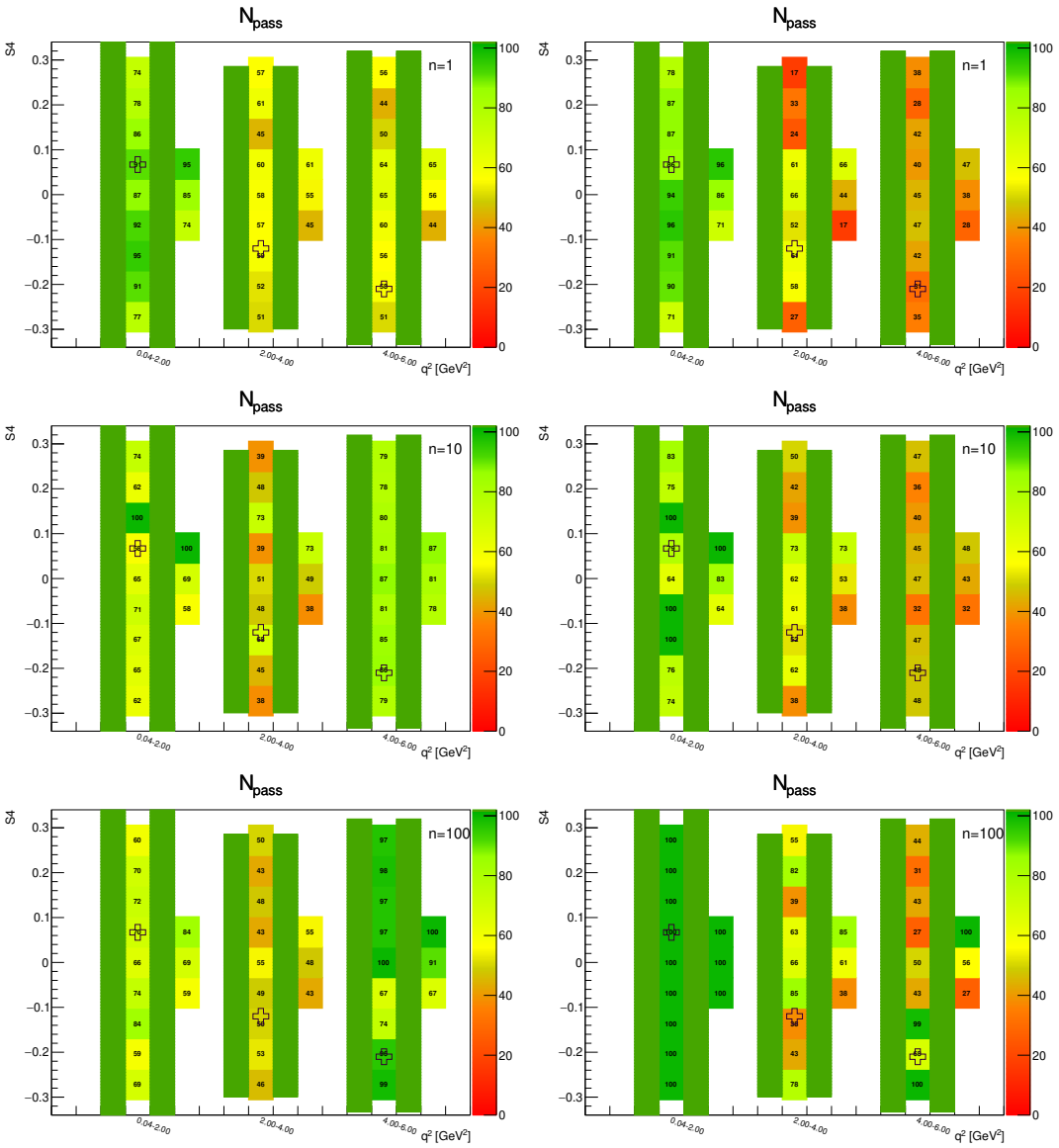

Figure A.7: Toy-MC studies of the S_4-fold, with r=0.5. Figures show the number of successfully passed fits on the toy-MC data without (left) and with acceptance (right) on the parameter S_4. The green bands represent fit-p.d.f. positivity range. The top figures correspond to the Run-1 like number of events (n = 1), while the middle and the bottom to 10× and 100× larger simulated samples.

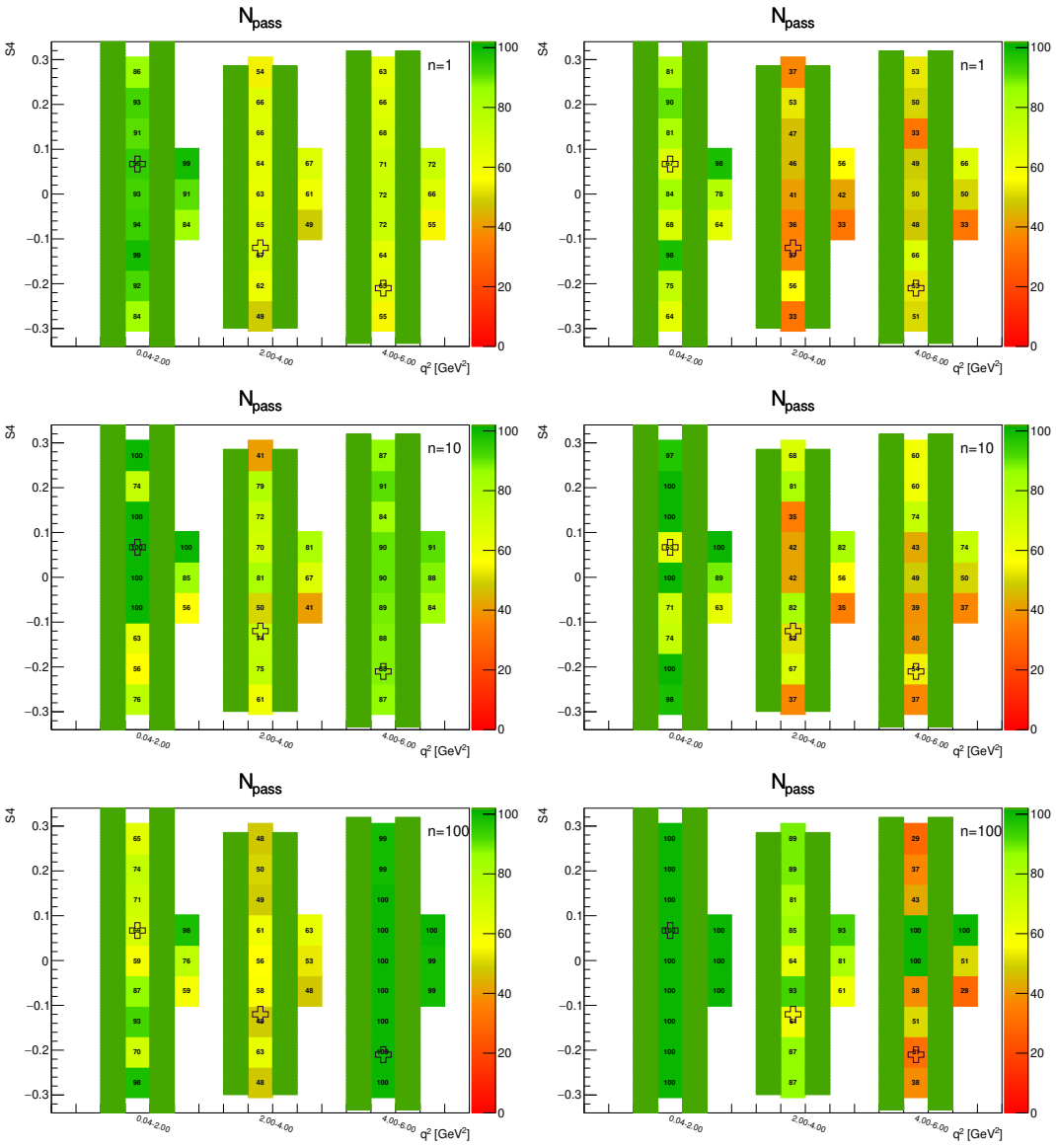

Figure A.8: Toy-MC studies of the S_4-fold, with r=1. Figures show the number of successfully passed fits on the toy-MC data without (left) and with acceptance (right) on the parameter S_4. The green bands represent fit-p.d.f. positivity range. The top figures correspond to the Run-1 like number of events (n = 1), while the middle and the bottom to 10× and 100× larger simulated samples.

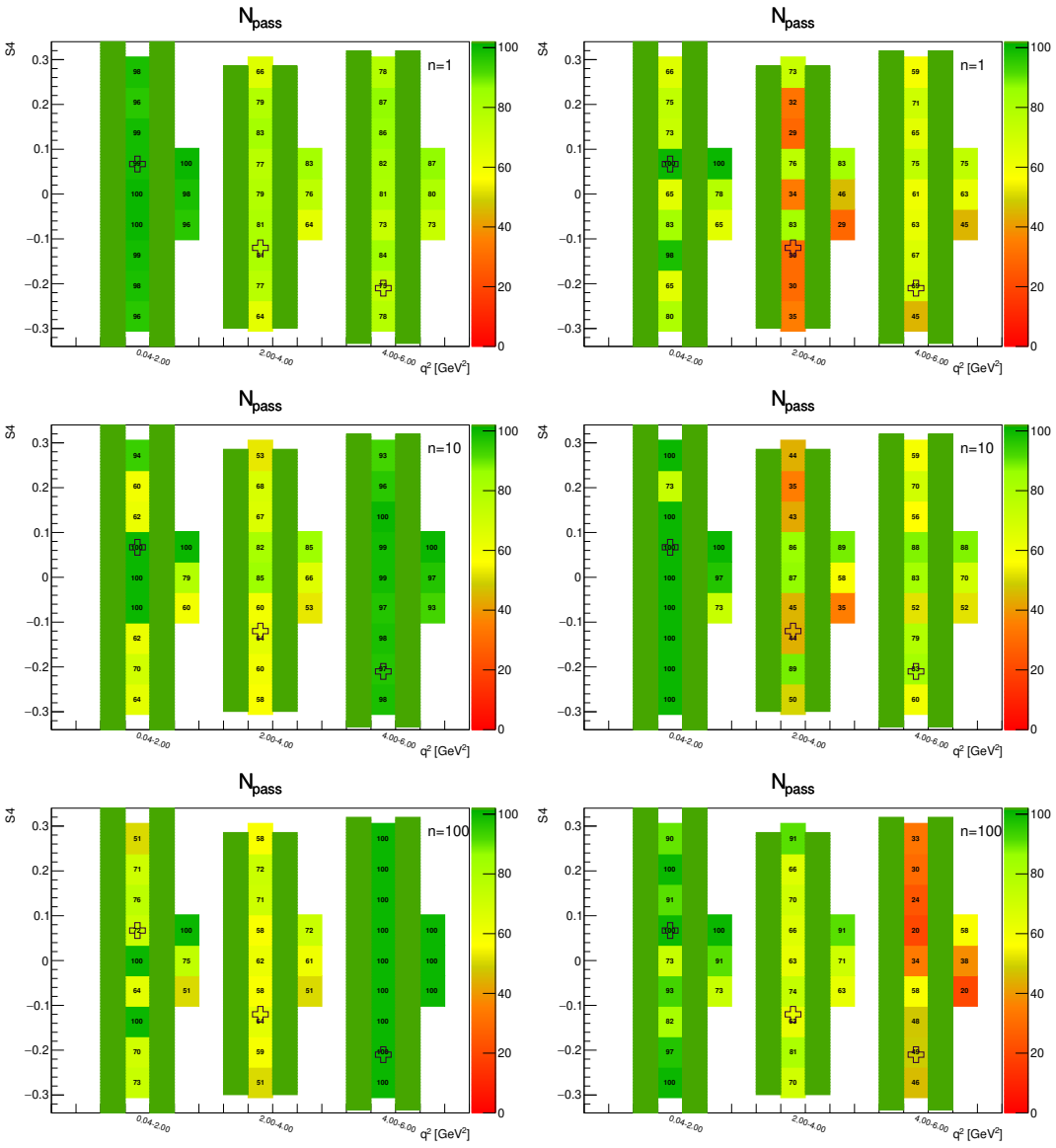

Figure A.9: Toy-MC studies of the S_4-fold, with r=2. Figures show the number of successfully passed fits on the toy-MC data without (left) and with acceptance (right) on the parameter S_4. The green bands represent fit-p.d.f. positivity range. The top figures correspond to the Run-1 like number of events (n = 1), while the middle and the bottom to 10× and 100× larger simulated samples.

A.2.4 S_5-fold – parameter F_L

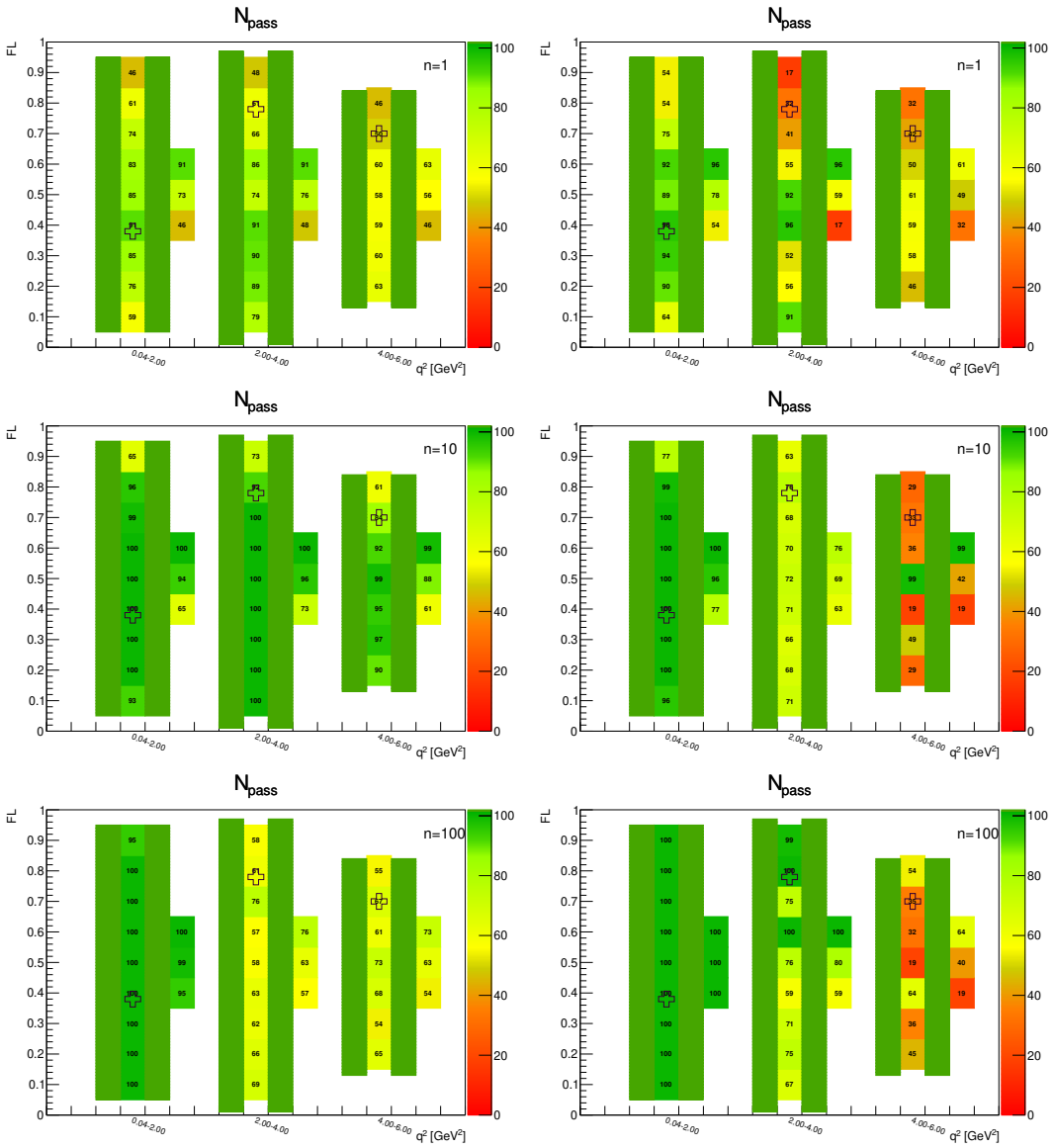

Figure A.10: Toy-MC studies of the S_5-fold, with r=0.5. Figures show the number of successfully passed fits on the toy-MC data without (left) and with acceptance (right) on the parameter F_L. The green bands represent fit-p.d.f. positivity range. The top figures correspond to the Run-1 like number of events (n = 1), while the middle and the bottom to 10× and 100× larger simulated samples.

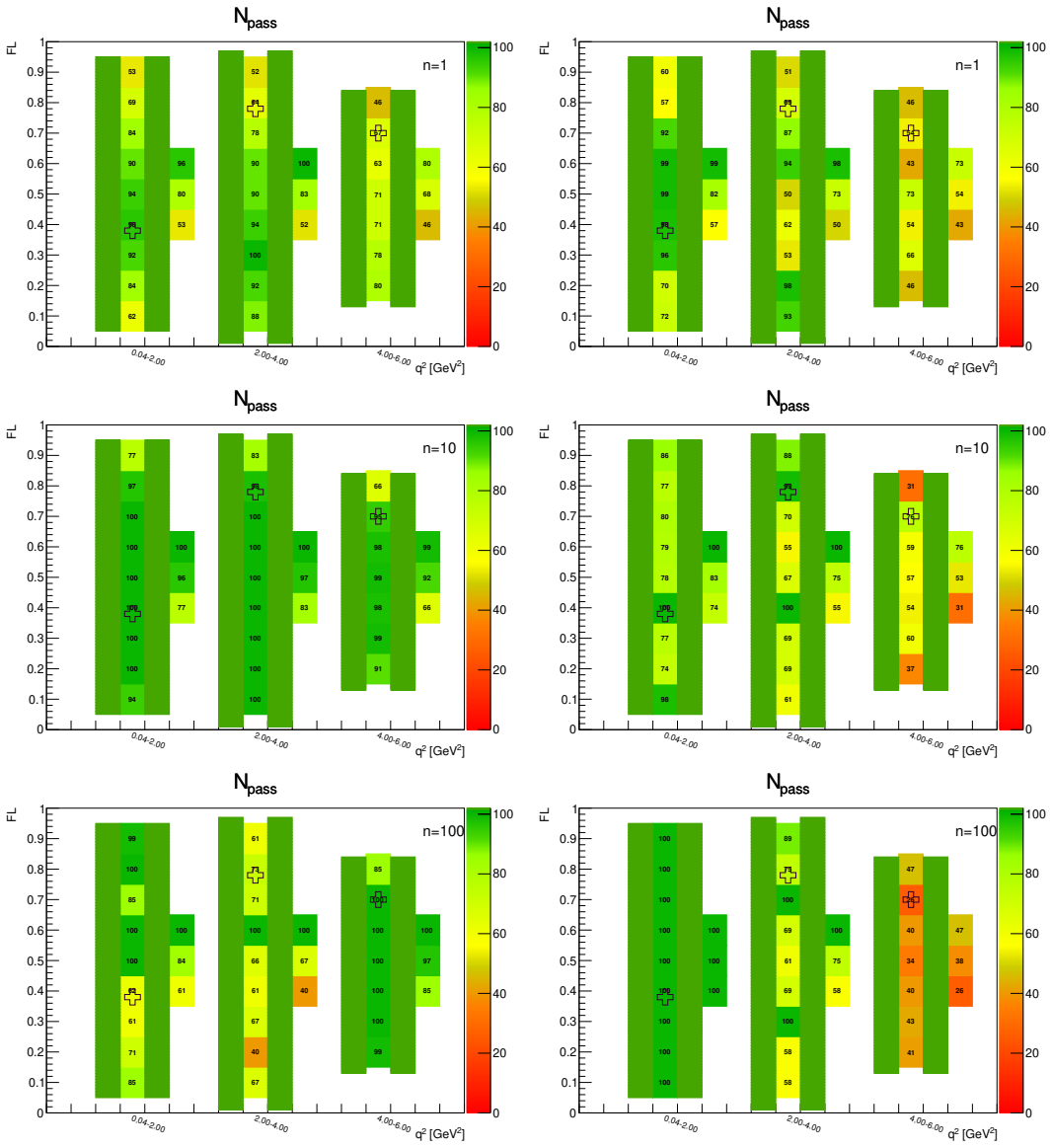

Figure A.11: Toy-MC studies of the S_5-fold, with r=1. Figures show the number of successfully passed fits on the toy-MC data without (left) and with acceptance (right) on the parameter F_L. The green bands represent fit-p.d.f. positivity range. The top figures correspond to the Run-1 like number of events (n = 1), while the middle and the bottom to 10× and 100× larger simulated samples.

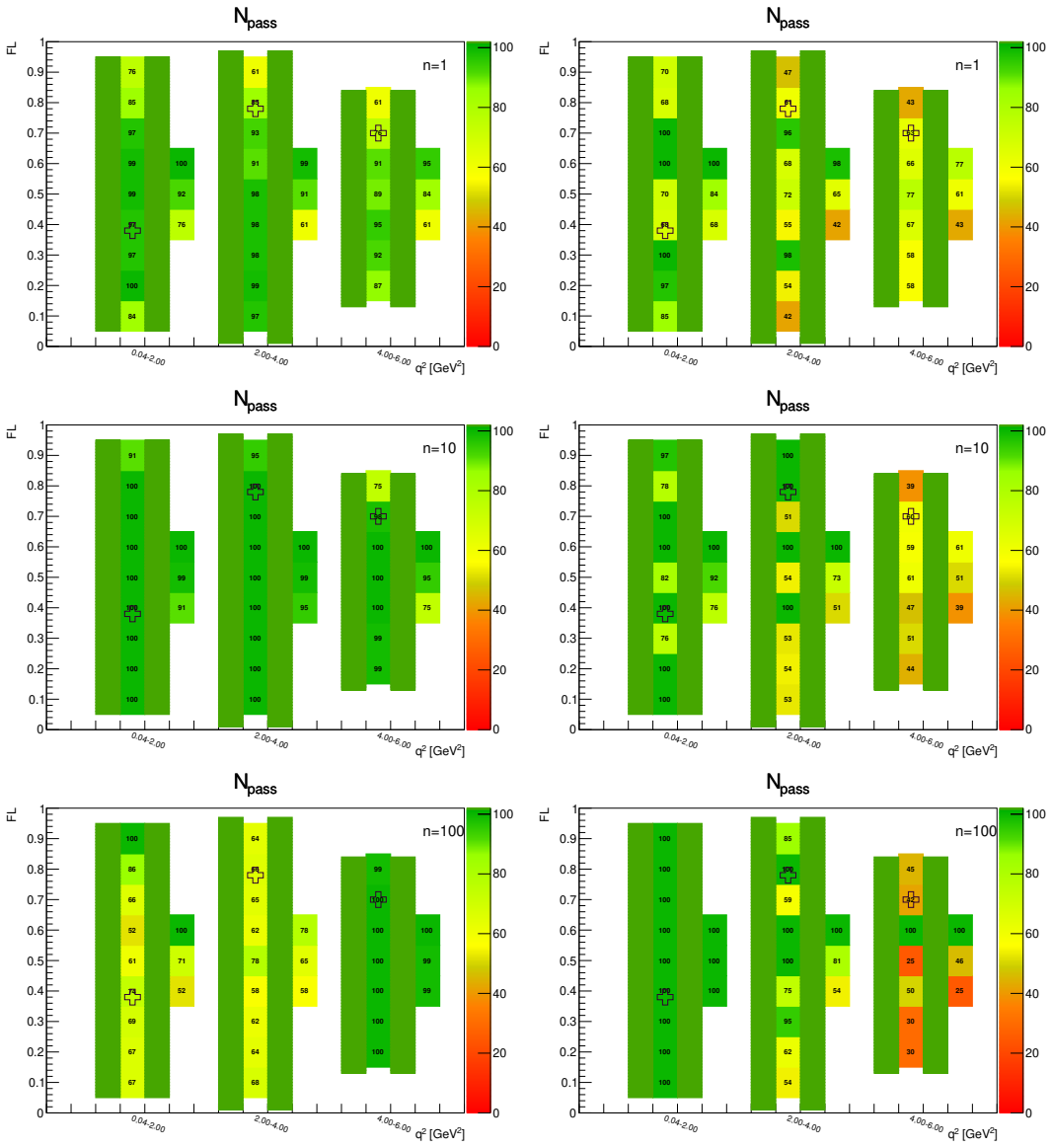

Figure A.12: Toy-MC studies of the S_5-fold, with r=2. Figures show the number of successfully passed fits on the toy-MC data without (left) and with acceptance (right) on the parameter F_L. The green bands represent fit-p.d.f. positivity range. The top figures correspond to the Run-1 like number of events (n = 1), while the middle and the bottom to 10× and 100× larger simulated samples.

A.2.5 S_5-fold – parameter S_3

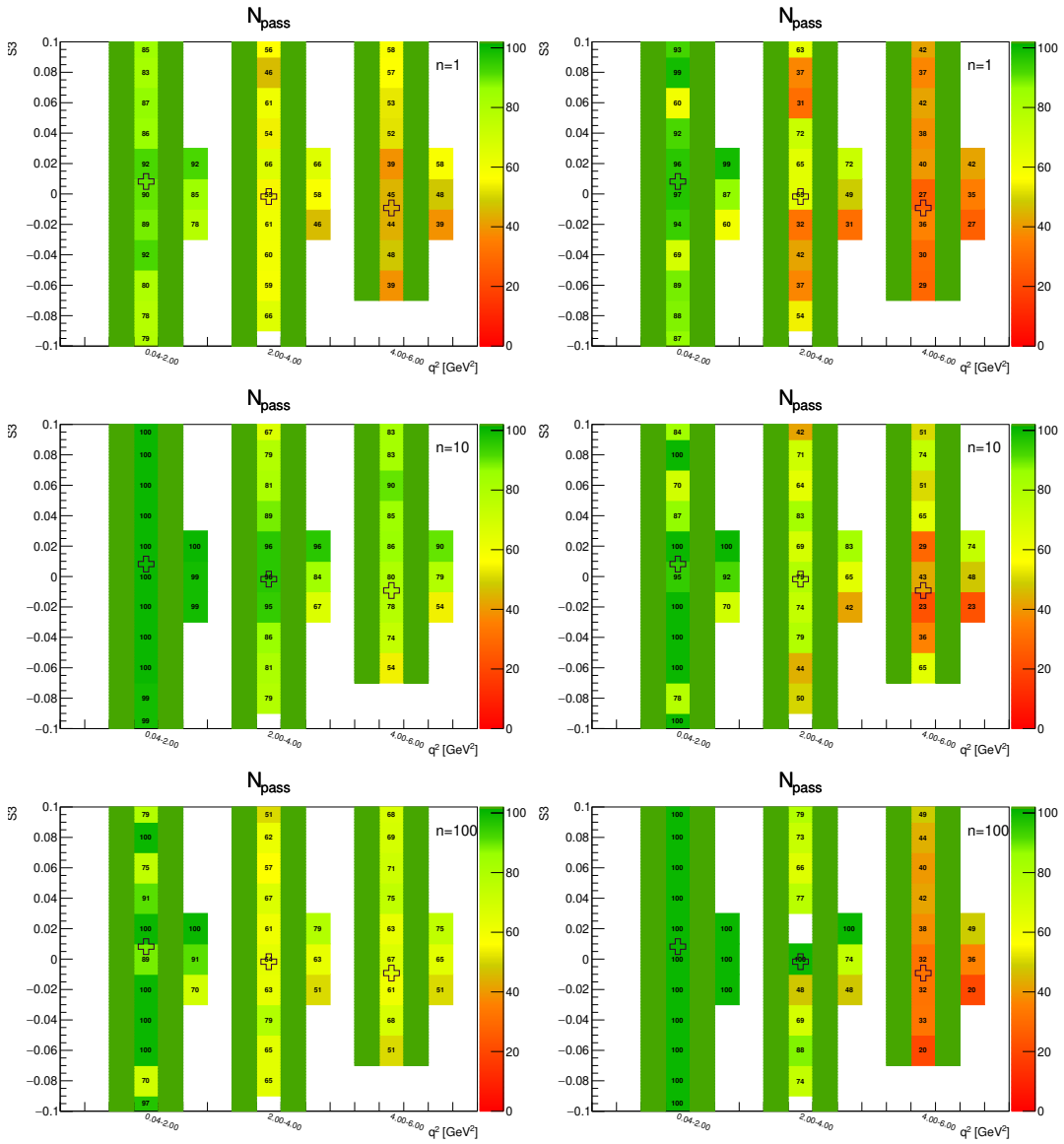

Figure A.13: Toy-MC studies of the S_5-fold, with r=0.5. Figures show the number of successfully passed fits on the toy-MC data without (left) and with acceptance (right) on the parameter S_3. The green bands represent fit-p.d.f. positivity range. The top figures correspond to the Run-1 like number of events (n = 1), while the middle and the bottom to 10× and 100× larger simulated samples.

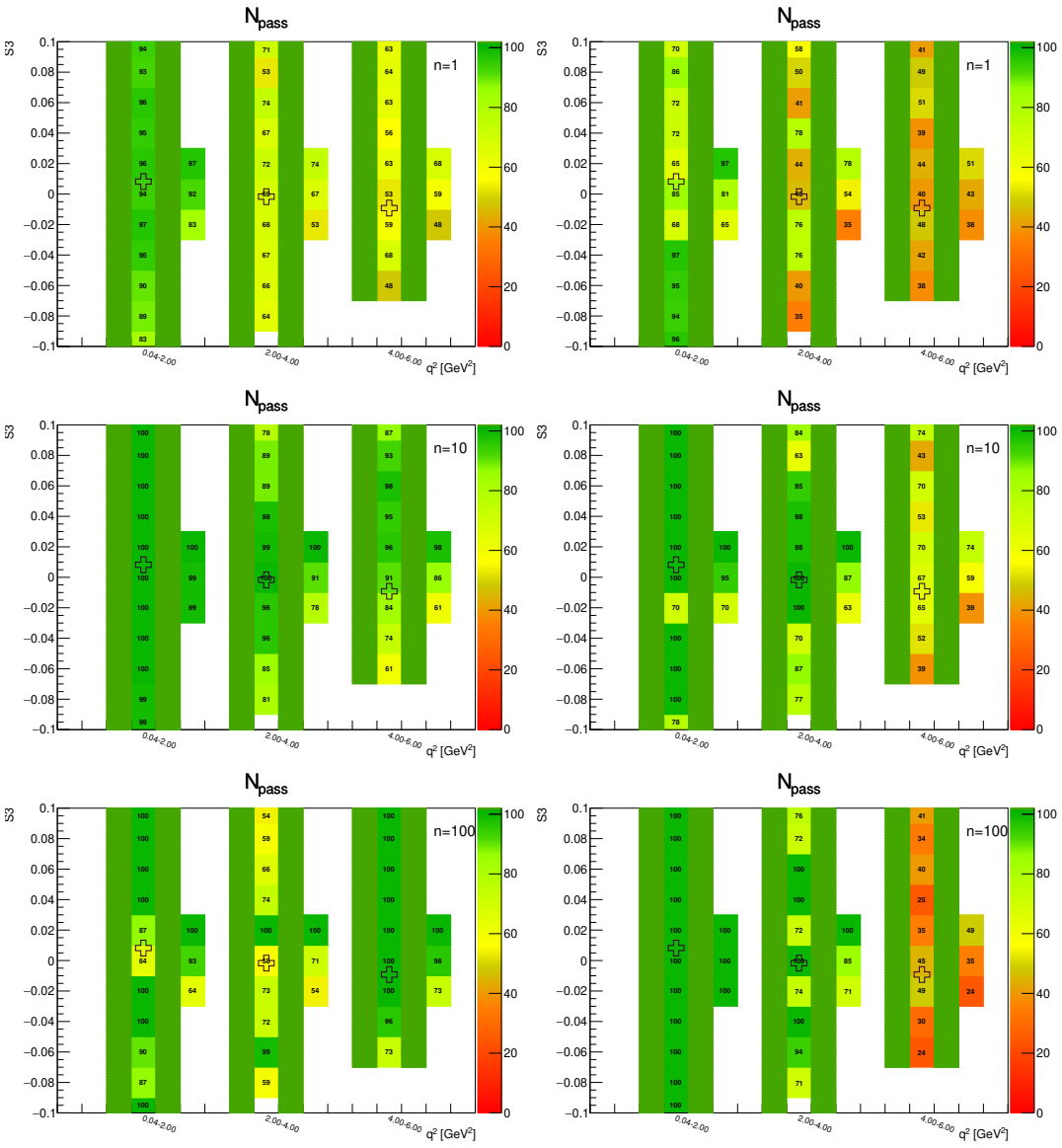

Figure A.14: Toy-MC studies of the S_5-fold, with r=1. Figures show the number of successfully passed fits on the toy-MC data without (left) and with acceptance (right) on the parameter S_3. The green bands represent fit-p.d.f. positivity range. The top figures correspond to the Run-1 like number of events (n = 1), while the middle and the bottom to 10× and 100× larger simulated samples.

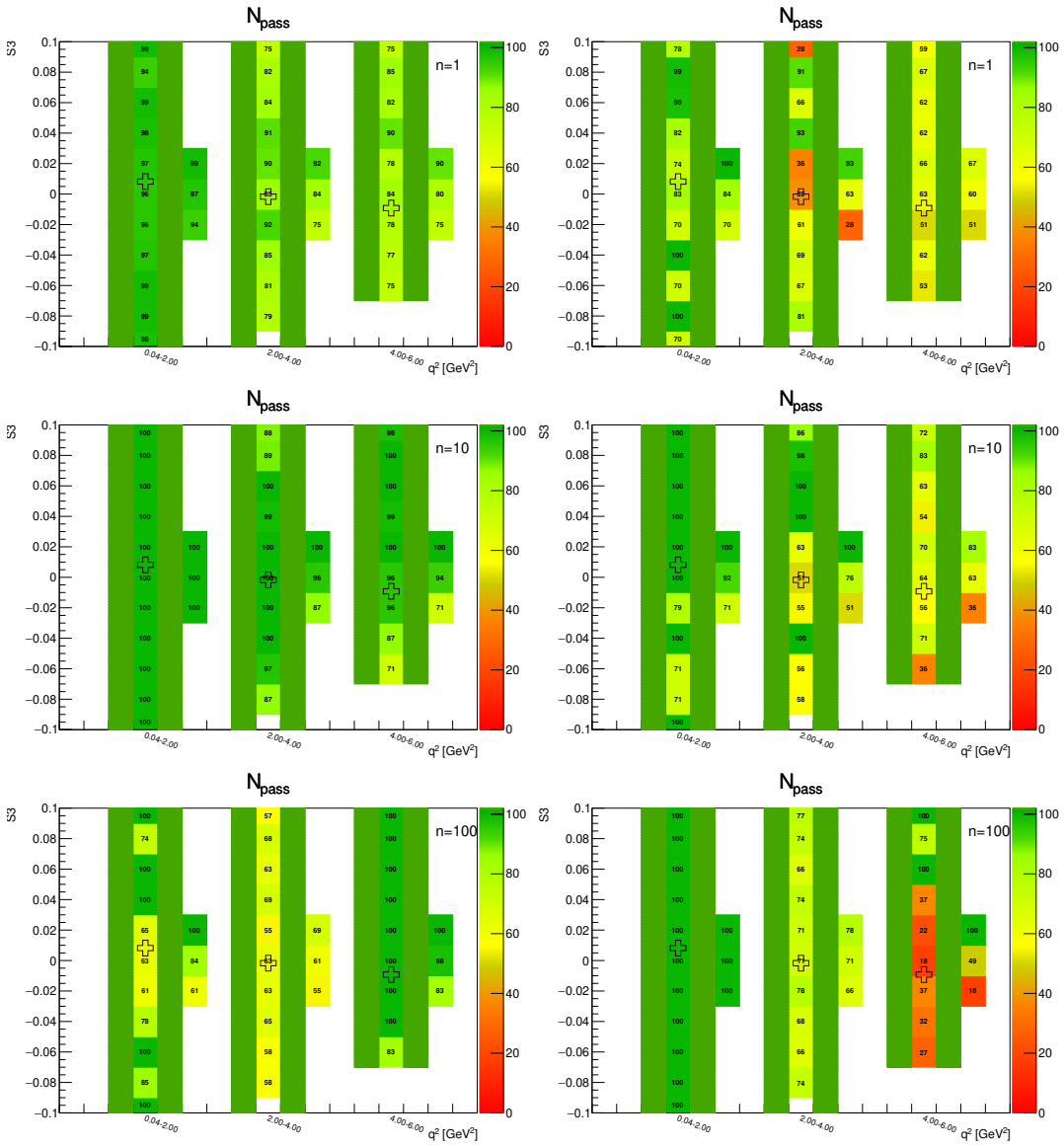

Figure A.15: Toy-MC studies of the S_5-fold, with r=2. Figures show the number of successfully passed fits on the toy-MC data without (left) and with acceptance (right) on the parameter S_3. The green bands represent fit-p.d.f. positivity range. The top figures correspond to the Run-1 like number of events (n = 1), while the middle and the bottom to 10× and 100× larger simulated samples.

A.2.6 S_5-fold – parameter S_5

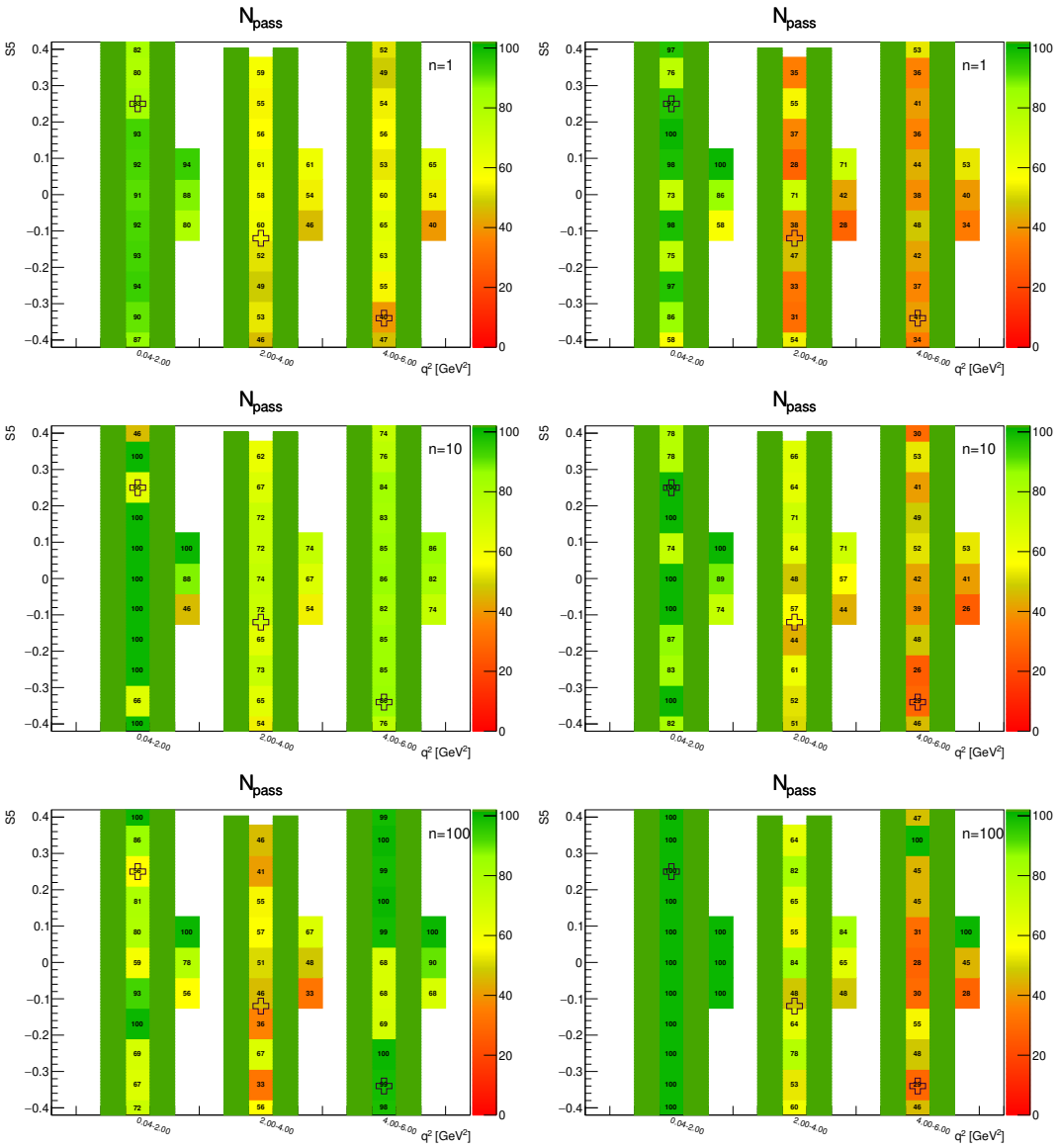

Figure A.16: Toy-MC studies of the S_5-fold, with r=0.5. Figures show the number of successfully passed fits on the toy-MC data without (left) and with acceptance (right) on the parameter S_5. The green bands represent fit-p.d.f. positivity range. The top figures correspond to the Run-1 like number of events (n = 1), while the middle and the bottom to 10× and 100× larger simulated samples.

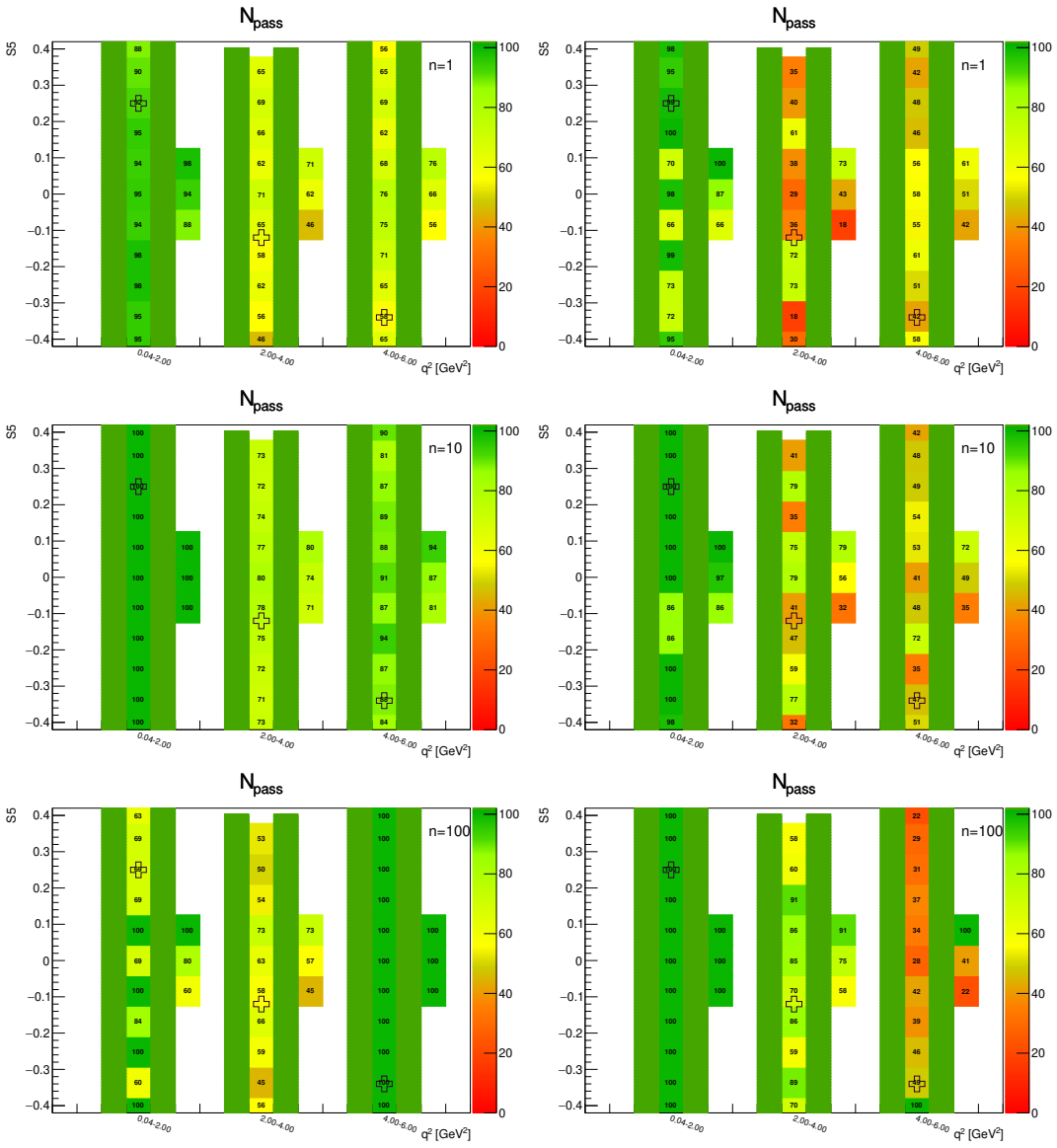

Figure A.17: Toy-MC studies of the S_5-fold, with r=1. Figures show the number of successfully passed fits on the toy-MC data without (left) and with acceptance (right) on the parameter S_5. The green bands represent fit-p.d.f. positivity range. The top figures correspond to the Run-1 like number of events (n = 1), while the middle and the bottom to 10× and 100× larger simulated samples.

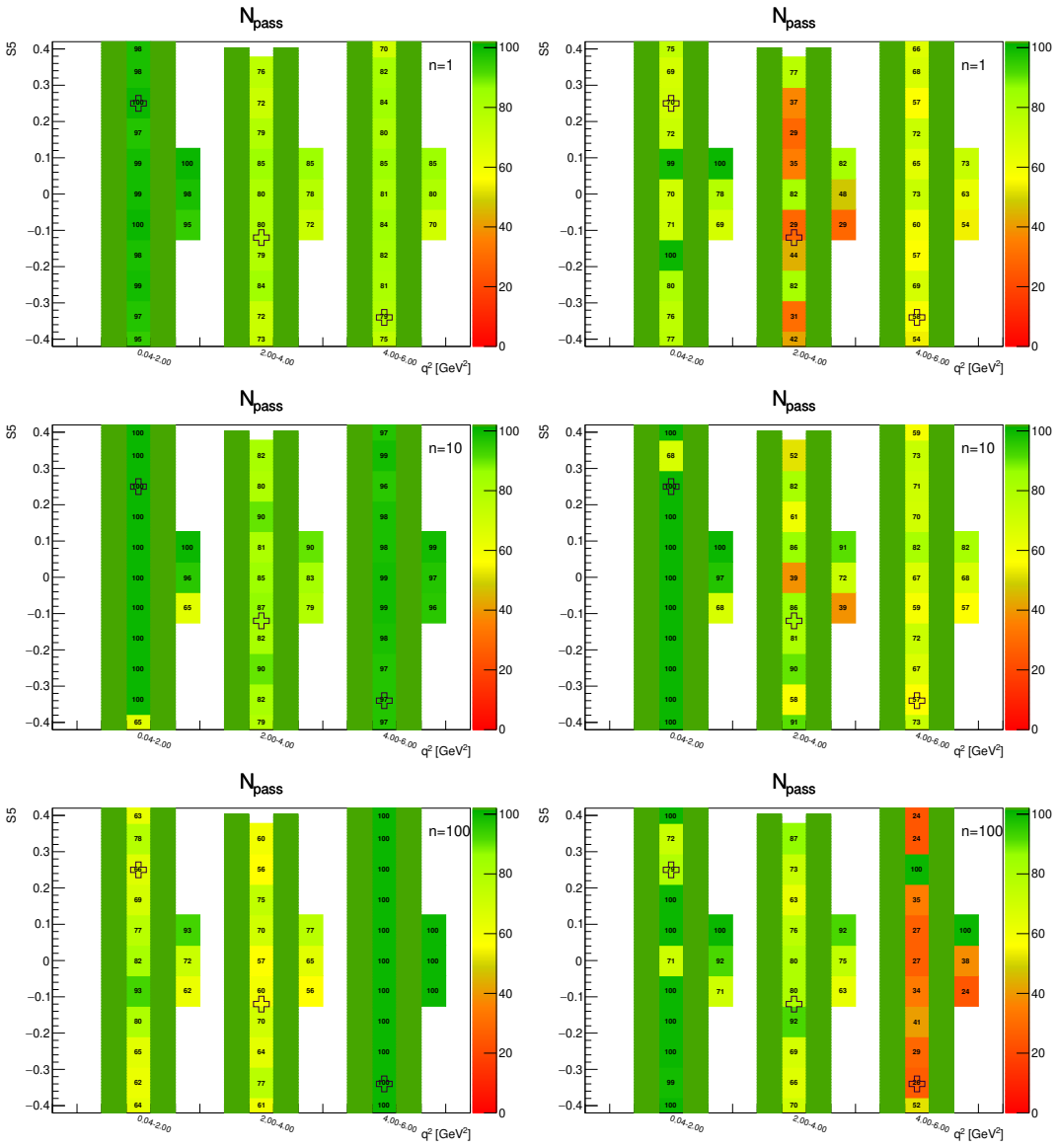

Figure A.18: Toy-MC studies of the S_5-fold, with r=2. Figures show the number of successfully passed fits on the toy-MC data without (left) and with acceptance (right) on the parameter S_5. The green bands represent fit-p.d.f. positivity range. The top figures correspond to the Run-1 like number of events (n = 1), while the middle and the bottom to 10× and 100× larger simulated samples.

A.2.7 S_7-fold – parameter F_L

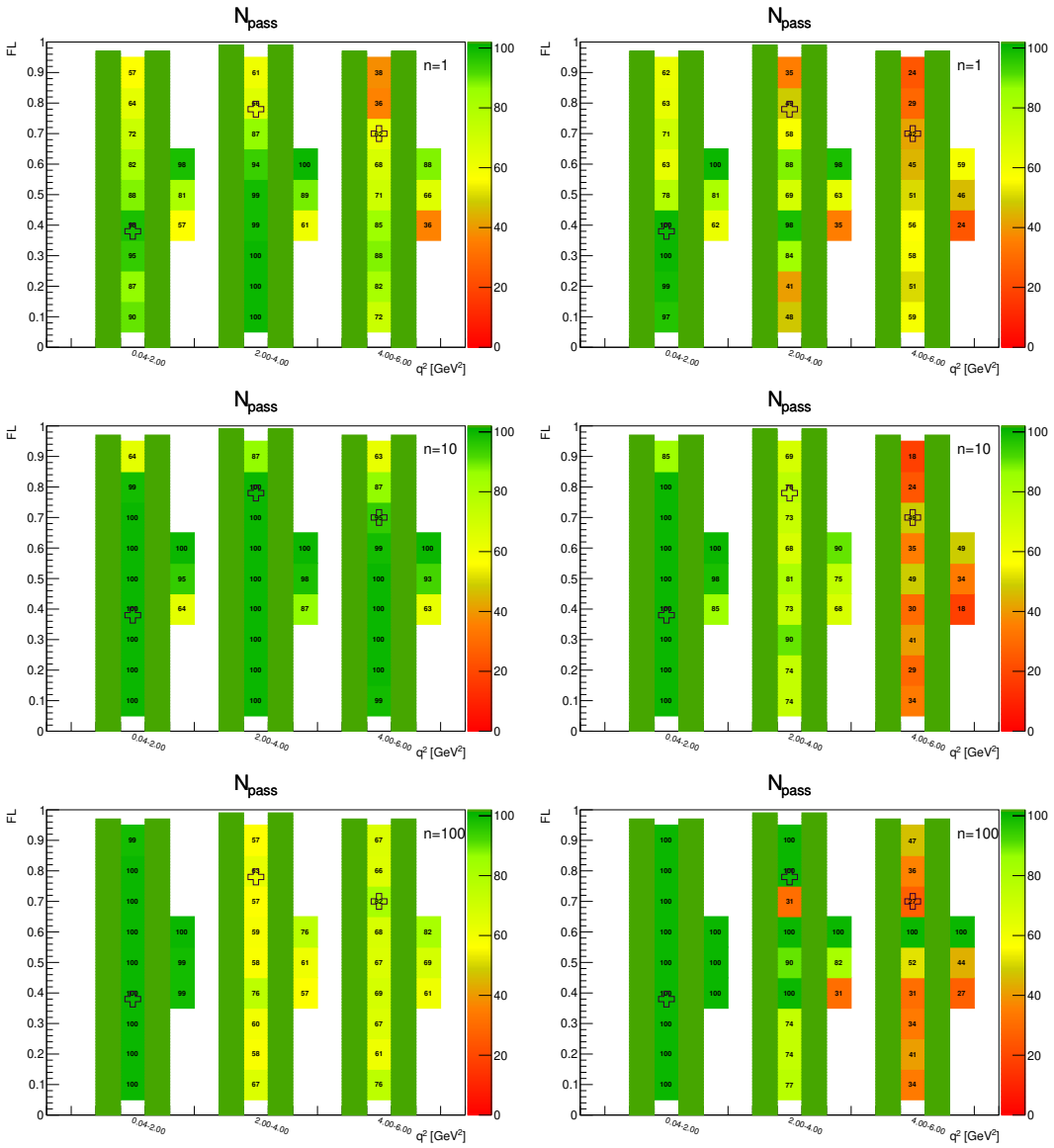

Figure A.19: Toy-MC studies of the S_7-fold, with r=0.5. Figures show the number of successfully passed fits on the toy-MC data without (left) and with acceptance (right) on the parameter F_L. The green bands represent fit-p.d.f. positivity range. The top figures correspond to the Run-1 like number of events (n = 1), while the middle and the bottom to 10× and 100× larger simulated samples.

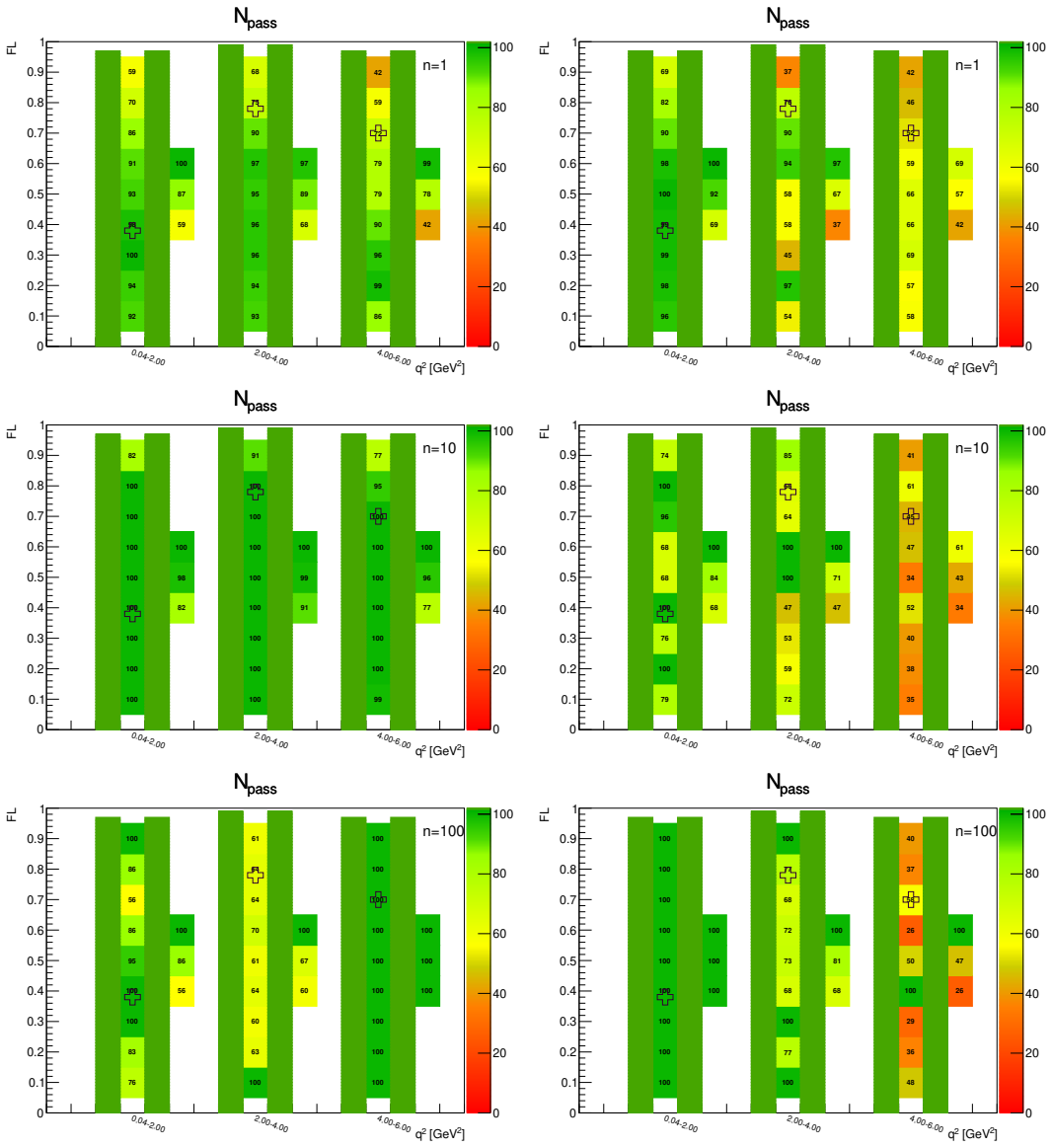

Figure A.20: Toy-MC studies of the S_7-fold, with r=1. Figures show the number of successfully passed fits on the toy-MC data without (left) and with acceptance (right) on the parameter F_L. The green bands represent fit-p.d.f. positivity range. The top figures correspond to the Run-1 like number of events (n = 1), while the middle and the bottom to 10× and 100× larger simulated samples.

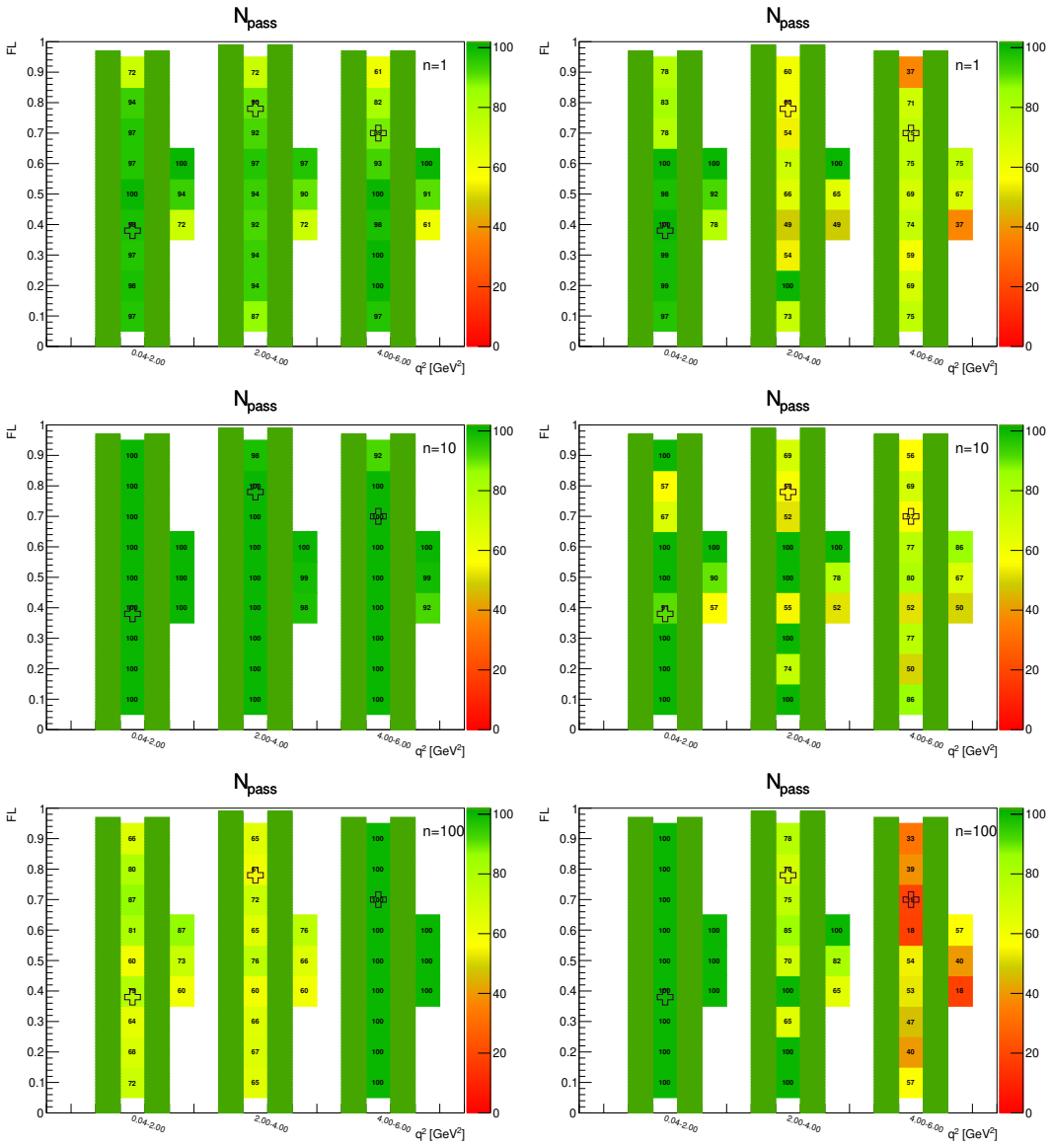

Figure A.21: Toy-MC studies of the S_7-fold, with r=2. Figures show the number of successfully passed fits on the toy-MC data without (left) and with acceptance (right) on the parameter F_L. The green bands represent fit-p.d.f. positivity range. The top figures correspond to the Run-1 like number of events (n = 1), while the middle and the bottom to 10× and 100× larger simulated samples.

A.2.8 S_7-fold – parameter S_3

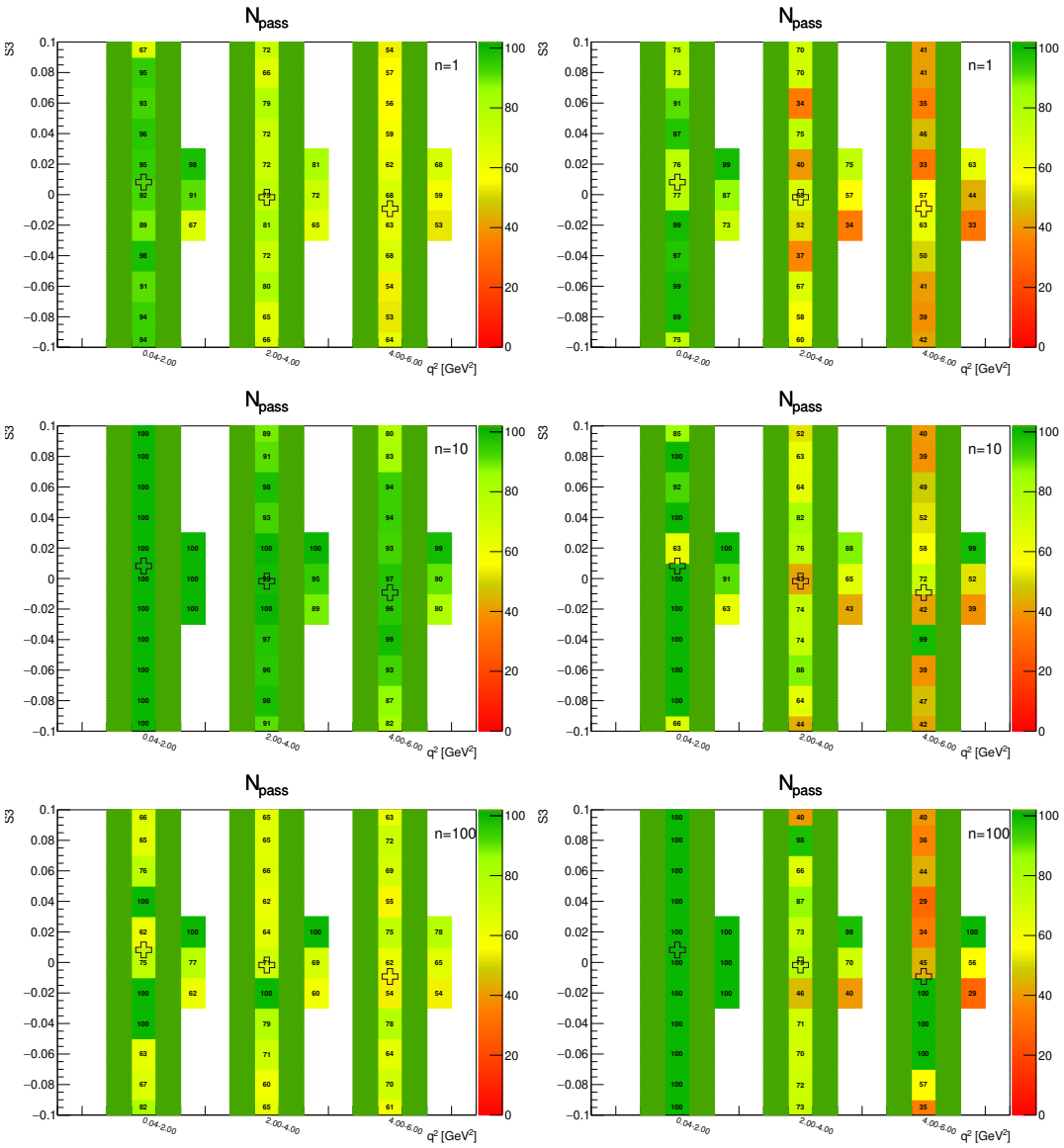

Figure A.22: Toy-MC studies of the S_7-fold, with r=0.5. Figures show the number of successfully passed fits on the toy-MC data without (left) and with acceptance (right) on the parameter S_3. The green bands represent fit-p.d.f. positivity range. The top figures correspond to the Run-1 like number of events (n = 1), while the middle and the bottom to 10× and 100× larger simulated samples.

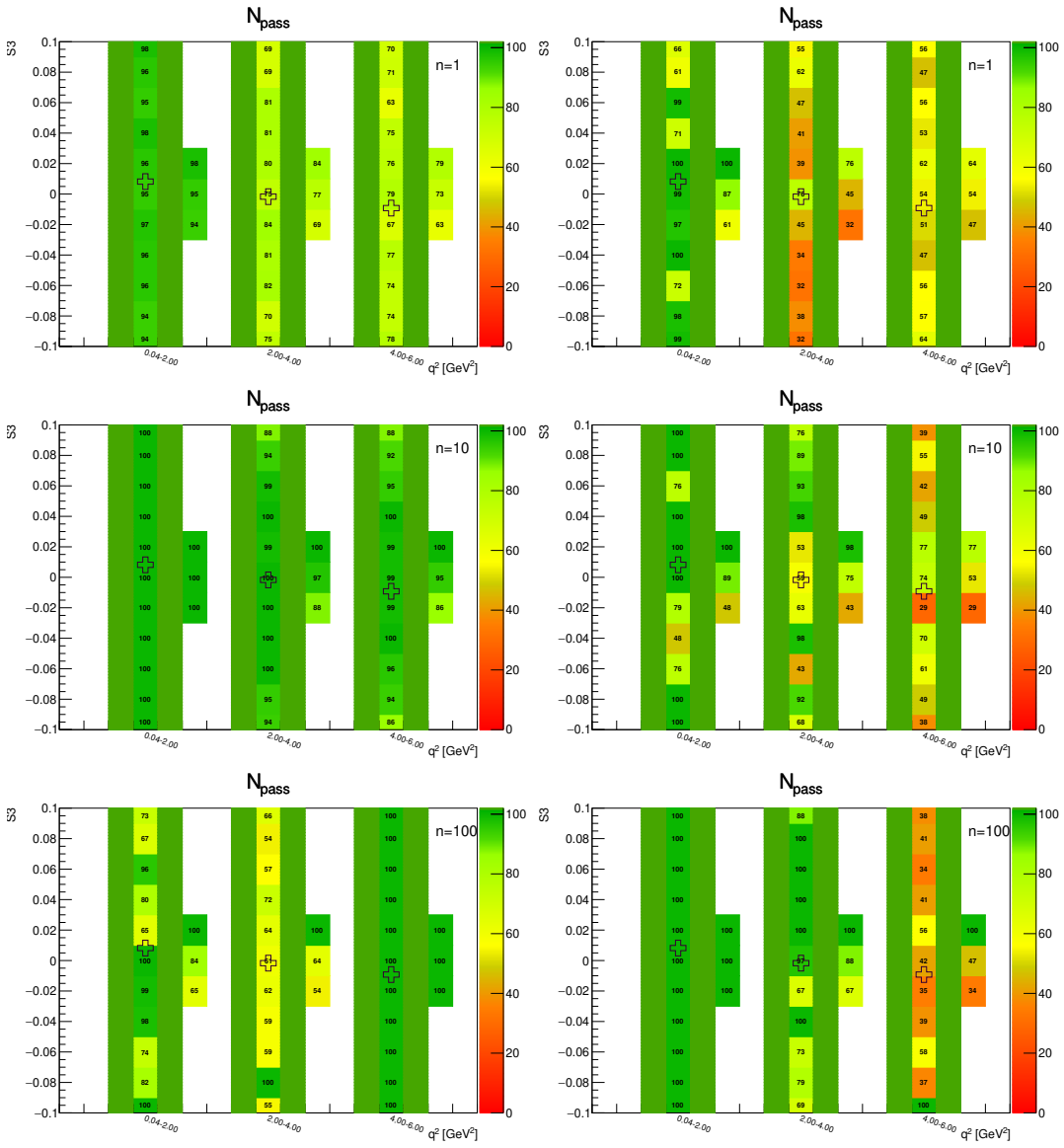

Figure A.23: Toy-MC studies of the S_7-fold, with r=1. Figures show the number of successfully passed fits on the toy-MC data without (left) and with acceptance (right) on the parameter S_3. The green bands represent fit-p.d.f. positivity range. The top figures correspond to the Run-1 like number of events (n = 1), while the middle and the bottom to 10× and 100× larger simulated samples.

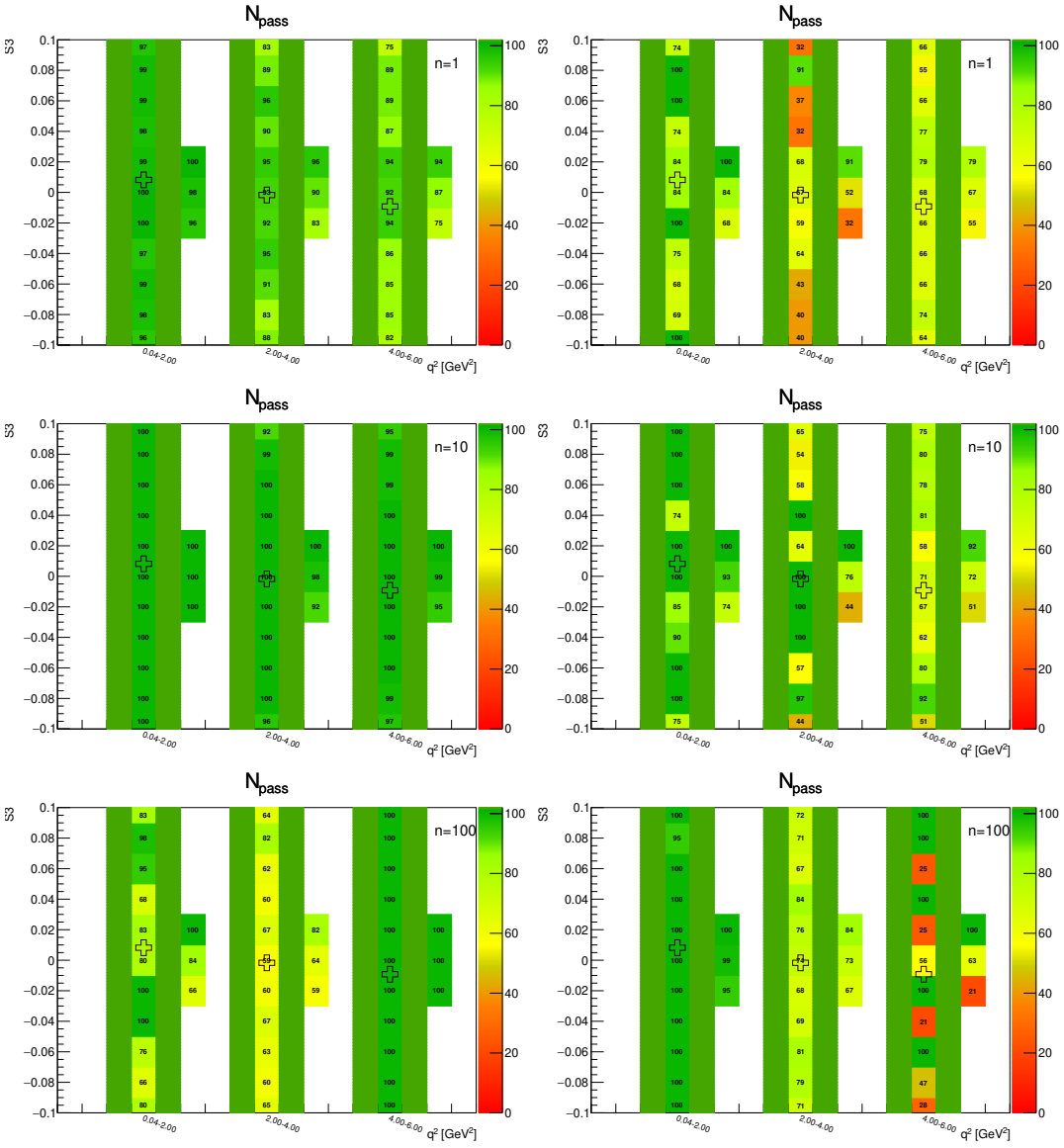

Figure A.24: Toy-MC studies of the S_7-fold, with r=2. Figures show the number of successfully passed fits on the toy-MC data without (left) and with acceptance (right) on the parameter S_3. The green bands represent fit-p.d.f. positivity range. The top figures correspond to the Run-1 like number of events (n = 1), while the middle and the bottom to 10× and 100× larger simulated samples.

A.2.9 S_7-fold – parameter S_7

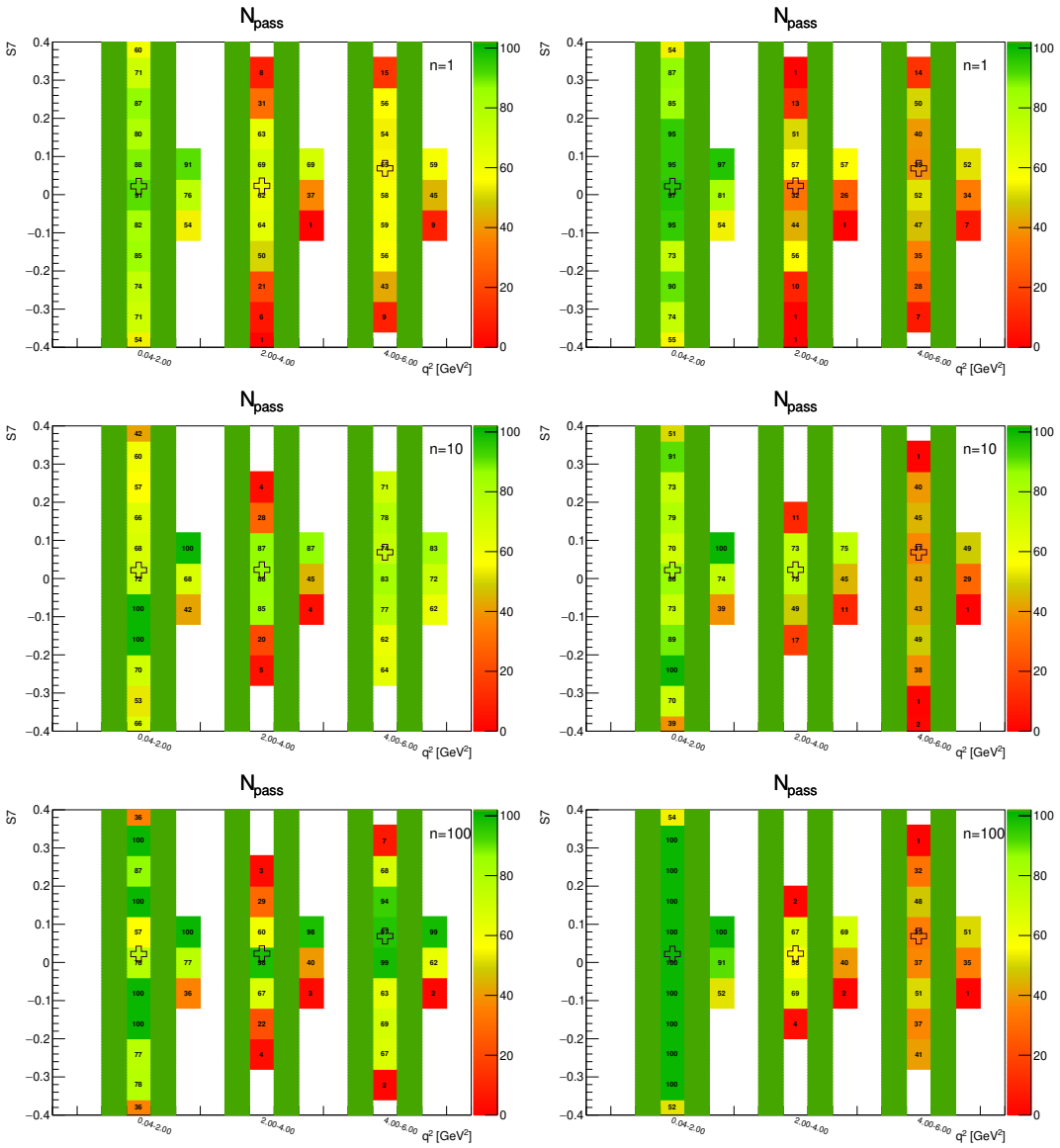

Figure A.25: Toy-MC studies of the S_7-fold, with r=0.5. Figures show the number of successfully passed fits on the toy-MC data without (left) and with acceptance (right) on the parameter S_7. The green bands represent fit-p.d.f. positivity range. The top figures correspond to the Run-1 like number of events (n = 1), while the middle and the bottom to 10× and 100× larger simulated samples.

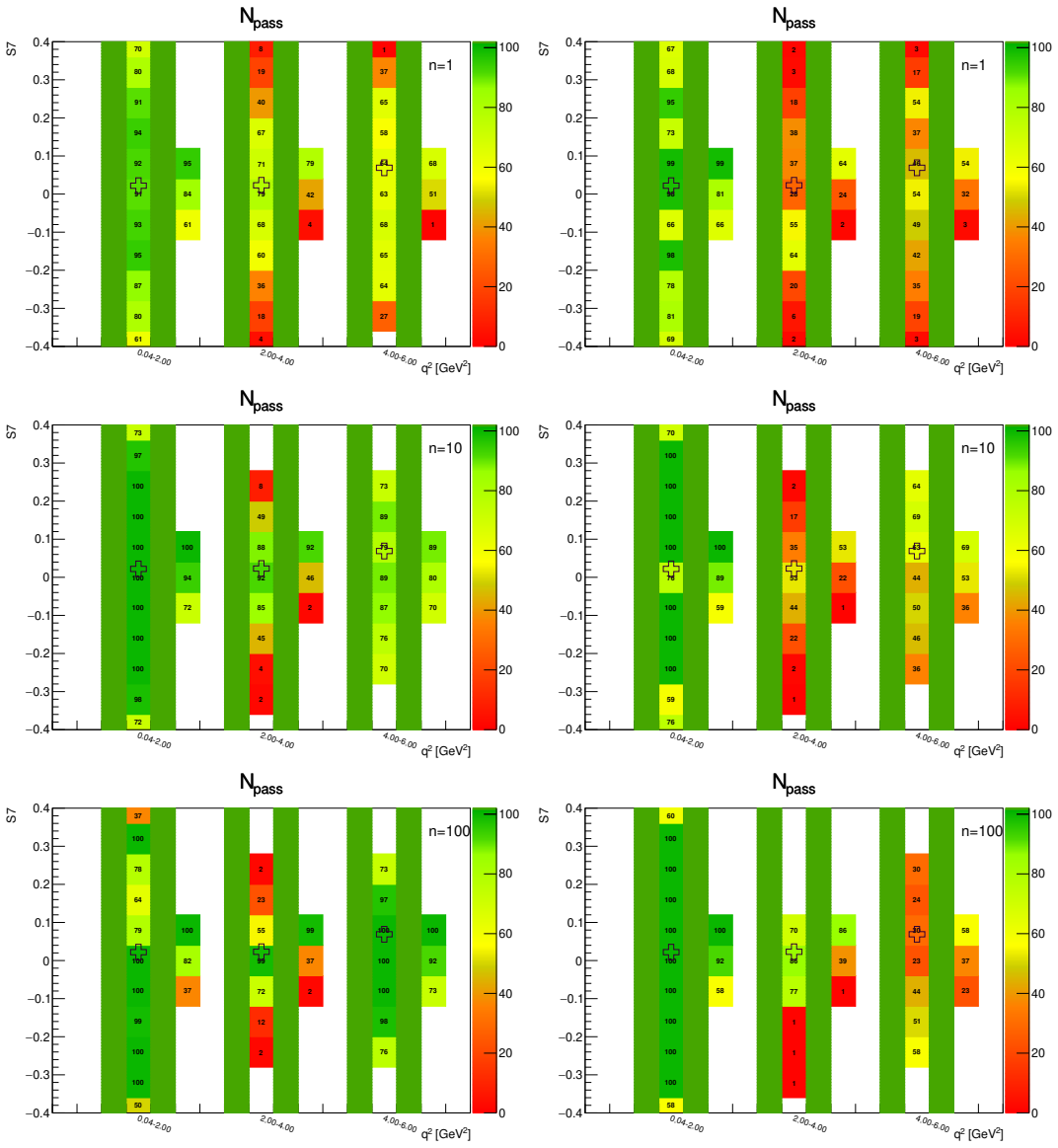

Figure A.26: Toy-MC studies of the S_7-fold, with r=1. Figures show the number of successfully passed fits on the toy-MC data without (left) and with acceptance (right) on the parameter S_7. The green bands represent fit-p.d.f. positivity range. The top figures correspond to the Run-1 like number of events (n = 1), while the middle and the bottom to 10× and 100× larger simulated samples.

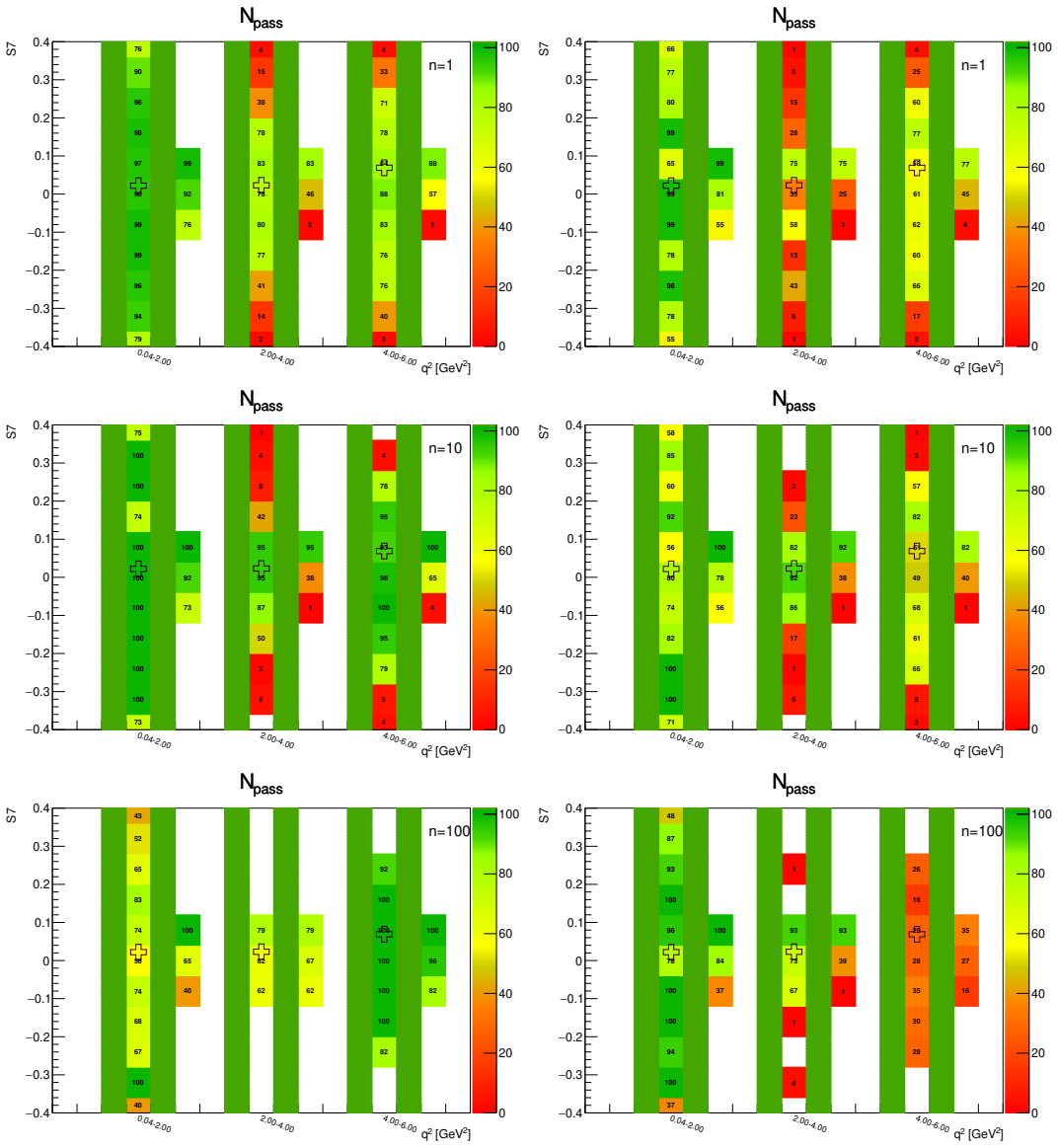

Figure A.27: Toy-MC studies of the S_7-fold, with r=2. Figures show the number of successfully passed fits on the toy-MC data without (left) and with acceptance (right) on the parameter S_7. The green bands represent fit-p.d.f. positivity range. The top figures correspond to the Run-1 like number of events (n = 1), while the middle and the bottom to 10× and 100× larger simulated samples.

A.2.10 S_8-fold – parameter F_L

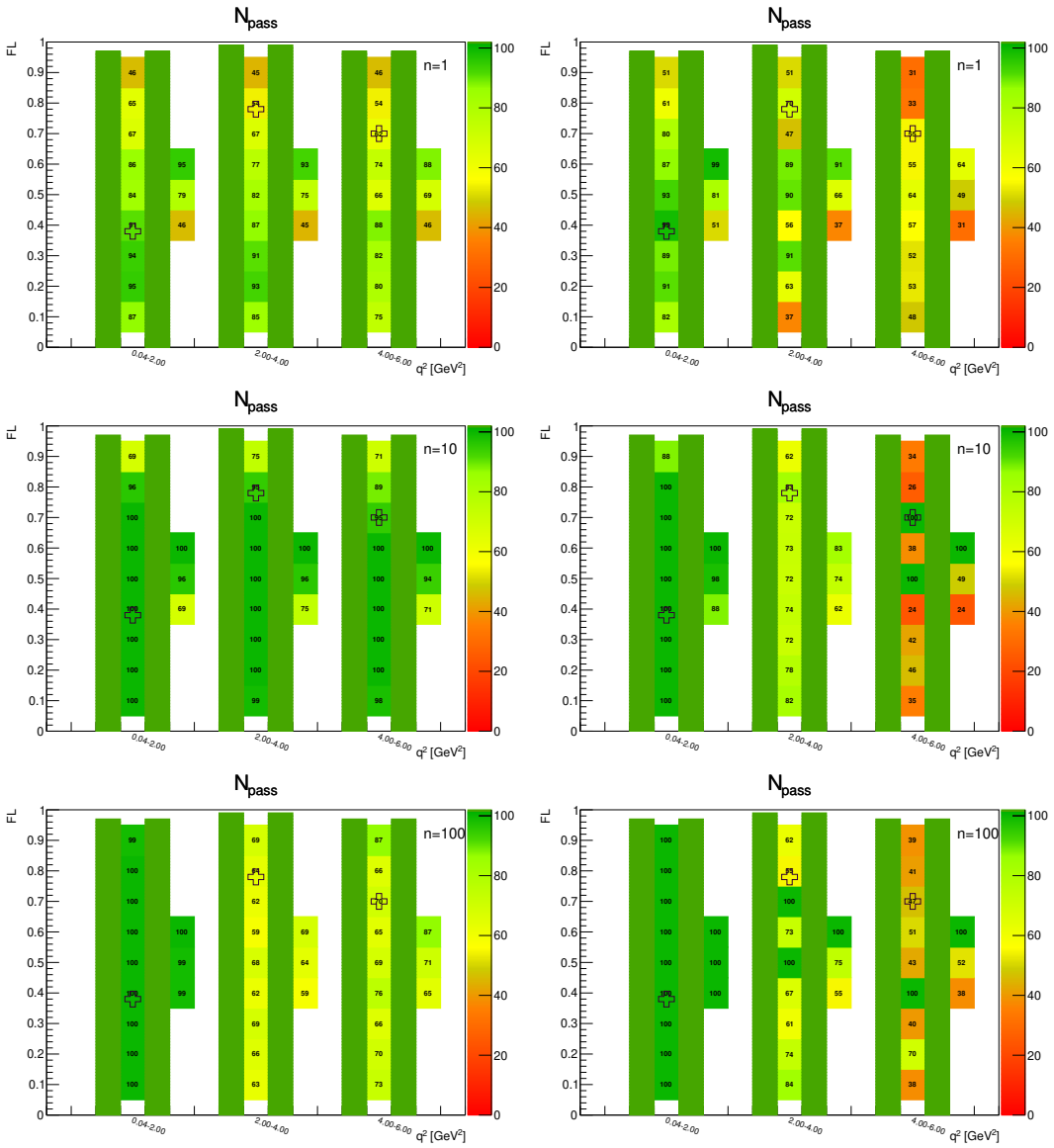

Figure A.28: Toy-MC studies of the S_8-fold, with r=0.5. Figures show the number of successfully passed fits on the toy-MC data without (left) and with acceptance (right) on the parameter F_L. The green bands represent fit-p.d.f. positivity range. The top figures correspond to the Run-1 like number of events (n = 1), while the middle and the bottom to 10× and 100× larger simulated samples.

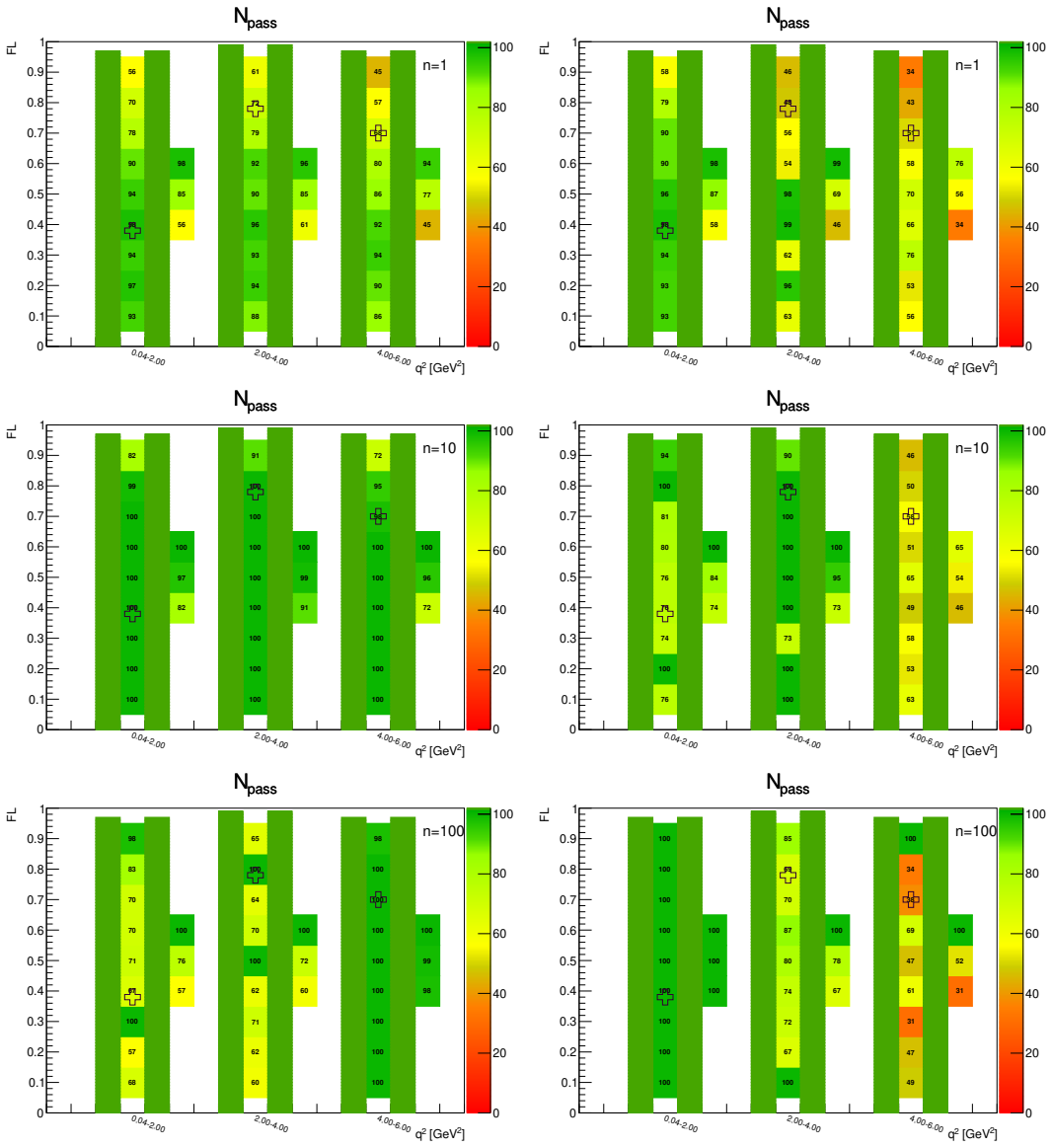

Figure A.29: Toy-MC studies of the S_8-fold, with r=1. Figures show the number of successfully passed fits on the toy-MC data without (left) and with acceptance (right) on the parameter F_L. The green bands represent fit-p.d.f. positivity range. The top figures correspond to the Run-1 like number of events (n = 1), while the middle and the bottom to 10× and 100× larger simulated samples.

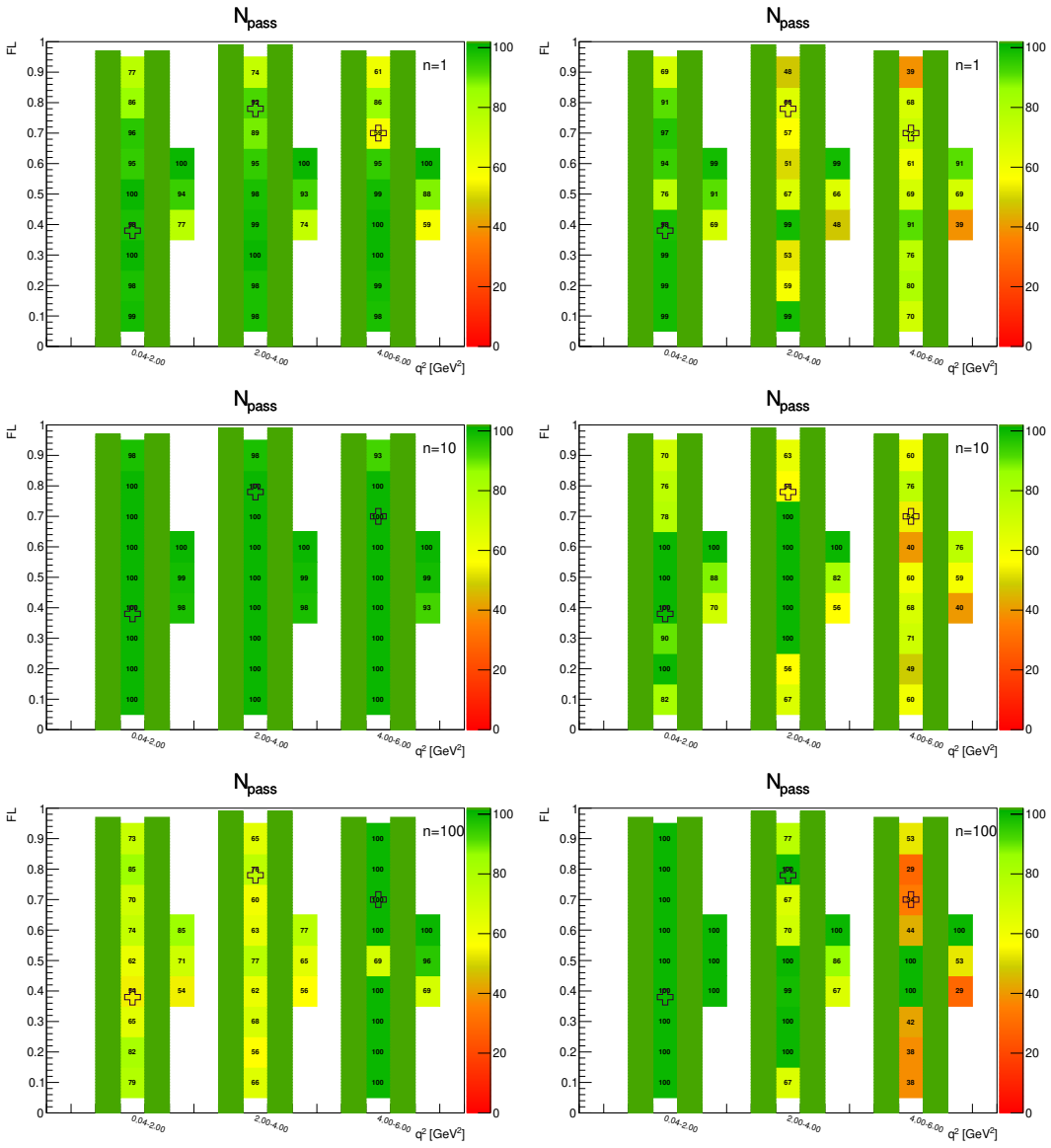

Figure A.30: Toy-MC studies of the S_8-fold, with r=2. Figures show the number of successfully passed fits on the toy-MC data without (left) and with acceptance (right) on the parameter F_L. The green bands represent fit-p.d.f. positivity range. The top figures correspond to the Run-1 like number of events (n = 1), while the middle and the bottom to 10× and 100× larger simulated samples.

A.2.11 S_8-fold – parameter S_3

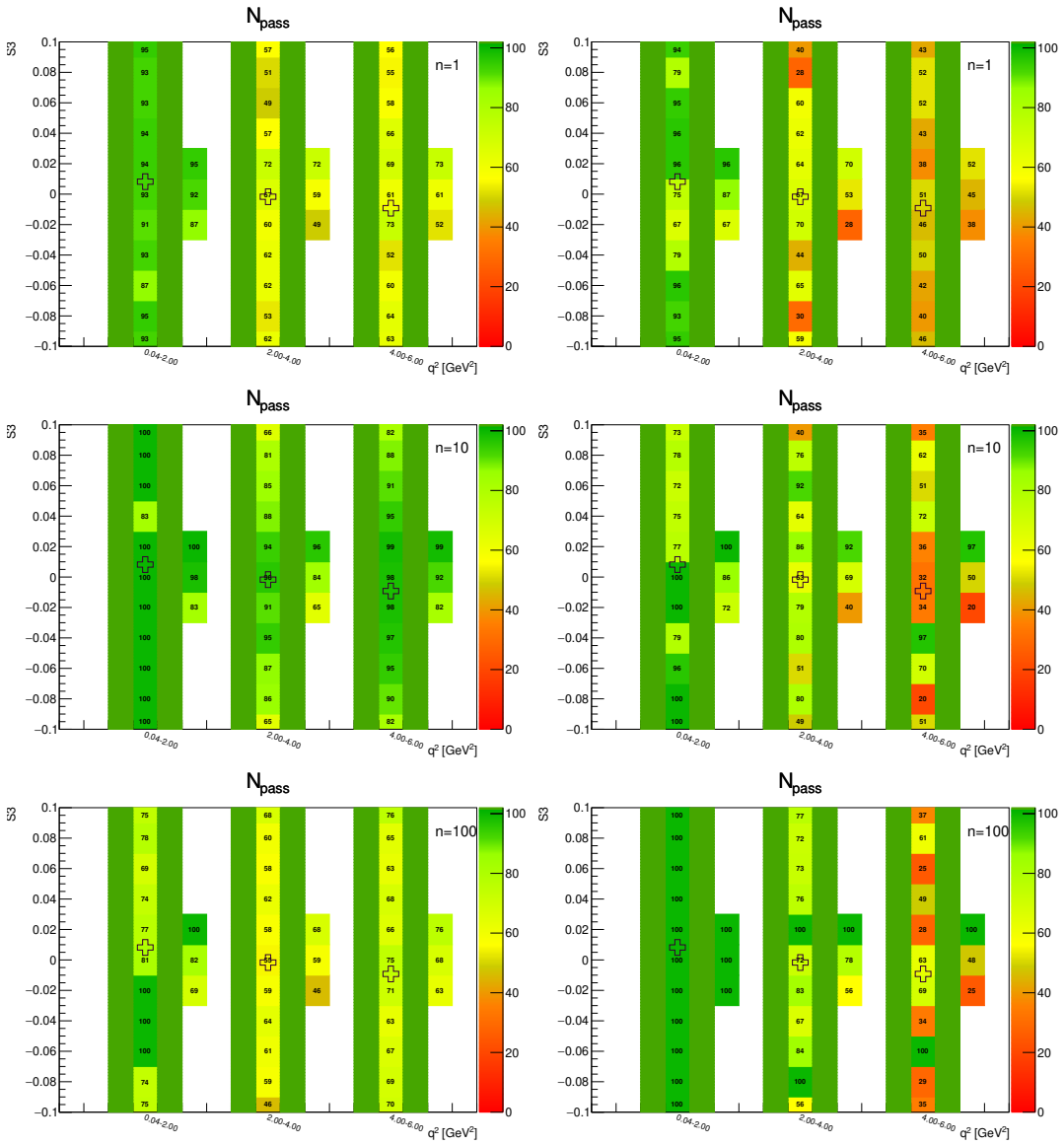

Figure A.31: Toy-MC studies of the S_8-fold, with r=0.5. Figures show the number of successfully passed fits on the toy-MC data without (left) and with acceptance (right) on the parameter S_3. The green bands represent fit-p.d.f. positivity range. The top figures correspond to the Run-1 like number of events (n = 1), while the middle and the bottom to 10× and 100× larger simulated samples.

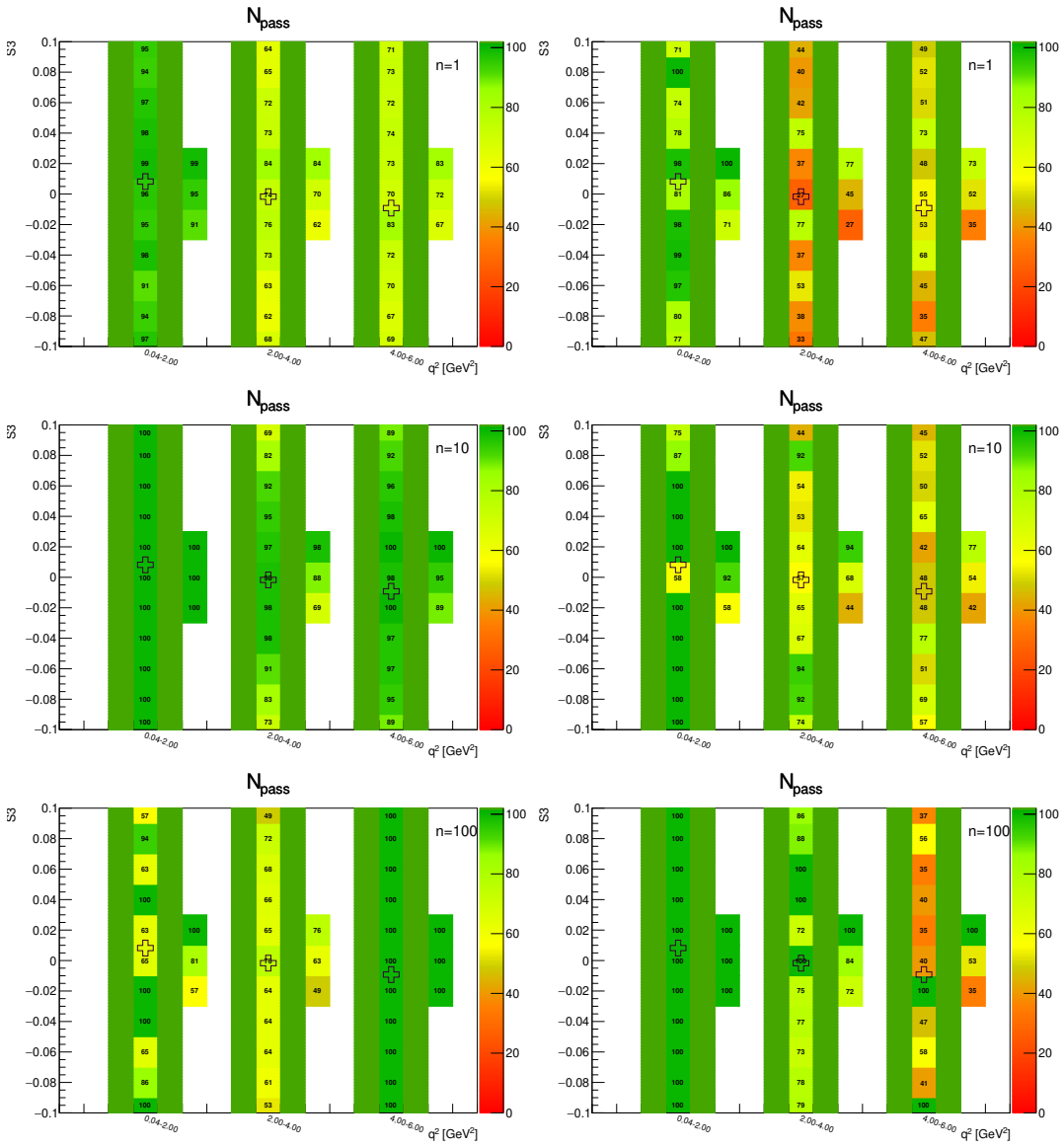

Figure A.32: Toy-MC studies of the S_8-fold, with r=1. Figures show the number of successfully passed fits on the toy-MC data without (left) and with acceptance (right) on the parameter S_3. The green bands represent fit-p.d.f. positivity range. The top figures correspond to the Run-1 like number of events (n = 1), while the middle and the bottom to 10× and 100× larger simulated samples.

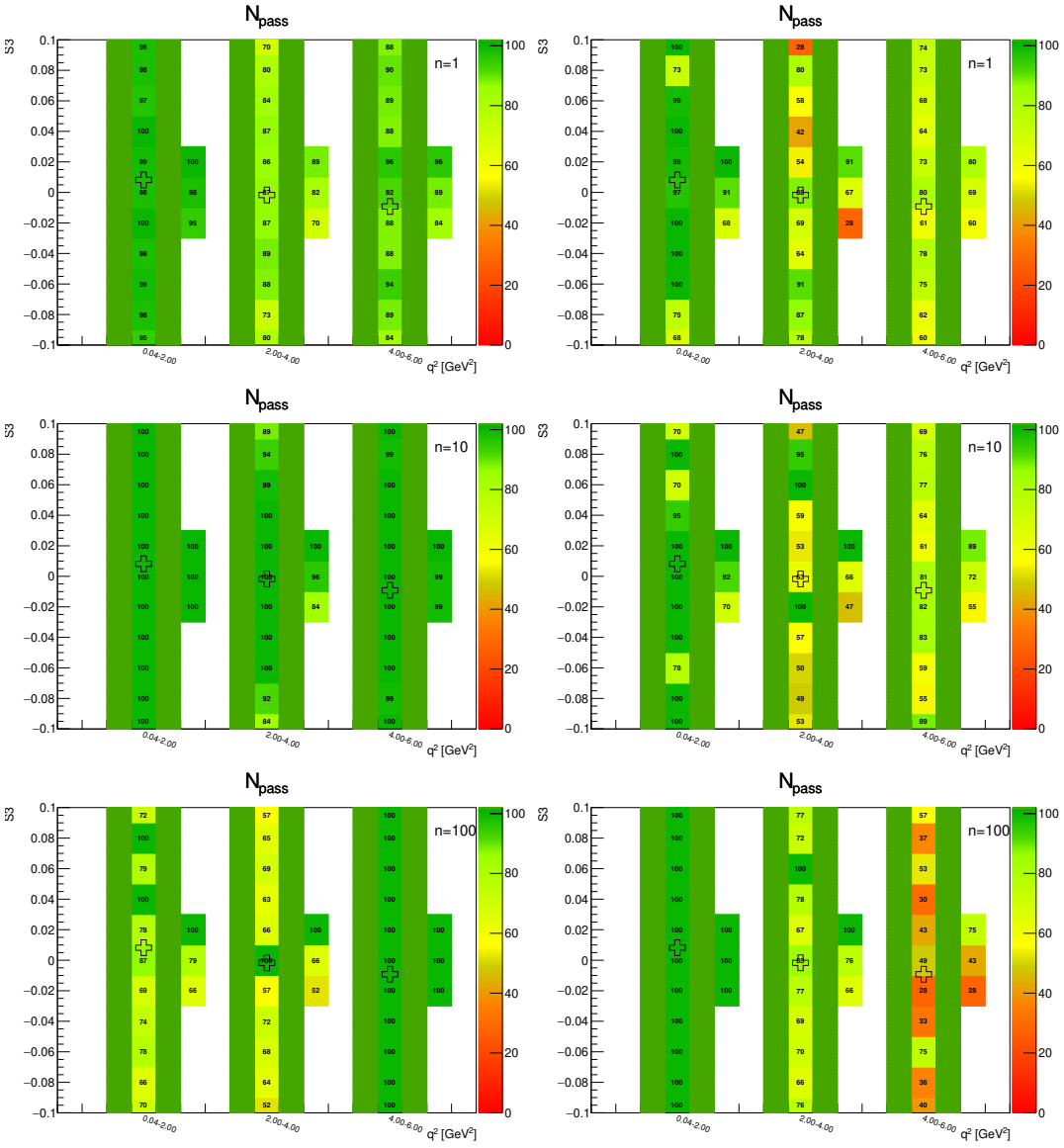

Figure A.33: Toy-MC studies of the S_8-fold, with r=2. Figures show the number of successfully passed fits on the toy-MC data without (left) and with acceptance (right) on the parameter S_3. The green bands represent fit-p.d.f. positivity range. The top figures correspond to the Run-1 like number of events (n = 1), while the middle and the bottom to 10× and 100× larger simulated samples.

A.2.12 S_8-fold – parameter S_8

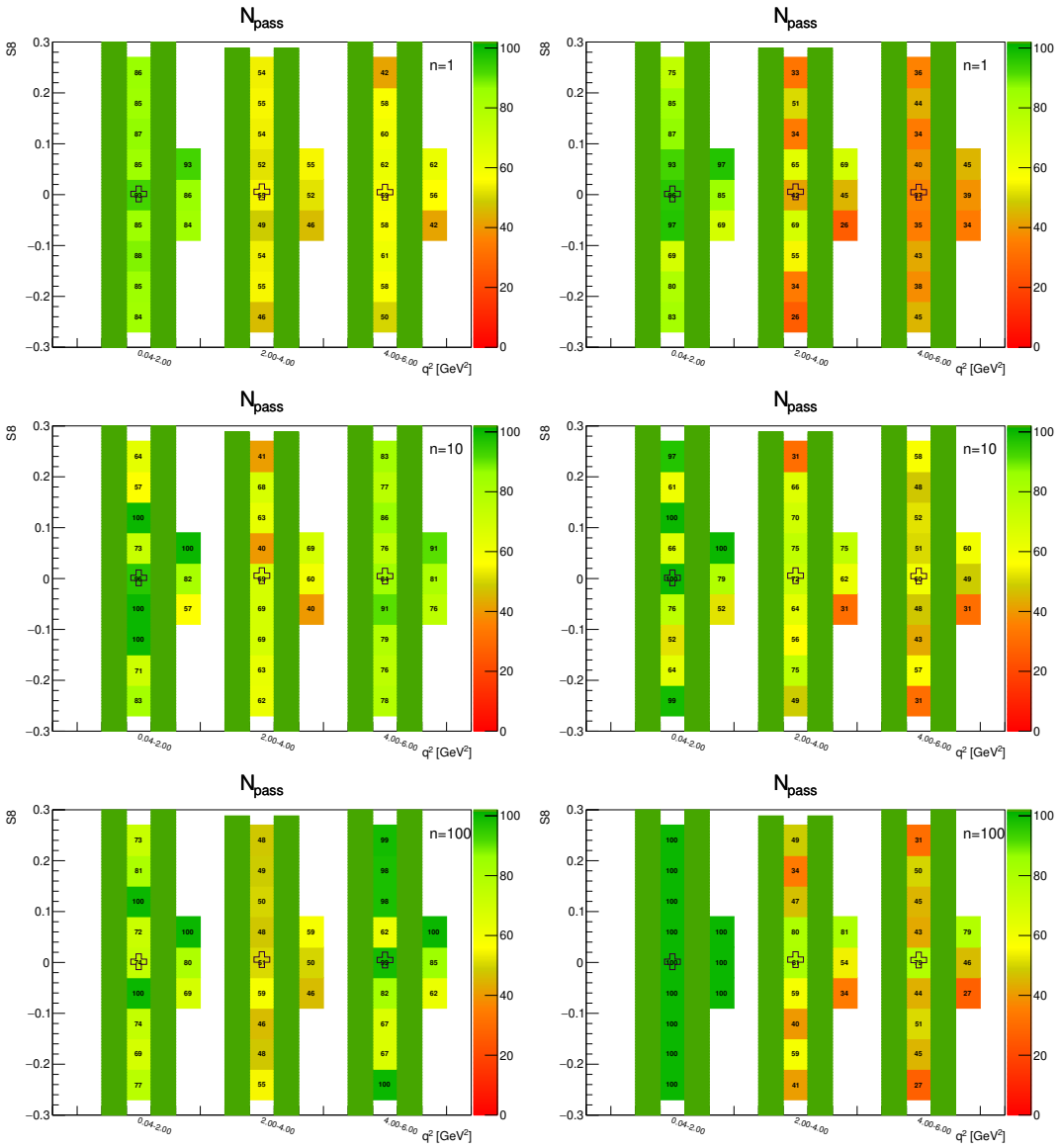

Figure A.34: Toy-MC studies of the S_8-fold, with r=0.5. Figures show the number of successfully passed fits on the toy-MC data without (left) and with acceptance (right) on the parameter S_8. The green bands represent fit-p.d.f. positivity range. The top figures correspond to the Run-1 like number of events (n = 1), while the middle and the bottom to 10× and 100× larger simulated samples.

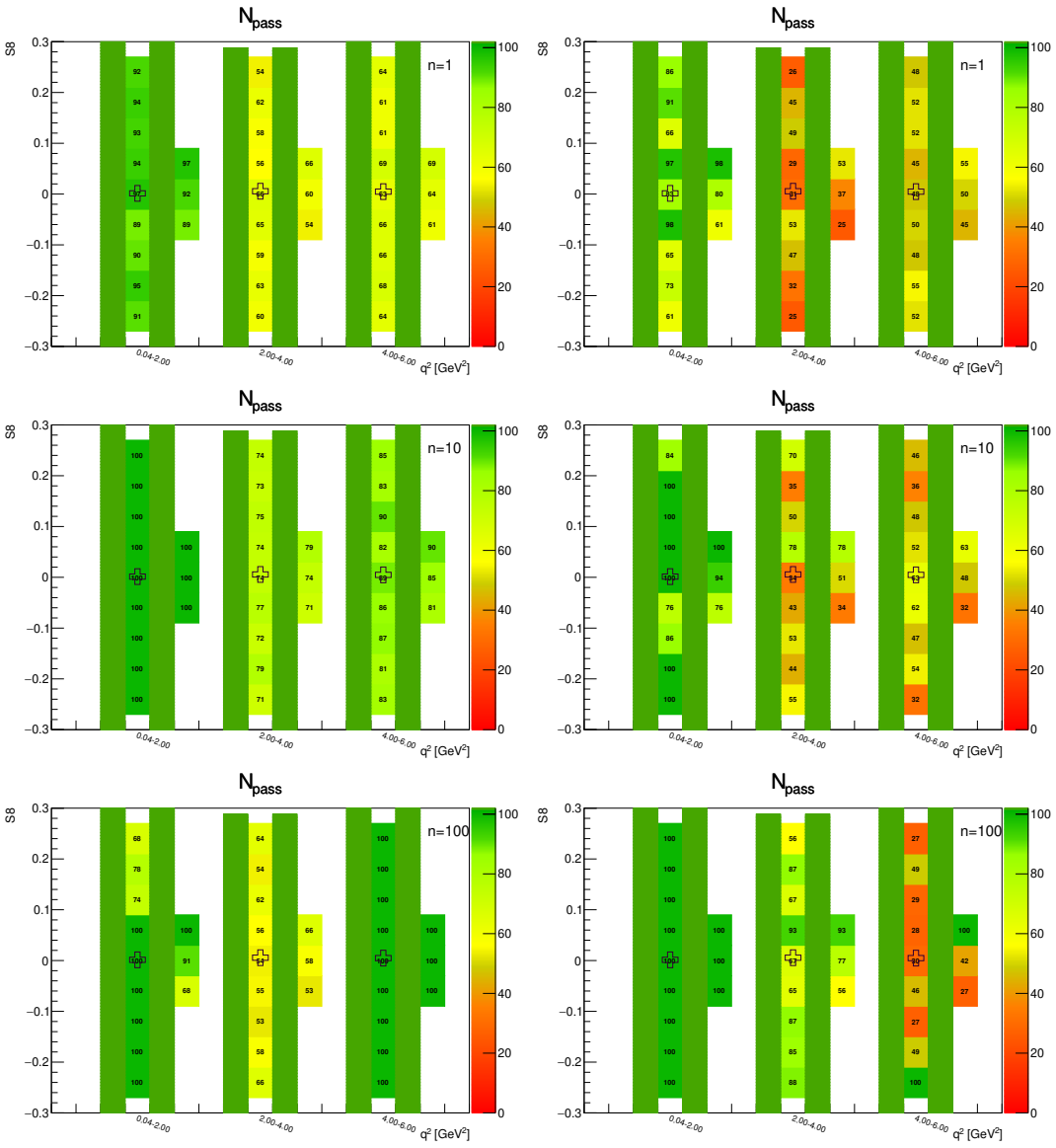

Figure A.35: Toy-MC studies of the S_8-fold, with r=1. Figures show the number of successfully passed fits on the toy-MC data without (left) and with acceptance (right) on the parameter S_8. The green bands represent fit-p.d.f. positivity range. The top figures correspond to the Run-1 like number of events (n = 1), while the middle and the bottom to 10× and 100× larger simulated samples.

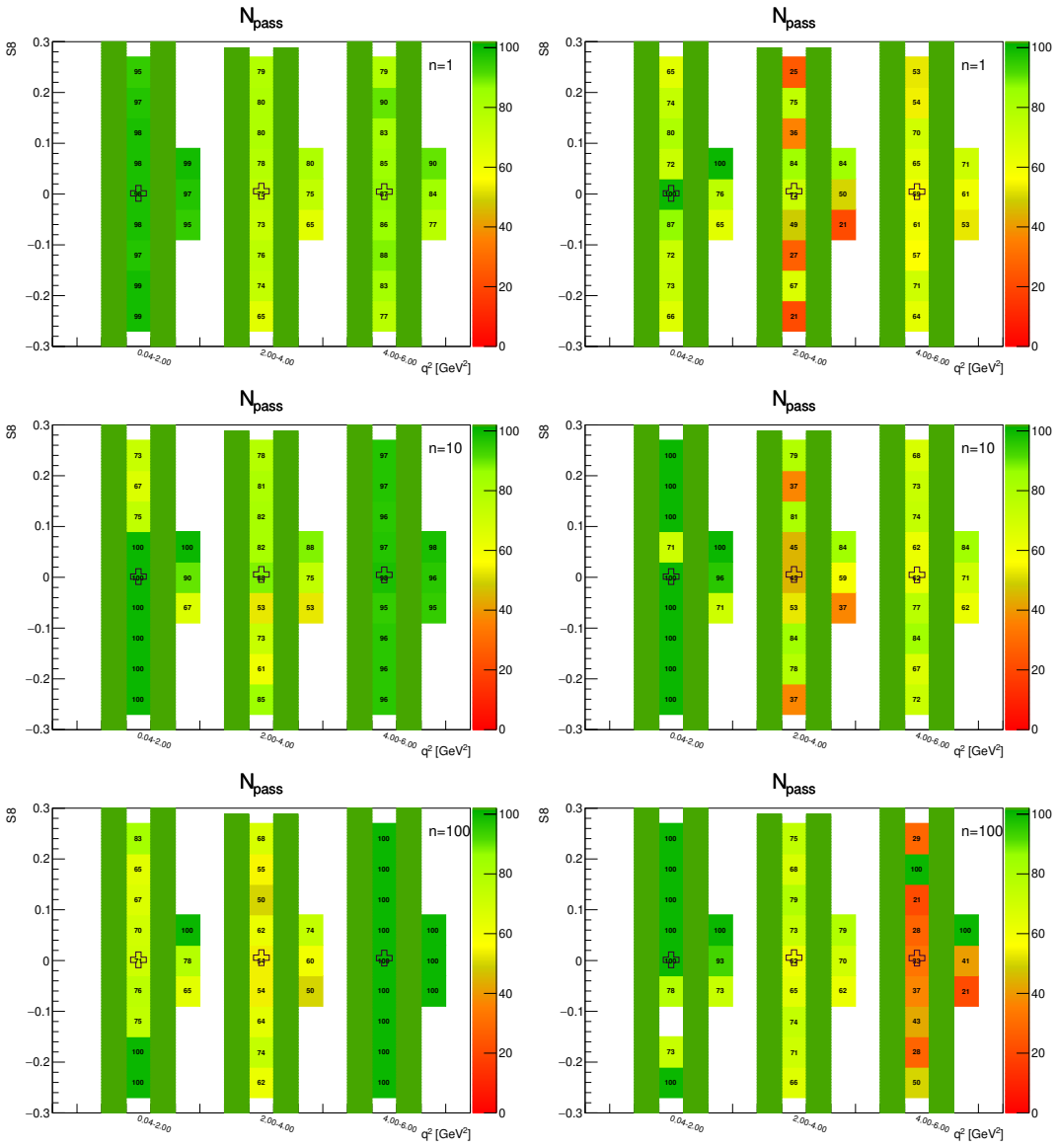

Figure A.36: Toy-MC studies of the S_8-fold, with r=2. Figures show the number of successfully passed fits on the toy-MC data without (left) and with acceptance (right) on the parameter S_8. The green bands represent fit-p.d.f. positivity range. The top figures correspond to the Run-1 like number of events (n = 1), while the middle and the bottom to 10× and 100× larger simulated samples.

A.3 Fit Validation – Plots of the Fit Error

A.3.1 S_4-fold – parameter F_L

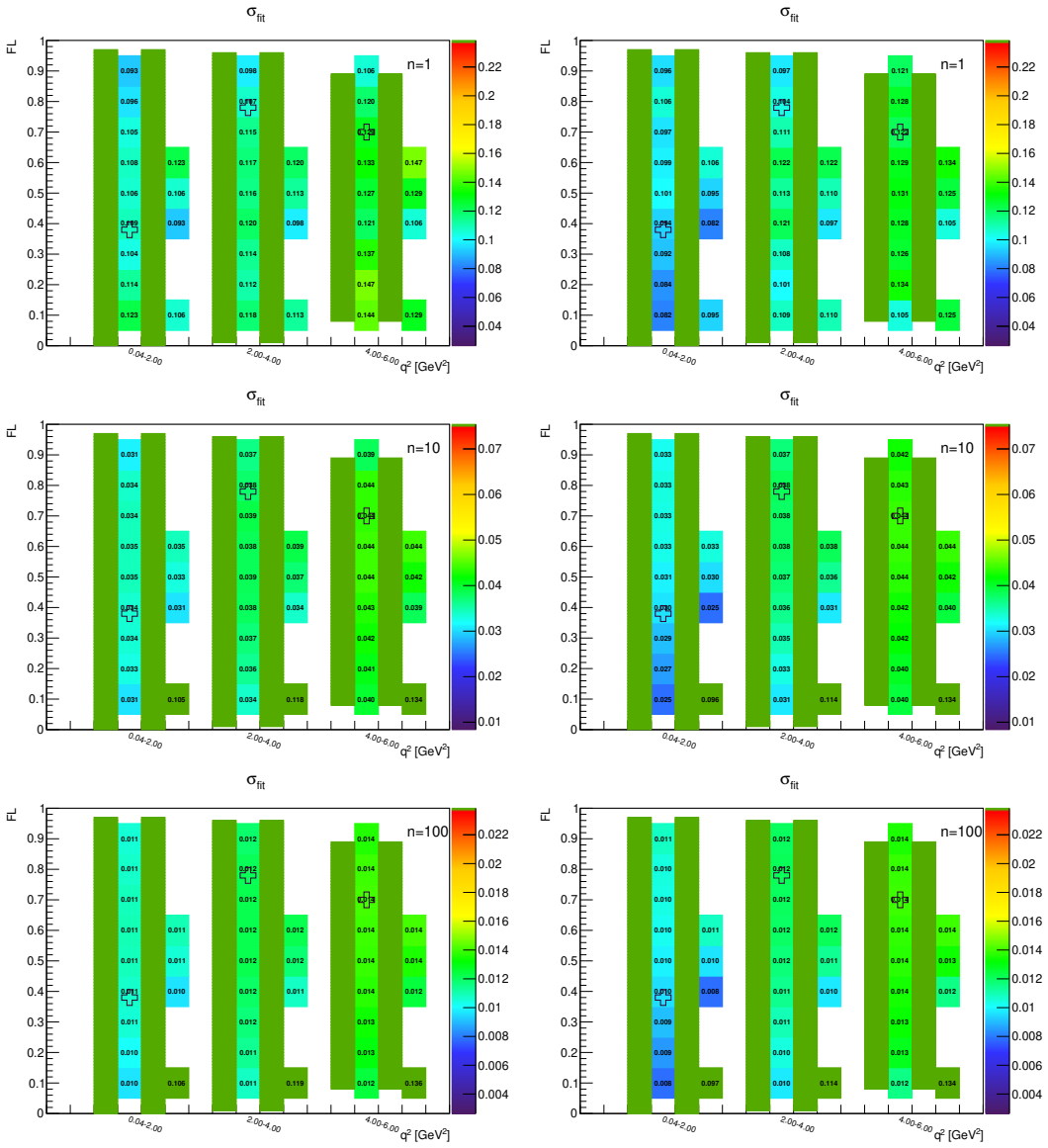

Figure A.37: Toy-MC studies of the S_4-fold, with $r = 0.5$. Figures show the parameter fit error without (left) and with acceptance (right) on the parameter F_L. The green bands represent fit-p.d.f. positivity range. The top figures correspond to the Run-1 like number of events (n = 1), while the middle and the bottom to 10× and 100× larger simulated samples.

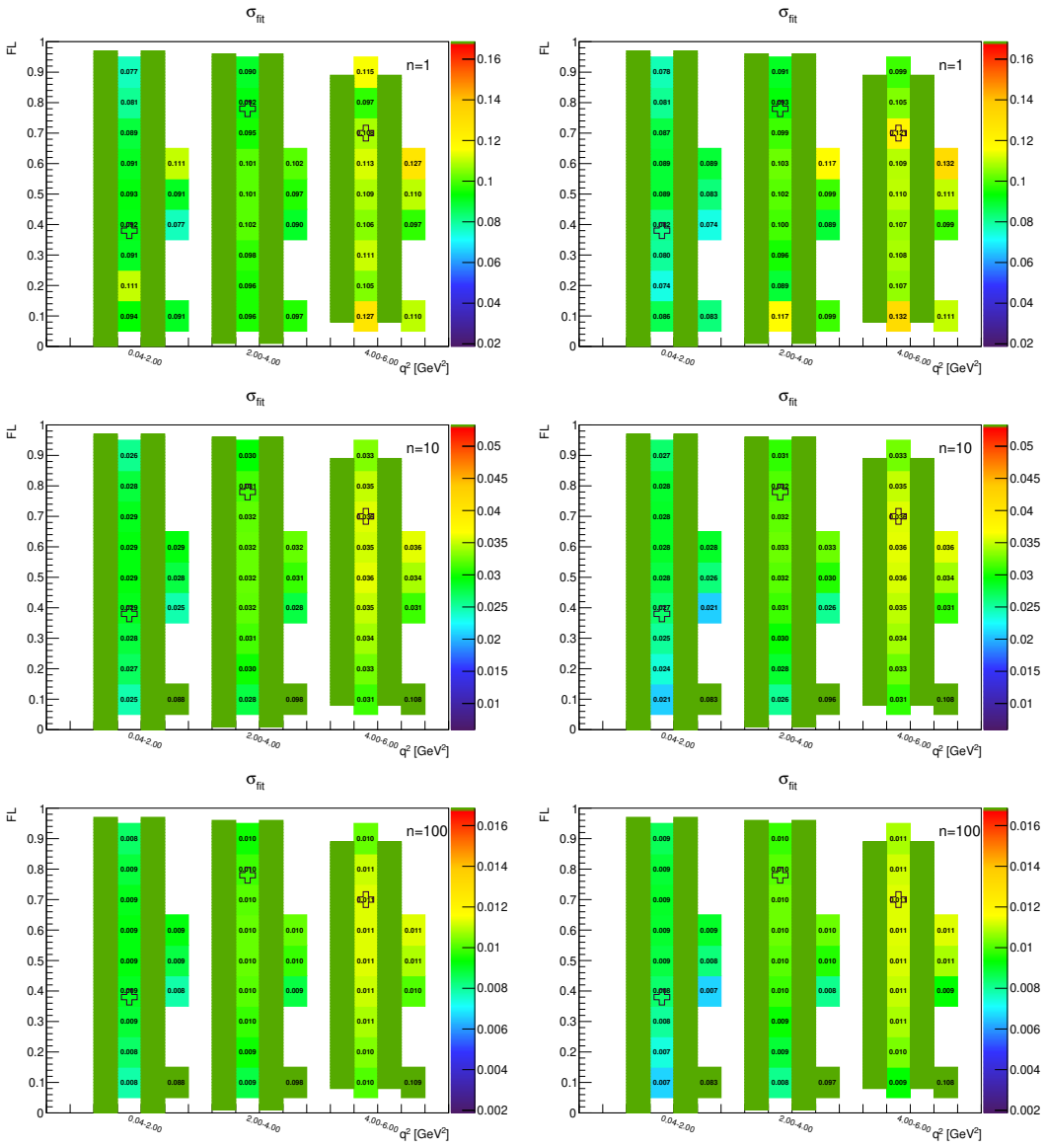

Figure A.38: Toy-MC studies of the S_4-fold, with $r = 1$. Figures show the parameter fit error without (left) and with acceptance (right) on the parameter F_L. The green bands represent fit-p.d.f. positivity range. The top figures correspond to the Run-1 like number of events (n = 1), while the middle and the bottom to 10× and 100× larger simulated samples.

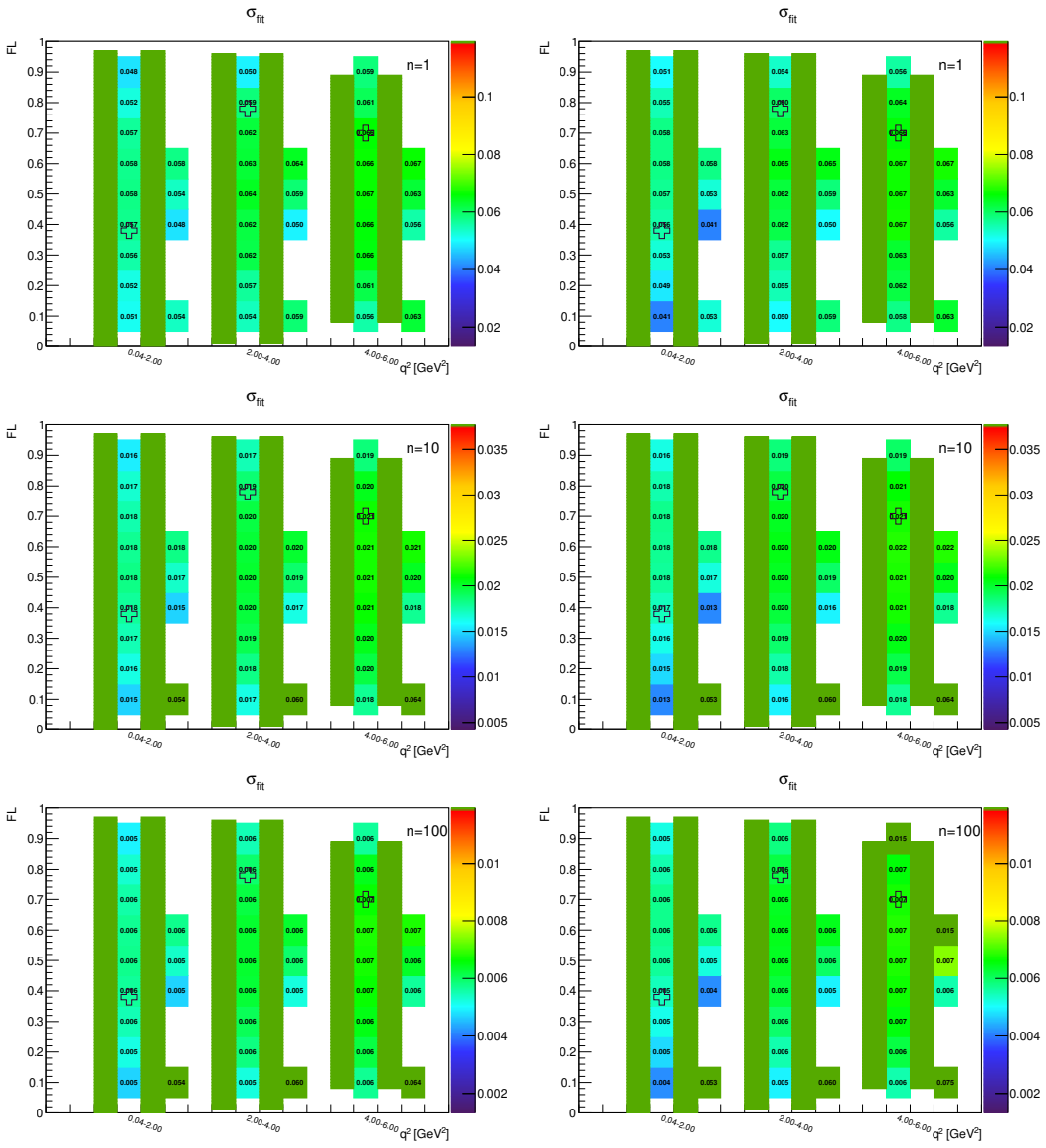

Figure A.39: Toy-MC studies of the S_4-fold, with $r = 2$. Figures show the parameter fit error without (left) and with acceptance (right) on the parameter F_L. The green bands represent fit-p.d.f. positivity range. The top figures correspond to the Run-1 like number of events (n = 1), while the middle and the bottom to 10× and 100× larger simulated samples.

A.3.2 S_4-fold – parameter S_3

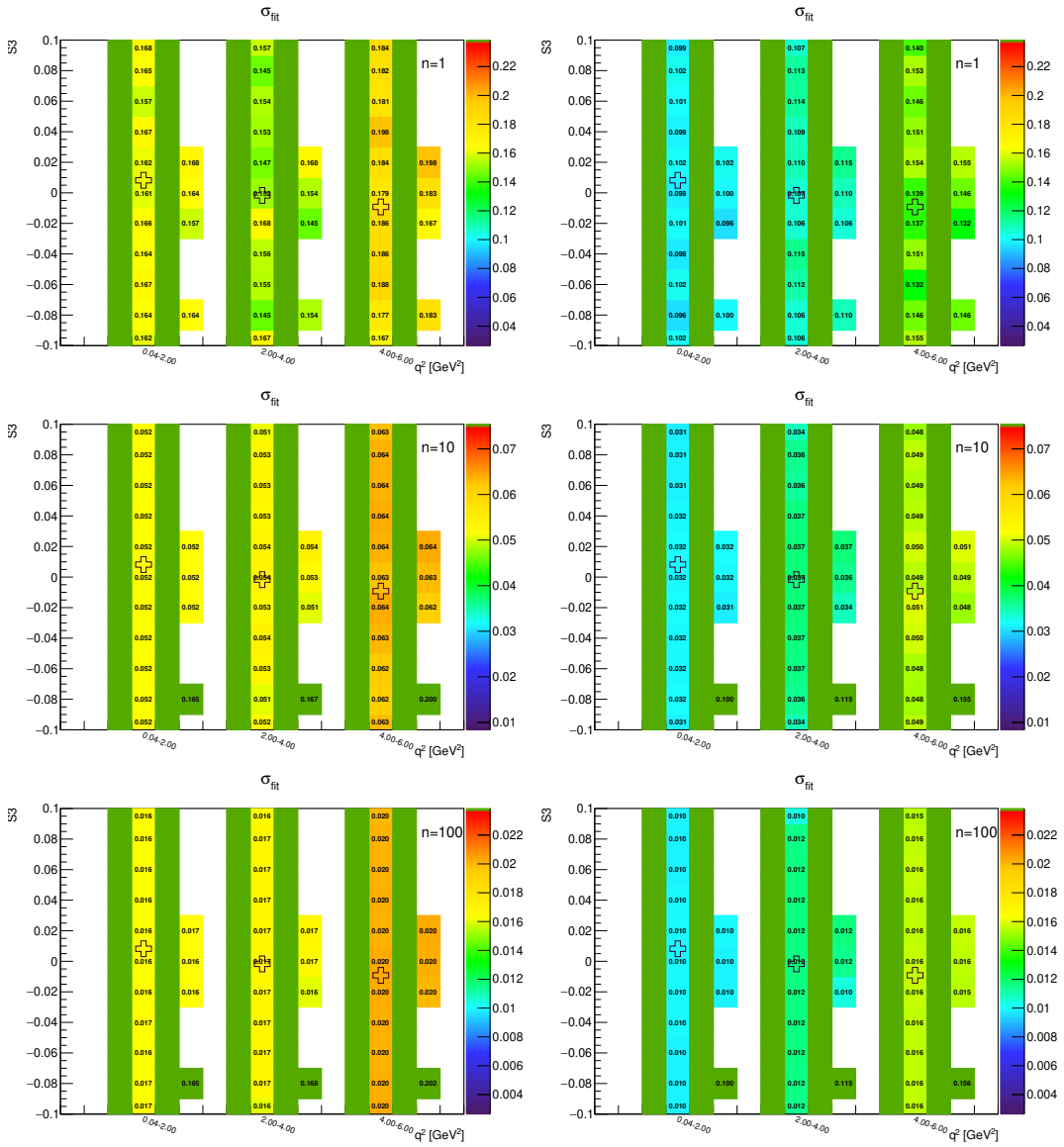

Figure A.40: Toy-MC studies of the S_4-fold, with $r = 0.5$. Figures show the parameter fit error without (left) and with acceptance (right) on the parameter S_3. The green bands represent fit-p.d.f. positivity range. The top figures correspond to the Run-1 like number of events (n = 1), while the middle and the bottom to 10× and 100× larger simulated samples.

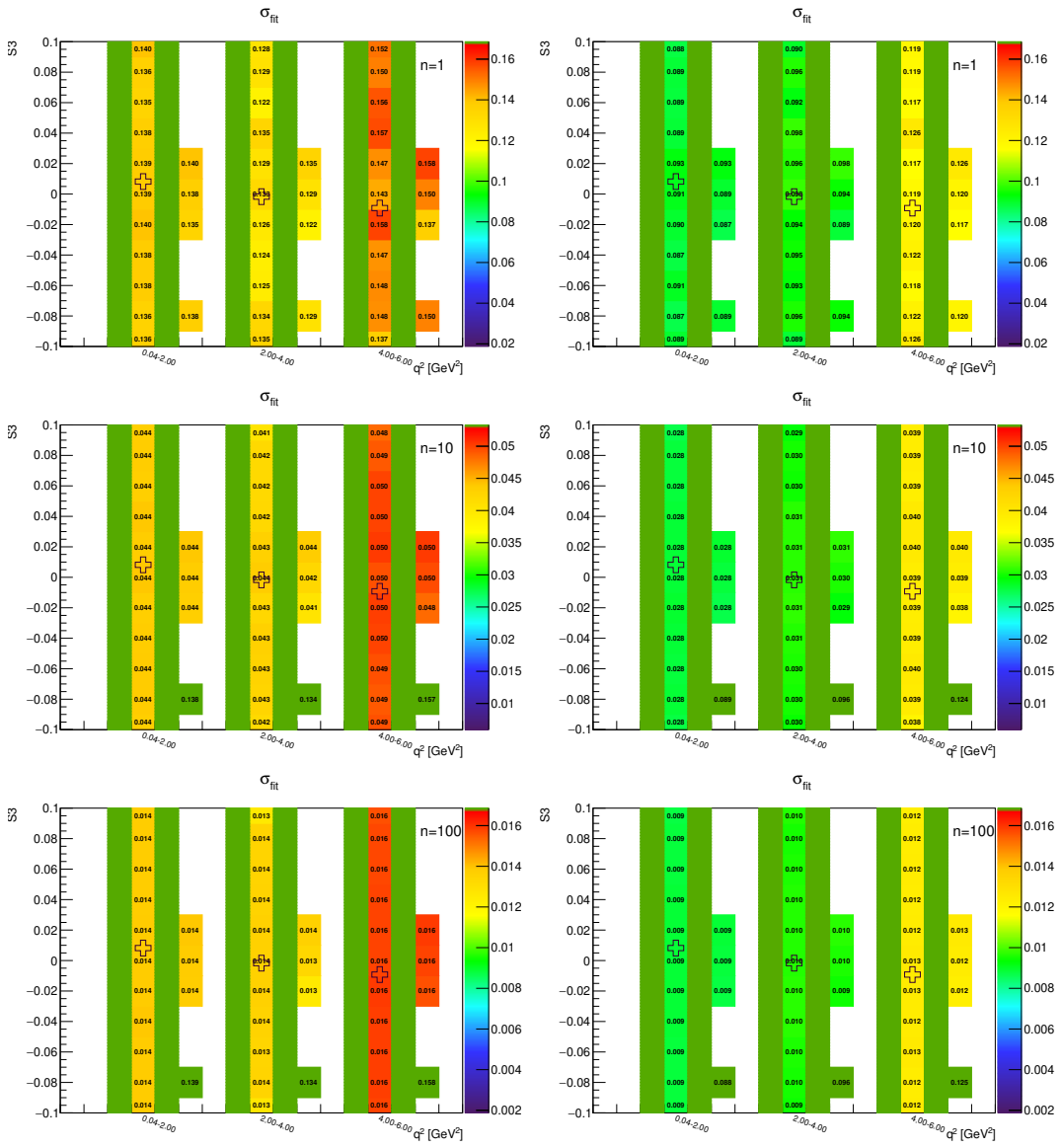

Figure A.41: Toy-MC studies of the S_4-fold, with $r = 1$. Figures show the parameter fit error without (left) and with acceptance (right) on the parameter S_3. The green bands represent fit-p.d.f. positivity range. The top figures correspond to the Run-1 like number of events (n = 1), while the middle and the bottom to 10× and 100× larger simulated samples.

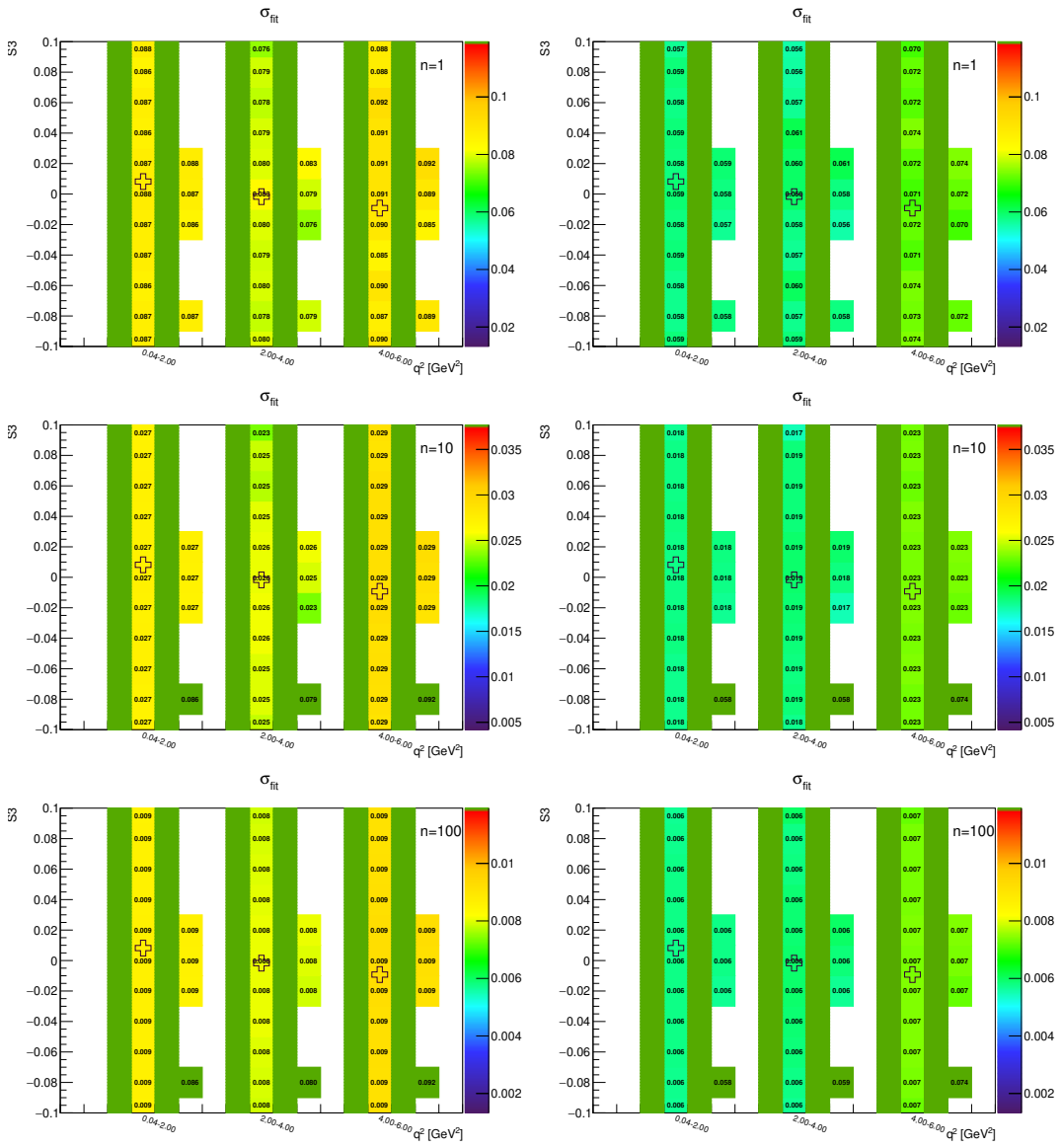

Figure A.42: Toy-MC studies of the S_4-fold, with $r = 2$. Figures show the parameter fit error without (left) and with acceptance (right) on the parameter S_3. The green bands represent fit-p.d.f. positivity range. The top figures correspond to the Run-1 like number of events (n = 1), while the middle and the bottom to 10× and 100× larger simulated samples.

A.3.3 S_4-fold – parameter S_4

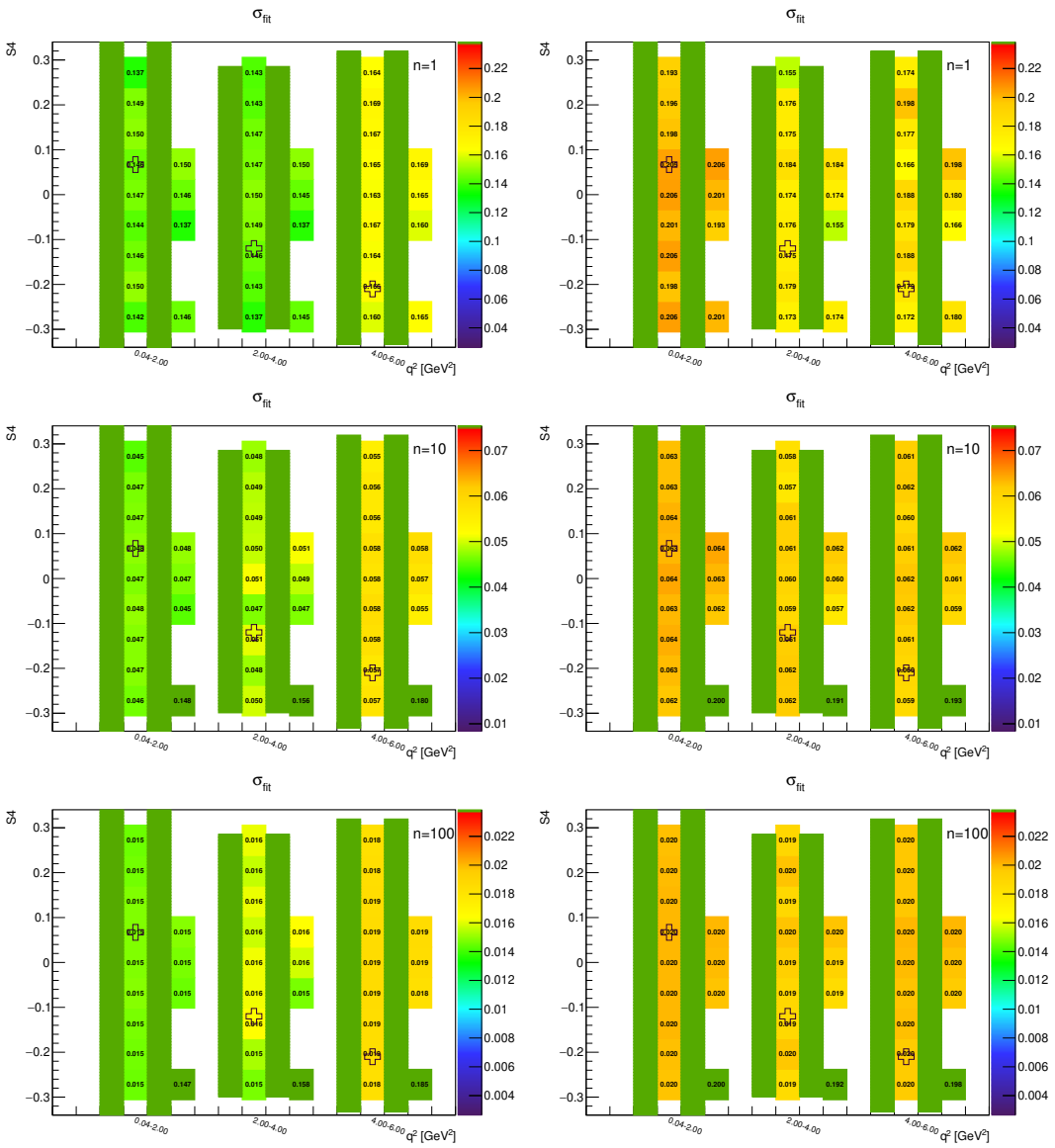

Figure A.43: Toy-MC studies of the S_4-fold, with $r = 0.5$. Figures show the parameter fit error without (left) and with acceptance (right) on the parameter S_4. The green bands represent fit-p.d.f. positivity range. The top figures correspond to the Run-1 like number of events (n = 1), while the middle and the bottom to 10× and 100× larger simulated samples.

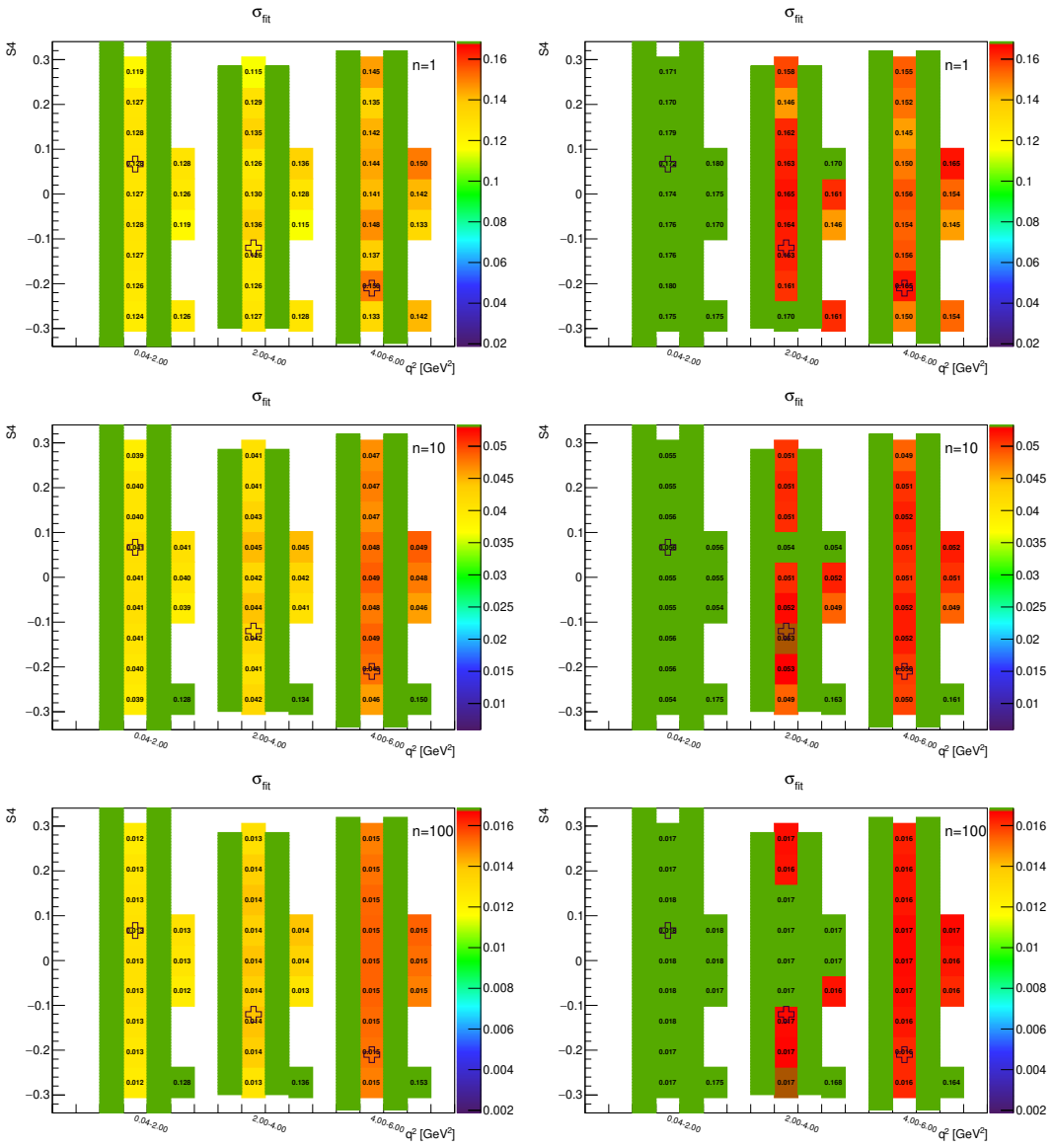

Figure A.44: Toy-MC studies of the S_4-fold, with $r = 1$. Figures show the parameter fit error without (left) and with acceptance (right) on the parameter S_4. The green bands represent fit-p.d.f. positivity range. The top figures correspond to the Run-1 like number of events (n = 1), while the middle and the bottom to 10× and 100× larger simulated samples.

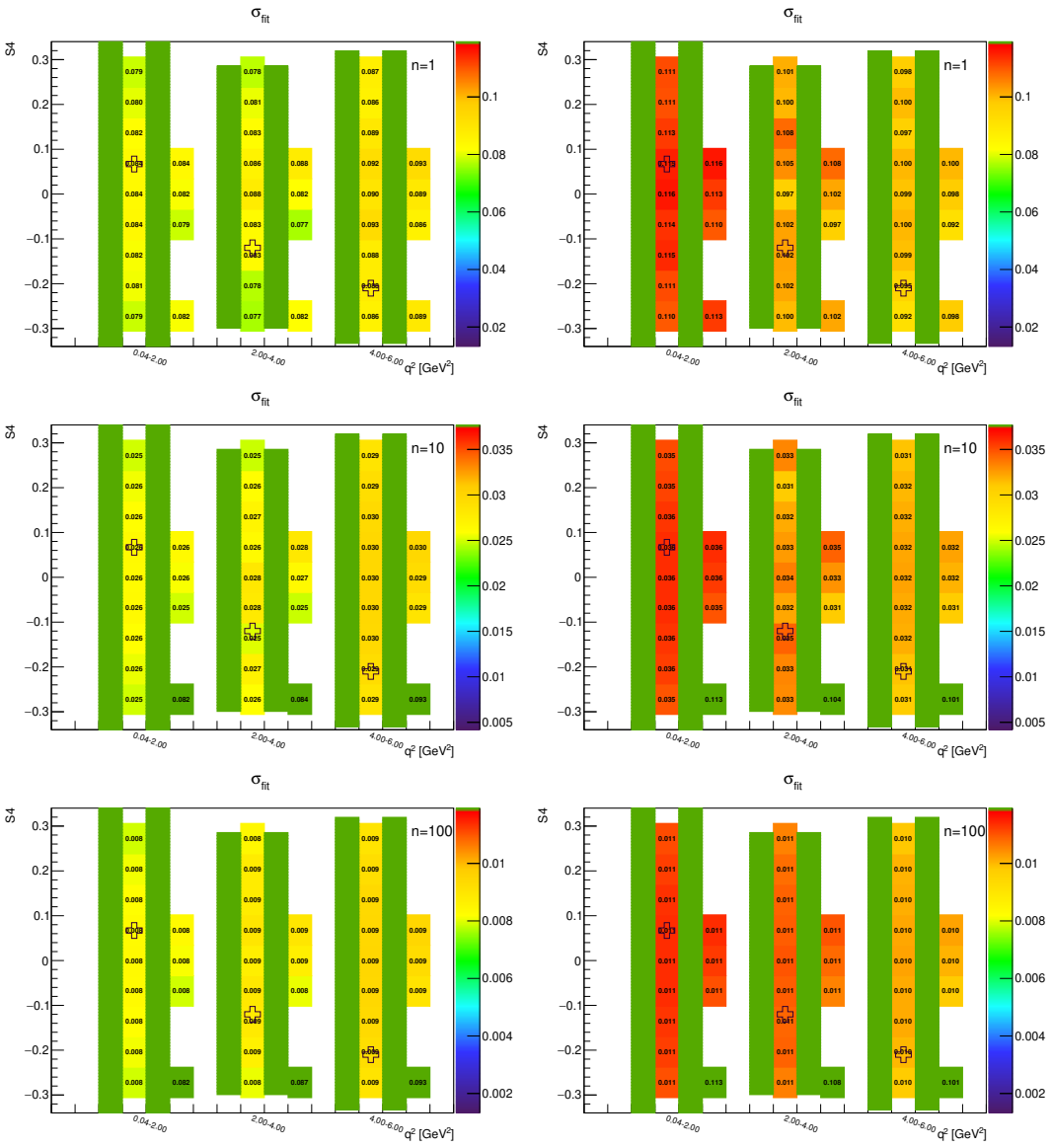

Figure A.45: Toy-MC studies of the S_4-fold, with $r = 2$. Figures show the parameter fit error without (left) and with acceptance (right) on the parameter S_4. The green bands represent fit-p.d.f. positivity range. The top figures correspond to the Run-1 like number of events (n = 1), while the middle and the bottom to 10× and 100× larger simulated samples.

A.3.4 S_5-fold – parameter F_L

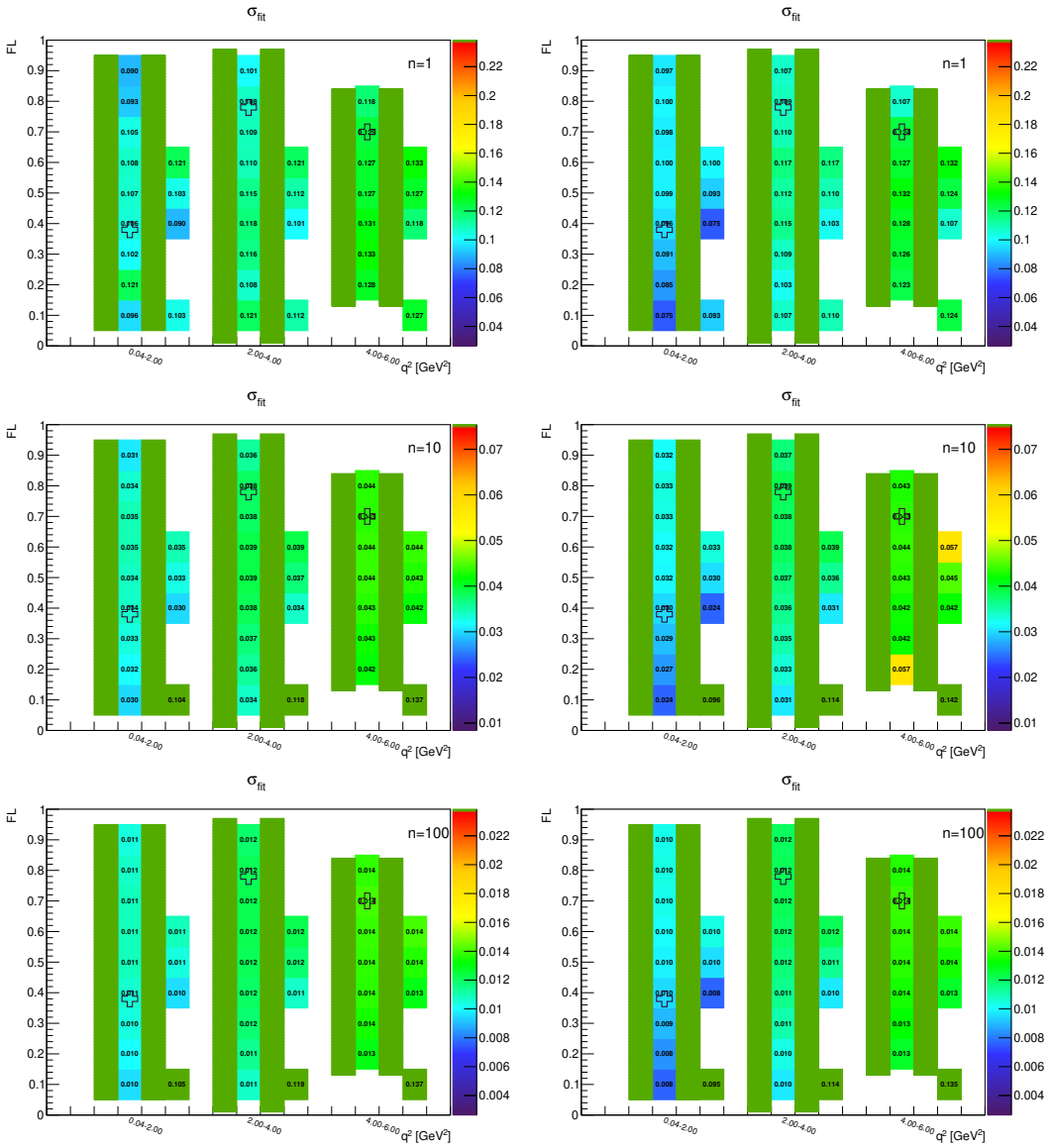

Figure A.46: Toy-MC studies of the S_5-fold, with $r = 0.5$. Figures show the parameter fit error without (left) and with acceptance (right) on the parameter F_L. The green bands represent fit-p.d.f. positivity range. The top figures correspond to the Run-1 like number of events (n = 1), while the middle and the bottom to 10× and 100× larger simulated samples.

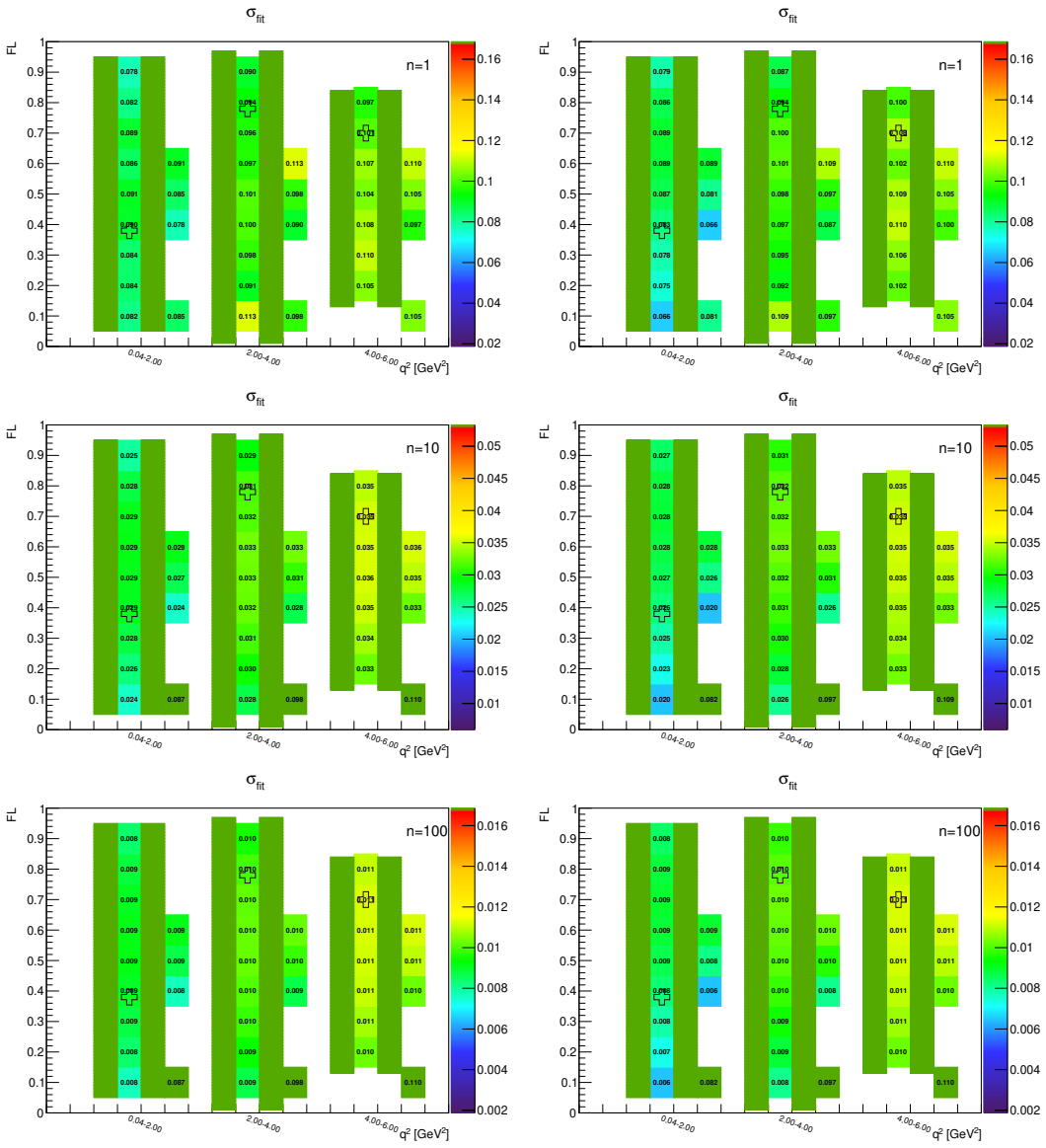

Figure A.47: Toy-MC studies of the S_5-fold, with $r = 1$. Figures show the parameter fit error without (left) and with acceptance (right) on the parameter F_L. The green bands represent fit-p.d.f. positivity range. The top figures correspond to the Run-1 like number of events (n = 1), while the middle and the bottom to 10× and 100× larger simulated samples.

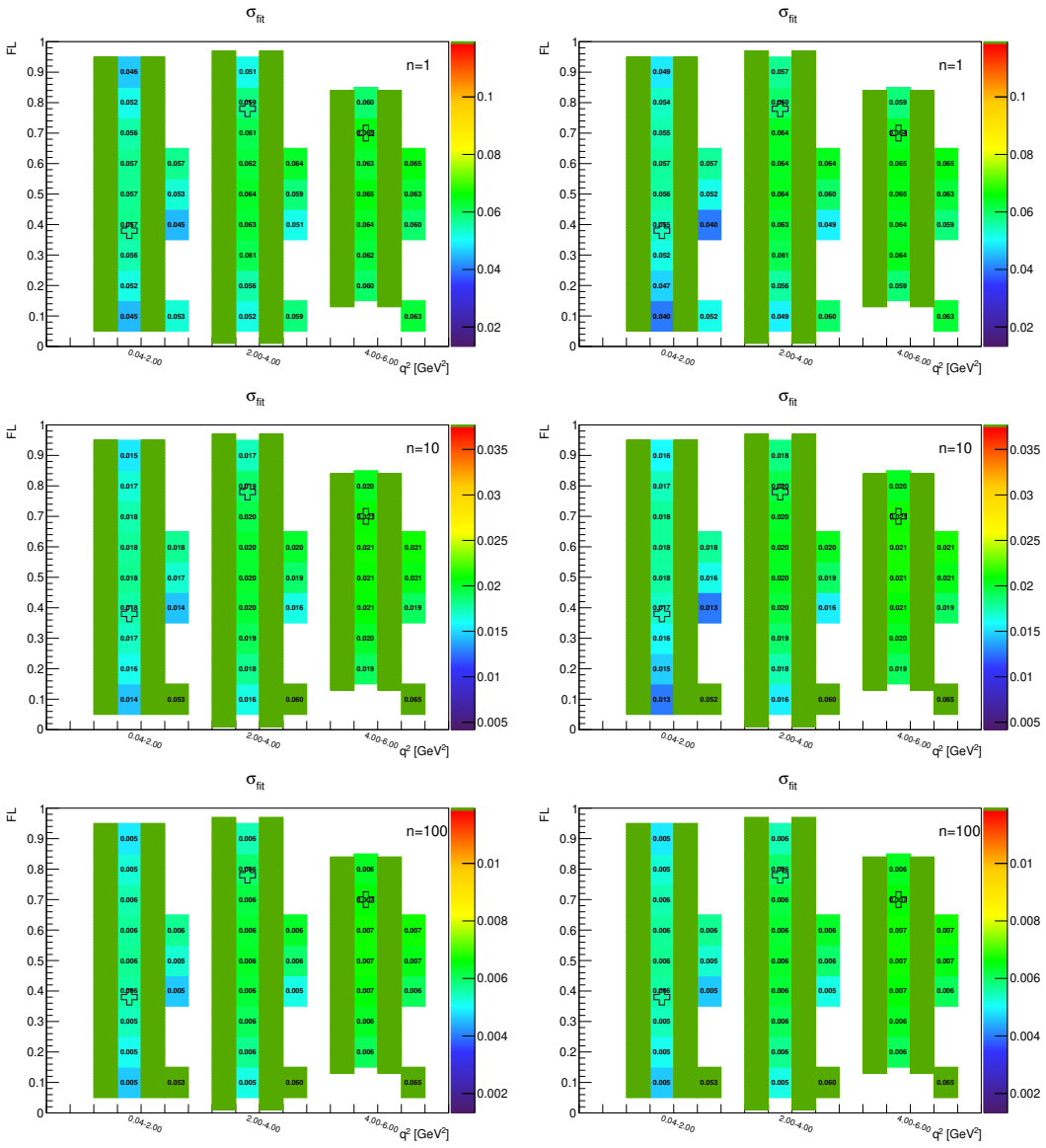

Figure A.48: Toy-MC studies of the S_5-fold, with $r = 2$. Figures show the parameter fit error without (left) and with acceptance (right) on the parameter F_L. The green bands represent fit-p.d.f. positivity range. The top figures correspond to the Run-1 like number of events (n = 1), while the middle and the bottom to 10× and 100× larger simulated samples.

A.3.5 S_5-fold – parameter S_3

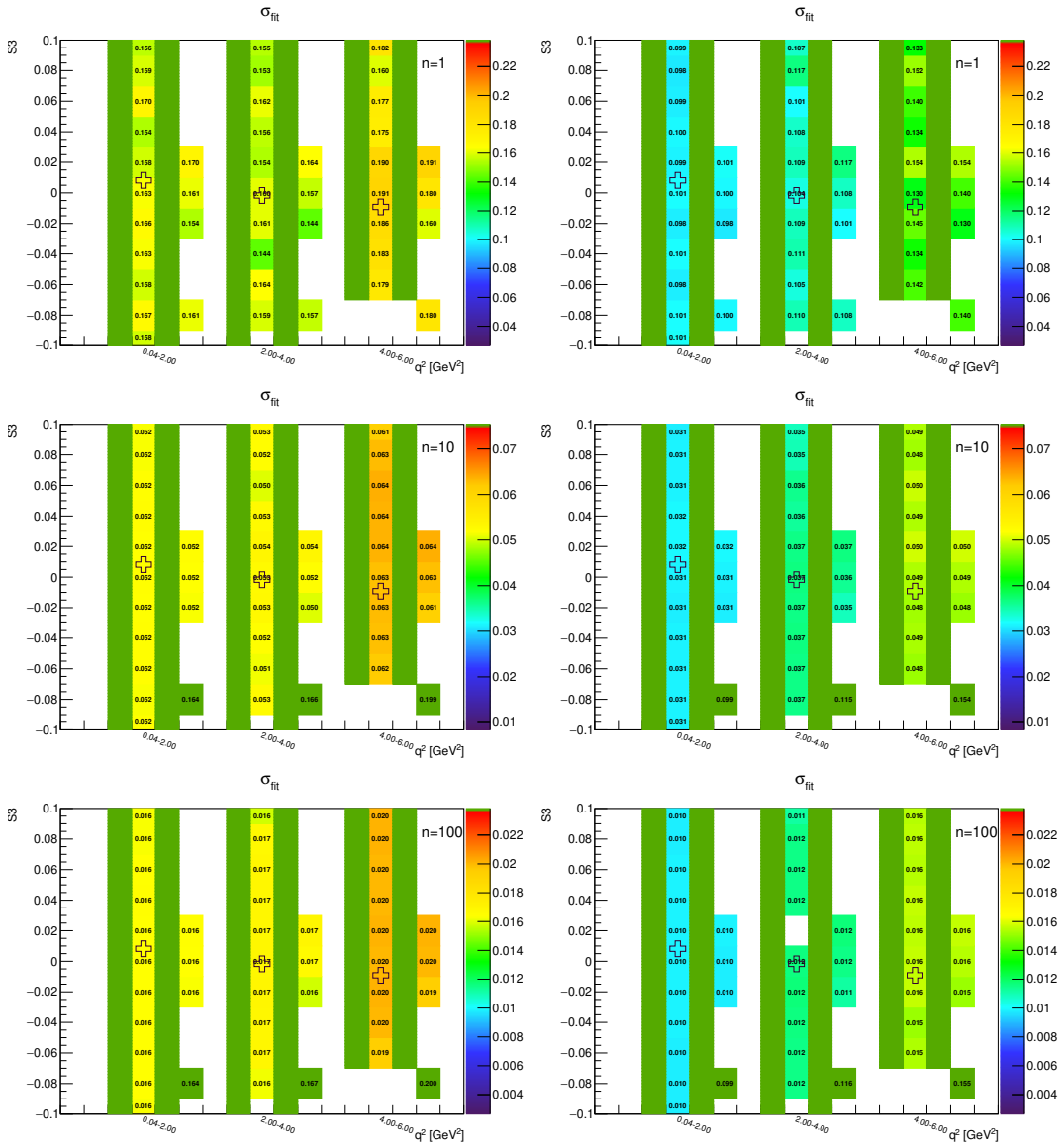

Figure A.49: Toy-MC studies of the S_5-fold, with $r = 0.5$. Figures show the parameter fit error without (left) and with acceptance (right) on the parameter S_3. The green bands represent fit-p.d.f. positivity range. The top figures correspond to the Run-1 like number of events (n = 1), while the middle and the bottom to 10× and 100× larger simulated samples.

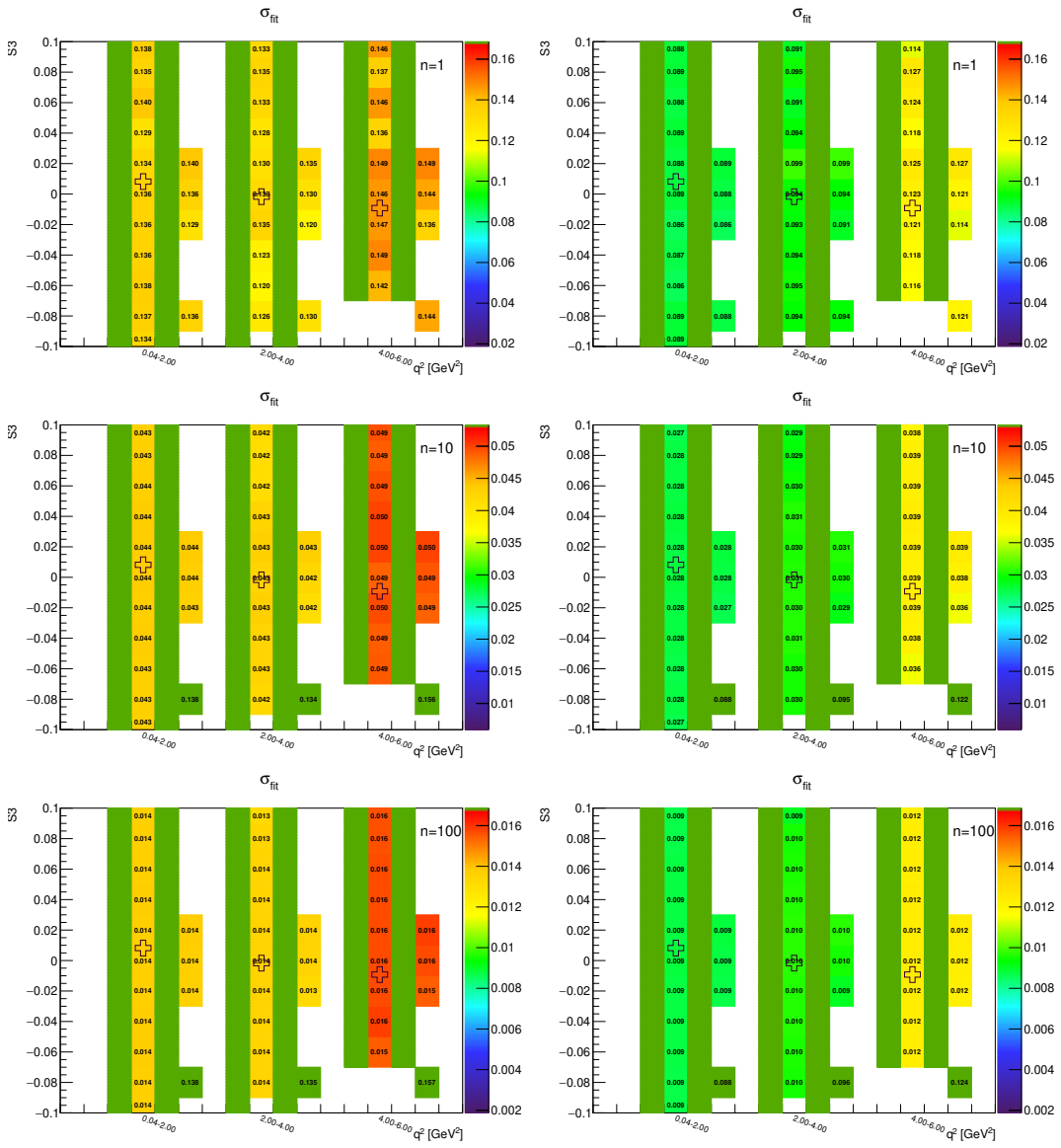

Figure A.50: Toy-MC studies of the S_5-fold, with $r = 1$. Figures show the parameter fit error without (left) and with acceptance (right) on the parameter S_3. The green bands represent fit-p.d.f. positivity range. The top figures correspond to the Run-1 like number of events (n = 1), while the middle and the bottom to 10× and 100× larger simulated samples.

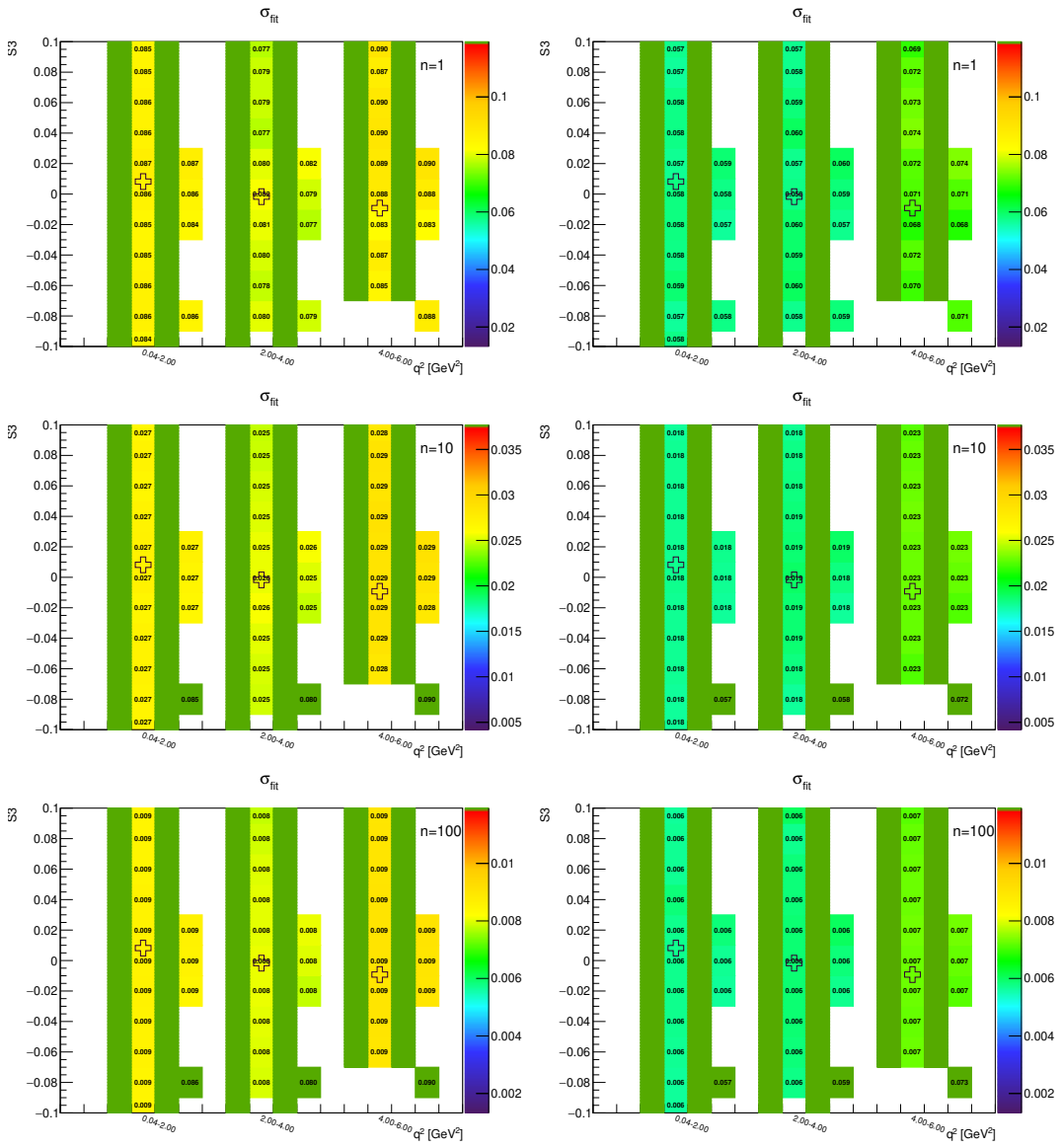

Figure A.51: Toy-MC studies of the S_5-fold, with $r = 2$. Figures show the parameter fit error without (left) and with acceptance (right) on the parameter S_3. The green bands represent fit-p.d.f. positivity range. The top figures correspond to the Run-1 like number of events (n = 1), while the middle and the bottom to 10× and 100× larger simulated samples.

A.3.6 S_5-fold – parameter S_5

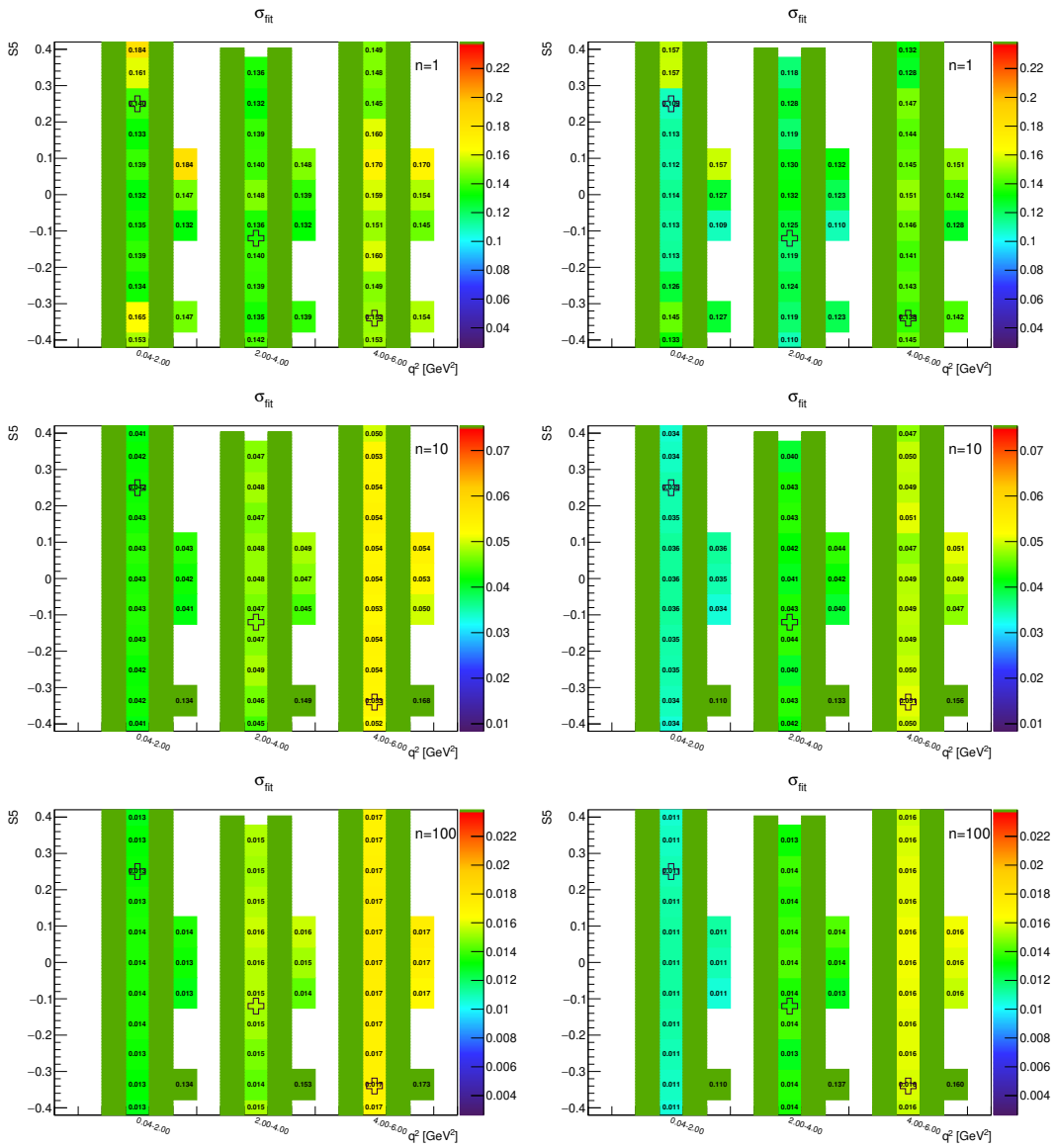

Figure A.52: Toy-MC studies of the S_5-fold, with $r = 0.5$. Figures show the parameter fit error without (left) and with acceptance (right) on the parameter S_5. The green bands represent fit-p.d.f. positivity range. The top figures correspond to the Run-1 like number of events (n = 1), while the middle and the bottom to 10× and 100× larger simulated samples.

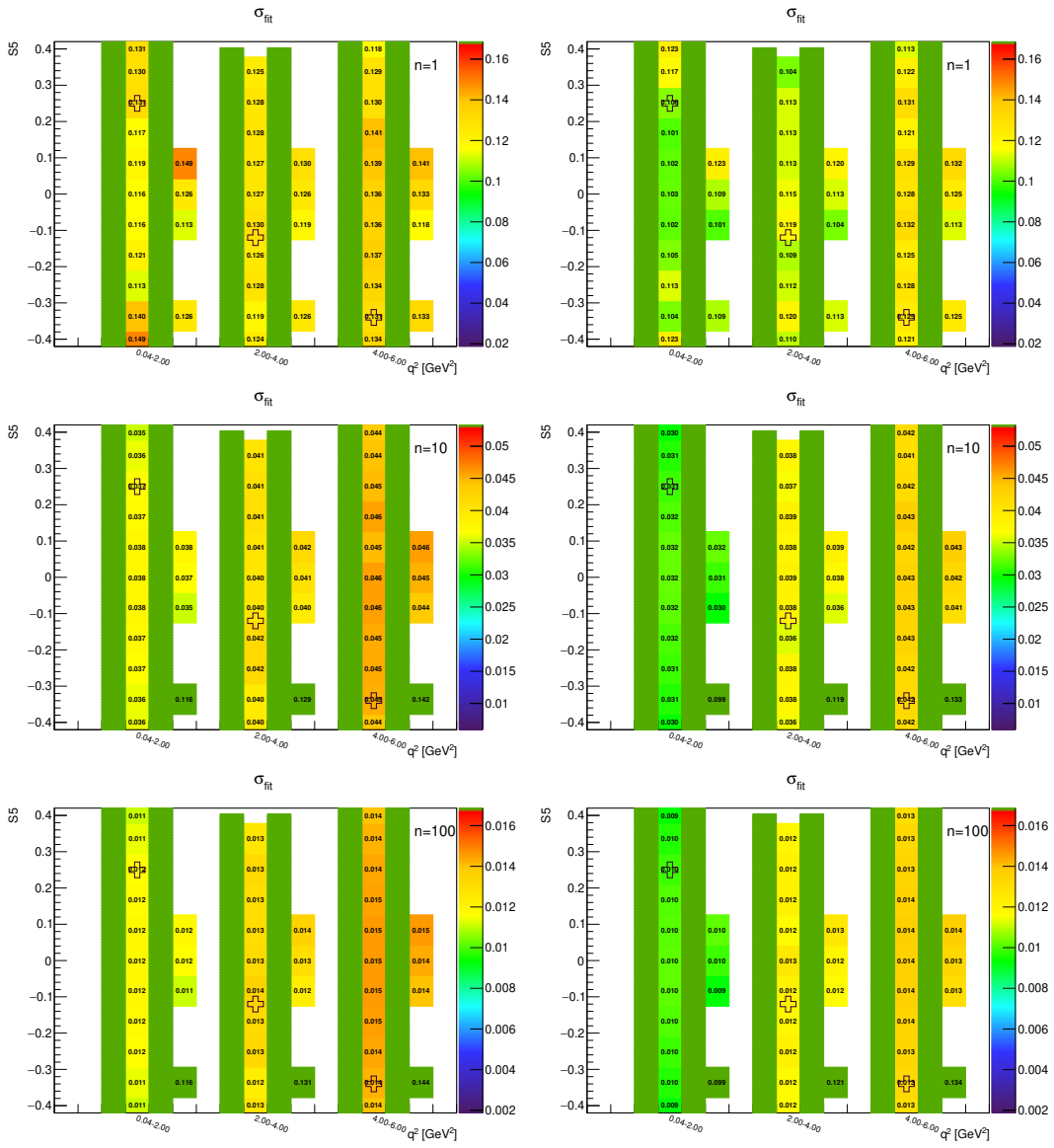

Figure A.53: Toy-MC studies of the S_5-fold, with $r = 1$. Figures show the parameter fit error without (left) and with acceptance (right) on the parameter S_5. The green bands represent fit-p.d.f. positivity range. The top figures correspond to the Run-1 like number of events (n = 1), while the middle and the bottom to 10× and 100× larger simulated samples.

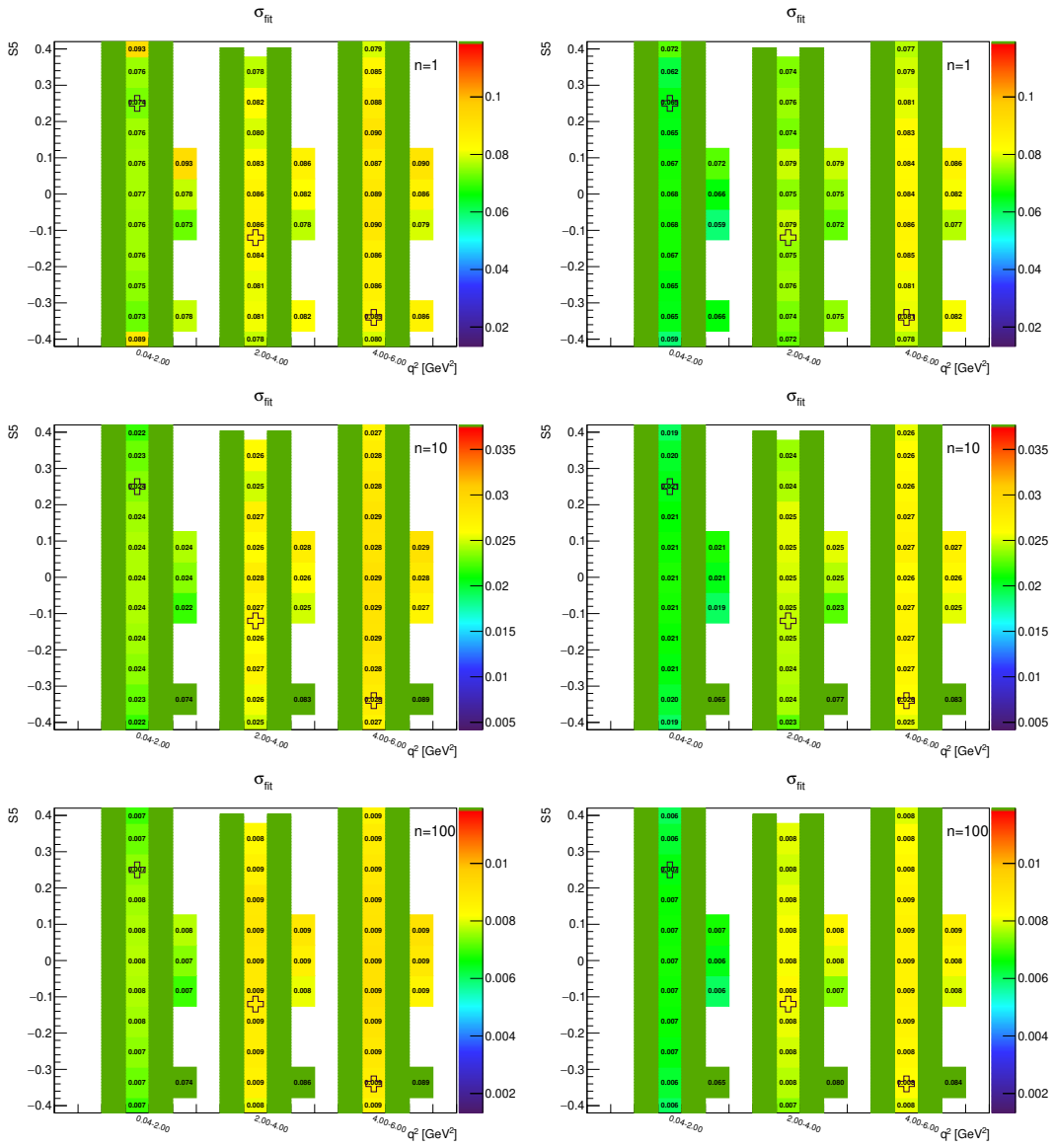

Figure A.54: Toy-MC studies of the S_5-fold, with $r = 2$. Figures show the parameter fit error without (left) and with acceptance (right) on the parameter S_5. The green bands represent fit-p.d.f. positivity range. The top figures correspond to the Run-1 like number of events (n = 1), while the middle and the bottom to 10× and 100× larger simulated samples.

A.3.7 S_7-fold – parameter F_L

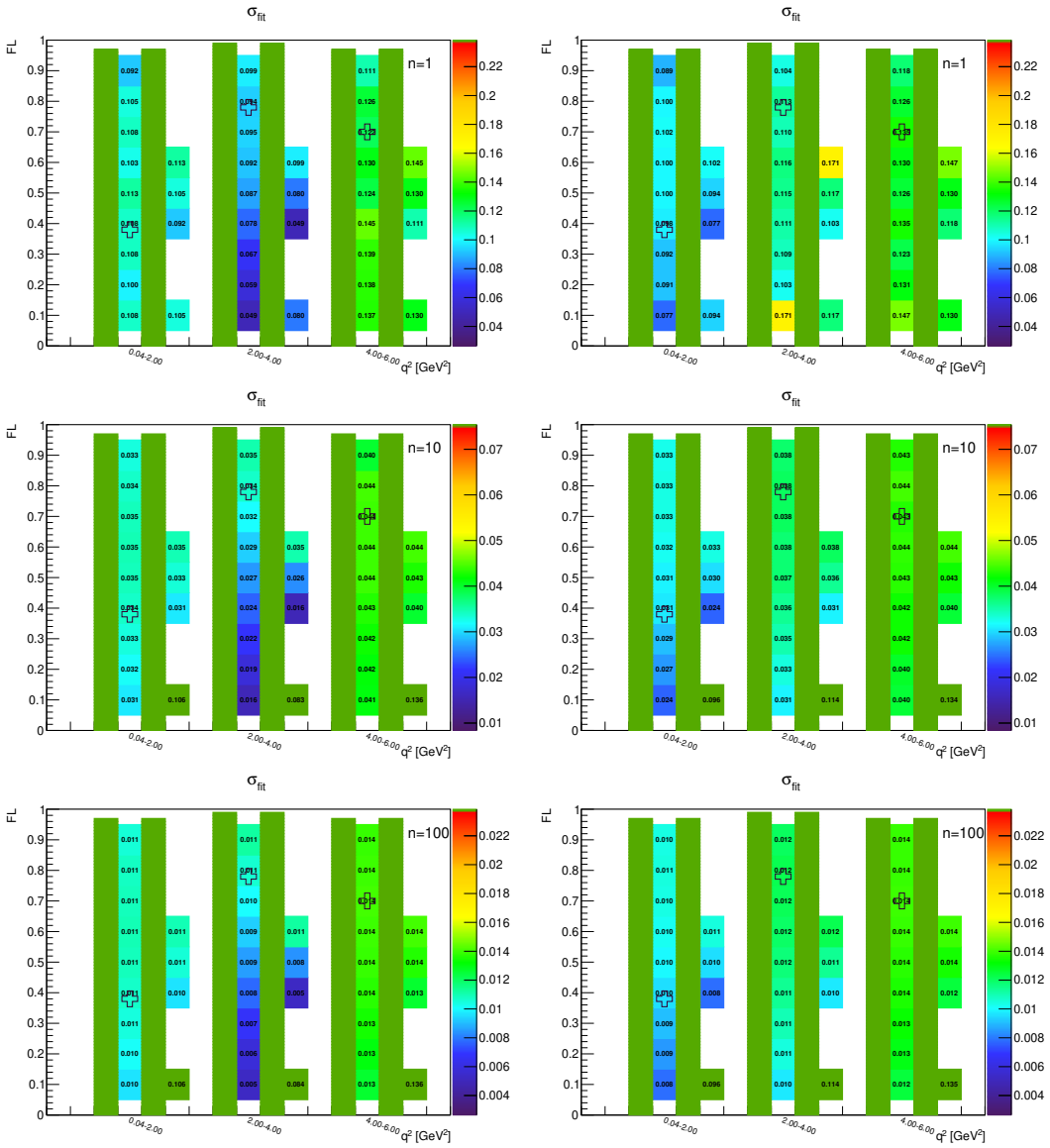

Figure A.55: Toy-MC studies of the S_7-fold, with $r = 0.5$. Figures show the parameter fit error without (left) and with acceptance (right) on the parameter F_L. The green bands represent fit-p.d.f. positivity range. The top figures correspond to the Run-1 like number of events (n = 1), while the middle and the bottom to 10× and 100× larger simulated samples.

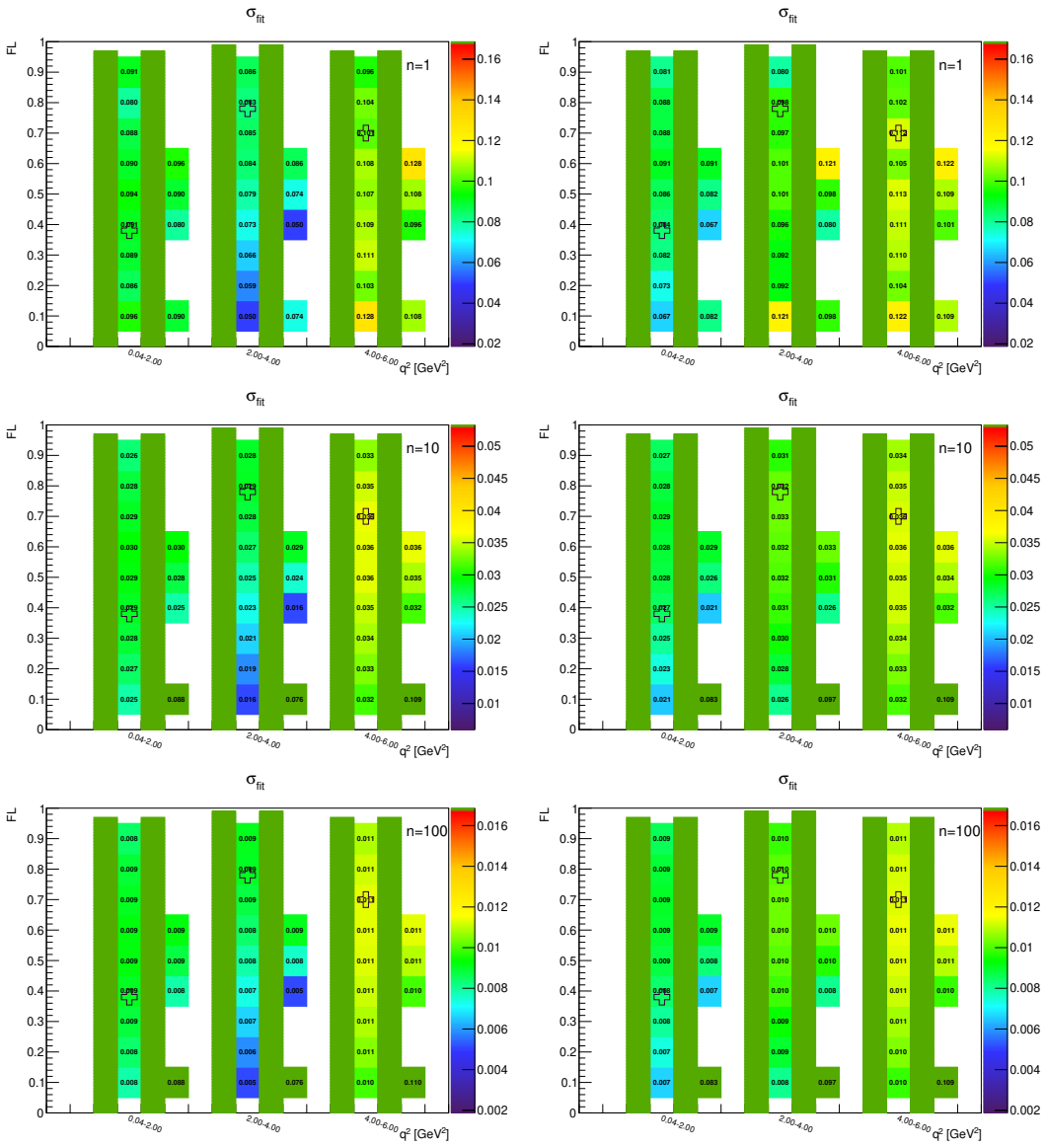

Figure A.56: Toy-MC studies of the S_7-fold, with $r = 1$. Figures show the parameter fit error without (left) and with acceptance (right) on the parameter F_L. The green bands represent fit-p.d.f. positivity range. The top figures correspond to the Run-1 like number of events (n = 1), while the middle and the bottom to 10× and 100× larger simulated samples.

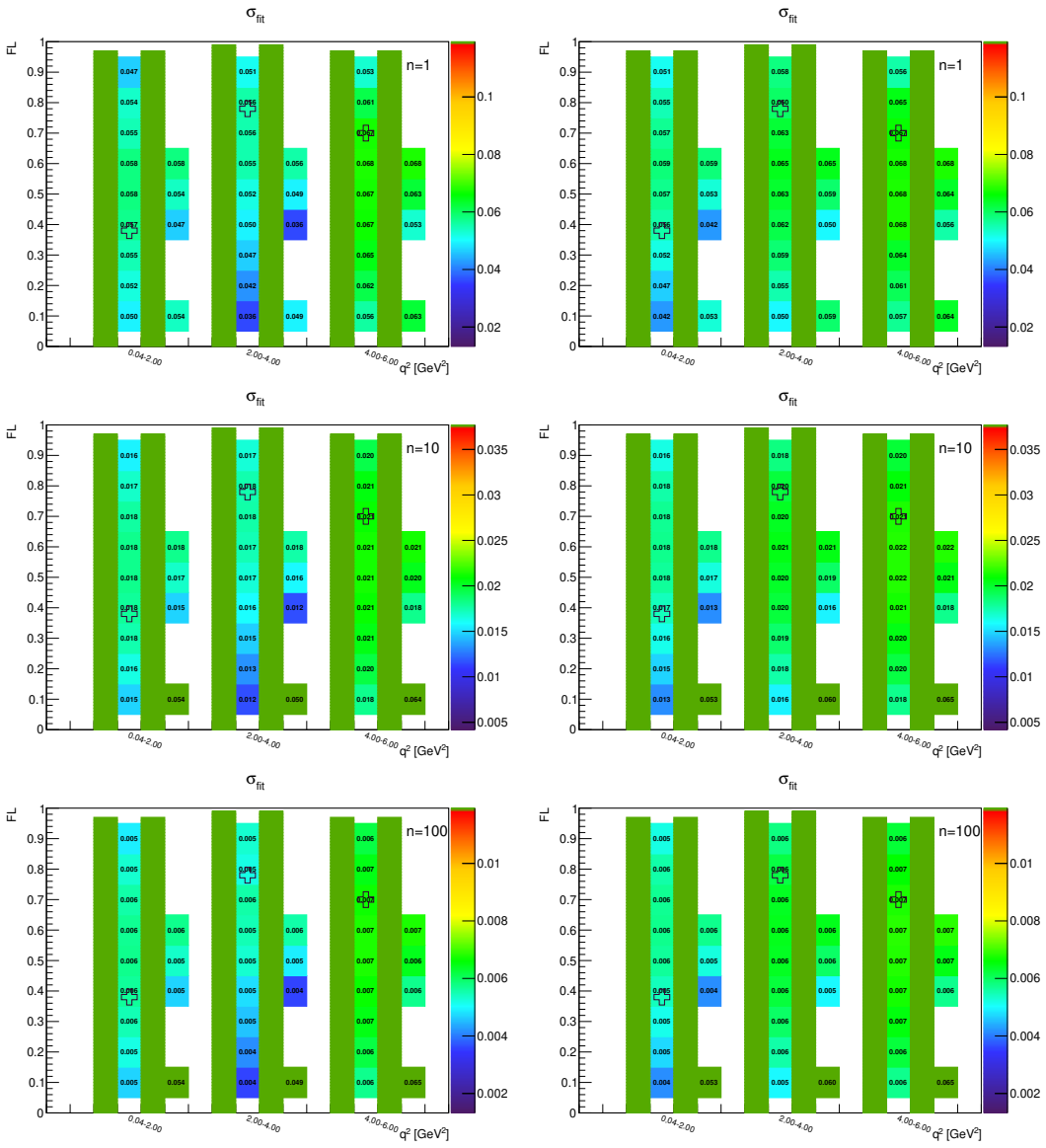

Figure A.57: Toy-MC studies of the S_7-fold, with $r = 2$. Figures show the parameter fit error without (left) and with acceptance (right) on the parameter F_L. The green bands represent fit-p.d.f. positivity range. The top figures correspond to the Run-1 like number of events (n = 1), while the middle and the bottom to 10× and 100× larger simulated samples.

A.3.8 S_7-fold – parameter S_3

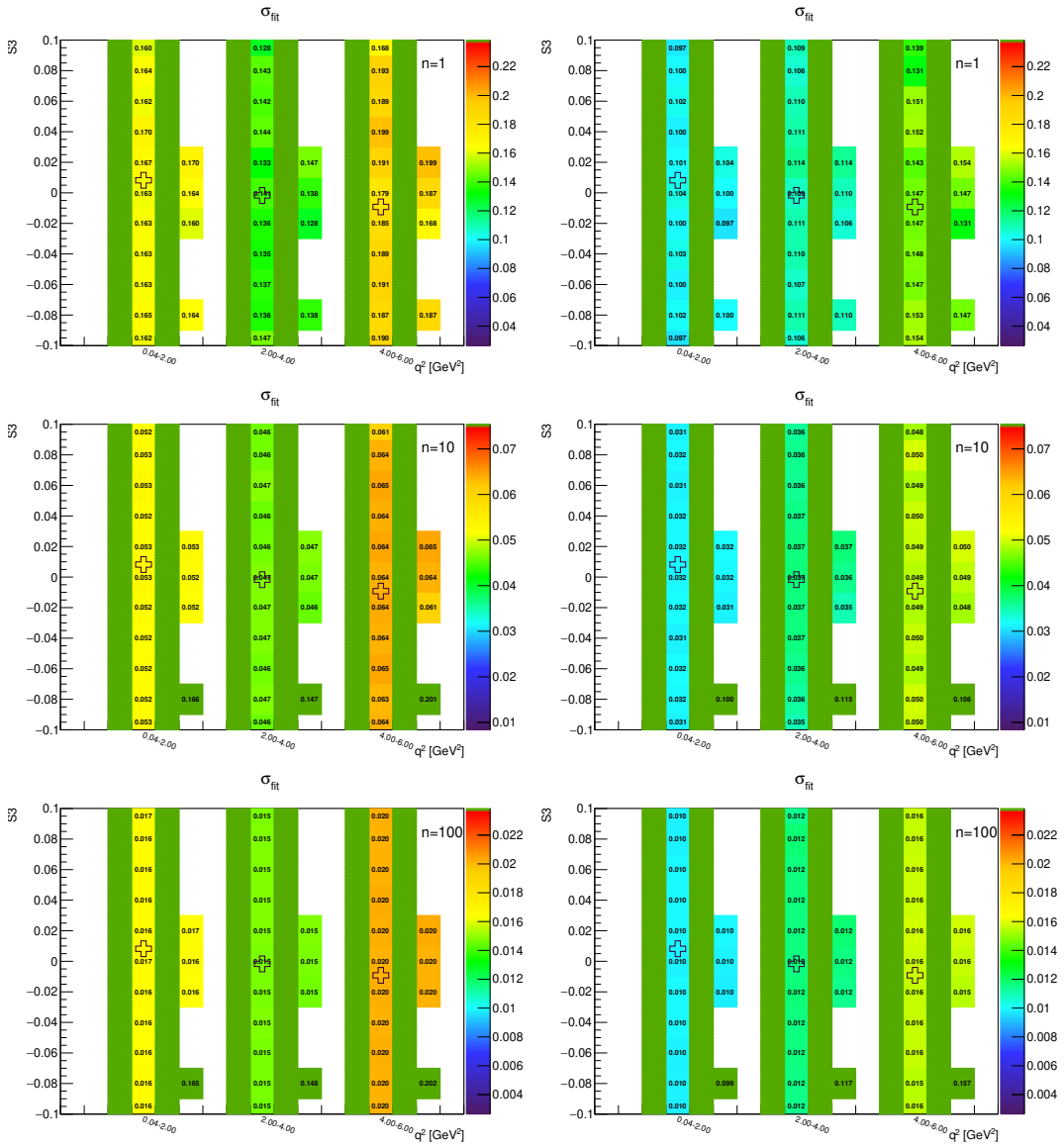

Figure A.58: Toy-MC studies of the S_7-fold, with $r = 0.5$. Figures show the parameter fit error without (left) and with acceptance (right) on the parameter S_3. The green bands represent fit-p.d.f. positivity range. The top figures correspond to the Run-1 like number of events (n = 1), while the middle and the bottom to 10× and 100× larger simulated samples.

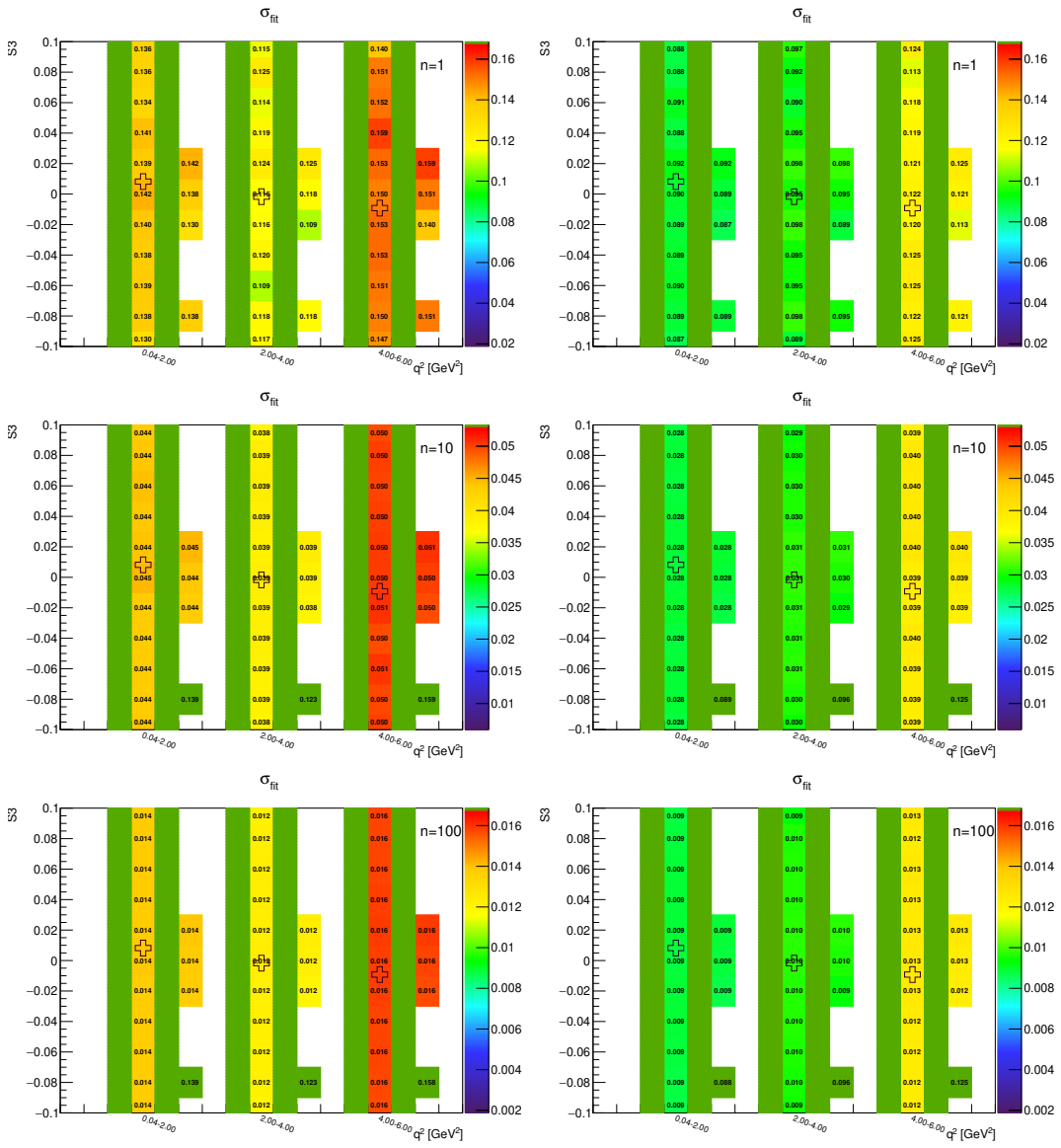

Figure A.59: Toy-MC studies of the S_7-fold, with $r = 1$. Figures show the parameter fit error without (left) and with acceptance (right) on the parameter S_3. The green bands represent fit-p.d.f. positivity range. The top figures correspond to the Run-1 like number of events (n = 1), while the middle and the bottom to 10× and 100× larger simulated samples.

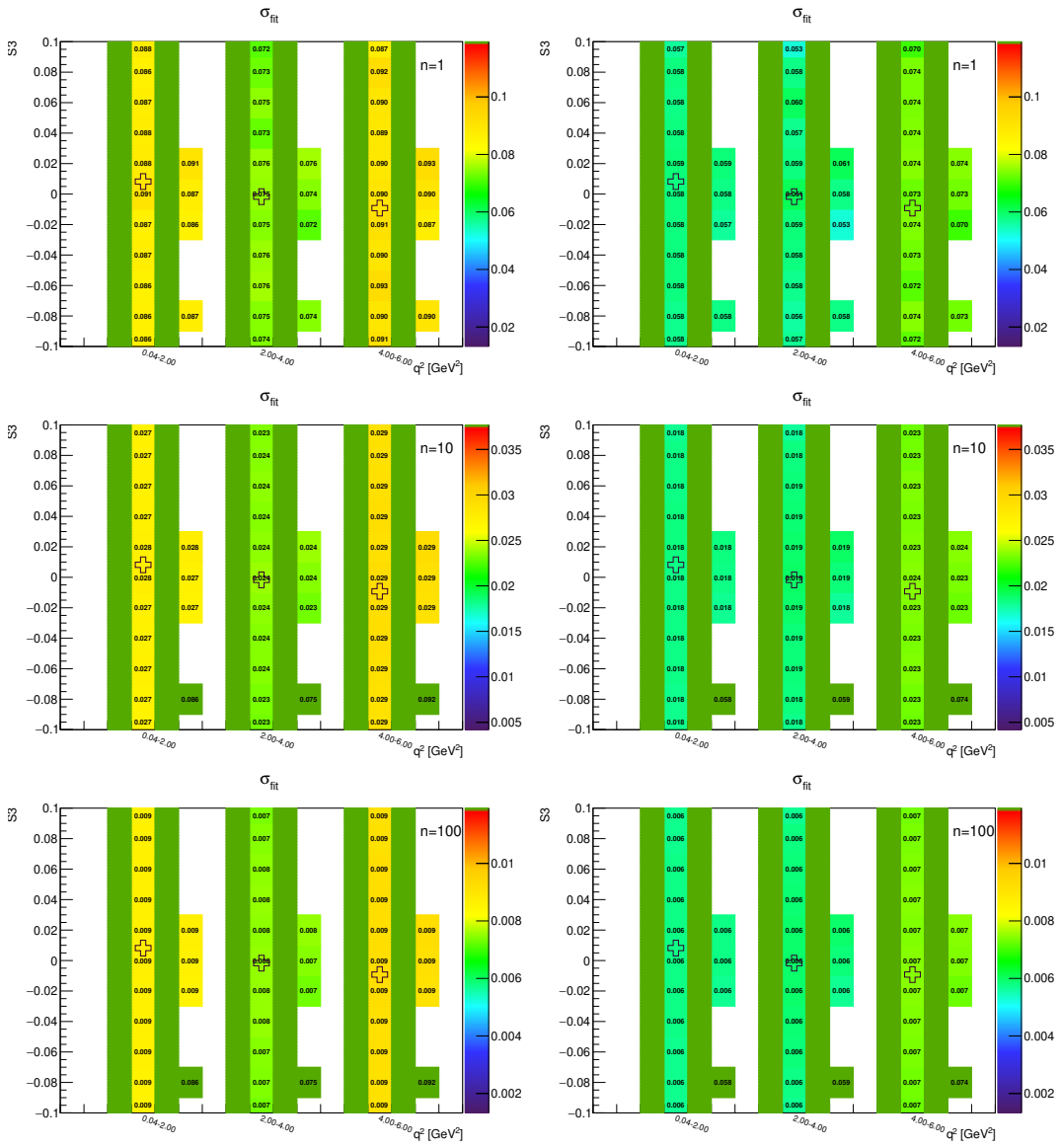

Figure A.60: Toy-MC studies of the S_7-fold, with $r = 2$. Figures show the parameter fit error without (left) and with acceptance (right) on the parameter S_3. The green bands represent fit-p.d.f. positivity range. The top figures correspond to the Run-1 like number of events (n = 1), while the middle and the bottom to 10× and 100× larger simulated samples.

A.3.9 S_7-fold – parameter S_7

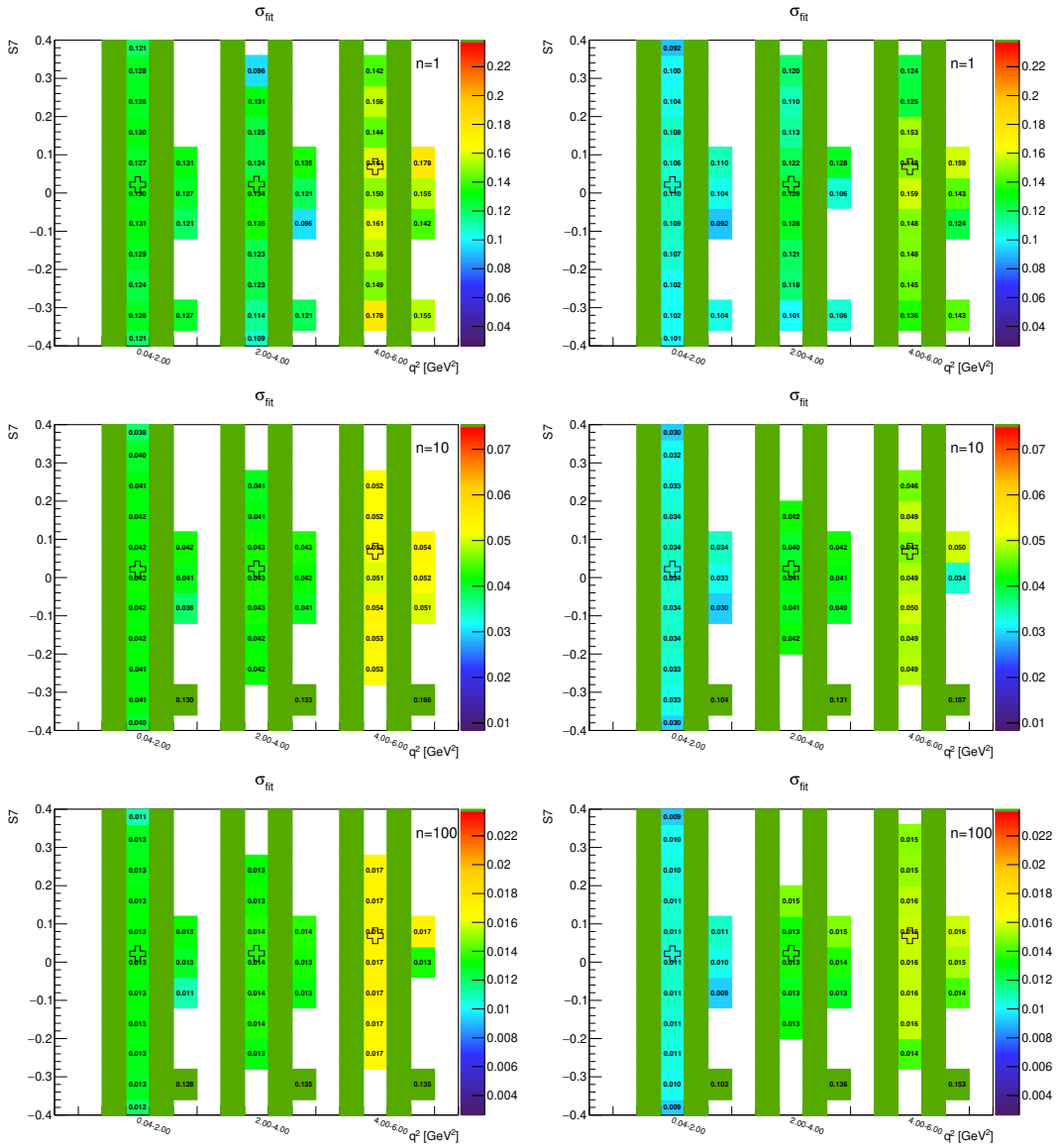

Figure A.61: Toy-MC studies of the S_7-fold, with $r = 0.5$. Figures show the parameter fit error without (left) and with acceptance (right) on the parameter S_7. The green bands represent fit-p.d.f. positivity range. The top figures correspond to the Run-1 like number of events (n = 1), while the middle and the bottom to 10× and 100× larger simulated samples.

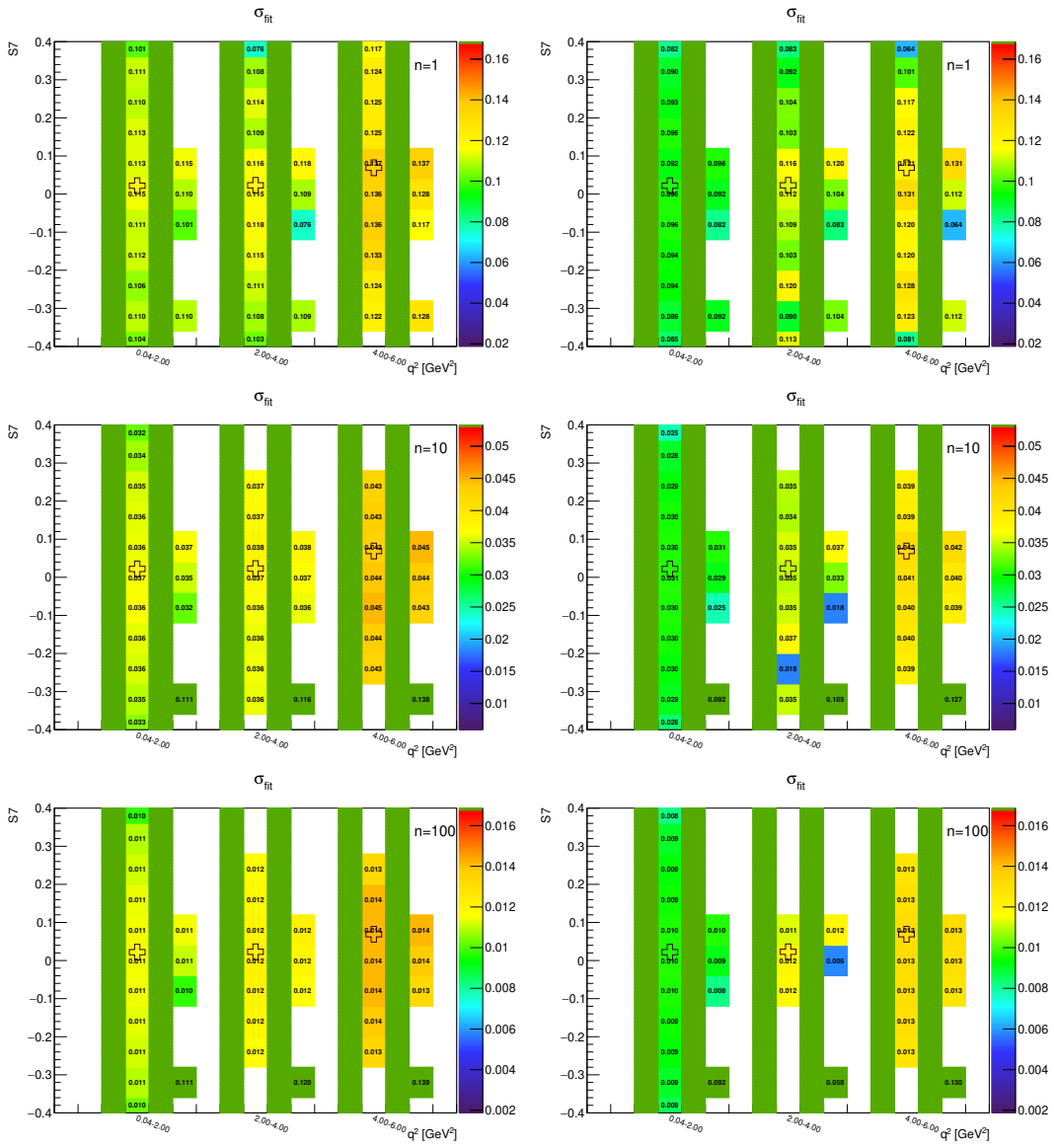

Figure A.62: Toy-MC studies of the S_7-fold, with $r = 1$. Figures show the parameter fit error without (left) and with acceptance (right) on the parameter S_7. The green bands represent fit-p.d.f. positivity range. The top figures correspond to the Run-1 like number of events (n = 1), while the middle and the bottom to 10× and 100× larger simulated samples.

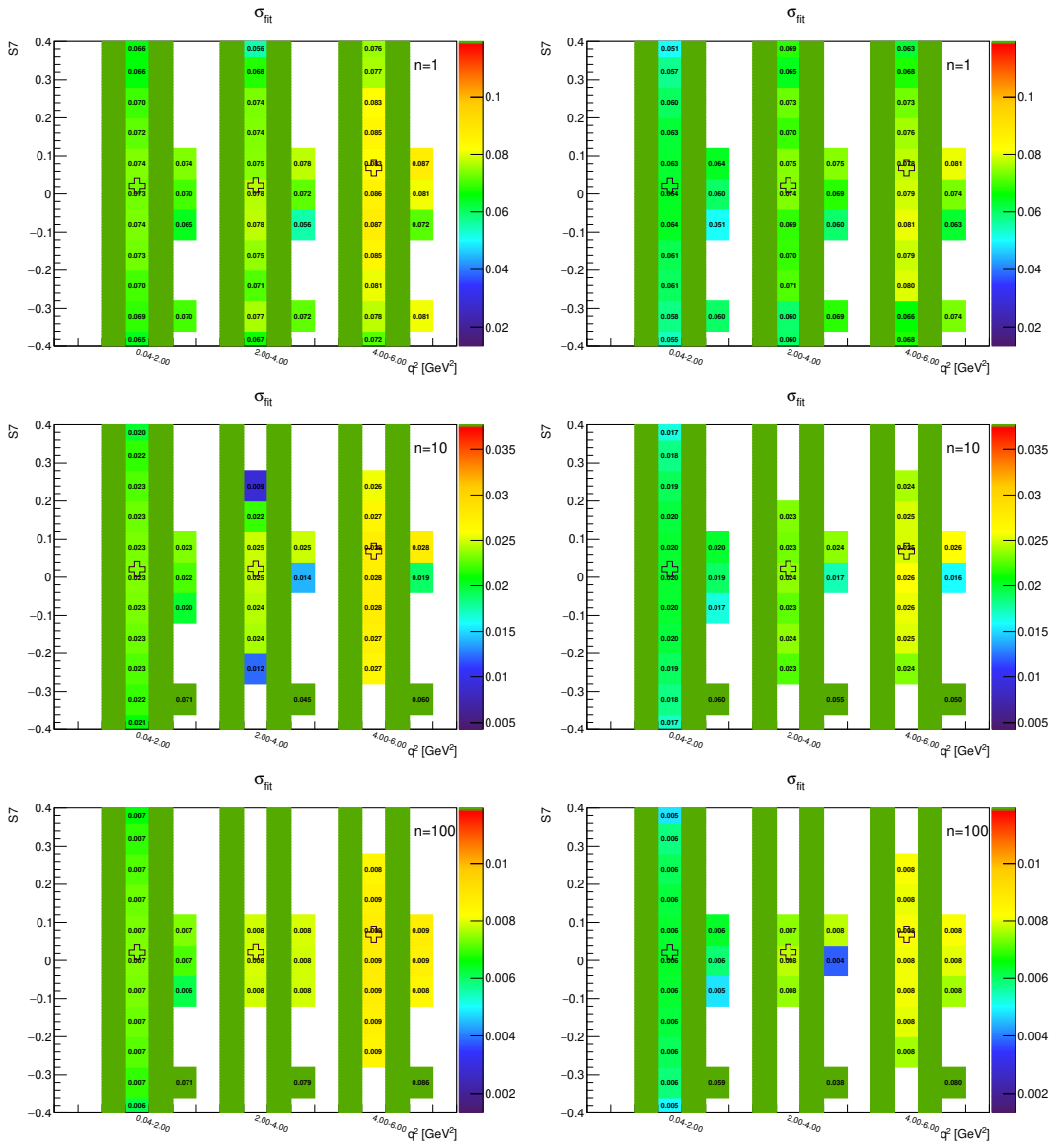

Figure A.63: Toy-MC studies of the S_7-fold, with $r = 2$. Figures show the parameter fit error without (left) and with acceptance (right) on the parameter S_7. The green bands represent fit-p.d.f. positivity range. The top figures correspond to the Run-1 like number of events (n = 1), while the middle and the bottom to 10× and 100× larger simulated samples.

A.3.10 S_8-fold – parameter F_L

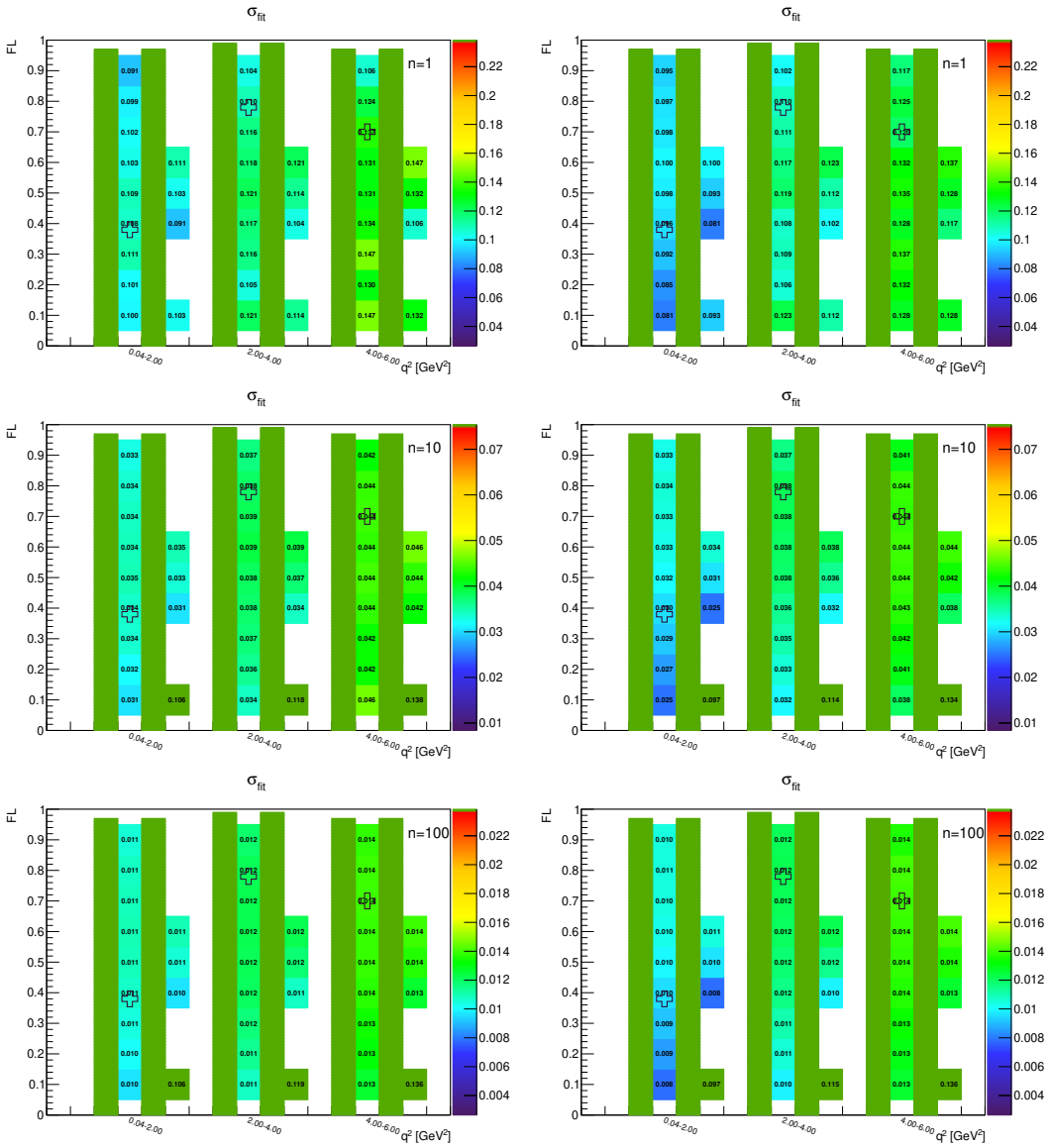

Figure A.64: Toy-MC studies of the S_8-fold, with $r = 0.5$. Figures show the parameter fit error without (left) and with acceptance (right) on the parameter F_L. The green bands represent fit-p.d.f. positivity range. The top figures correspond to the Run-1 like number of events (n = 1), while the middle and the bottom to 10× and 100× larger simulated samples.

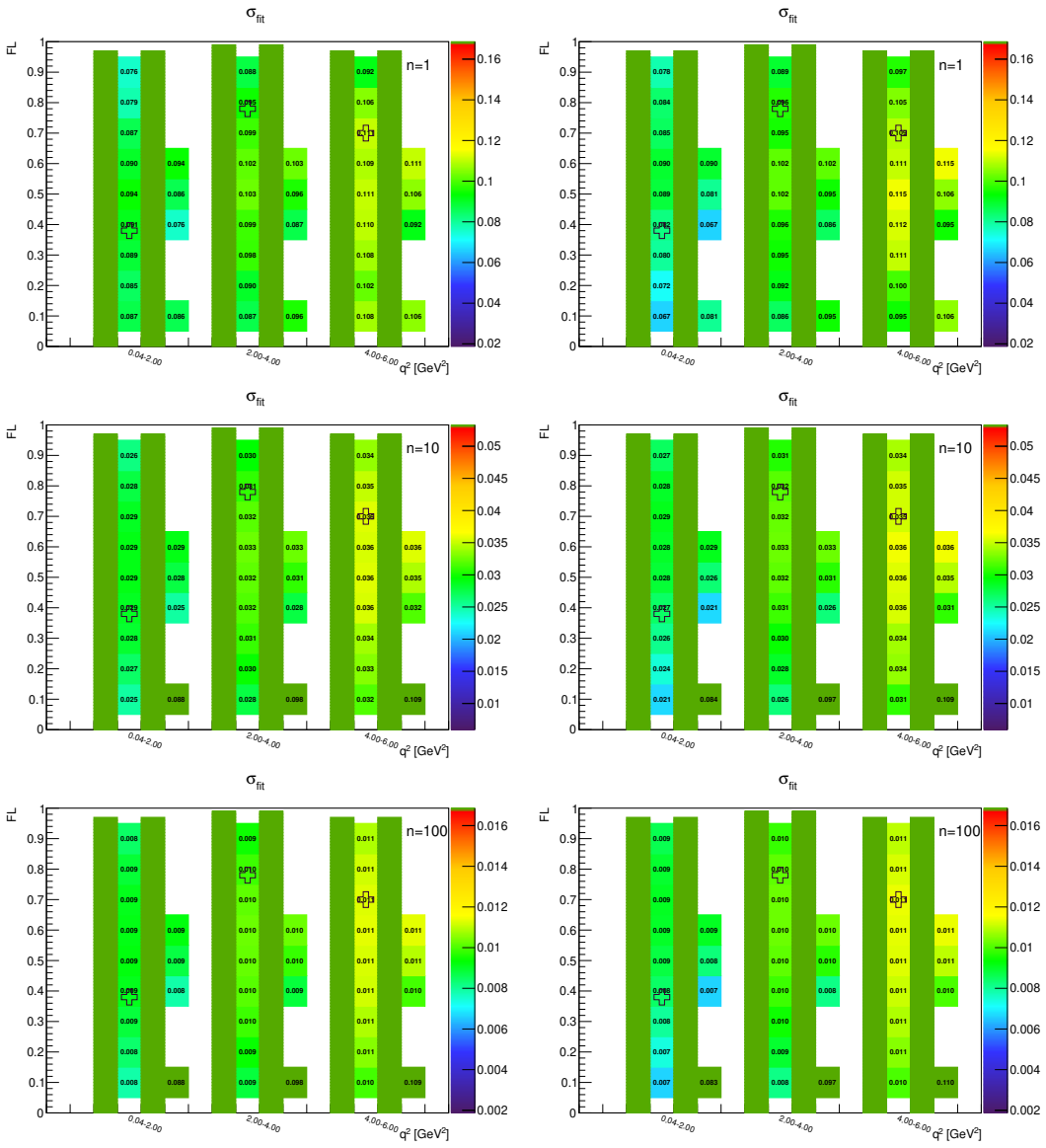

Figure A.65: Toy-MC studies of the S_8-fold, with $r = 1$. Figures show the parameter fit error without (left) and with acceptance (right) on the parameter F_L. The green bands represent fit-p.d.f. positivity range. The top figures correspond to the Run-1 like number of events (n = 1), while the middle and the bottom to 10× and 100× larger simulated samples.

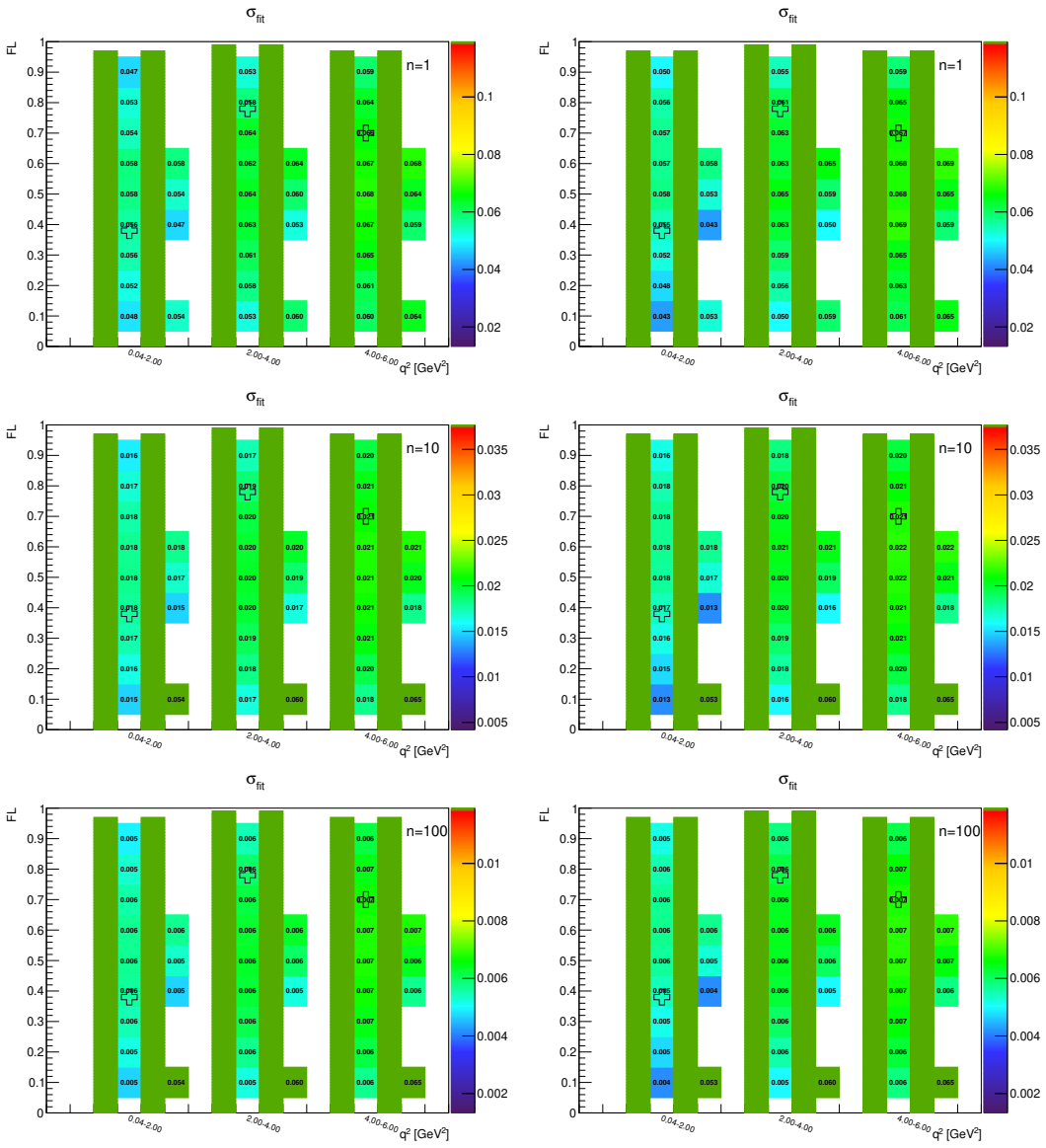

Figure A.66: Toy-MC studies of the S_8-fold, with $r = 2$. Figures show the parameter fit error without (left) and with acceptance (right) on the parameter F_L. The green bands represent fit-p.d.f. positivity range. The top figures correspond to the Run-1 like number of events (n = 1), while the middle and the bottom to 10× and 100× larger simulated samples.

A.3.11 S_8-fold – parameter S_3

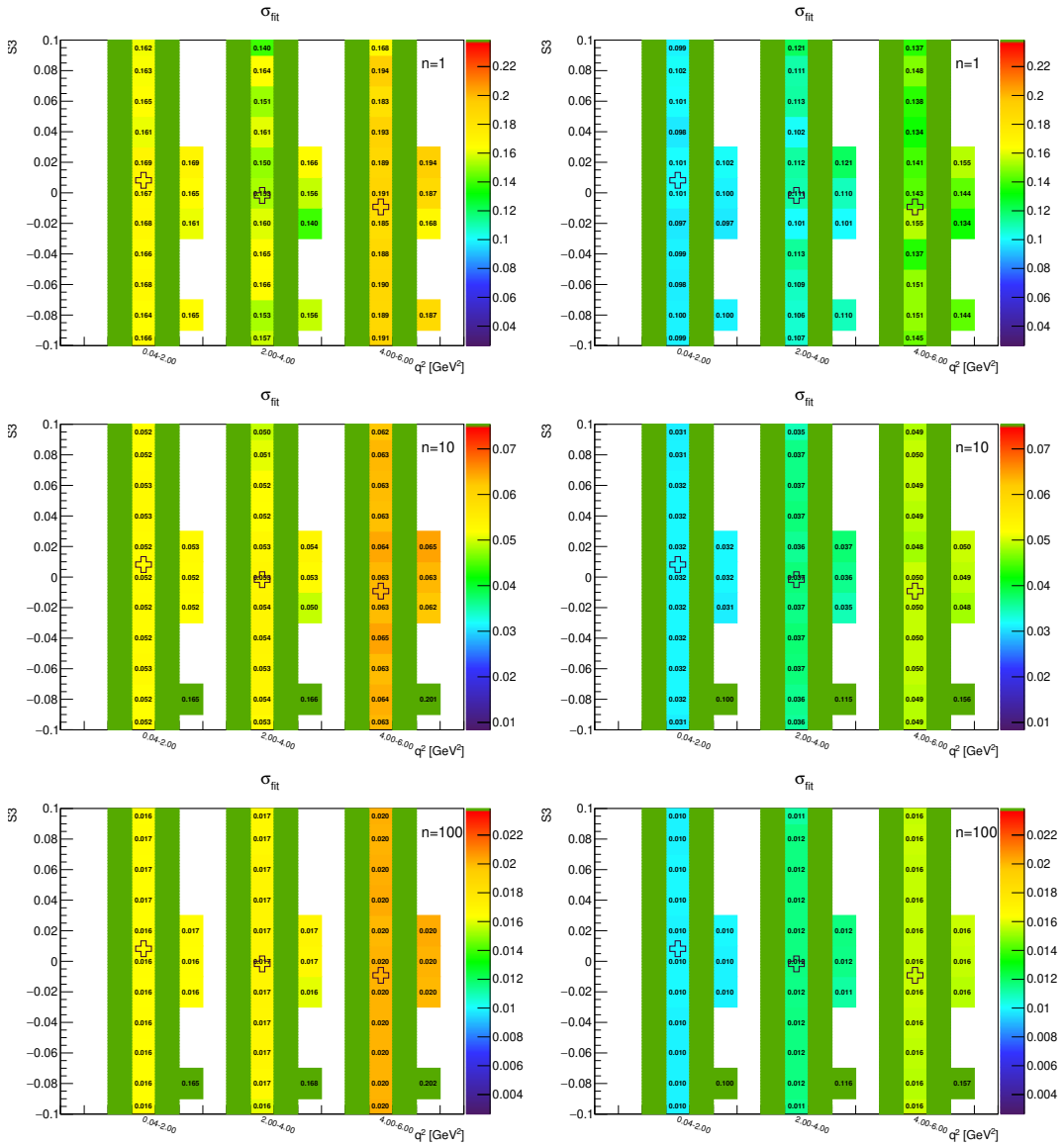

Figure A.67: Toy-MC studies of the S_8-fold, with $r = 0.5$. Figures show the parameter fit error without (left) and with acceptance (right) on the parameter S_3. The green bands represent fit-p.d.f. positivity range. The top figures correspond to the Run-1 like number of events (n = 1), while the middle and the bottom to 10× and 100× larger simulated samples.

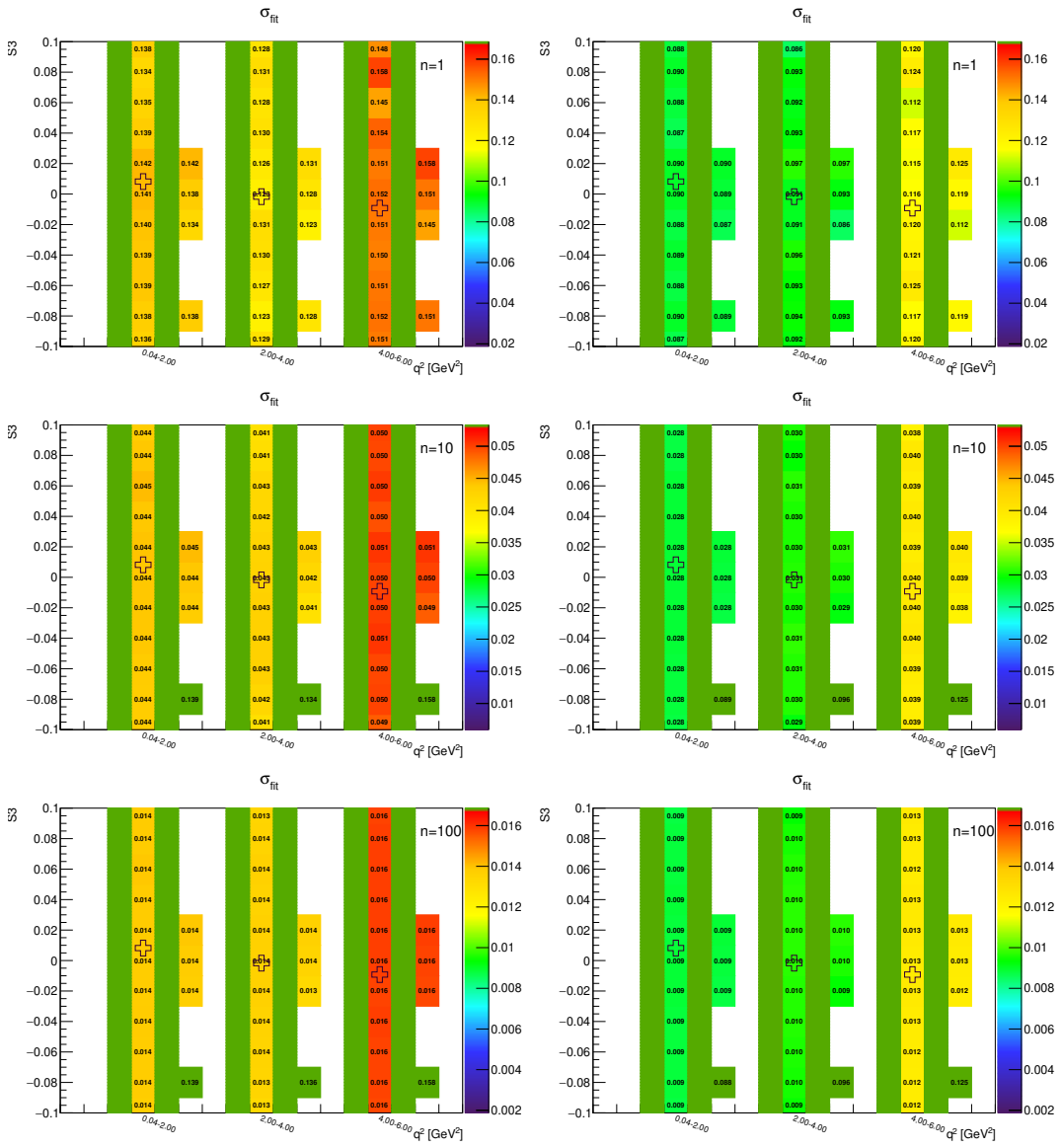

Figure A.68: Toy-MC studies of the S_8-fold, with $r = 1$. Figures show the parameter fit error without (left) and with acceptance (right) on the parameter S_3. The green bands represent fit-p.d.f. positivity range. The top figures correspond to the Run-1 like number of events (n = 1), while the middle and the bottom to 10× and 100× larger simulated samples.

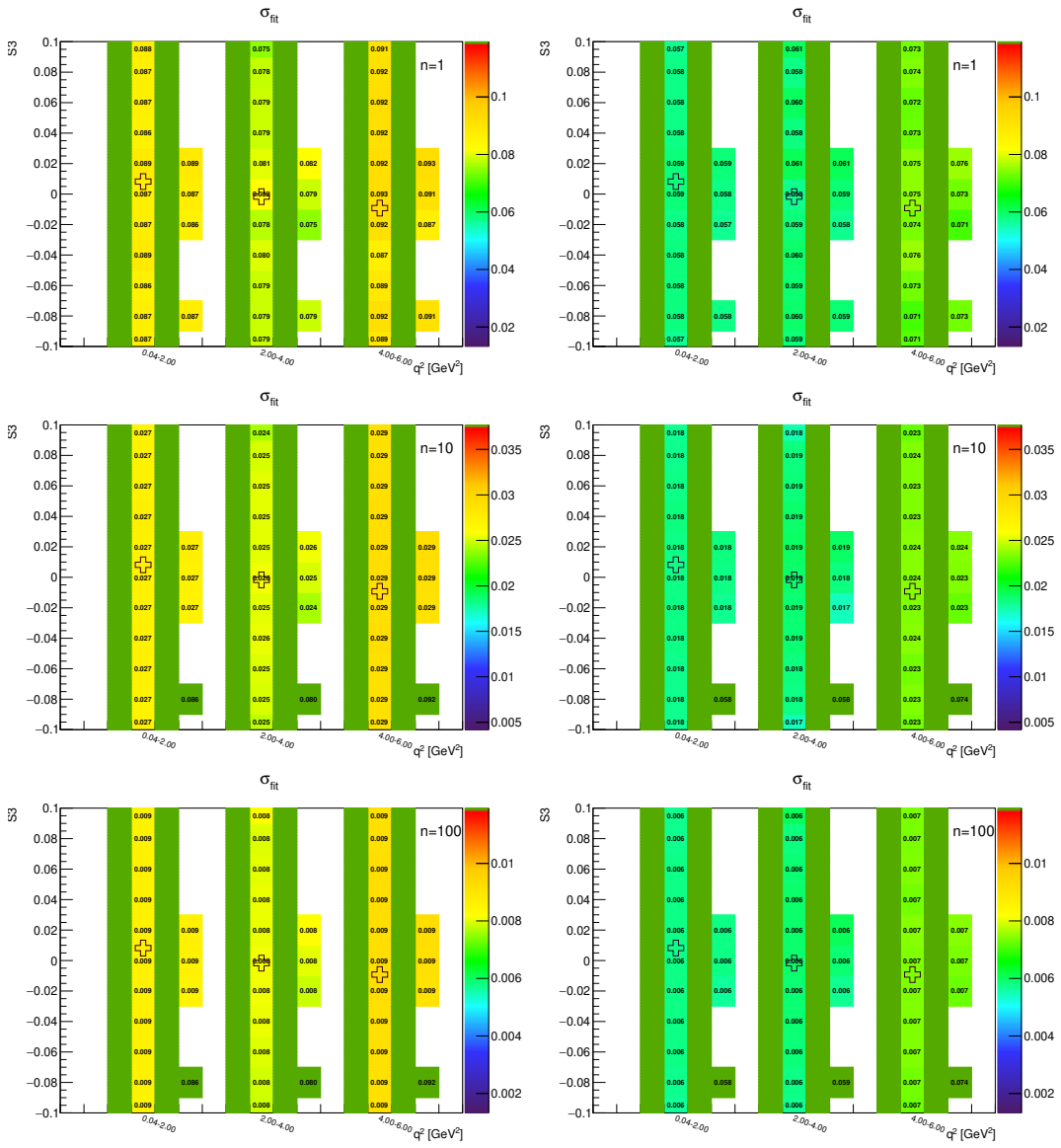

Figure A.69: Toy-MC studies of the S_8-fold, with $r = 2$. Figures show the parameter fit error without (left) and with acceptance (right) on the parameter S_3. The green bands represent fit-p.d.f. positivity range. The top figures correspond to the Run-1 like number of events (n = 1), while the middle and the bottom to 10× and 100× larger simulated samples.

A.3.12 S_8-fold – parameter S_8

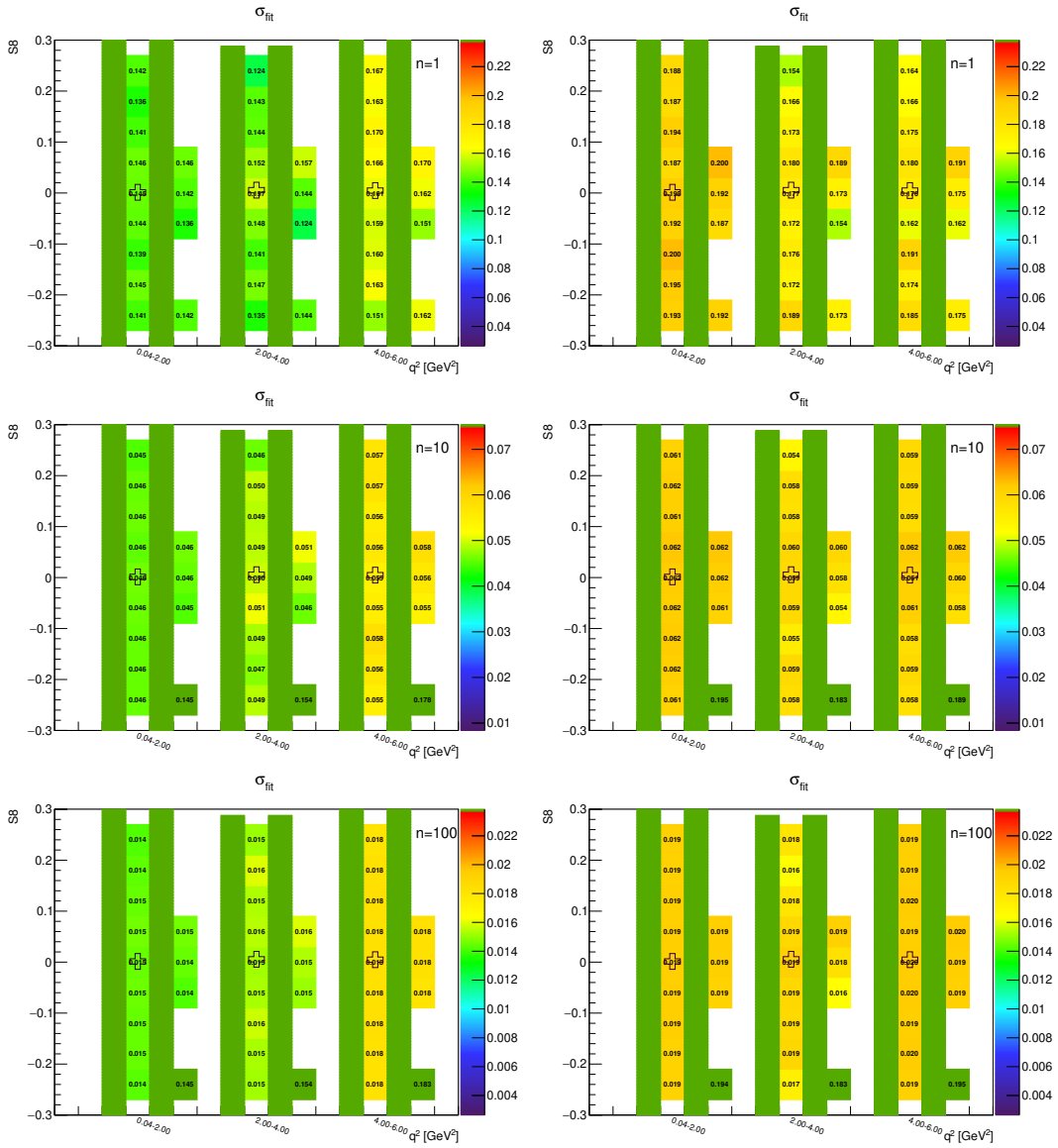

Figure A.70: Toy-MC studies of the S_8-fold, with $r = 0.5$. Figures show the parameter fit error without (left) and with acceptance (right) on the parameter S_8. The green bands represent fit-p.d.f. positivity range. The top figures correspond to the Run-1 like number of events (n = 1), while the middle and the bottom to 10× and 100× larger simulated samples.

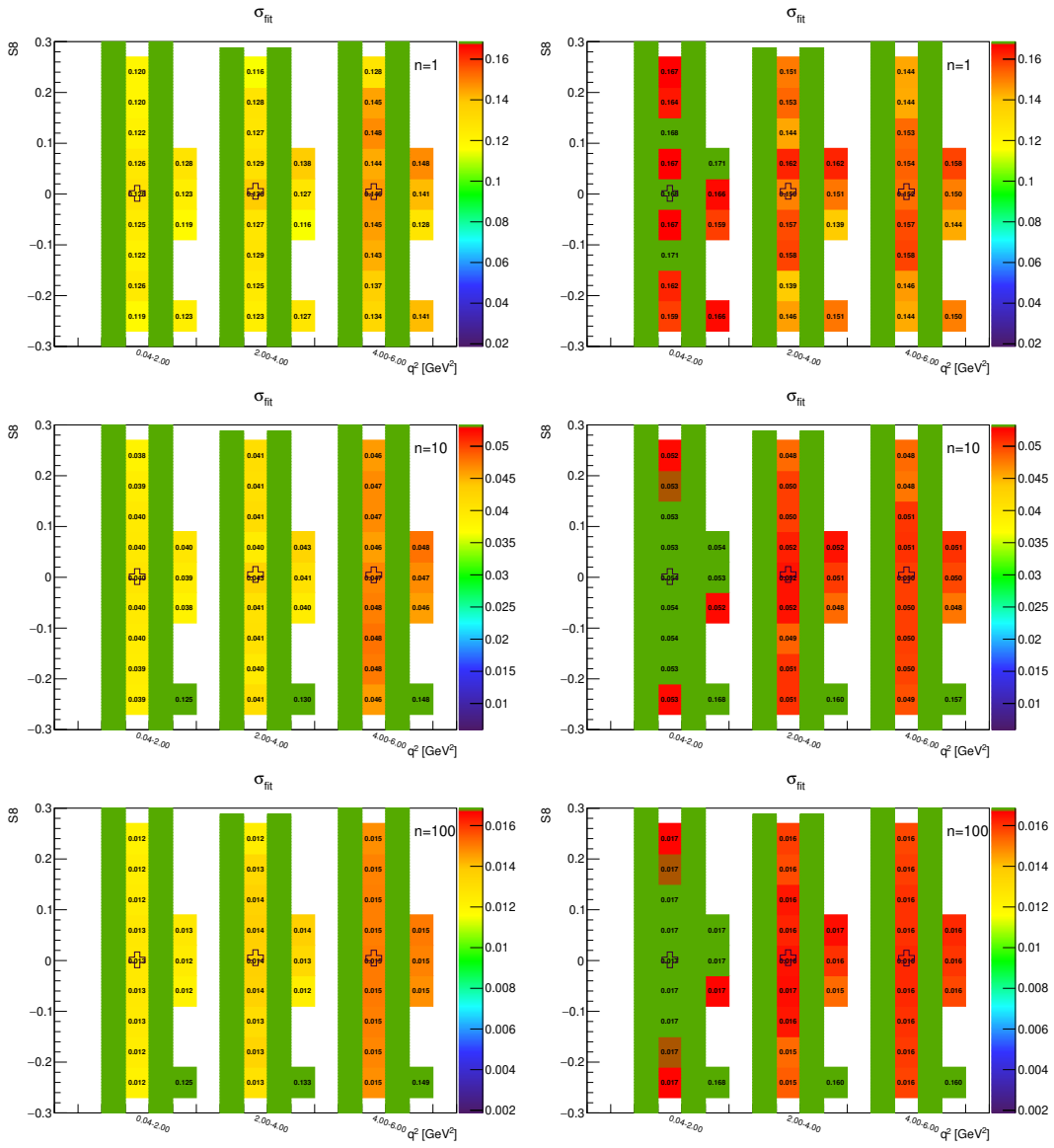

Figure A.71: Toy-MC studies of the S_8-fold, with $r = 1$. Figures show the parameter fit error without (left) and with acceptance (right) on the parameter S_8. The green bands represent fit-p.d.f. positivity range. The top figures correspond to the Run-1 like number of events (n = 1), while the middle and the bottom to 10× and 100× larger simulated samples.

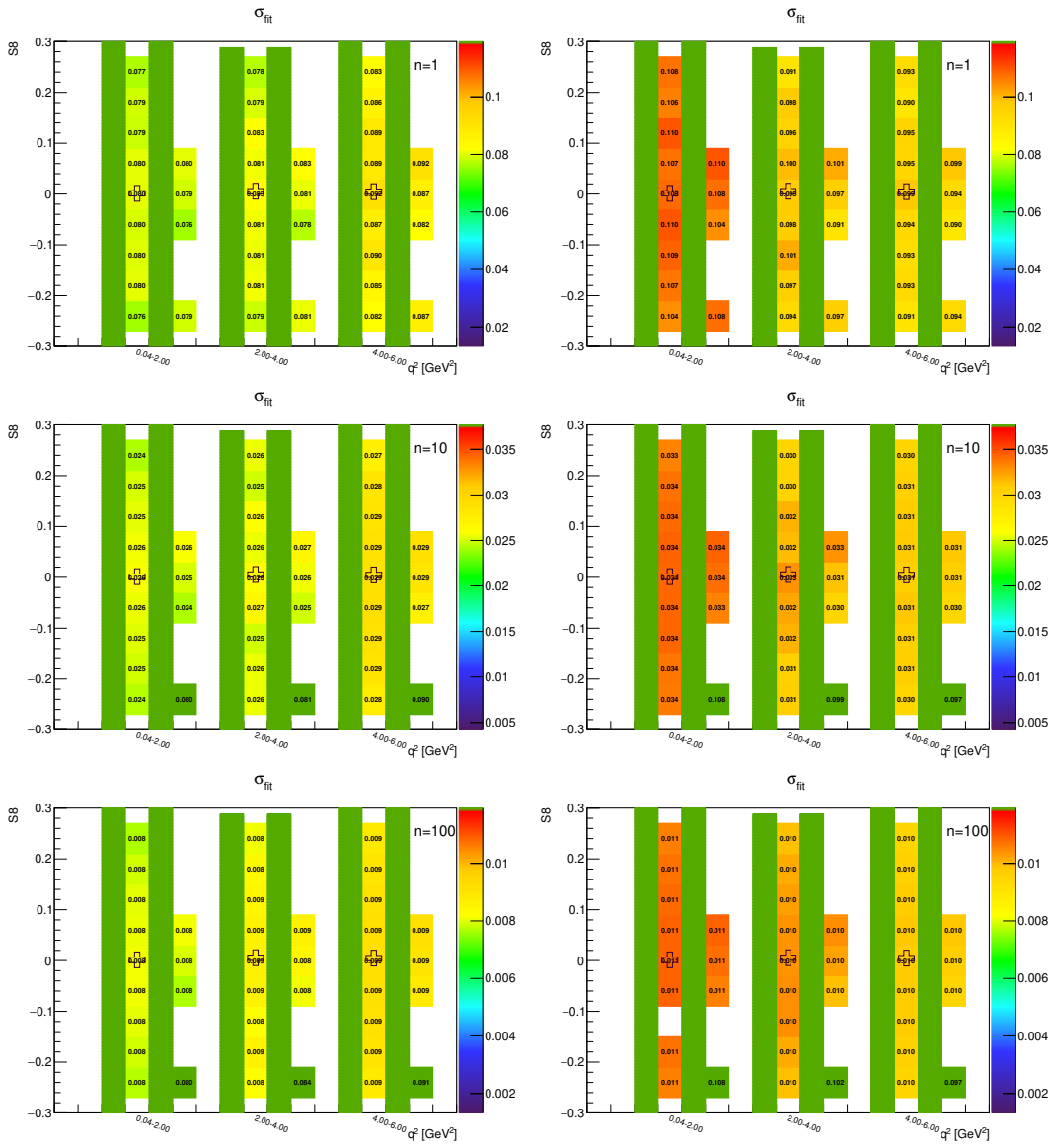

Figure A.72: Toy-MC studies of the S_8-fold, with $r = 2$. Figures show the parameter fit error without (left) and with acceptance (right) on the parameter S_8. The green bands represent fit-p.d.f. positivity range. The top figures correspond to the Run-1 like number of events (n = 1), while the middle and the bottom to 10× and 100× larger simulated samples.

A.4 Fit Validation – Plots of Pull Mean

A.4.1 S_4-fold – parameter F_L

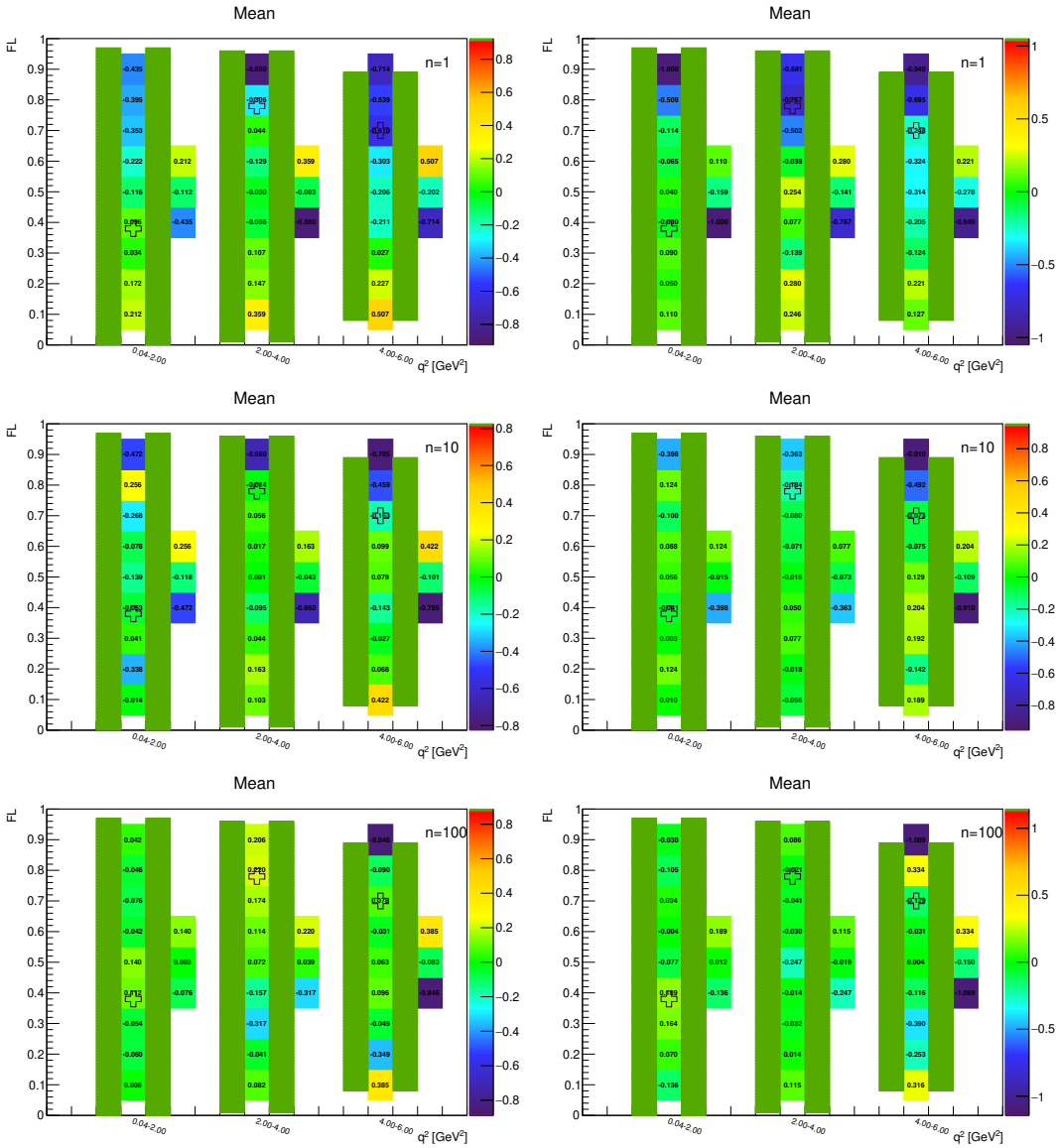

Figure A.73: Toy-MC studies of the S_4-fold, with $r = 0.5$. Figures show the pull mean without (left) and with acceptance (right) on the parameter F_L. The green bands represent fit-p.d.f. positivity range. The top figures correspond to the Run-1 like number of events (n = 1), while the middle and the bottom to 10× and 100× larger simulated samples.

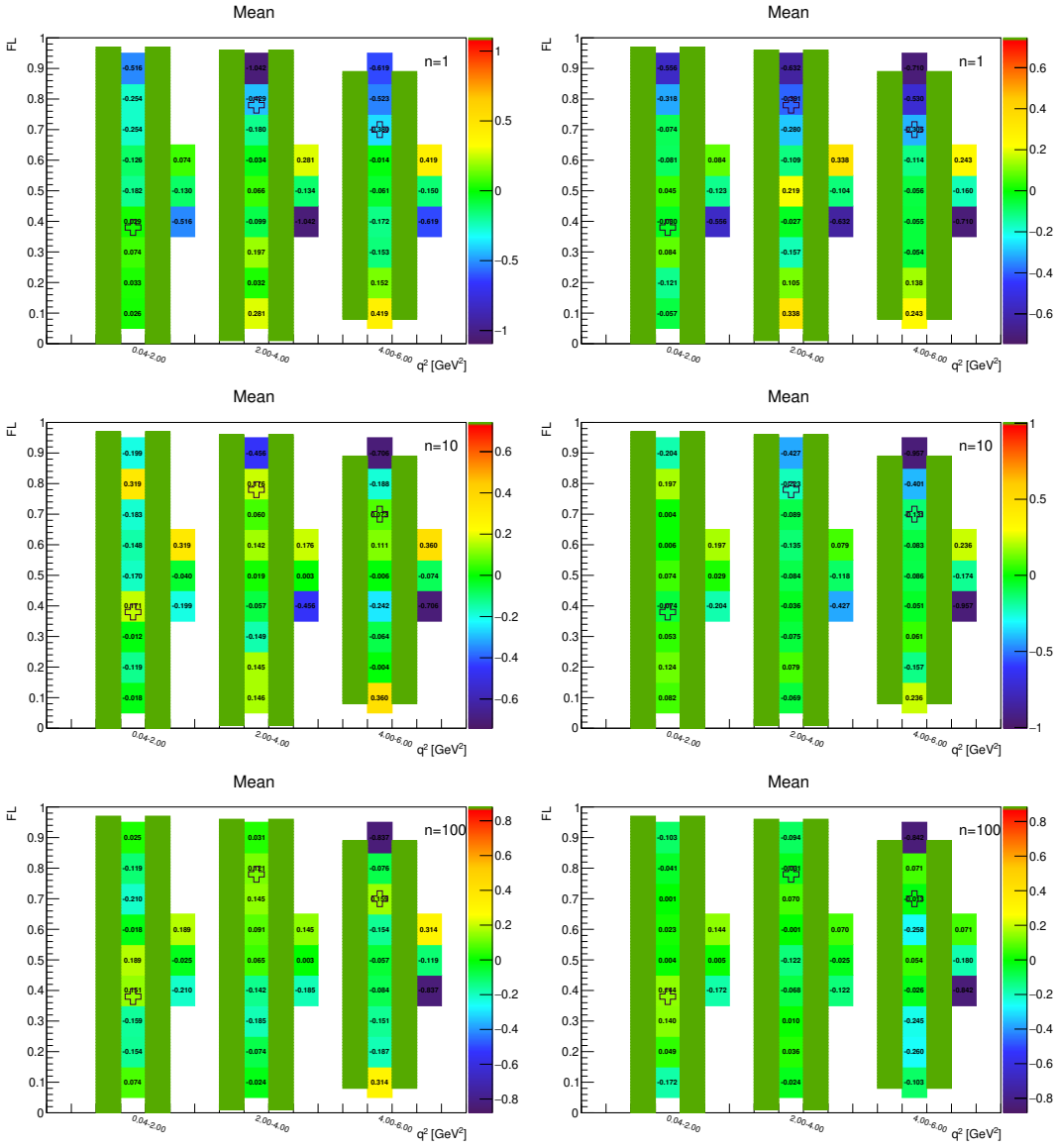

Figure A.74: Toy-MC studies of the S_4-fold, with $r = 1$. Figures show the pull mean without (left) and with acceptance (right) on the parameter F_L. The green bands represent fit-p.d.f. positivity range. The top figures correspond to the Run-1 like number of events (n = 1), while the middle and the bottom to 10× and 100× larger simulated samples.

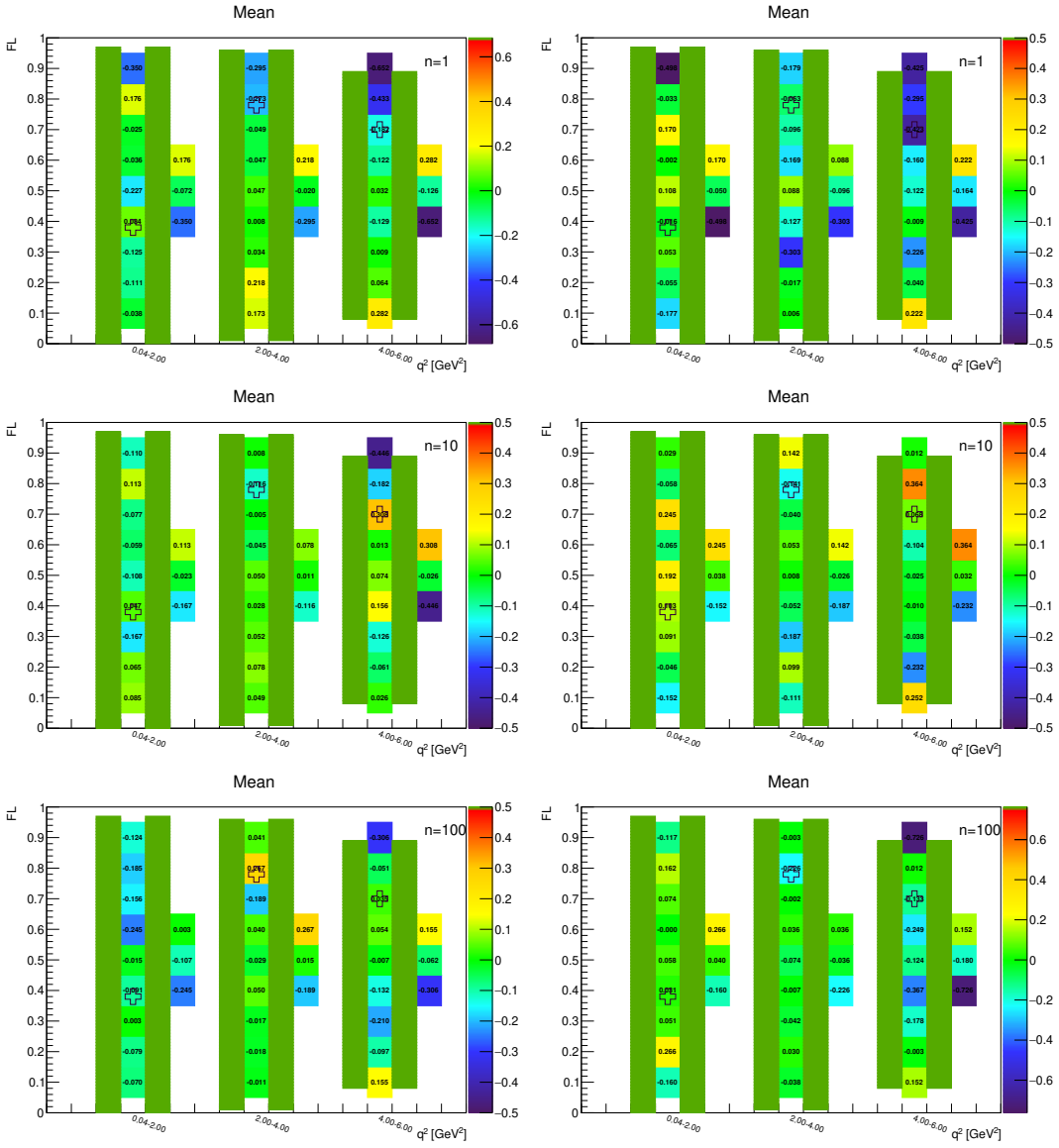

Figure A.75: Toy-MC studies of the S_4-fold, with $r = 2$. Figures show the pull mean without (left) and with acceptance (right) on the parameter F_L. The green bands represent fit-p.d.f. positivity range. The top figures correspond to the Run-1 like number of events (n = 1), while the middle and the bottom to 10× and 100× larger simulated samples.

A.4.2 S_4-fold – parameter S_3

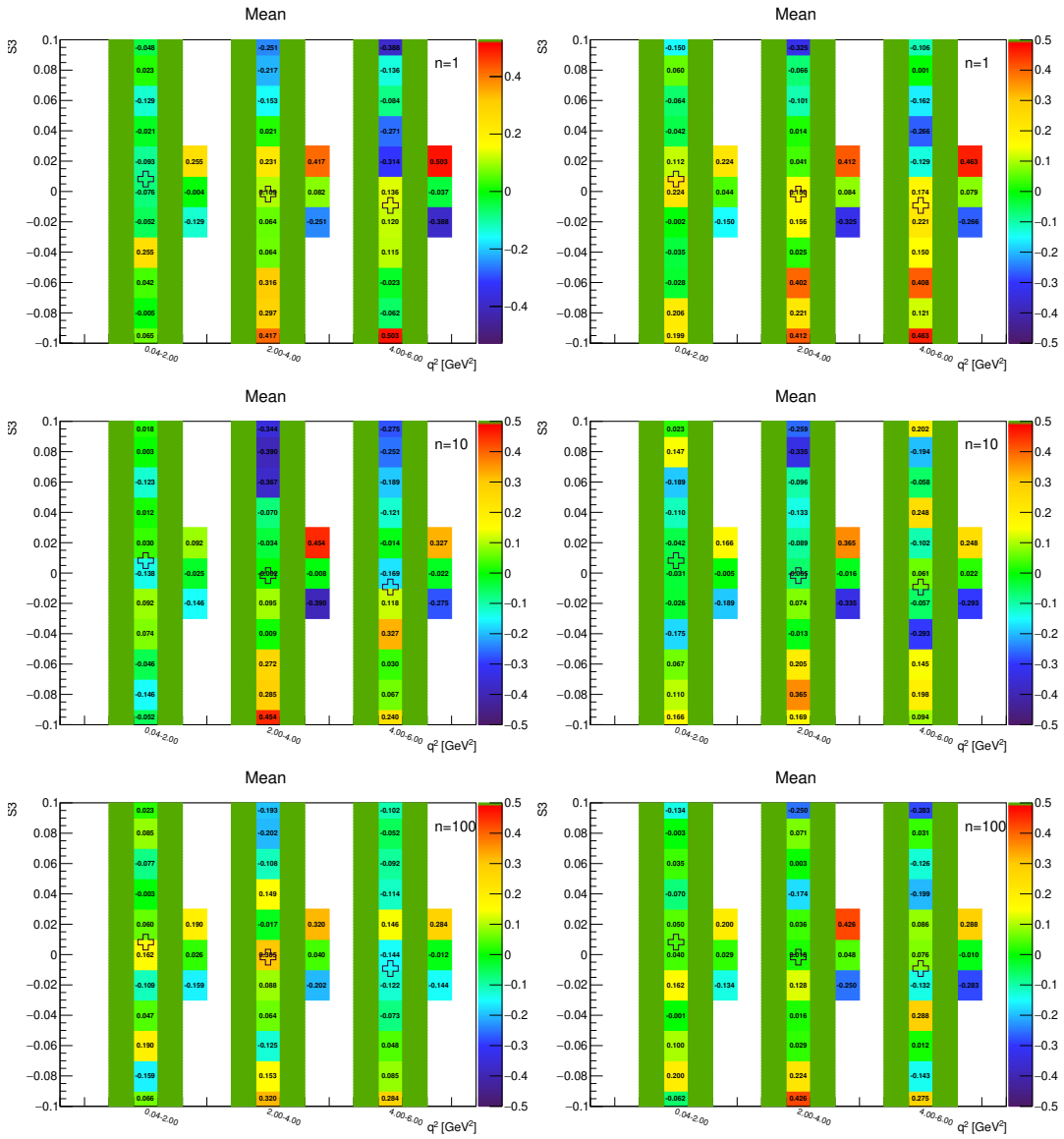

Figure A.76: Toy-MC studies of the S_4-fold, with $r = 0.5$. Figures show the pull mean without (left) and with acceptance (right) on the parameter S_3. The green bands represent fit-p.d.f. positivity range. The top figures correspond to the Run-1 like number of events (n = 1), while the middle and the bottom to 10× and 100× larger simulated samples.

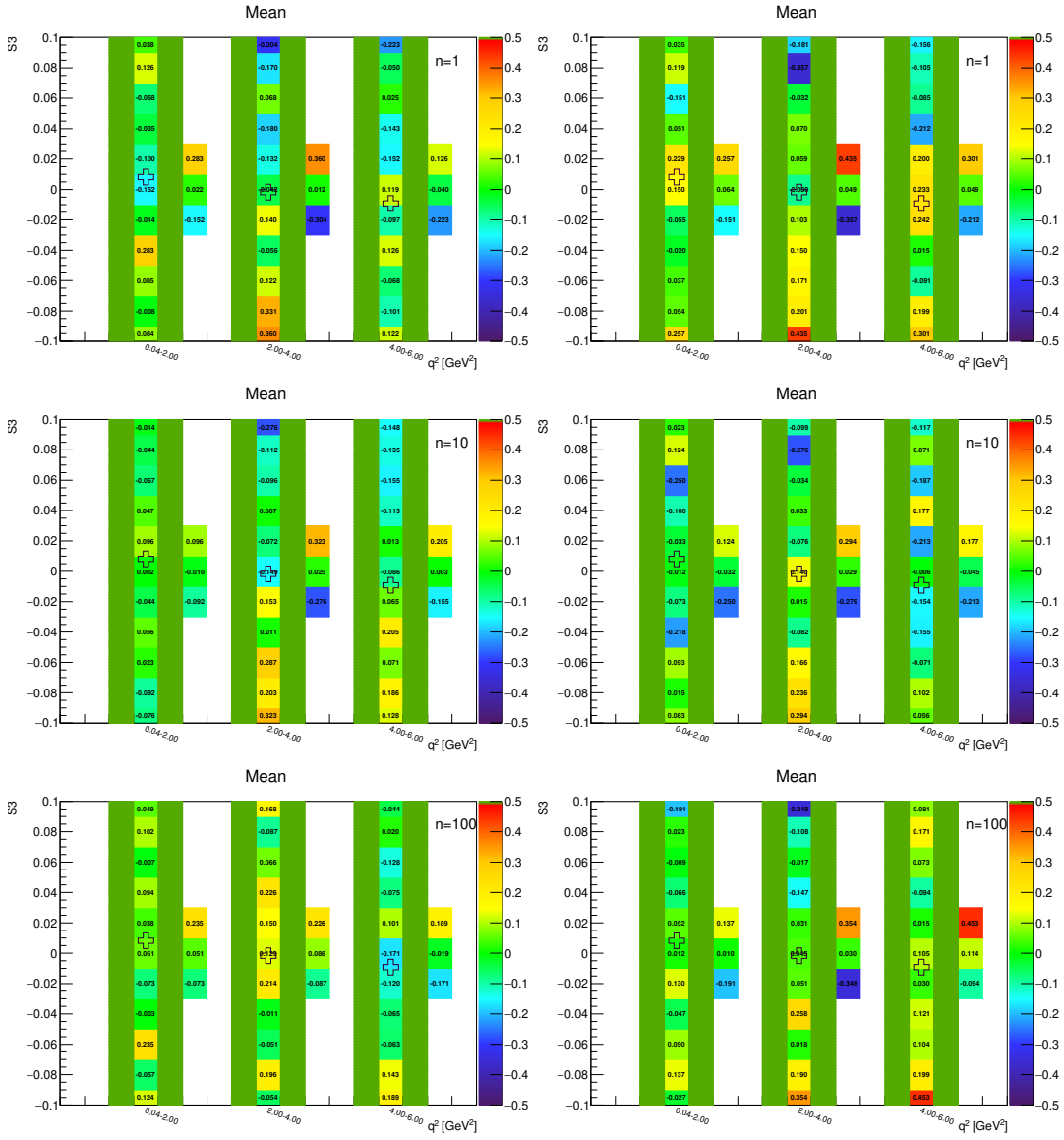

Figure A.77: Toy-MC studies of the S_4-fold, with $r = 1$. Figures show the pull mean without (left) and with acceptance (right) on the parameter S_3. The green bands represent fit-p.d.f. positivity range. The top figures correspond to the Run-1 like number of events (n = 1), while the middle and the bottom to 10× and 100× larger simulated samples.

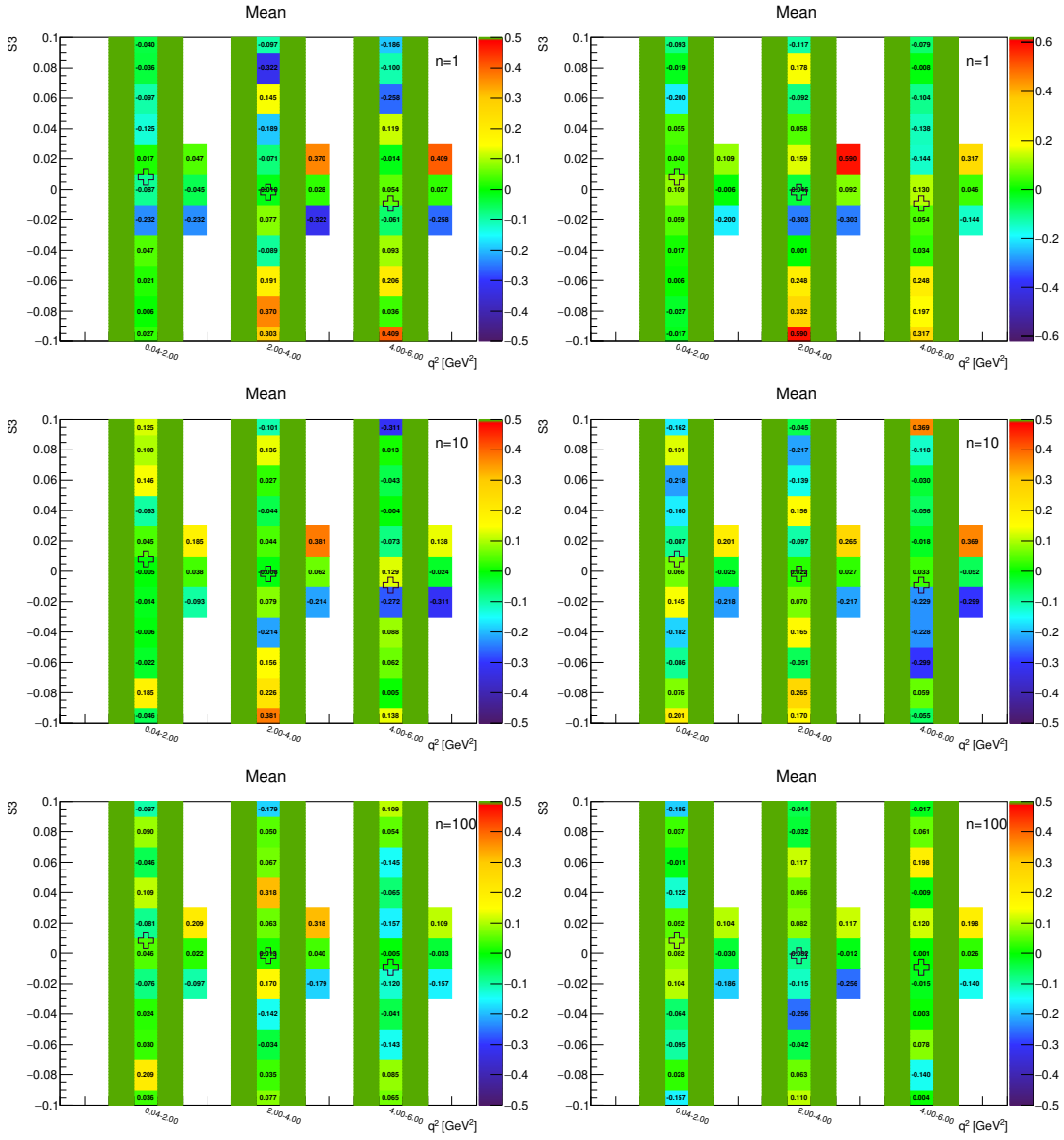

Figure A.78: Toy-MC studies of the S_4-fold, with $r = 2$. Figures show the pull mean without (left) and with acceptance (right) on the parameter S_3. The green bands represent fit-p.d.f. positivity range. The top figures correspond to the Run-1 like number of events (n = 1), while the middle and the bottom to 10× and 100× larger simulated samples.

A.4.3 S_4-fold – parameter S_4

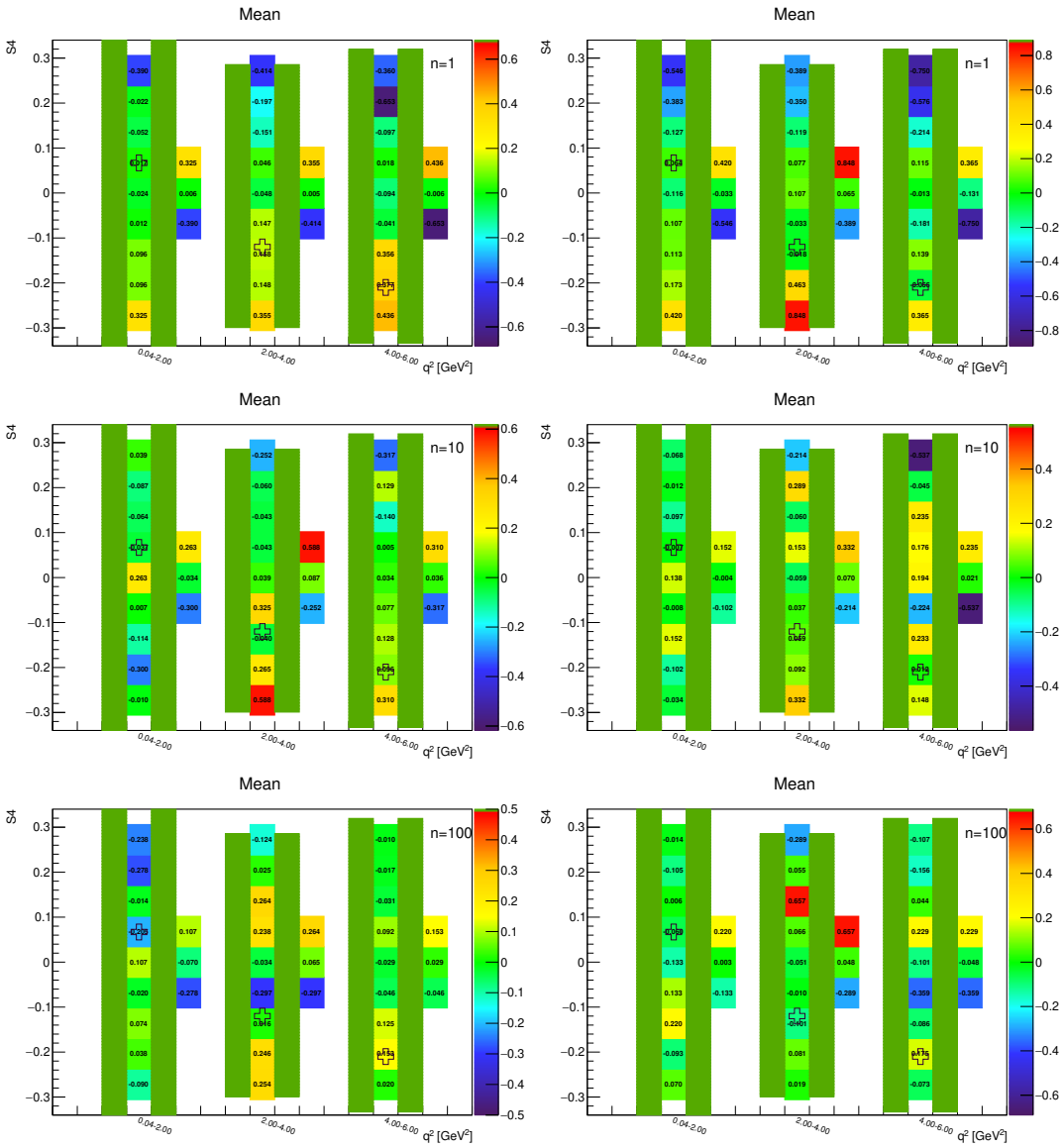

Figure A.79: Toy-MC studies of the S_4-fold, with $r = 0.5$. Figures show the pull mean without (left) and with acceptance (right) on the parameter S_4. The green bands represent fit-p.d.f. positivity range. The top figures correspond to the Run-1 like number of events (n = 1), while the middle and the bottom to 10× and 100× larger simulated samples.

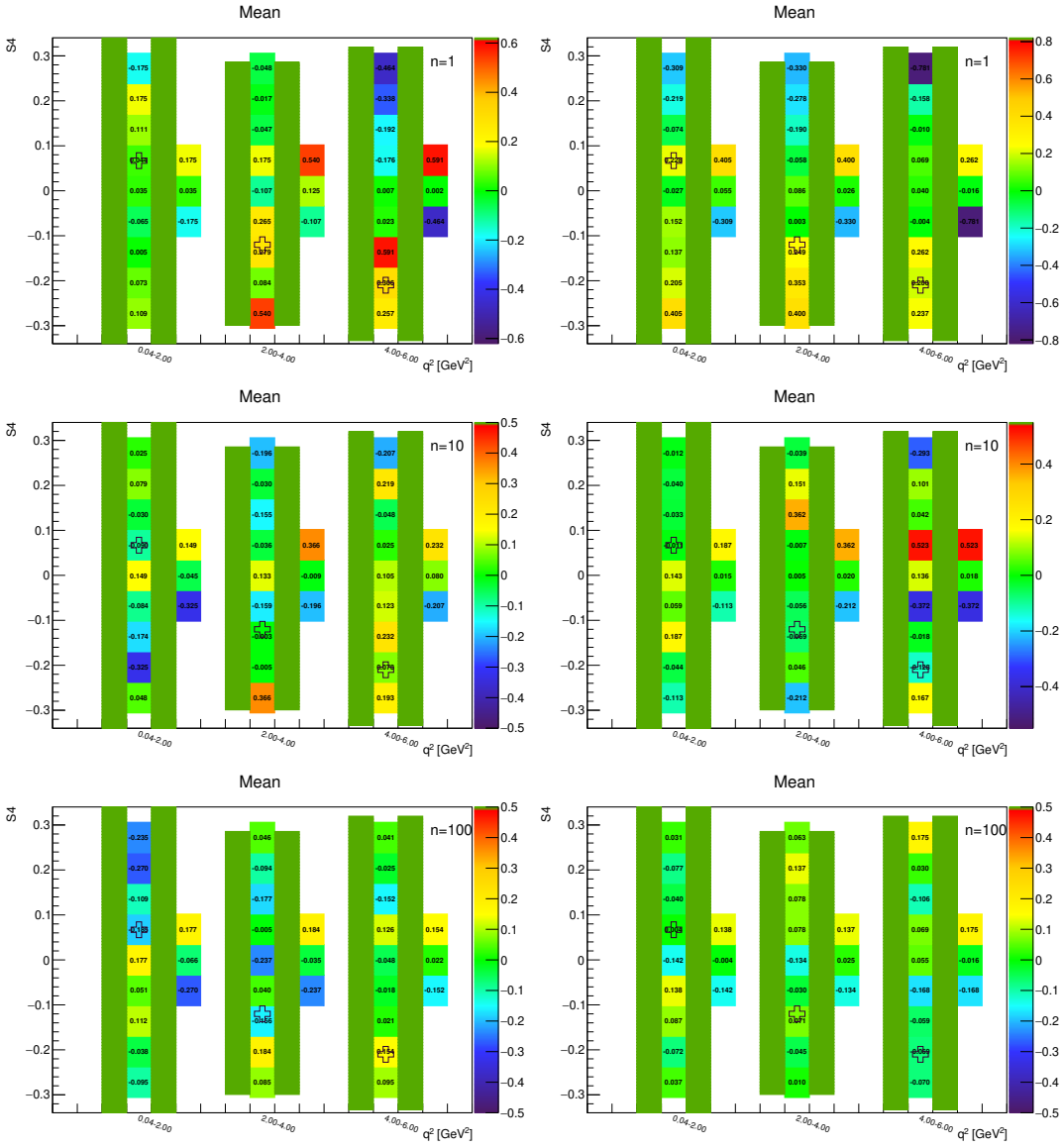

Figure A.80: Toy-MC studies of the S_4-fold, with $r = 1$. Figures show the pull mean without (left) and with acceptance (right) on the parameter S_4. The green bands represent fit-p.d.f. positivity range. The top figures correspond to the Run-1 like number of events (n = 1), while the middle and the bottom to 10× and 100× larger simulated samples.

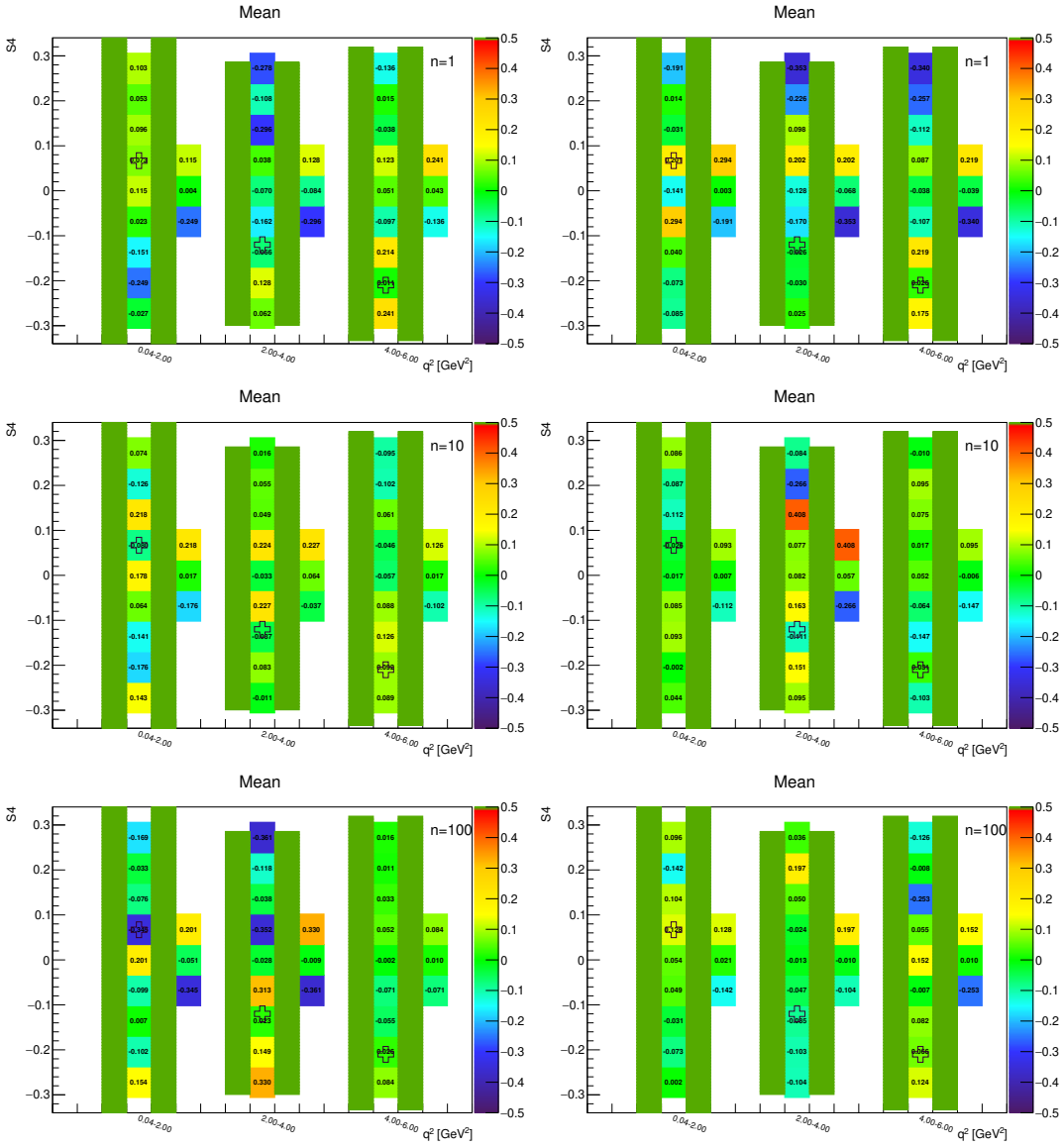

Figure A.81: Toy-MC studies of the S_4-fold, with $r = 2$. Figures show the pull mean without (left) and with acceptance (right) on the parameter S_4. The green bands represent fit-p.d.f. positivity range. The top figures correspond to the Run-1 like number of events (n = 1), while the middle and the bottom to 10× and 100× larger simulated samples.

A.4.4 S_5-fold – parameter F_L

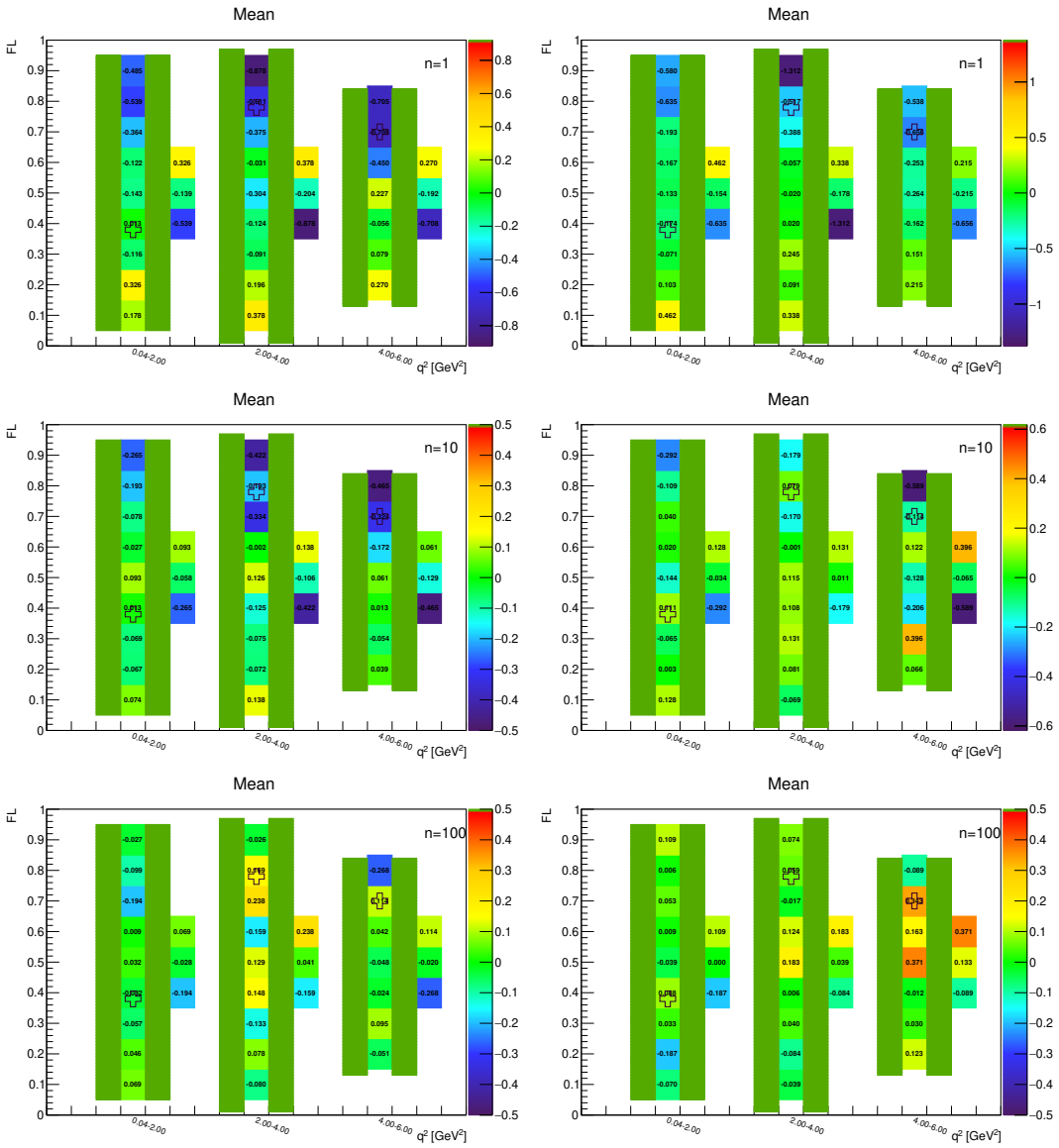

Figure A.82: Toy-MC studies of the S_5-fold, with $r = 0.5$. Figures show the pull mean without (left) and with acceptance (right) on the parameter F_L. The green bands represent fit-p.d.f. positivity range. The top figures correspond to the Run-1 like number of events (n = 1), while the middle and the bottom to 10× and 100× larger simulated samples.

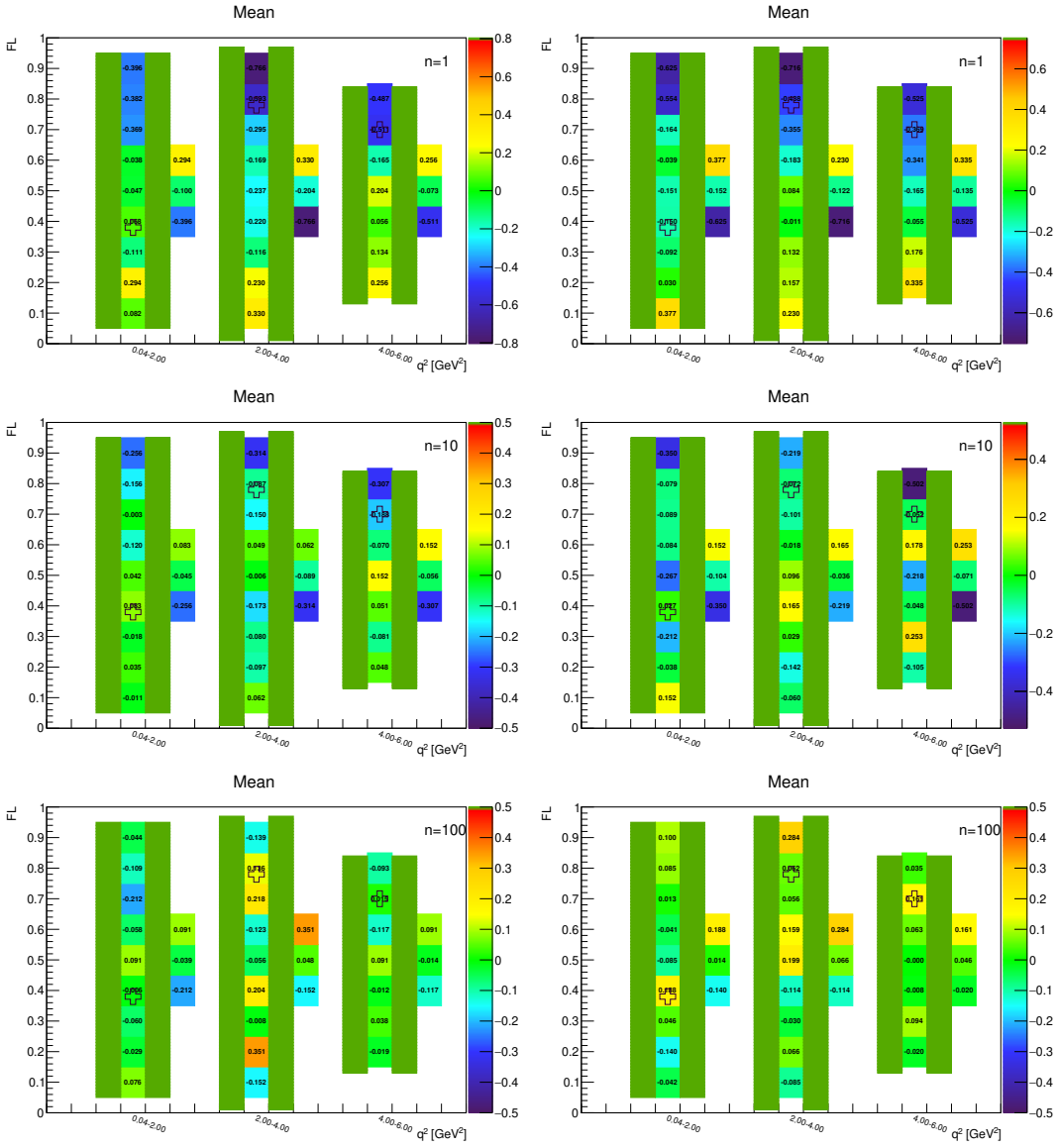

Figure A.83: Toy-MC studies of the S_5-fold, with $r = 1$. Figures show the pull mean without (left) and with acceptance (right) on the parameter F_L. The green bands represent fit-p.d.f. positivity range. The top figures correspond to the Run-1 like number of events (n = 1), while the middle and the bottom to 10× and 100× larger simulated samples.

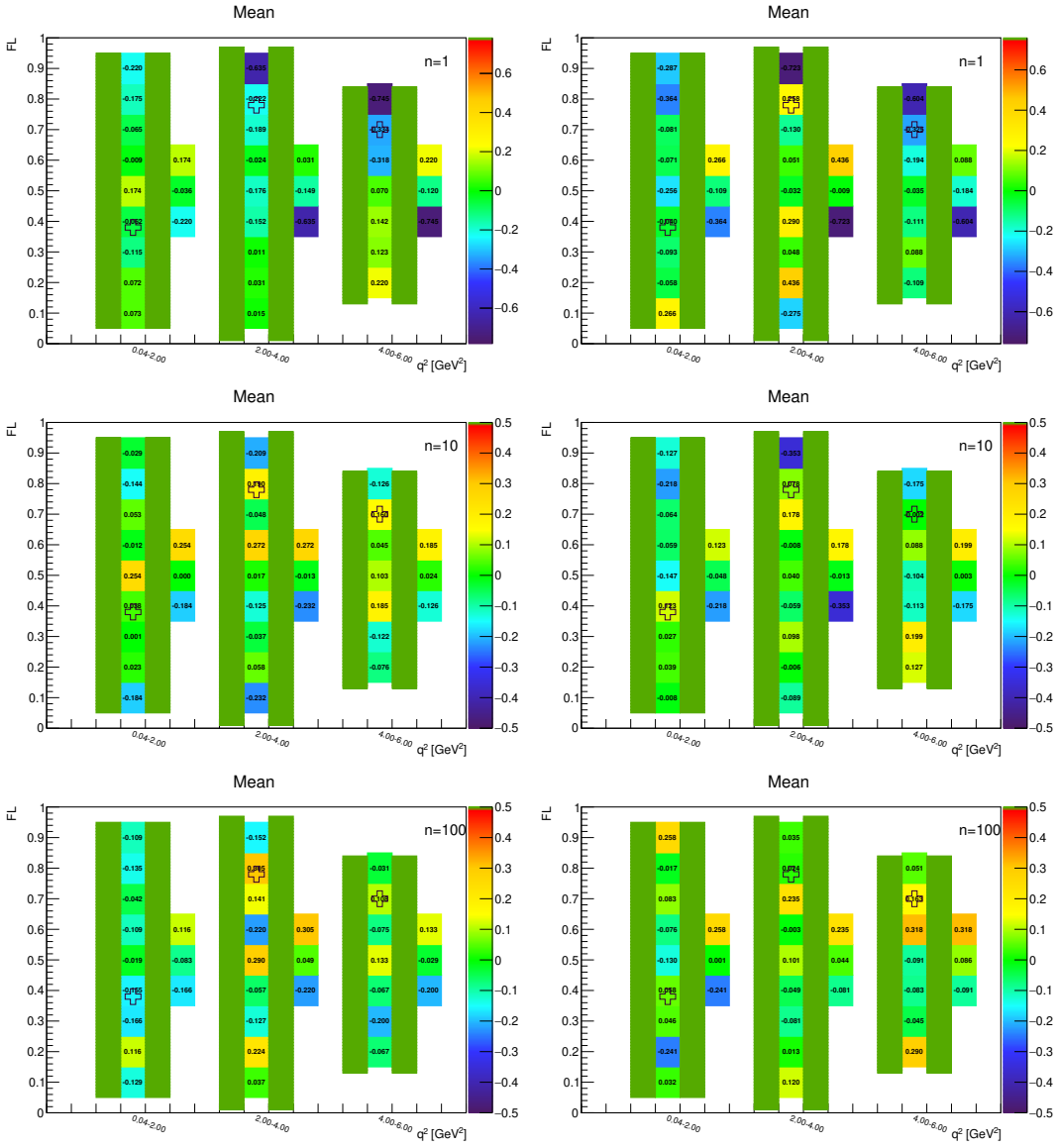

Figure A.84: Toy-MC studies of the S_5-fold, with $r = 2$. Figures show the pull mean without (left) and with acceptance (right) on the parameter F_L. The green bands represent fit-p.d.f. positivity range. The top figures correspond to the Run-1 like number of events (n = 1), while the middle and the bottom to 10× and 100× larger simulated samples.

A.4.5 S_5-fold – parameter S_3

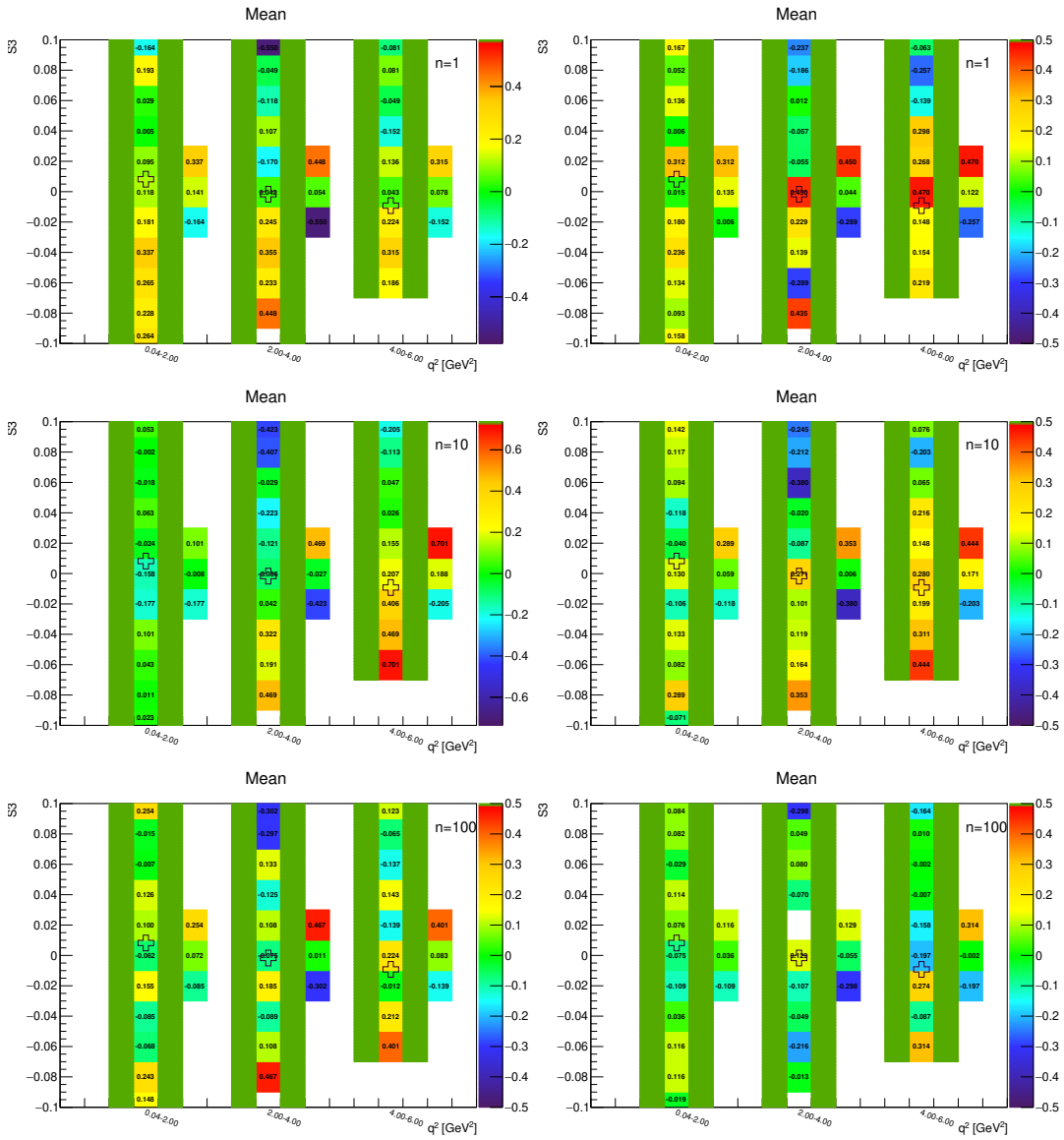

Figure A.85: Toy-MC studies of the S_5-fold, with $r = 0.5$. Figures show the pull mean without (left) and with acceptance (right) on the parameter S_3. The green bands represent fit-p.d.f. positivity range. The top figures correspond to the Run-1 like number of events (n = 1), while the middle and the bottom to 10× and 100× larger simulated samples.

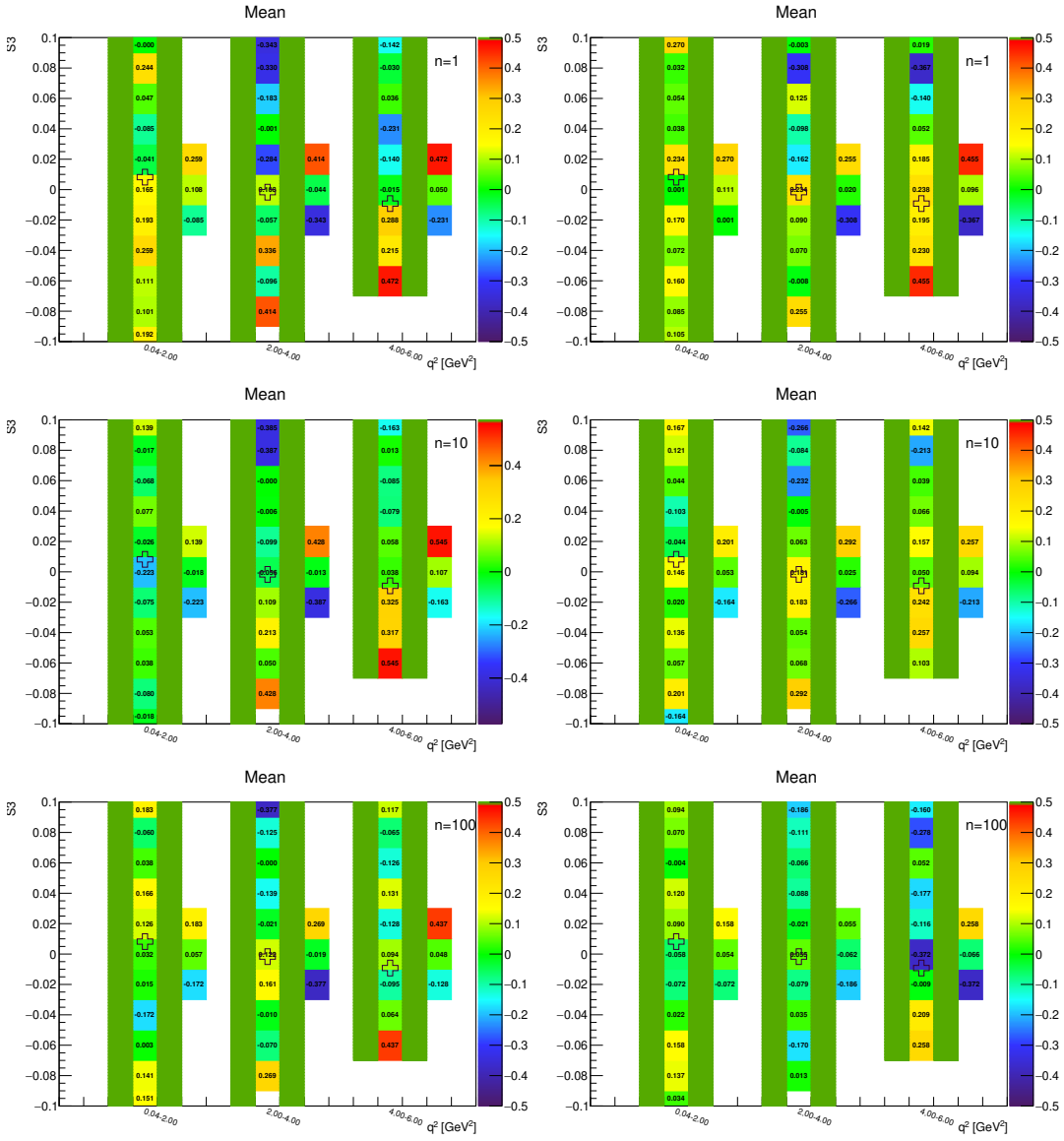

Figure A.86: Toy-MC studies of the S_5-fold, with $r = 1$. Figures show the pull mean without (left) and with acceptance (right) on the parameter S_3. The green bands represent fit-p.d.f. positivity range. The top figures correspond to the Run-1 like number of events (n = 1), while the middle and the bottom to 10× and 100× larger simulated samples.

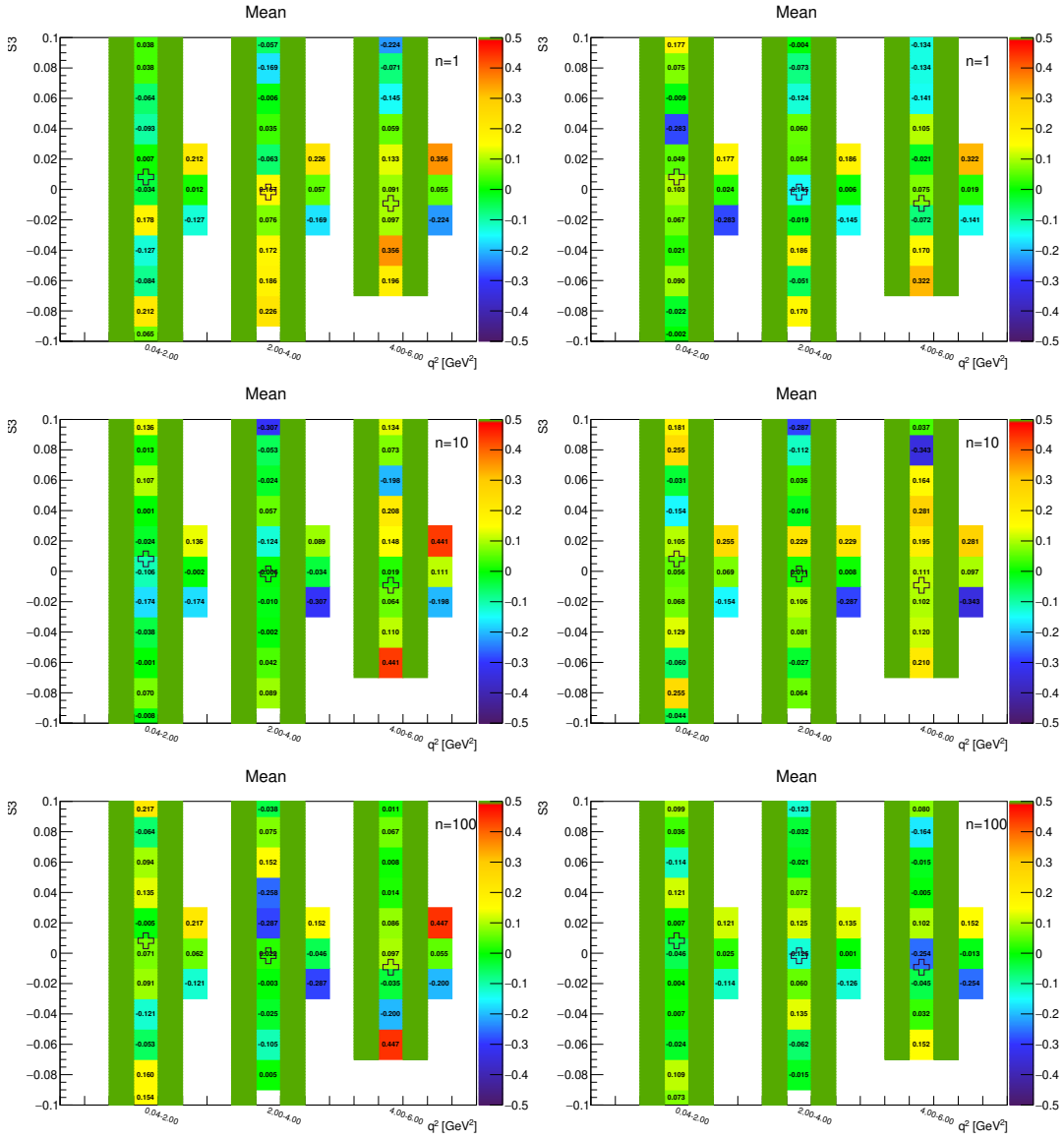

Figure A.87: Toy-MC studies of the S_5-fold, with $r = 2$. Figures show the pull mean without (left) and with acceptance (right) on the parameter S_3. The green bands represent fit-p.d.f. positivity range. The top figures correspond to the Run-1 like number of events (n = 1), while the middle and the bottom to 10× and 100× larger simulated samples.

A.4.6 S_5-fold – parameter S_5

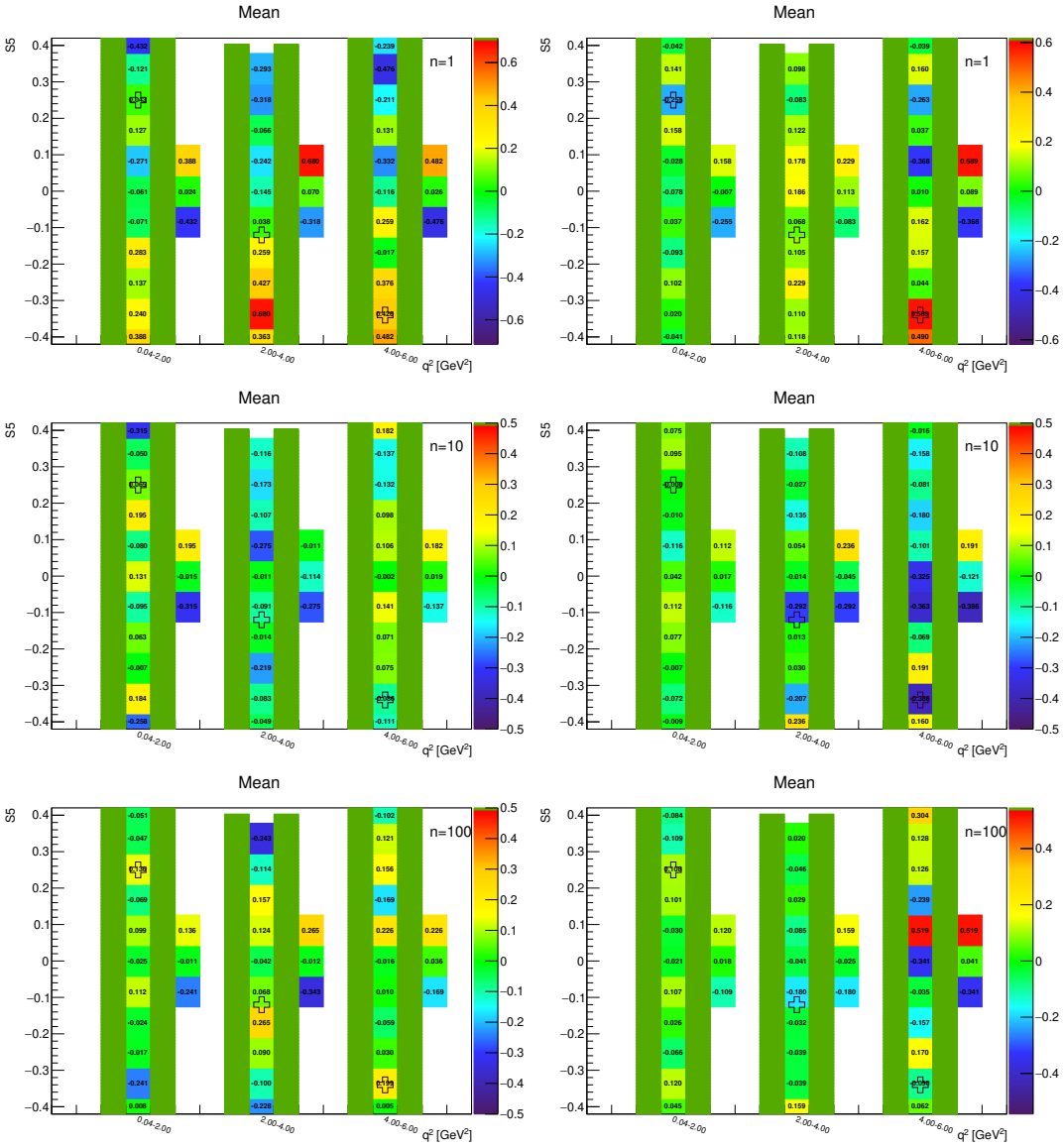

Figure A.88: Toy-MC studies of the S_5-fold, with $r = 0.5$. Figures show the pull mean without (left) and with acceptance (right) on the parameter S_5. The green bands represent fit-p.d.f. positivity range. The top figures correspond to the Run-1 like number of events (n = 1), while the middle and the bottom to 10× and 100× larger simulated samples.

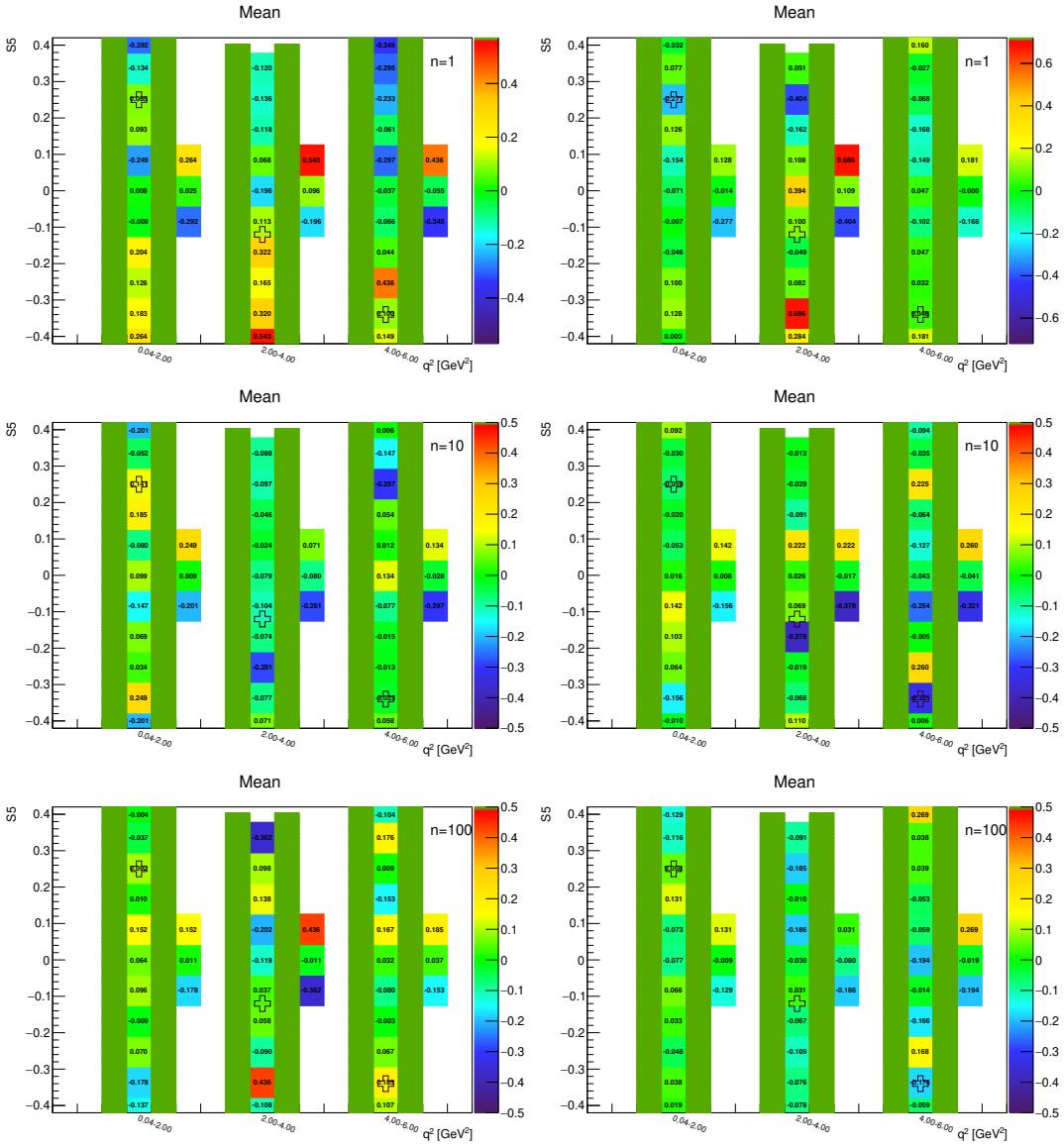

Figure A.89: Toy-MC studies of the S_5-fold, with $r = 1$. Figures show the pull mean without (left) and with acceptance (right) on the parameter S_5. The green bands represent fit-p.d.f. positivity range. The top figures correspond to the Run-1 like number of events (n = 1), while the middle and the bottom to 10× and 100× larger simulated samples.

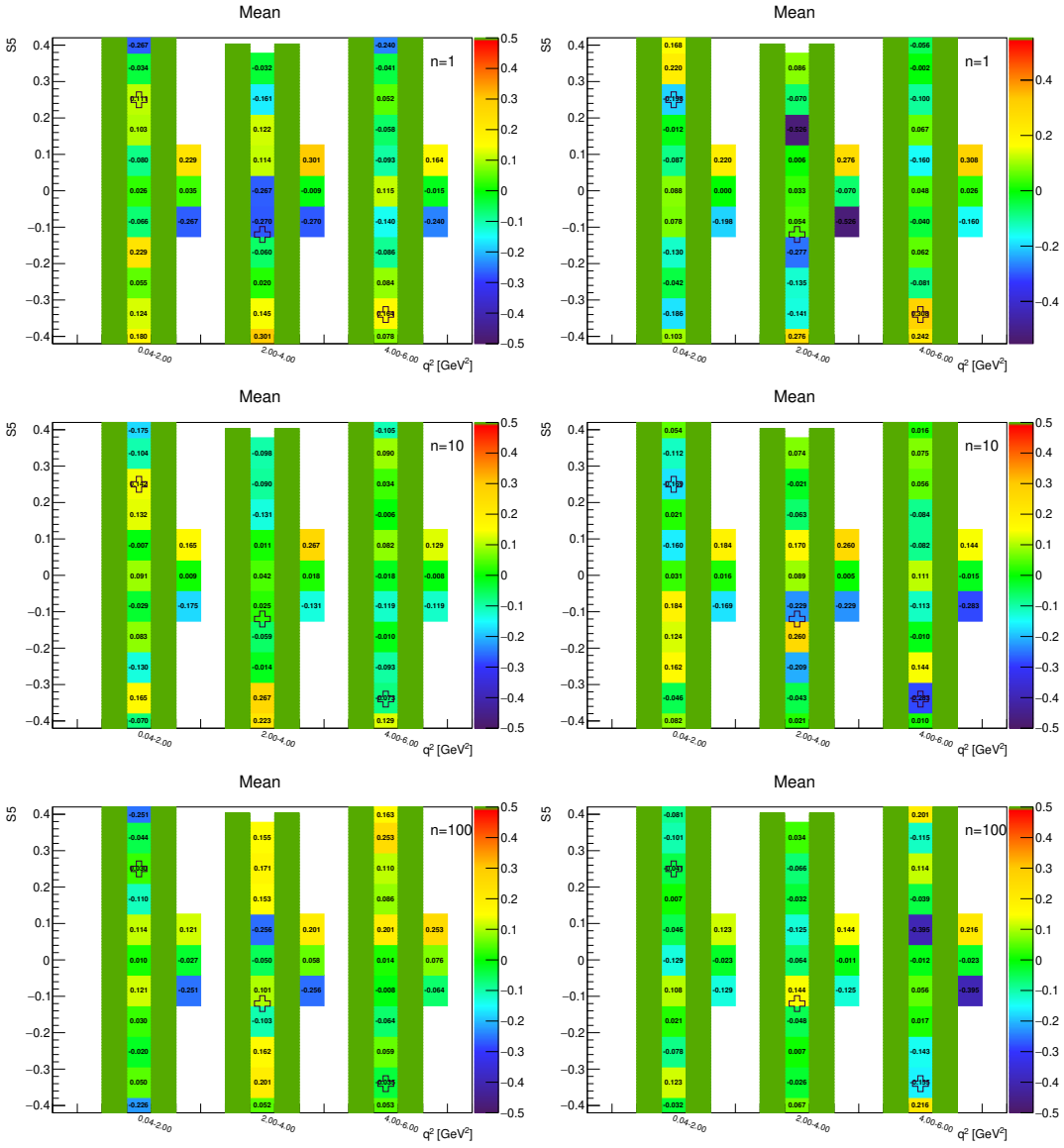

Figure A.90: Toy-MC studies of the S_5-fold, with $r = 2$. Figures show the pull mean without (left) and with acceptance (right) on the parameter S_5. The green bands represent fit-p.d.f. positivity range. The top figures correspond to the Run-1 like number of events (n = 1), while the middle and the bottom to 10× and 100× larger simulated samples.

A.4.7 S_7-fold – parameter F_L

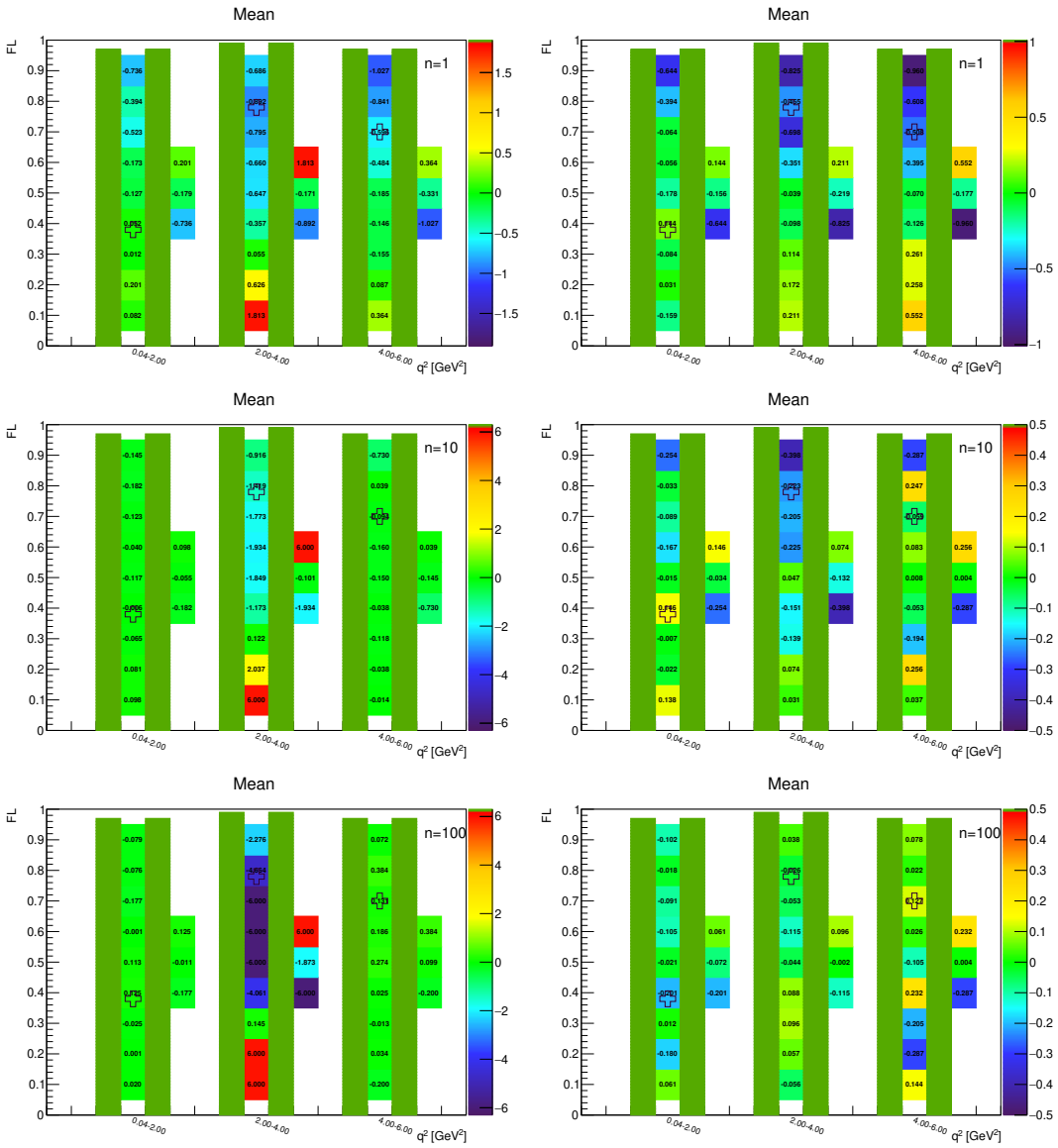

Figure A.91: Toy-MC studies of the S_7-fold, with $r = 0.5$. Figures show the pull mean without (left) and with acceptance (right) on the parameter F_L. The green bands represent fit-p.d.f. positivity range. The top figures correspond to the Run-1 like number of events (n = 1), while the middle and the bottom to 10× and 100× larger simulated samples.

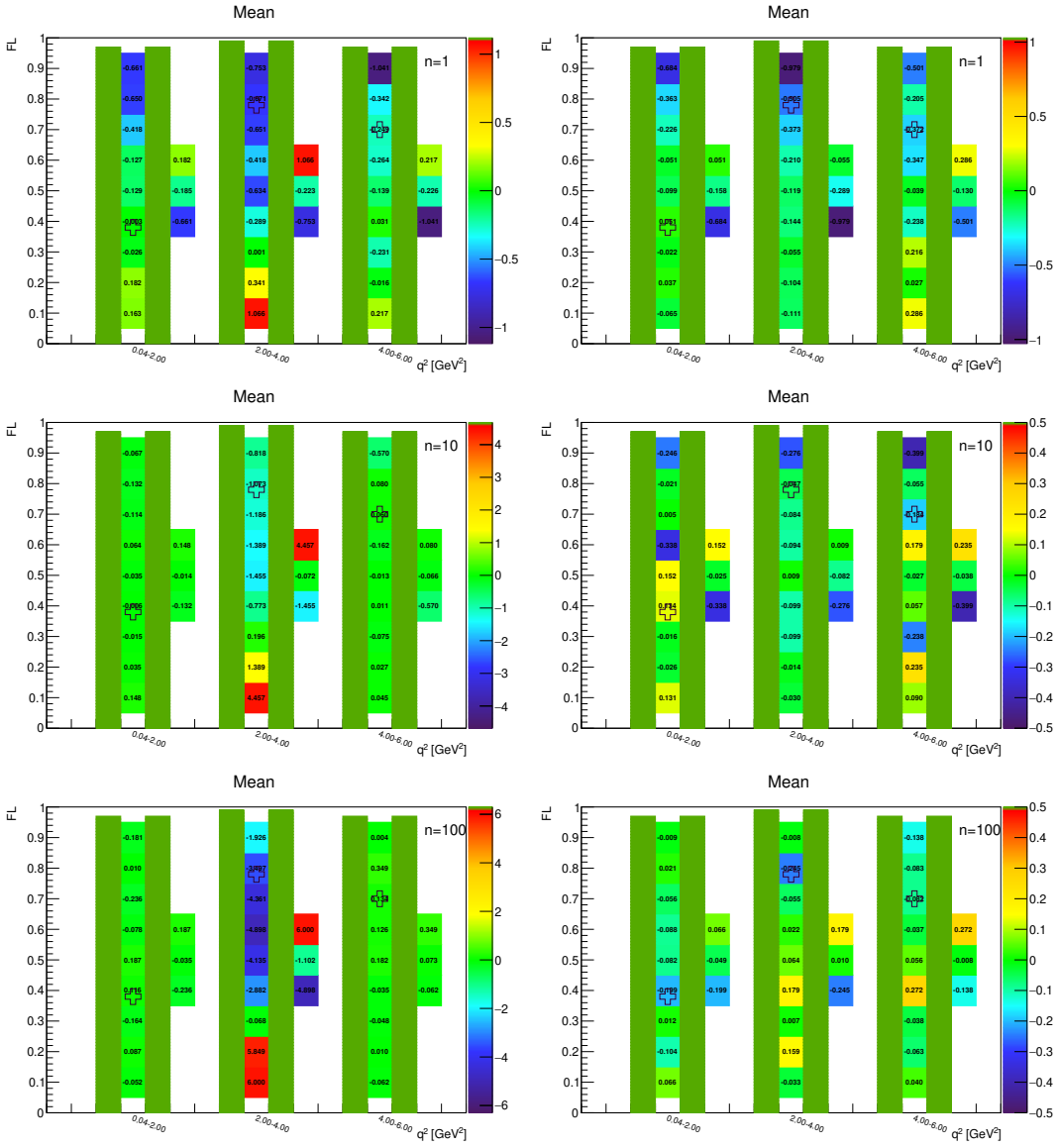

Figure A.92: Toy-MC studies of the S_7-fold, with $r = 1$. Figures show the pull mean without (left) and with acceptance (right) on the parameter F_L. The green bands represent fit-p.d.f. positivity range. The top figures correspond to the Run-1 like number of events (n = 1), while the middle and the bottom to 10× and 100× larger simulated samples.

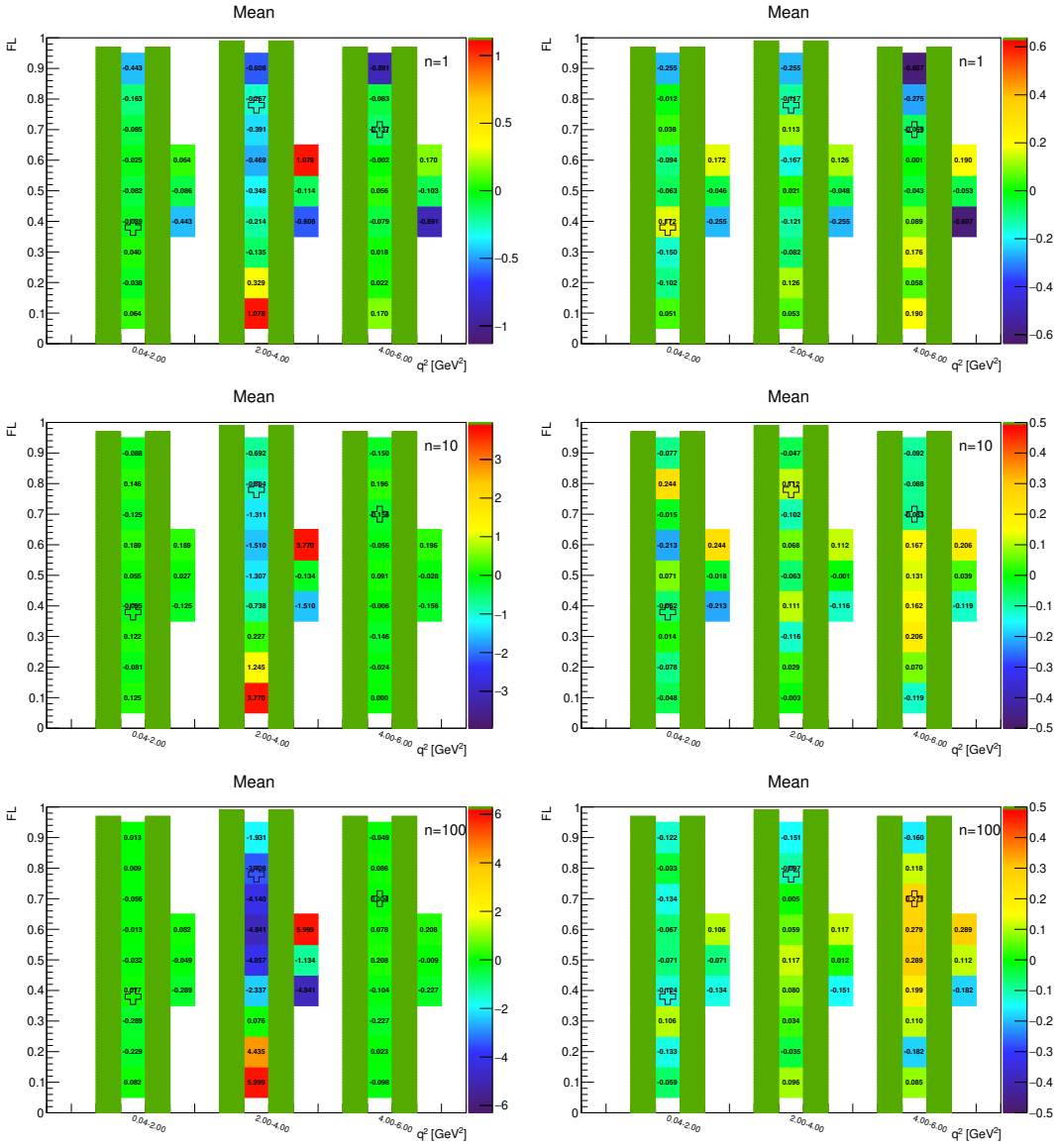

Figure A.93: Toy-MC studies of the S_7-fold, with $r = 2$. Figures show the pull mean without (left) and with acceptance (right) on the parameter F_L. The green bands represent fit-p.d.f. positivity range. The top figures correspond to the Run-1 like number of events (n = 1), while the middle and the bottom to 10× and 100× larger simulated samples.

A.4.8 S_7-fold – parameter S_3

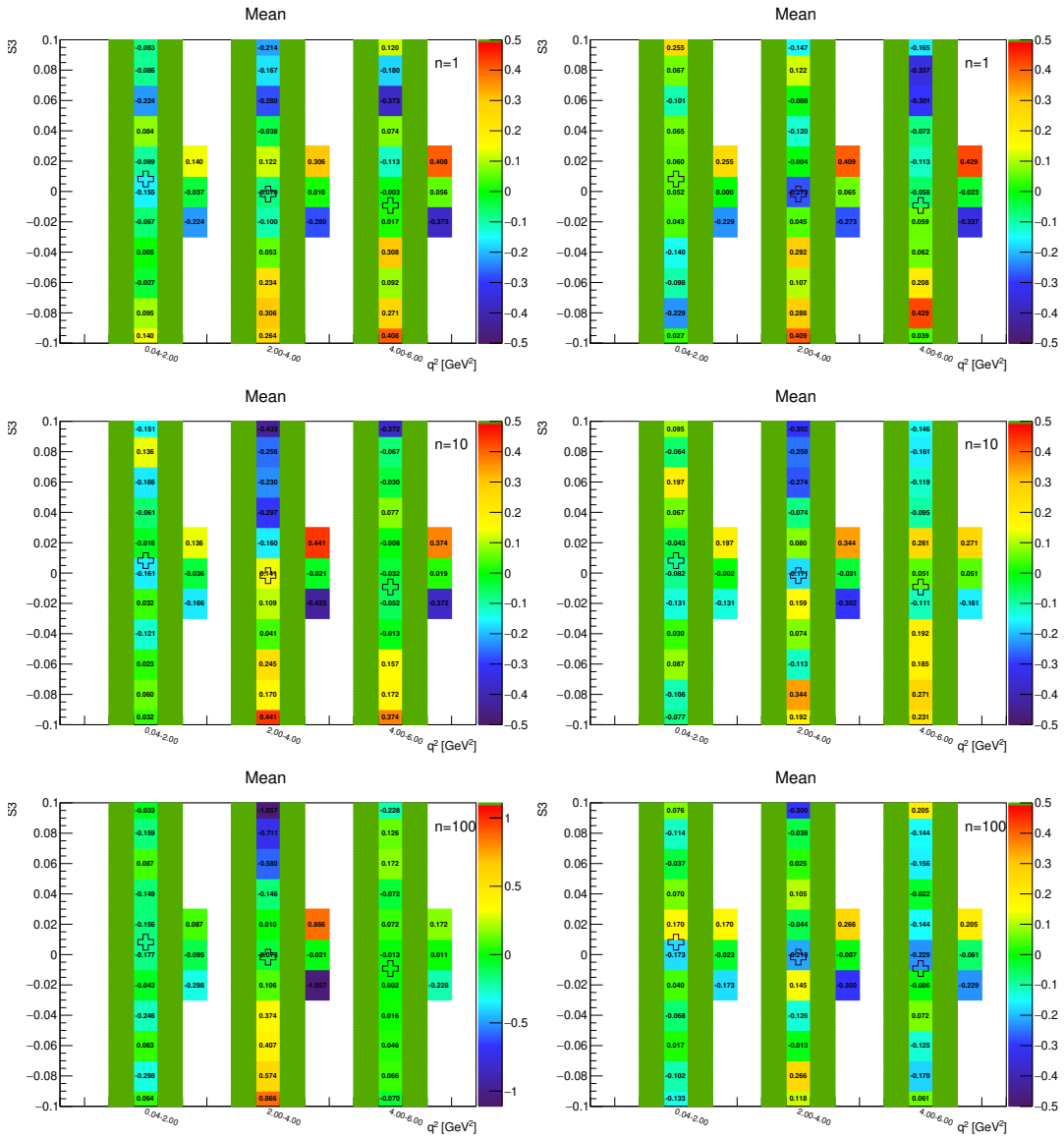

Figure A.94: Toy-MC studies of the S_7-fold, with $r = 0.5$. Figures show the pull mean without (left) and with acceptance (right) on the parameter S_3. The green bands represent fit-p.d.f. positivity range. The top figures correspond to the Run-1 like number of events (n = 1), while the middle and the bottom to 10× and 100× larger simulated samples.

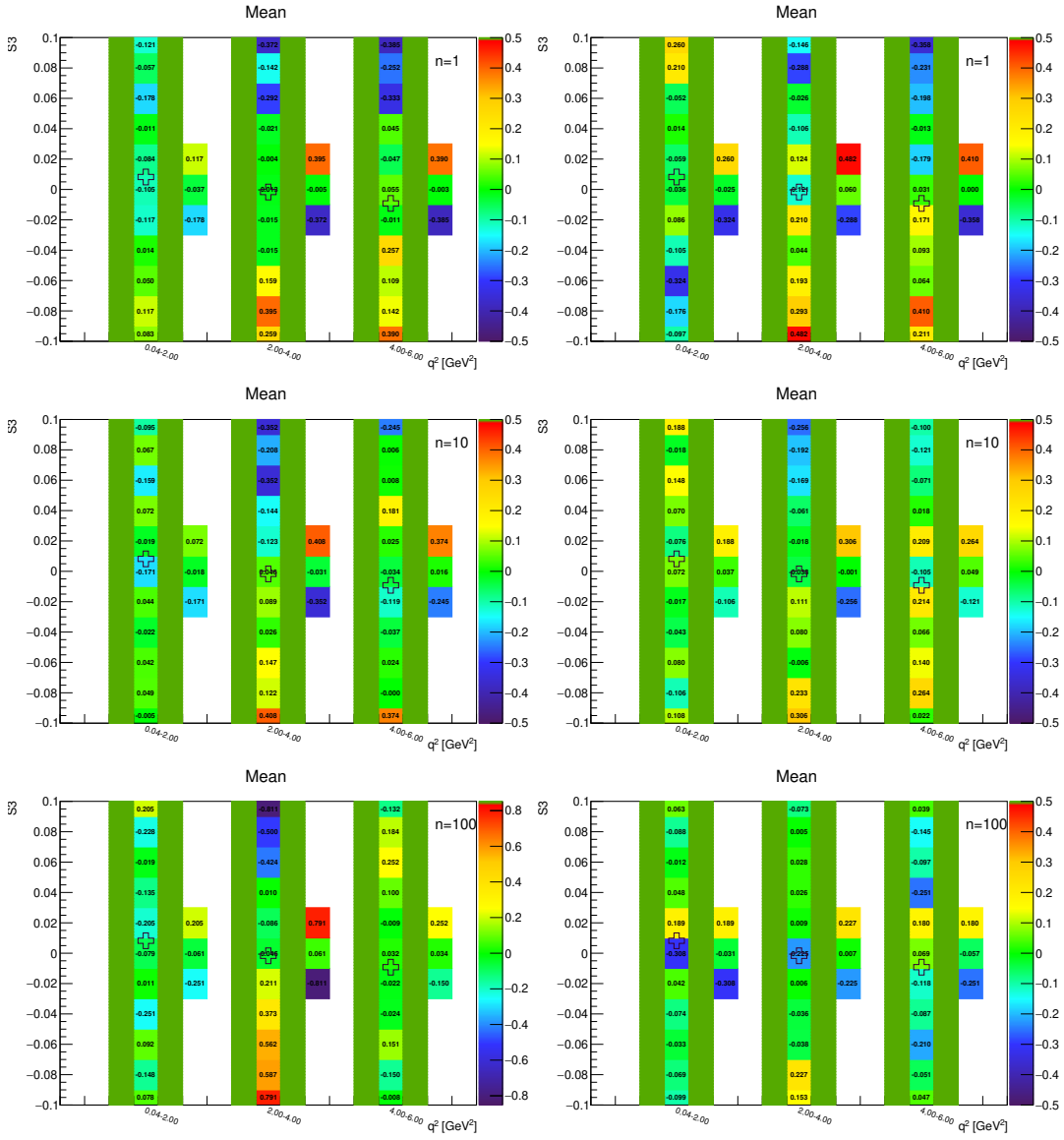

Figure A.95: Toy-MC studies of the S_7-fold, with $r = 1$. Figures show the pull mean without (left) and with acceptance (right) on the parameter S_3. The green bands represent fit-p.d.f. positivity range. The top figures correspond to the Run-1 like number of events (n = 1), while the middle and the bottom to 10× and 100× larger simulated samples.

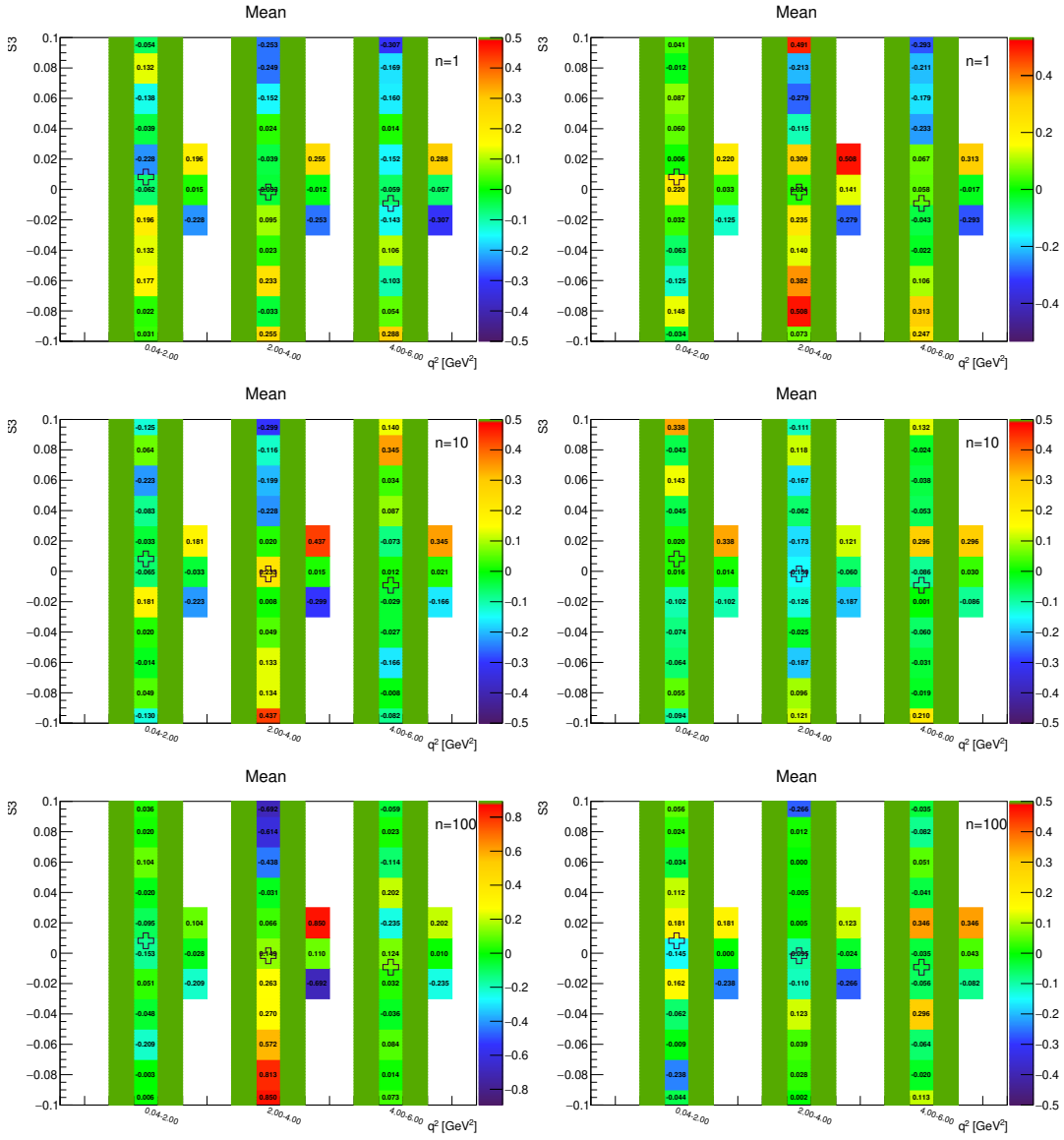

Figure A.96: Toy-MC studies of the S_7-fold, with $r = 2$. Figures show the pull mean without (left) and with acceptance (right) on the parameter S_3. The green bands represent fit-p.d.f. positivity range. The top figures correspond to the Run-1 like number of events (n = 1), while the middle and the bottom to 10× and 100× larger simulated samples.

A.4.9 S_7-fold – parameter S_7

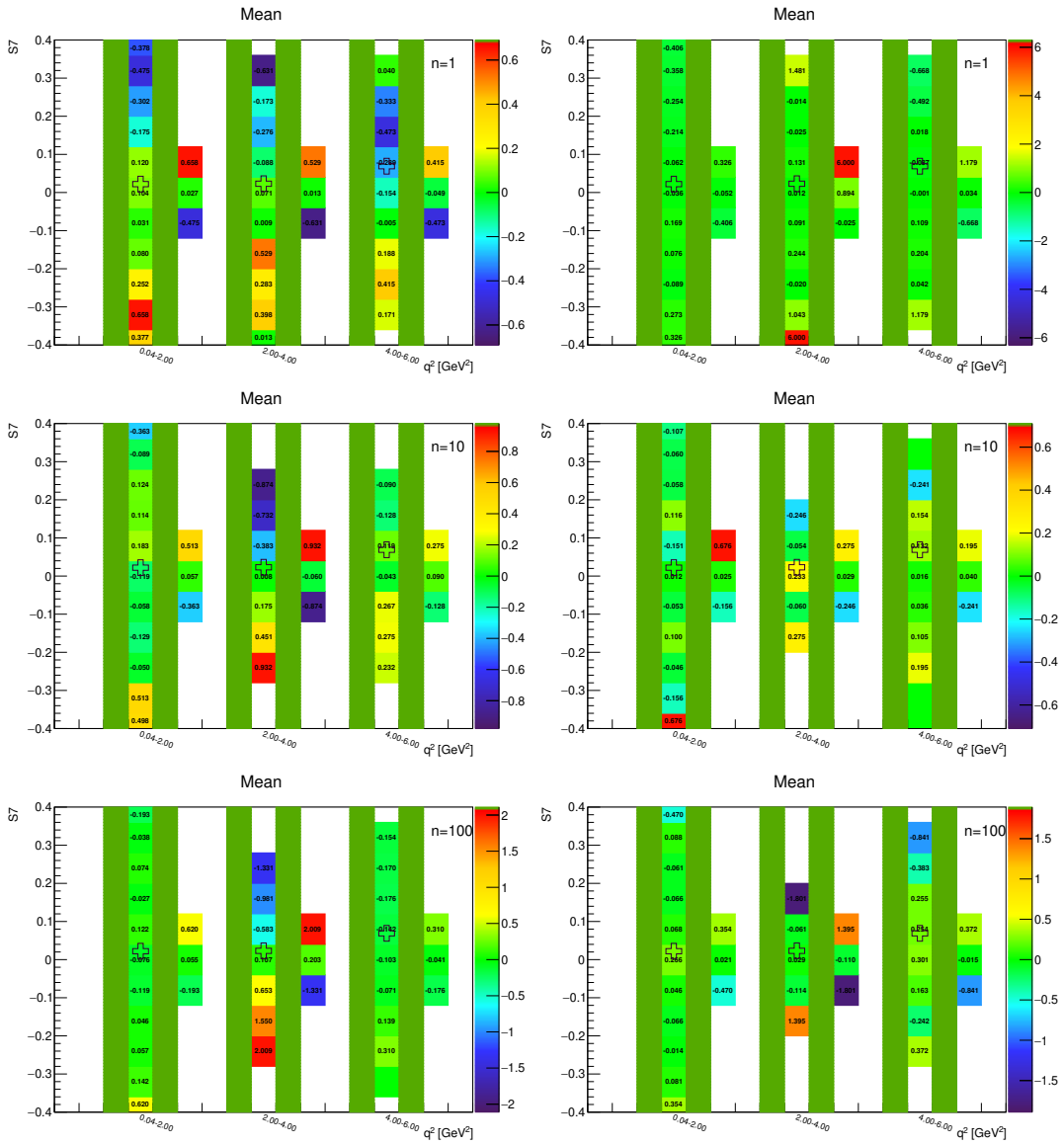

Figure A.97: Toy-MC studies of the S_7-fold, with $r = 0.5$. Figures show the pull mean without (left) and with acceptance (right) on the parameter S_7. The green bands represent fit-p.d.f. positivity range. The top figures correspond to the Run-1 like number of events (n = 1), while the middle and the bottom to 10× and 100× larger simulated samples.

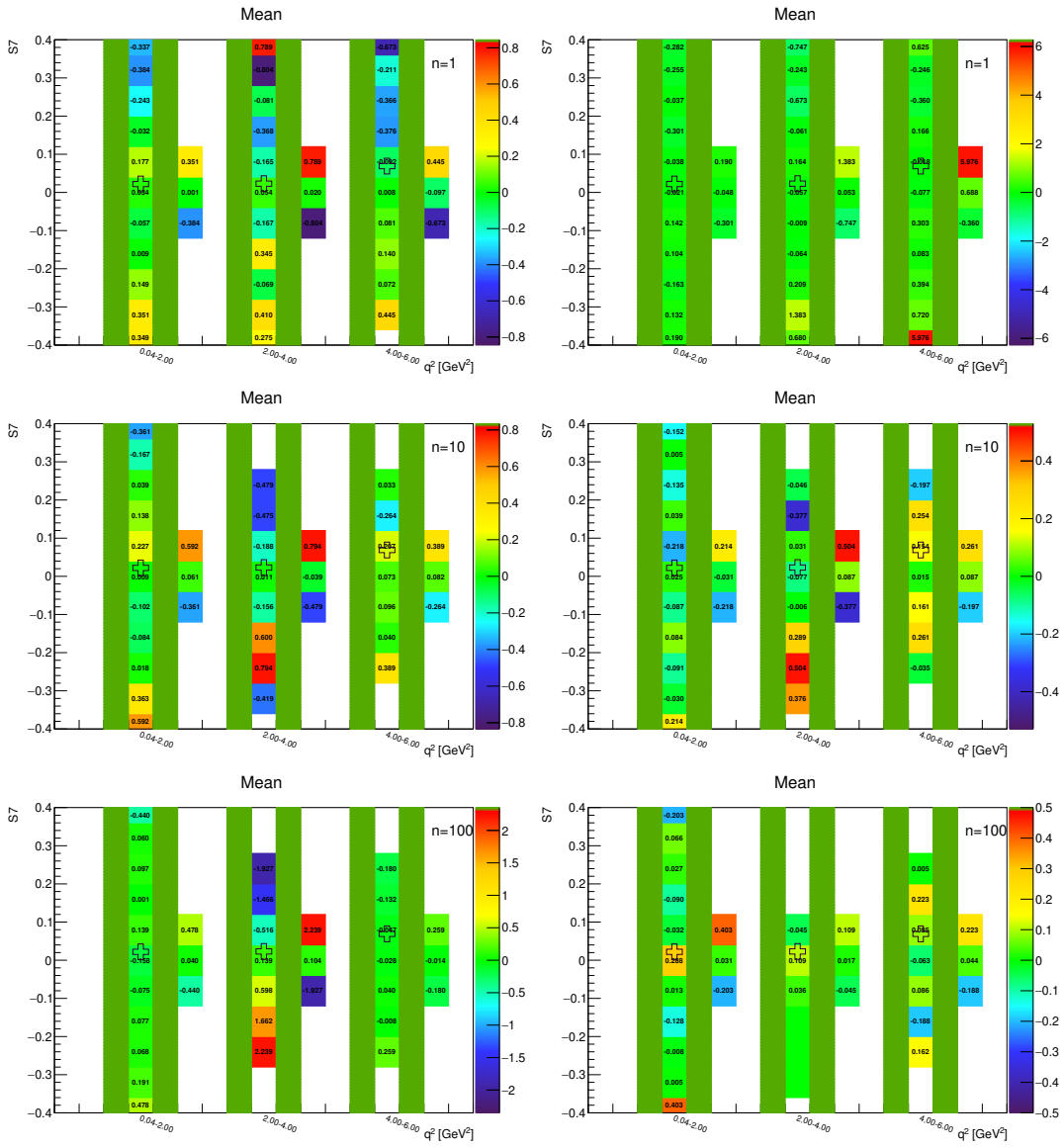

Figure A.98: Toy-MC studies of the S_7-fold, with $r = 1$. Figures show the pull mean without (left) and with acceptance (right) on the parameter S_7. The green bands represent fit-p.d.f. positivity range. The top figures correspond to the Run-1 like number of events (n = 1), while the middle and the bottom to 10× and 100× larger simulated samples.

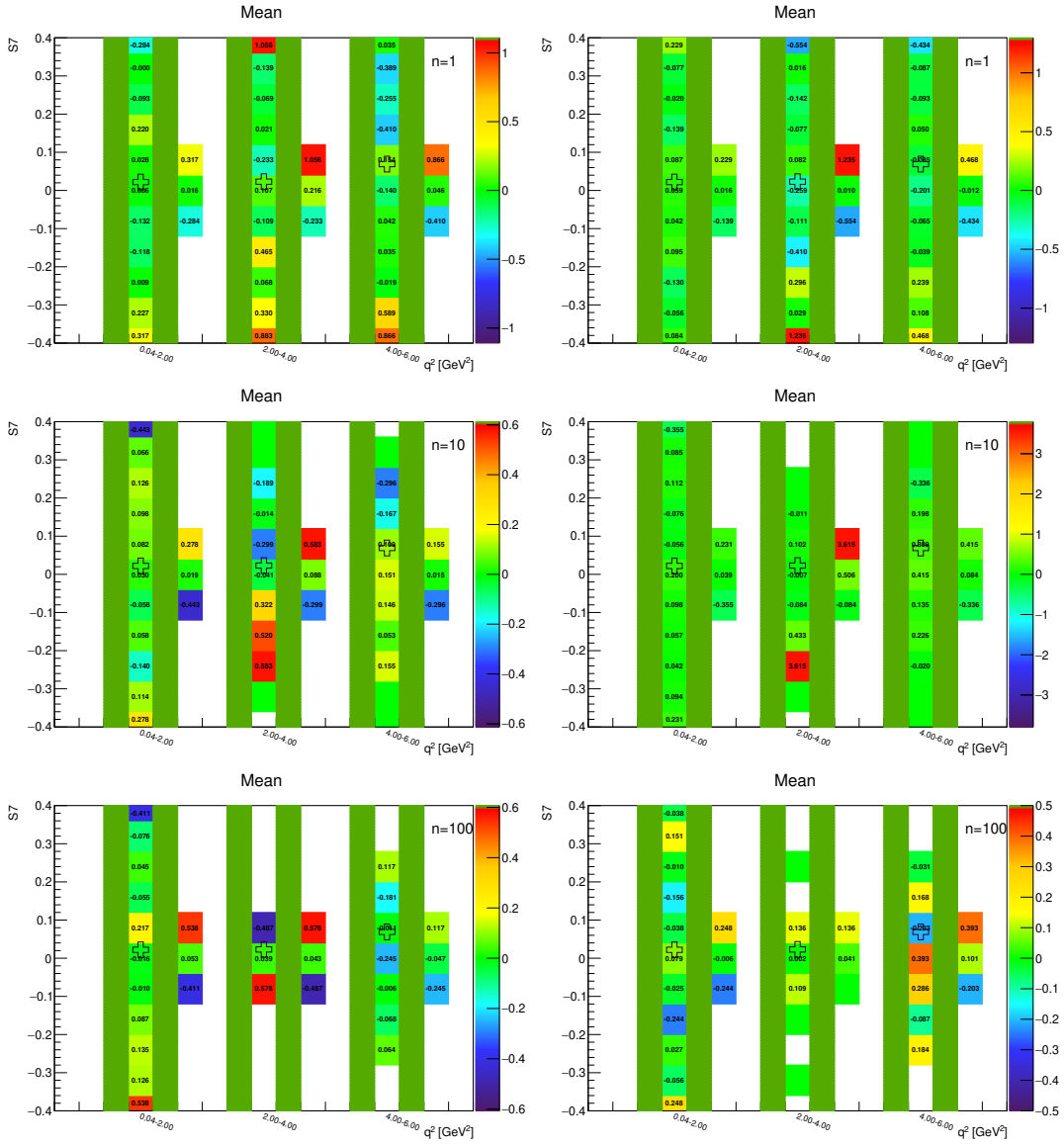

Figure A.99: Toy-MC studies of the S_7-fold, with $r = 2$. Figures show the pull mean without (left) and with acceptance (right) on the parameter S_7. The green bands represent fit-p.d.f. positivity range. The top figures correspond to the Run-1 like number of events (n = 1), while the middle and the bottom to 10× and 100× larger simulated samples.

A.4.10 S_8-fold – parameter F_L

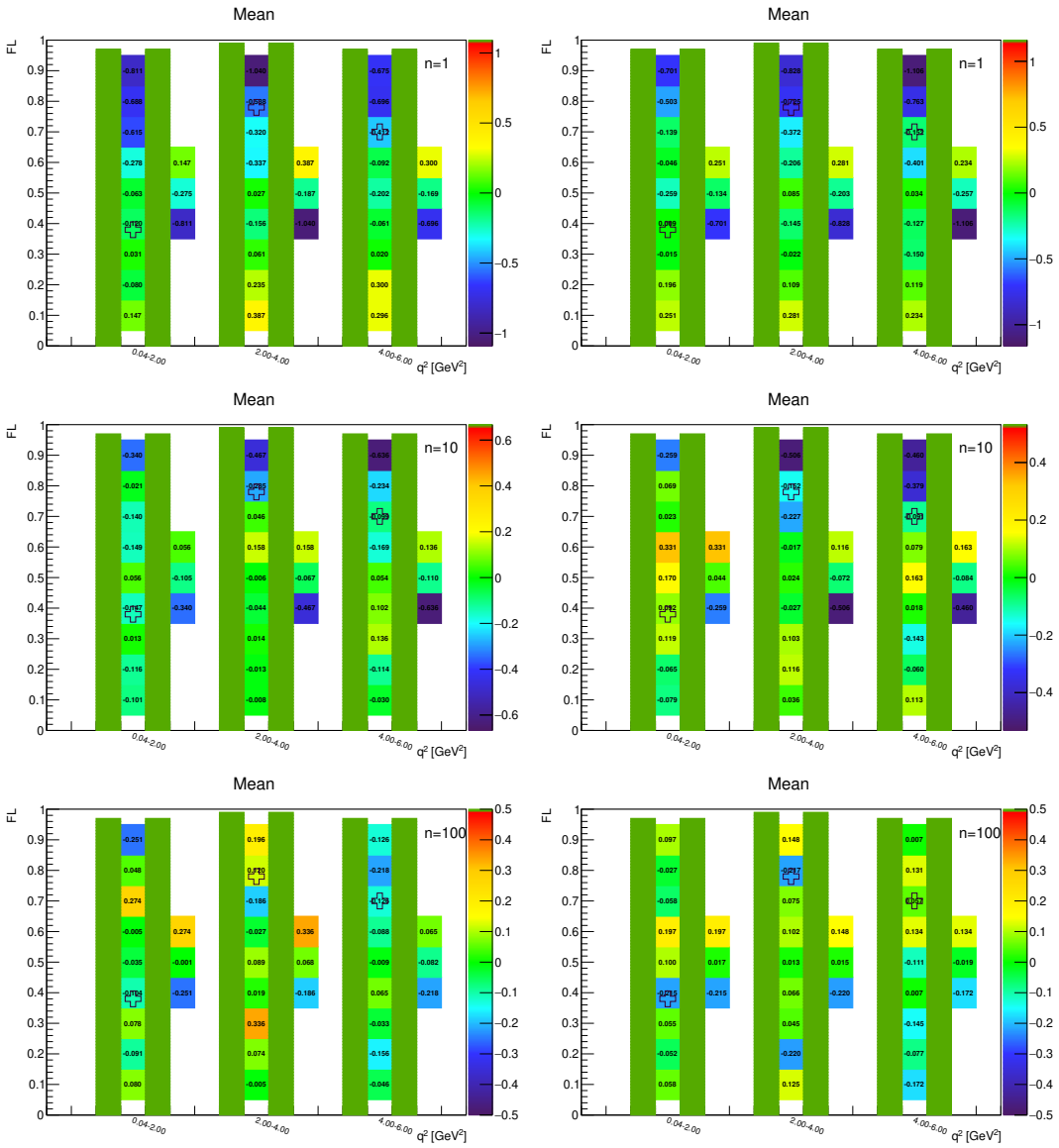

Figure A.100: Toy-MC studies of the S_8-fold, with $r = 0.5$. Figures show the pull mean without (left) and with acceptance (right) on the parameter F_L. The green bands represent fit-p.d.f. positivity range. The top figures correspond to the Run-1 like number of events (n = 1), while the middle and the bottom to 10× and 100× larger simulated samples.

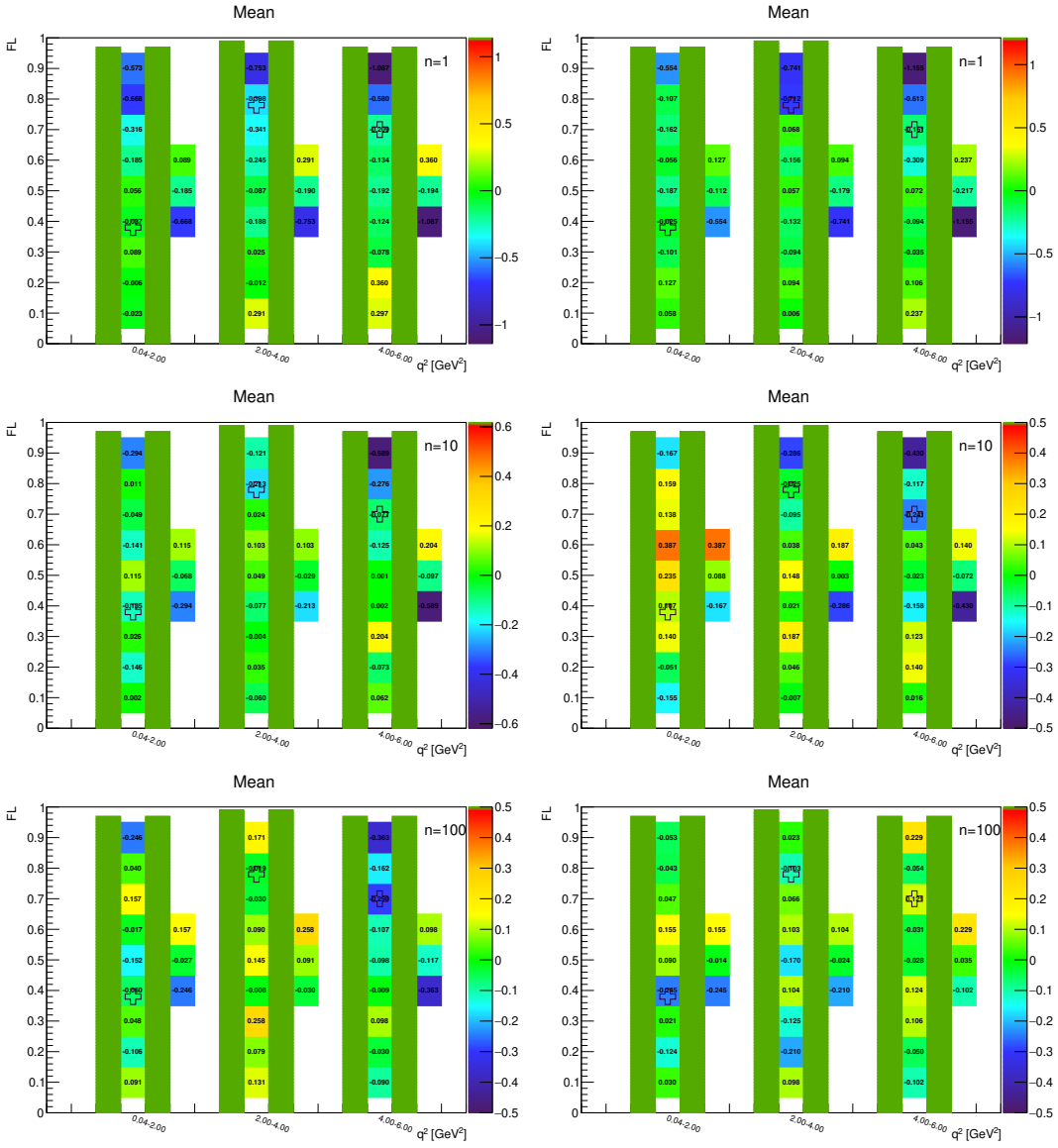

Figure A.101: Toy-MC studies of the S_8-fold, with $r = 1$. Figures show the pull mean without (left) and with acceptance (right) on the parameter F_L. The green bands represent fit-p.d.f. positivity range. The top figures correspond to the Run-1 like number of events (n = 1), while the middle and the bottom to 10× and 100× larger simulated samples.

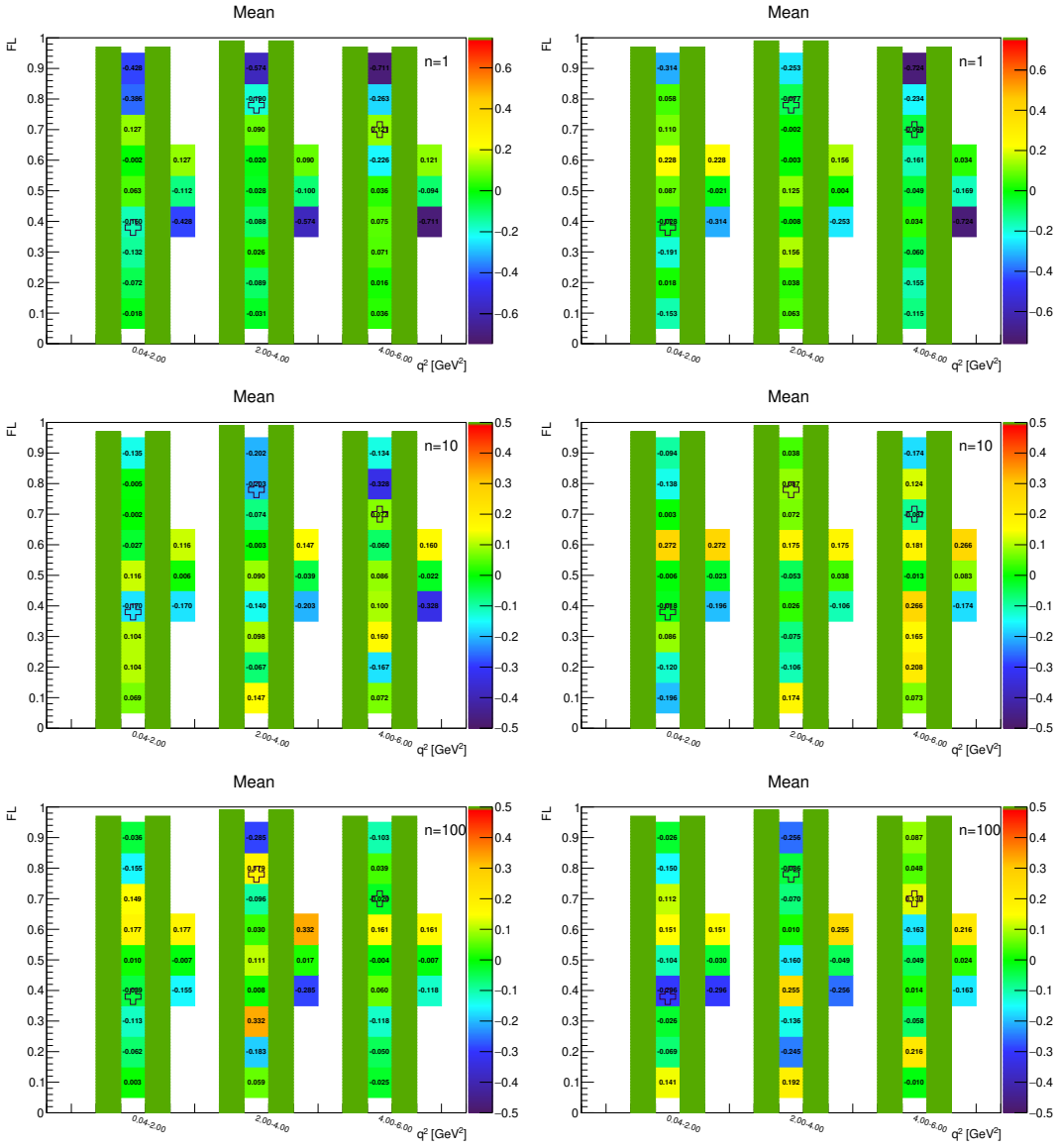

Figure A.102: Toy-MC studies of the S_8-fold, with $r = 2$. Figures show the pull mean without (left) and with acceptance (right) on the parameter F_L. The green bands represent fit-p.d.f. positivity range. The top figures correspond to the Run-1 like number of events (n = 1), while the middle and the bottom to 10× and 100× larger simulated samples.

A.4.11 S_8-fold – parameter S_3

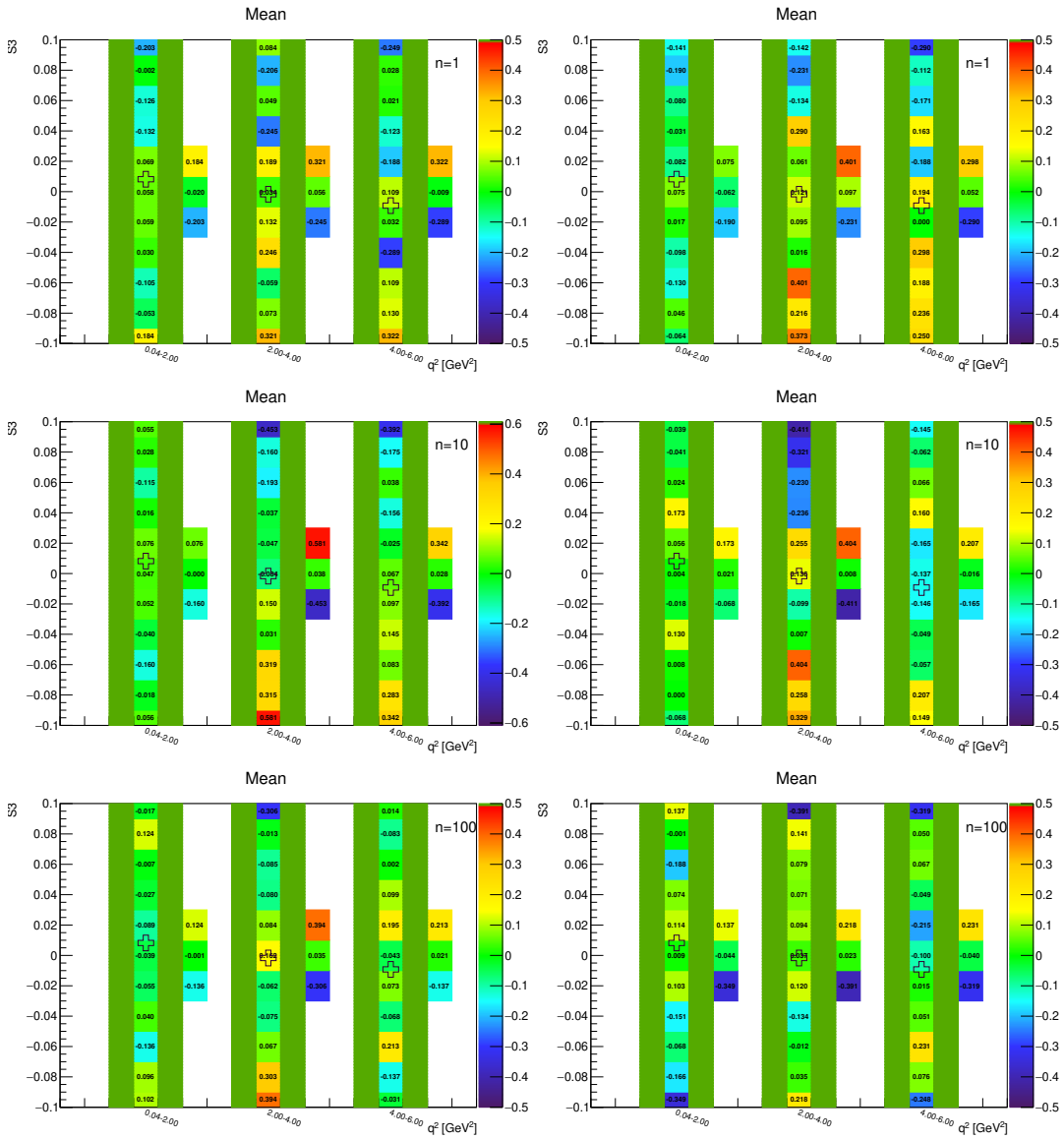

Figure A.103: Toy-MC studies of the S_8-fold, with $r = 0.5$. Figures show the pull mean without (left) and with acceptance (right) on the parameter S_3. The green bands represent fit-p.d.f. positivity range. The top figures correspond to the Run-1 like number of events (n = 1), while the middle and the bottom to 10× and 100× larger simulated samples.

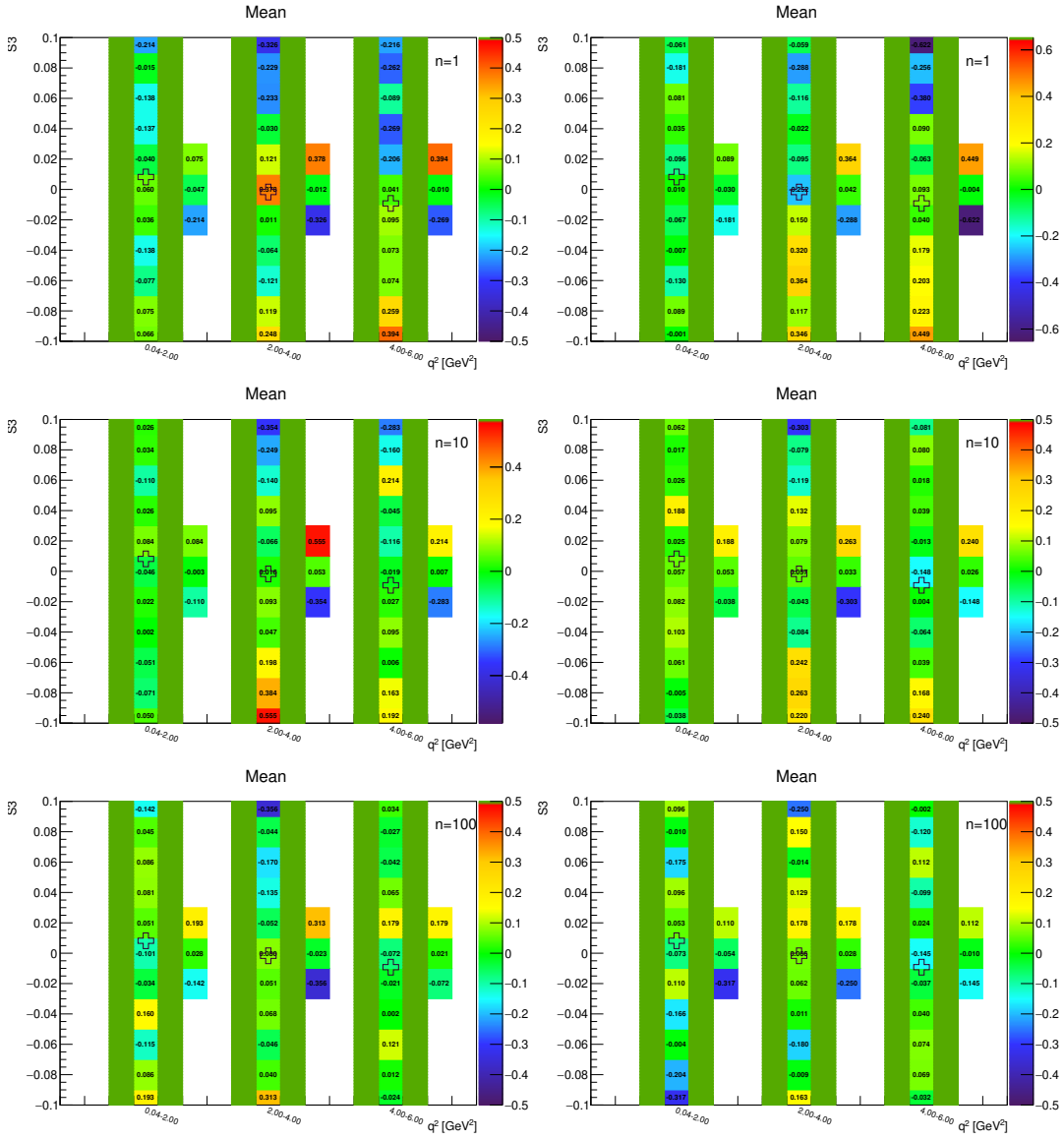

Figure A.104: Toy-MC studies of the S_8-fold, with $r = 1$. Figures show the pull mean without (left) and with acceptance (right) on the parameter S_3. The green bands represent fit-p.d.f. positivity range. The top figures correspond to the Run-1 like number of events (n = 1), while the middle and the bottom to 10× and 100× larger simulated samples.

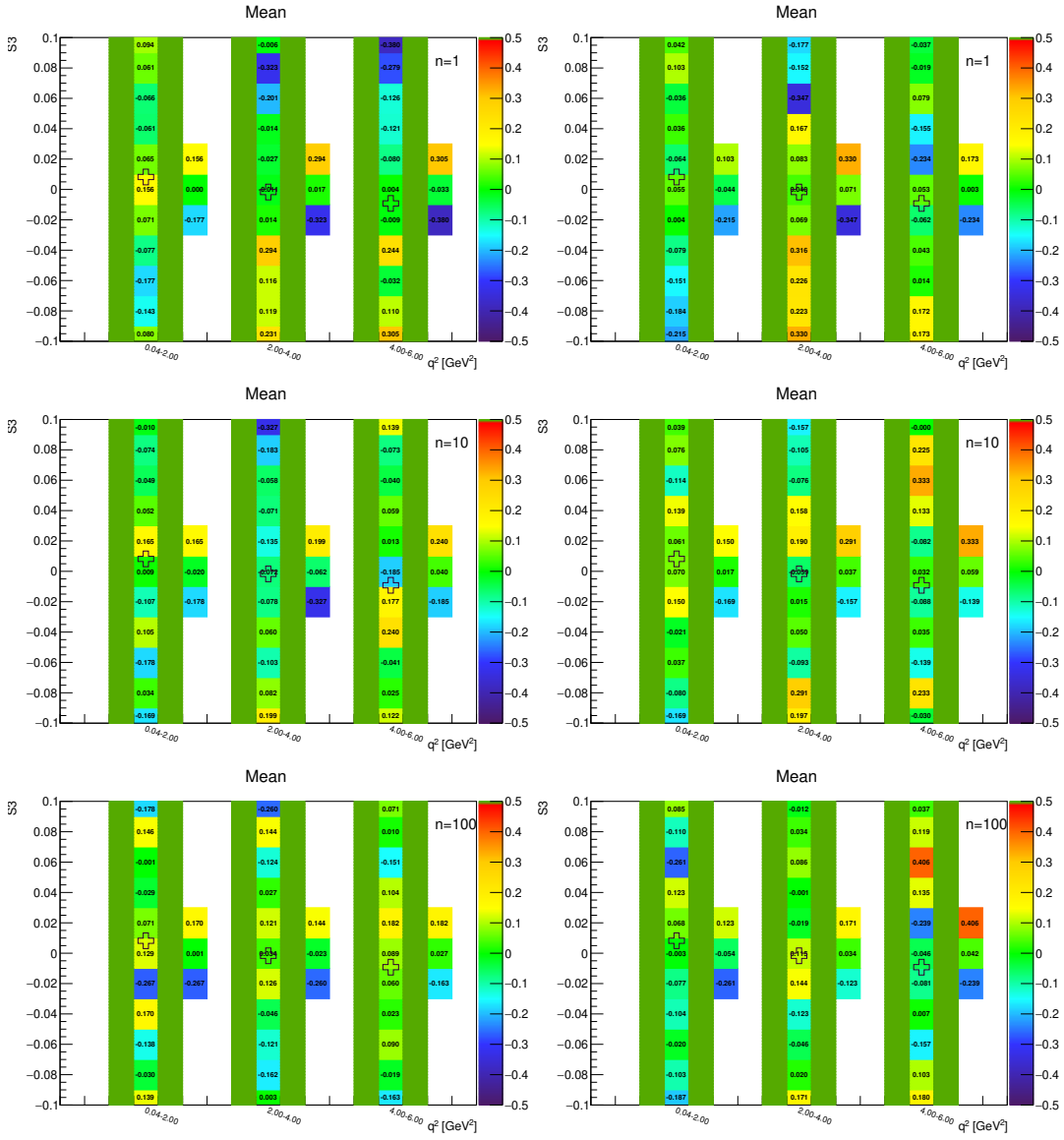

Figure A.105: Toy-MC studies of the S_8-fold, with $r = 2$. Figures show the pull mean without (left) and with acceptance (right) on the parameter S_3. The green bands represent fit-p.d.f. positivity range. The top figures correspond to the Run-1 like number of events (n = 1), while the middle and the bottom to 10× and 100× larger simulated samples.

A.4.12 S_8-fold – parameter S_8

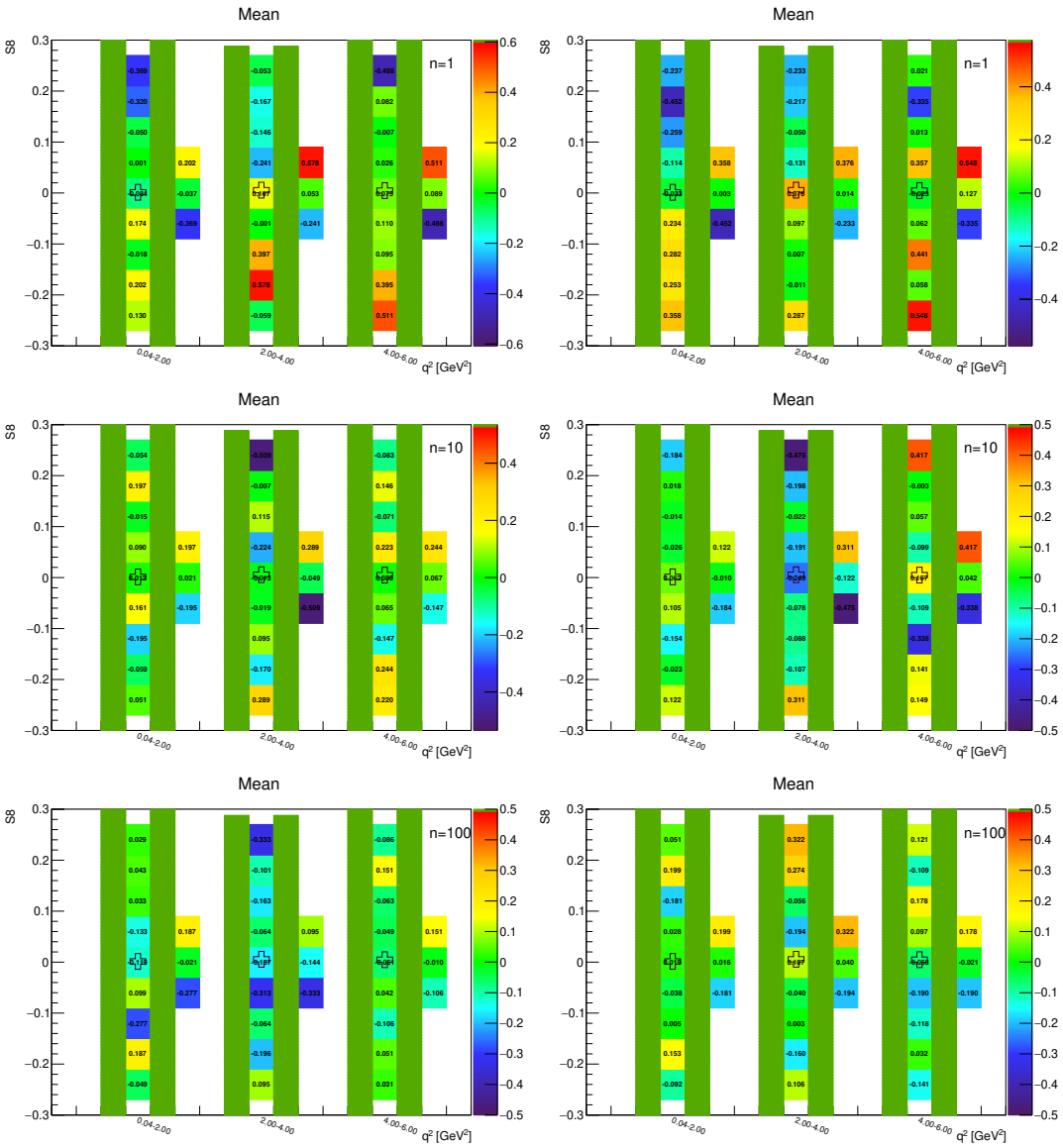

Figure A.106: Toy-MC studies of the S_8-fold, with $r = 0.5$. Figures show the pull mean without (left) and with acceptance (right) on the parameter S_8. The green bands represent fit-p.d.f. positivity range. The top figures correspond to the Run-1 like number of events (n = 1), while the middle and the bottom to 10× and 100× larger simulated samples.

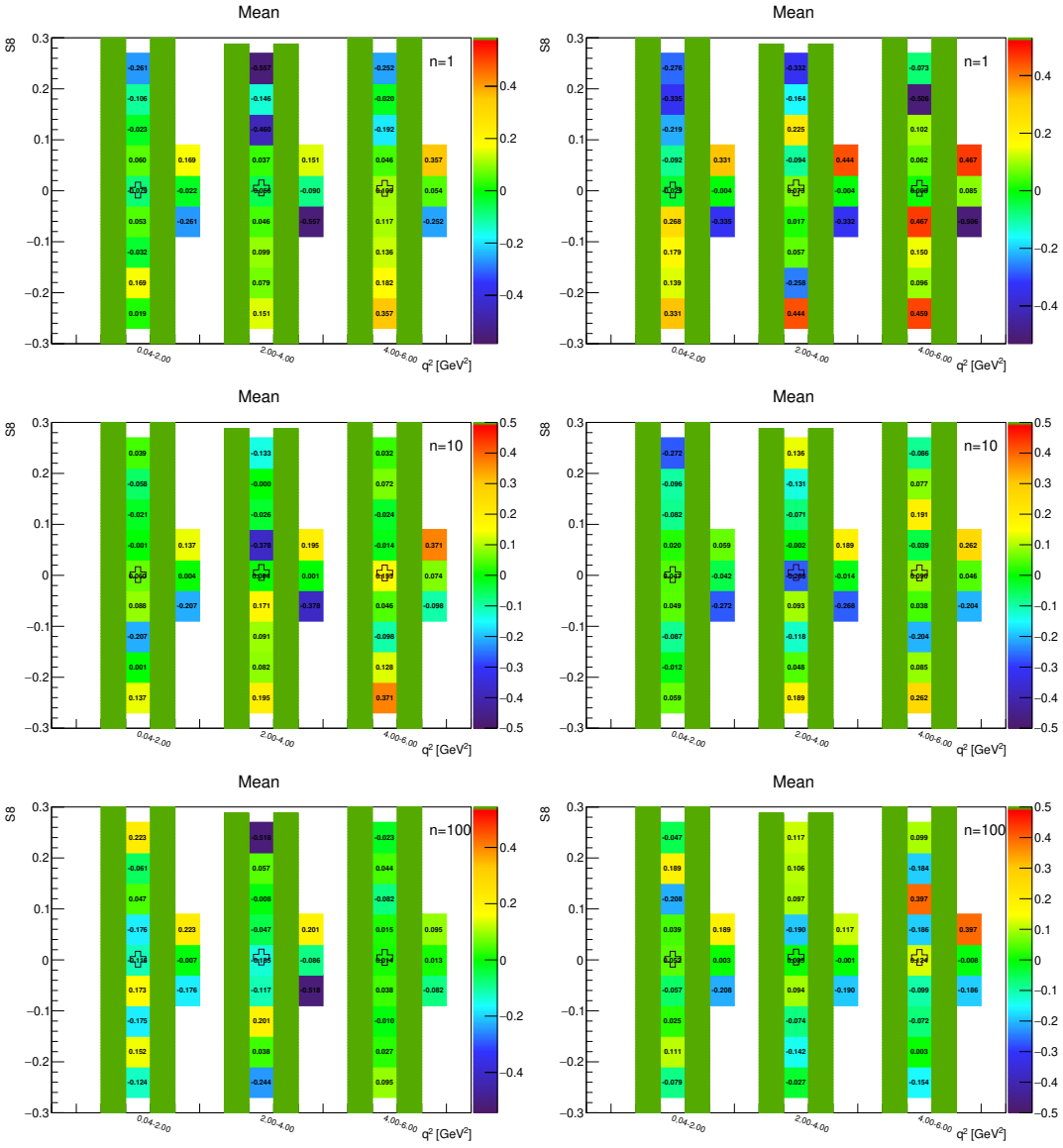

Figure A.107: Toy-MC studies of the S_8-fold, with $r = 1$. Figures show the pull mean without (left) and with acceptance (right) on the parameter S_8. The green bands represent fit-p.d.f. positivity range. The top figures correspond to the Run-1 like number of events (n = 1), while the middle and the bottom to 10× and 100× larger simulated samples.

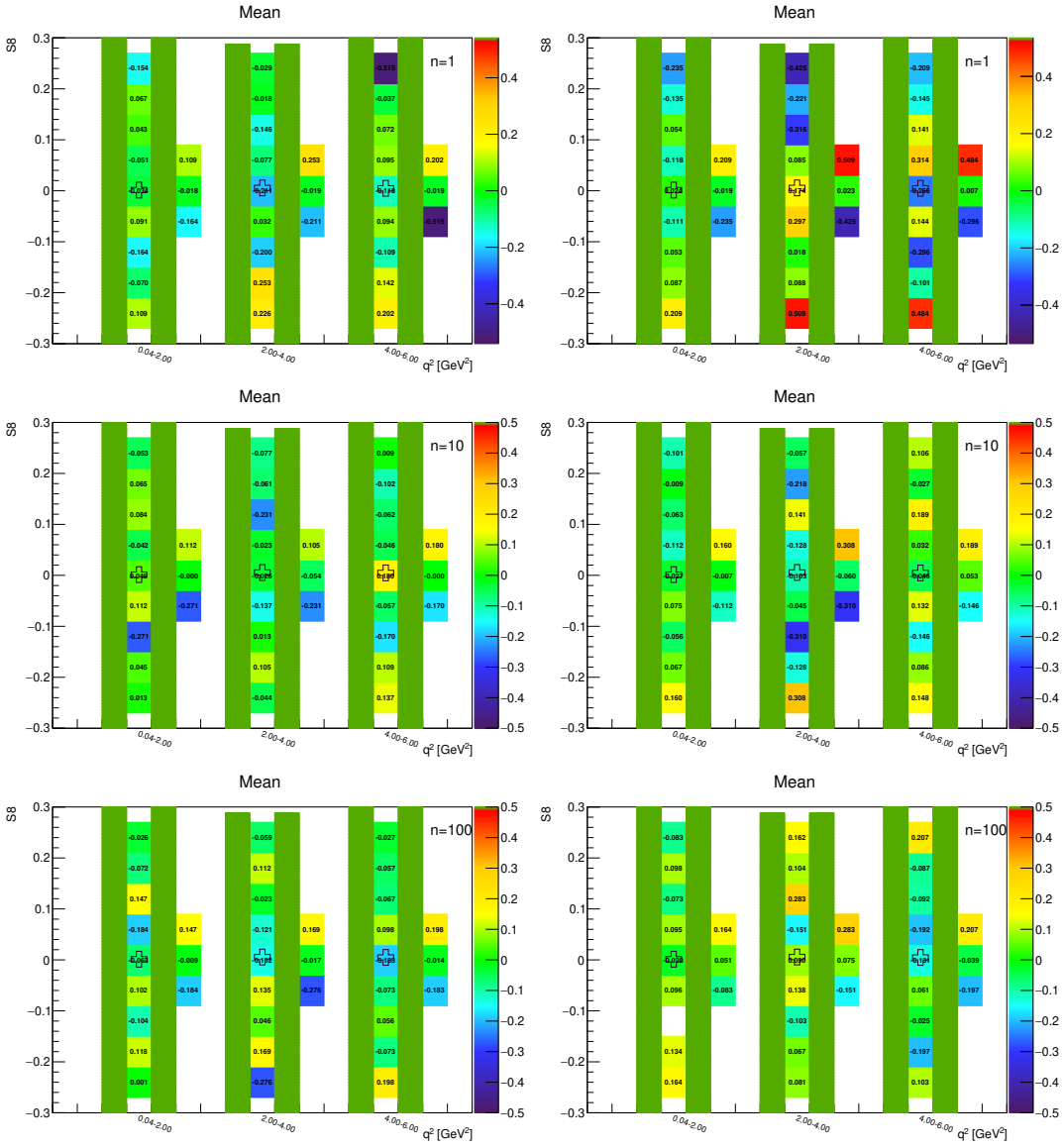

Figure A.108: Toy-MC studies of the S_8-fold, with $r = 2$. Figures show the pull mean without (left) and with acceptance (right) on the parameter S_8. The green bands represent fit-p.d.f. positivity range. The top figures correspond to the Run-1 like number of events (n = 1), while the middle and the bottom to 10× and 100× larger simulated samples.

A.5 Fit Validation – Plots of Pull RMS

A.5.1 S_4-fold – parameter F_L

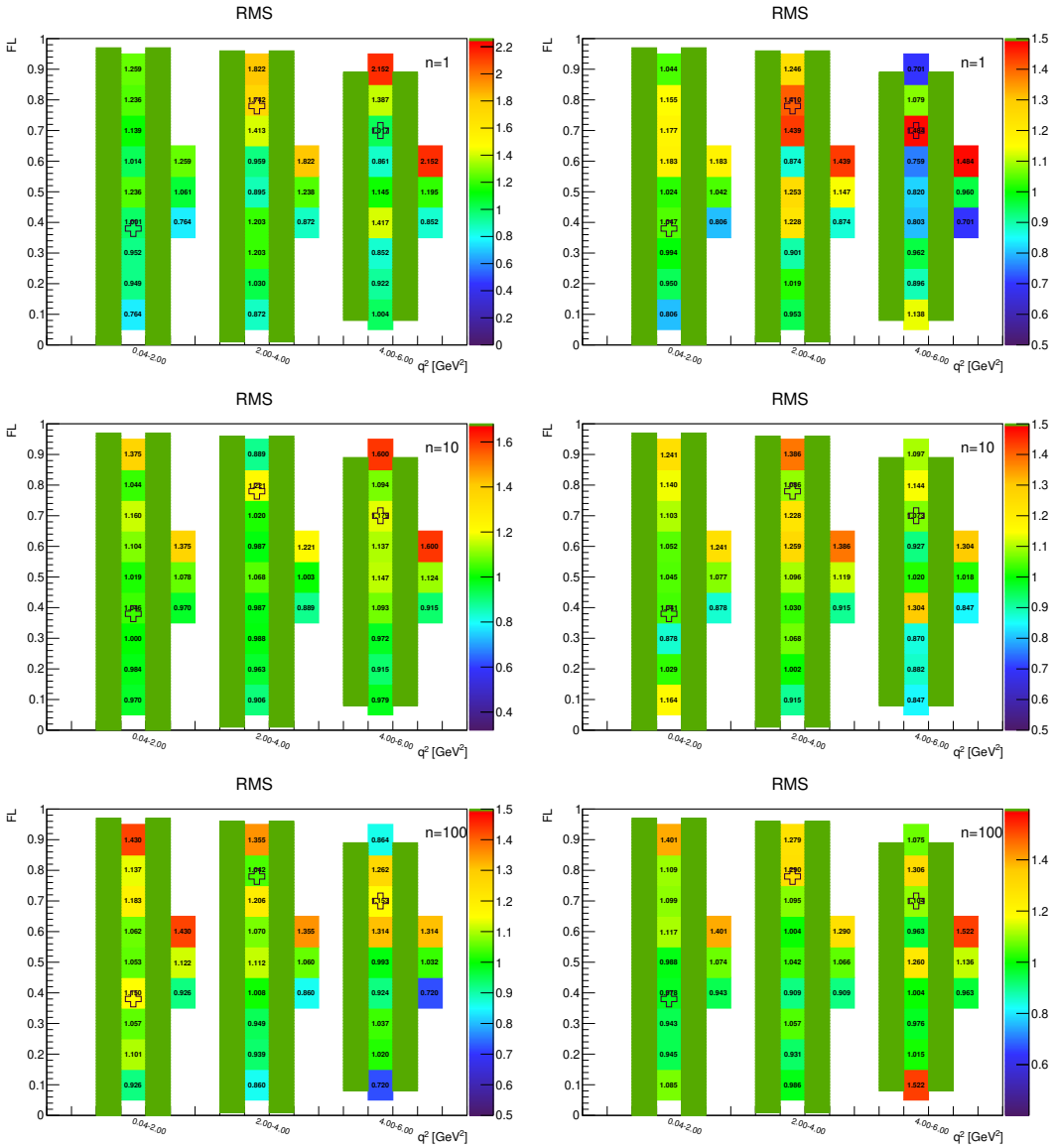

Figure A.109: Toy-MC studies of the S_4-fold, with $r = 0.5$. Figures show the pull RMS without (left) and with acceptance (right) on the parameter F_L. The green bands represent fit-p.d.f. positivity range. The top figures correspond to the Run-1 like number of events (n = 1), while the middle and the bottom to 10× and 100× larger simulated samples.

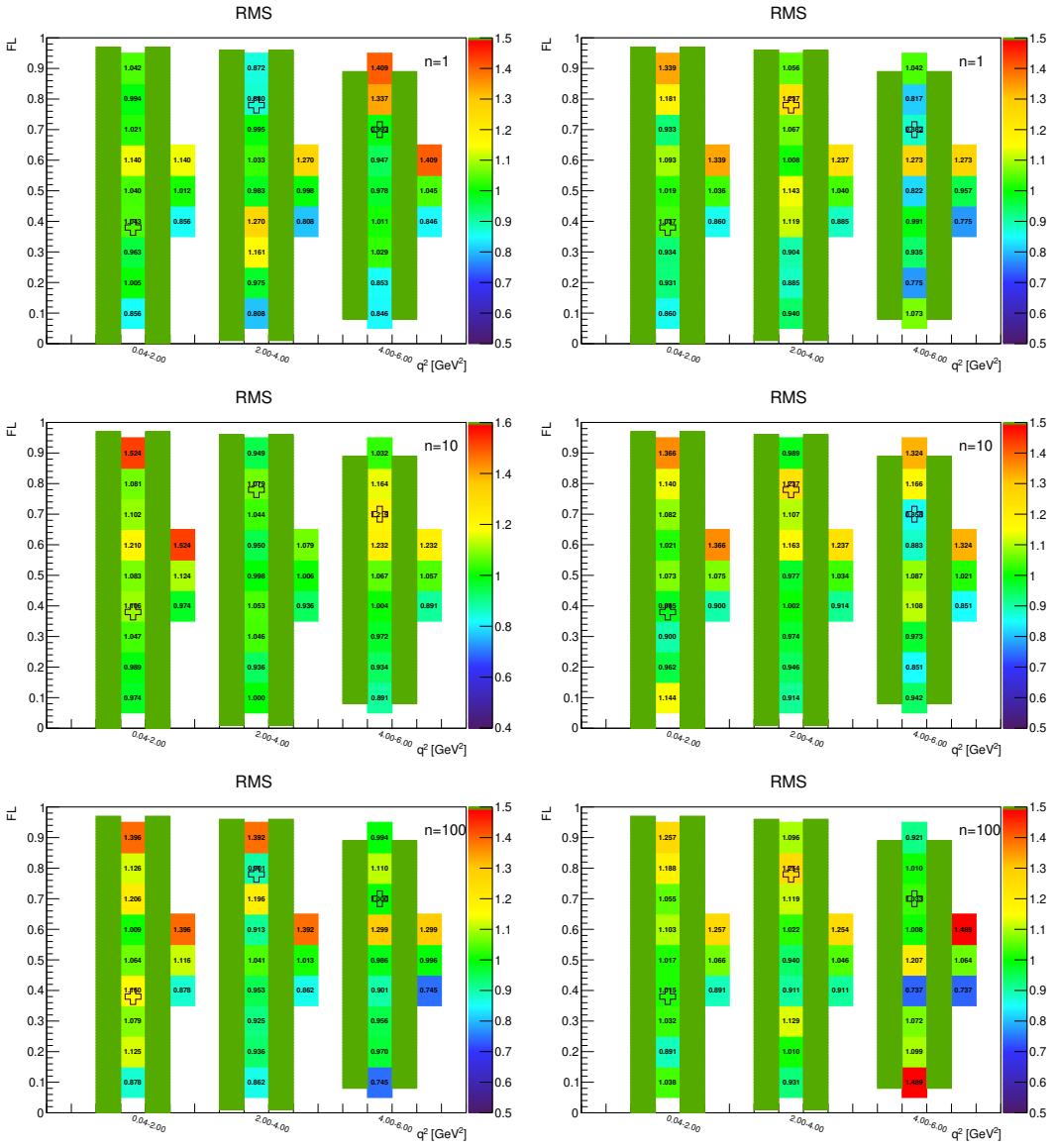

Figure A.110: Toy-MC studies of the S_4-fold, with $r = 1$. Figures show the pull RMS without (left) and with acceptance (right) on the parameter F_L. The green bands represent fit-p.d.f. positivity range. The top figures correspond to the Run-1 like number of events (n = 1), while the middle and the bottom to 10× and 100× larger simulated samples.

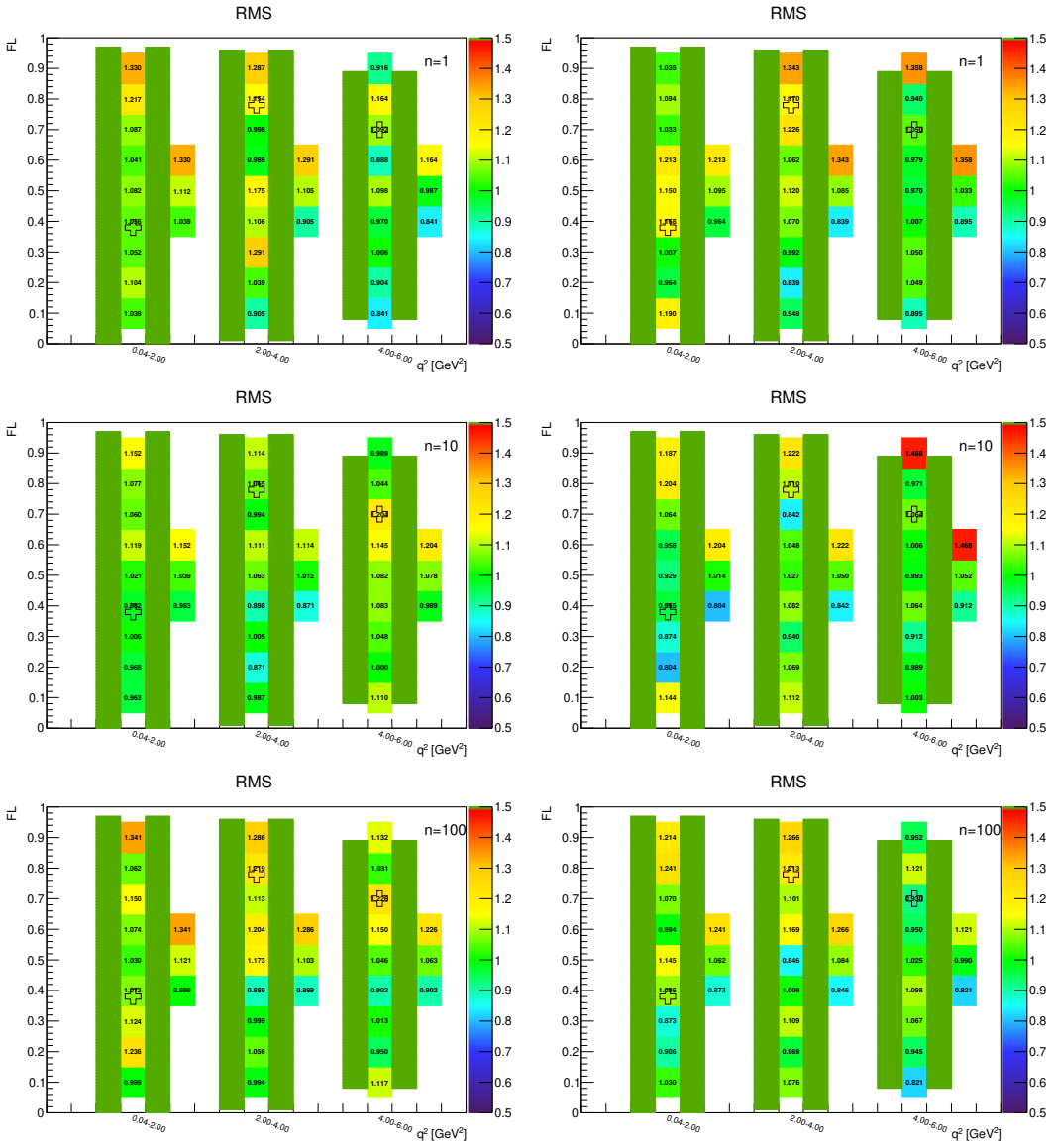

Figure A.111: Toy-MC studies of the S_4-fold, with $r = 2$. Figures show the pull RMS without (left) and with acceptance (right) on the parameter F_L. The green bands represent fit-p.d.f. positivity range. The top figures correspond to the Run-1 like number of events (n = 1), while the middle and the bottom to 10× and 100× larger simulated samples.

A.5.2 S_4-fold – parameter S_3

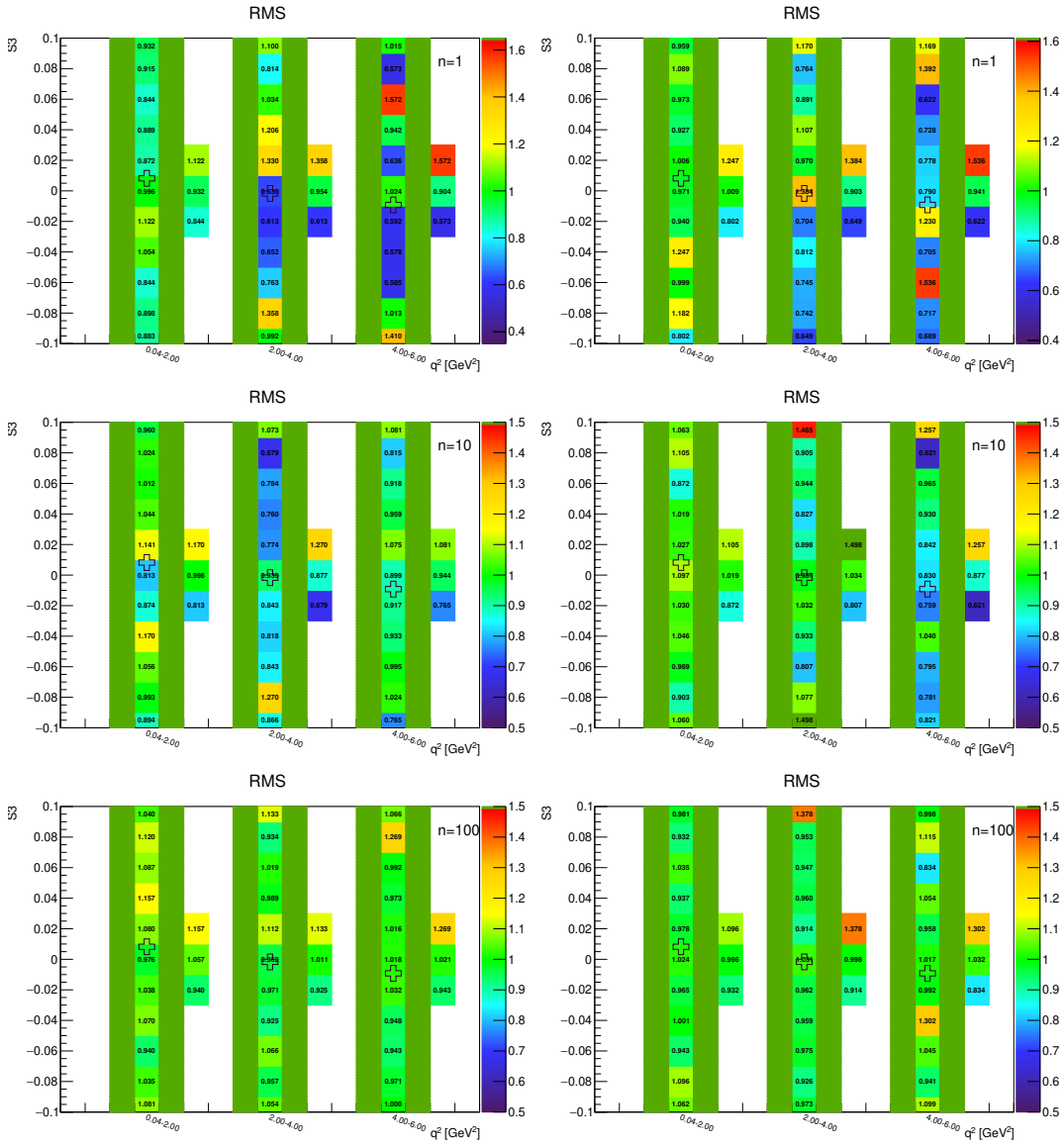

Figure A.112: Toy-MC studies of the S_4-fold, with $r = 0.5$. Figures show the pull RMS without (left) and with acceptance (right) on the parameter S_3. The green bands represent fit-p.d.f. positivity range. The top figures correspond to the Run-1 like number of events (n = 1), while the middle and the bottom to 10× and 100× larger simulated samples.

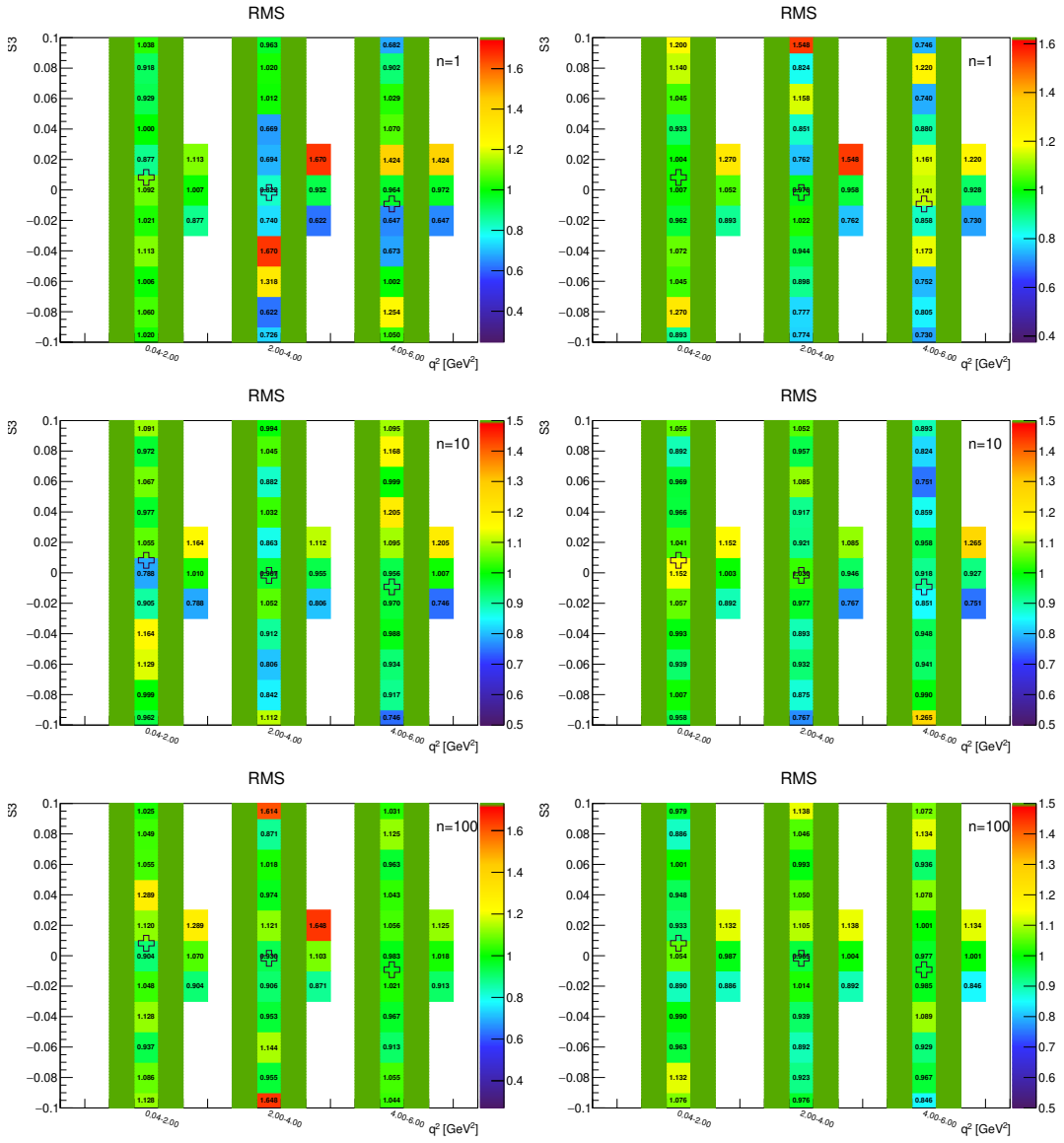

Figure A.113: Toy-MC studies of the S_4-fold, with $r = 1$. Figures show the pull RMS without (left) and with acceptance (right) on the parameter S_3. The green bands represent fit-p.d.f. positivity range. The top figures correspond to the Run-1 like number of events (n = 1), while the middle and the bottom to 10× and 100× larger simulated samples.

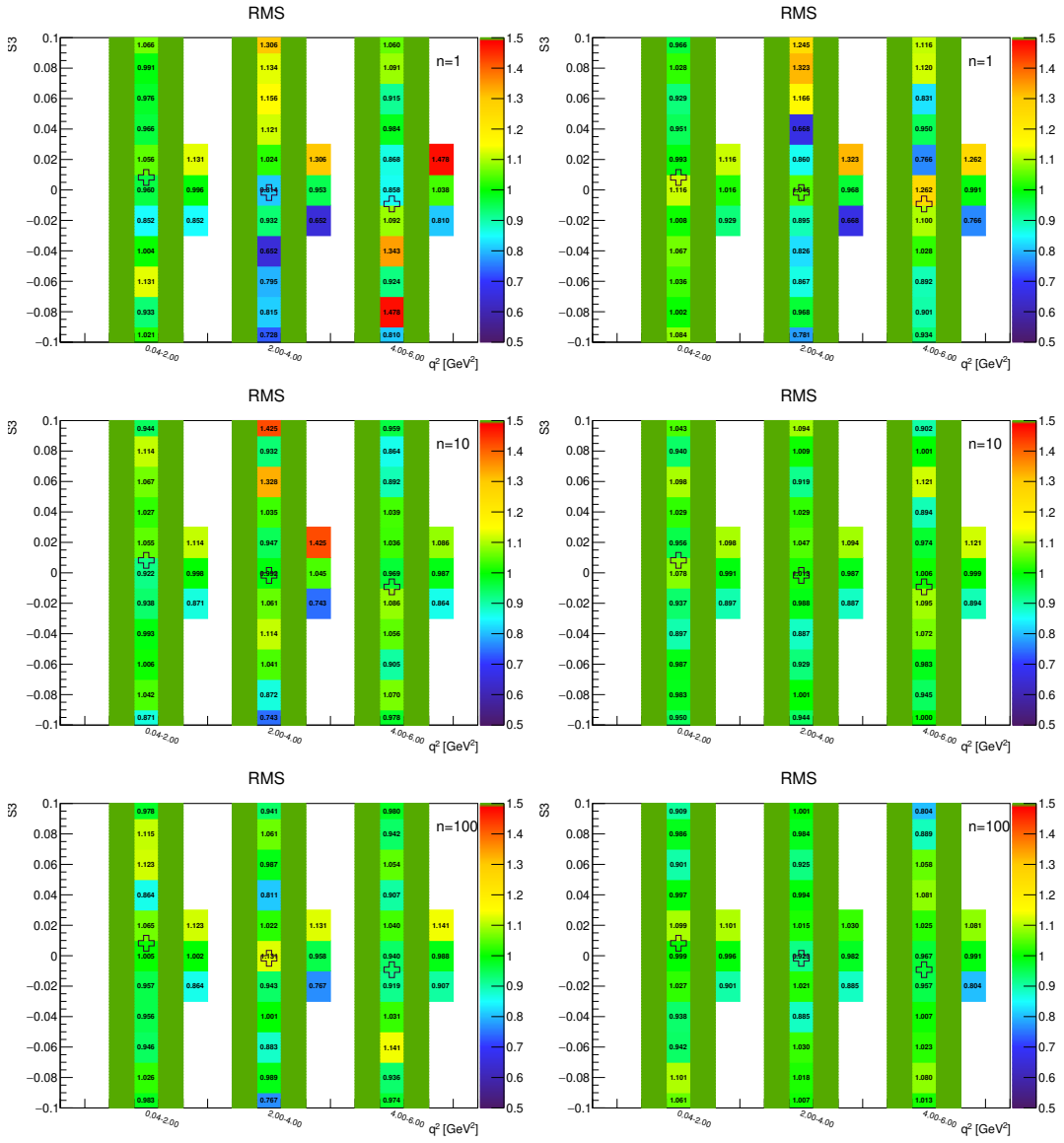

Figure A.114: Toy-MC studies of the S_4-fold, with $r = 2$. Figures show the pull RMS without (left) and with acceptance (right) on the parameter S_3. The green bands represent fit-p.d.f. positivity range. The top figures correspond to the Run-1 like number of events (n = 1), while the middle and the bottom to 10× and 100× larger simulated samples.

A.5.3 S_4-fold – parameter S_4

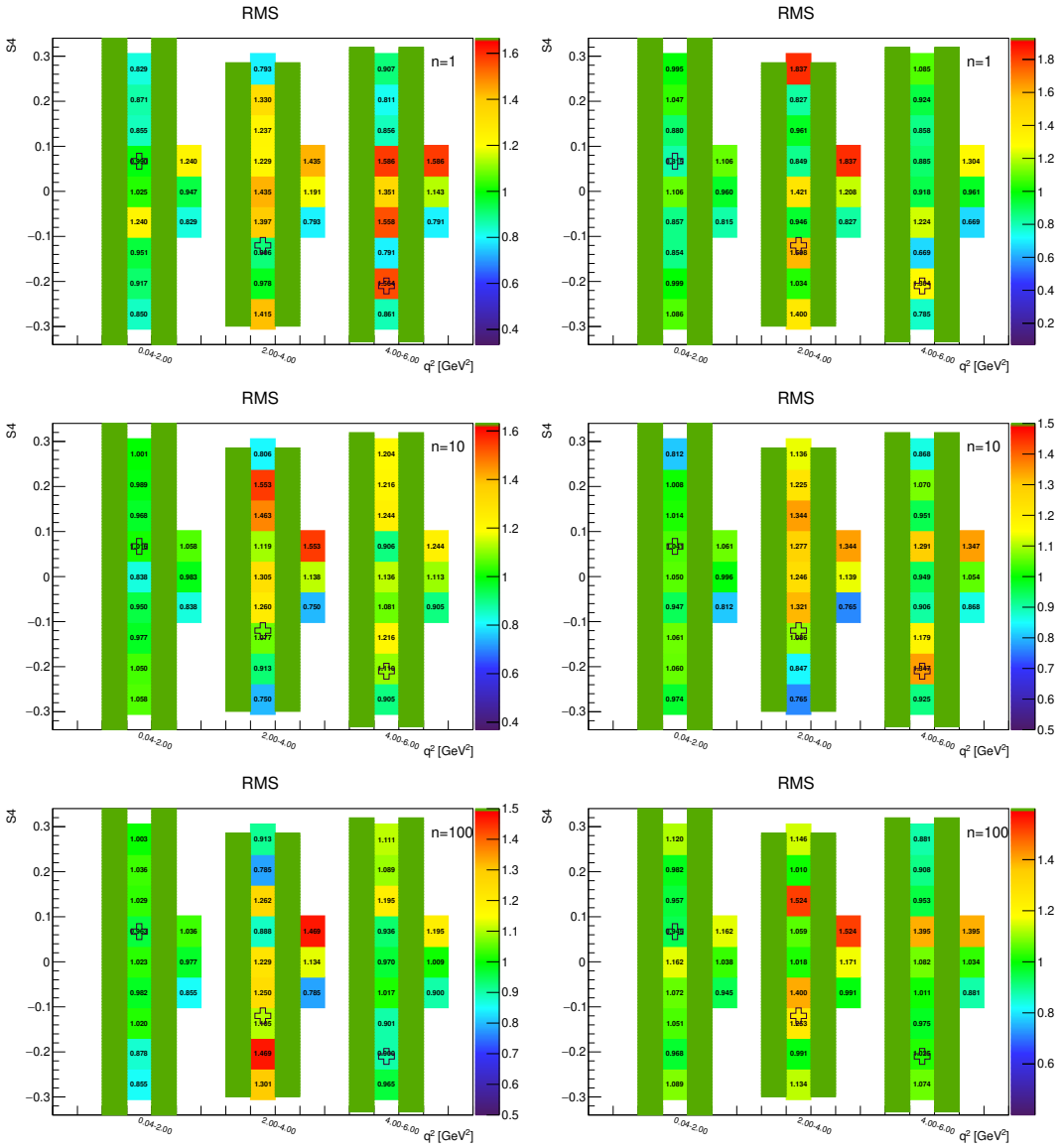

Figure A.115: Toy-MC studies of the S_4-fold, with $r = 0.5$. Figures show the pull RMS without (left) and with acceptance (right) on the parameter S_4. The green bands represent fit-p.d.f. positivity range. The top figures correspond to the Run-1 like number of events (n = 1), while the middle and the bottom to 10× and 100× larger simulated samples.

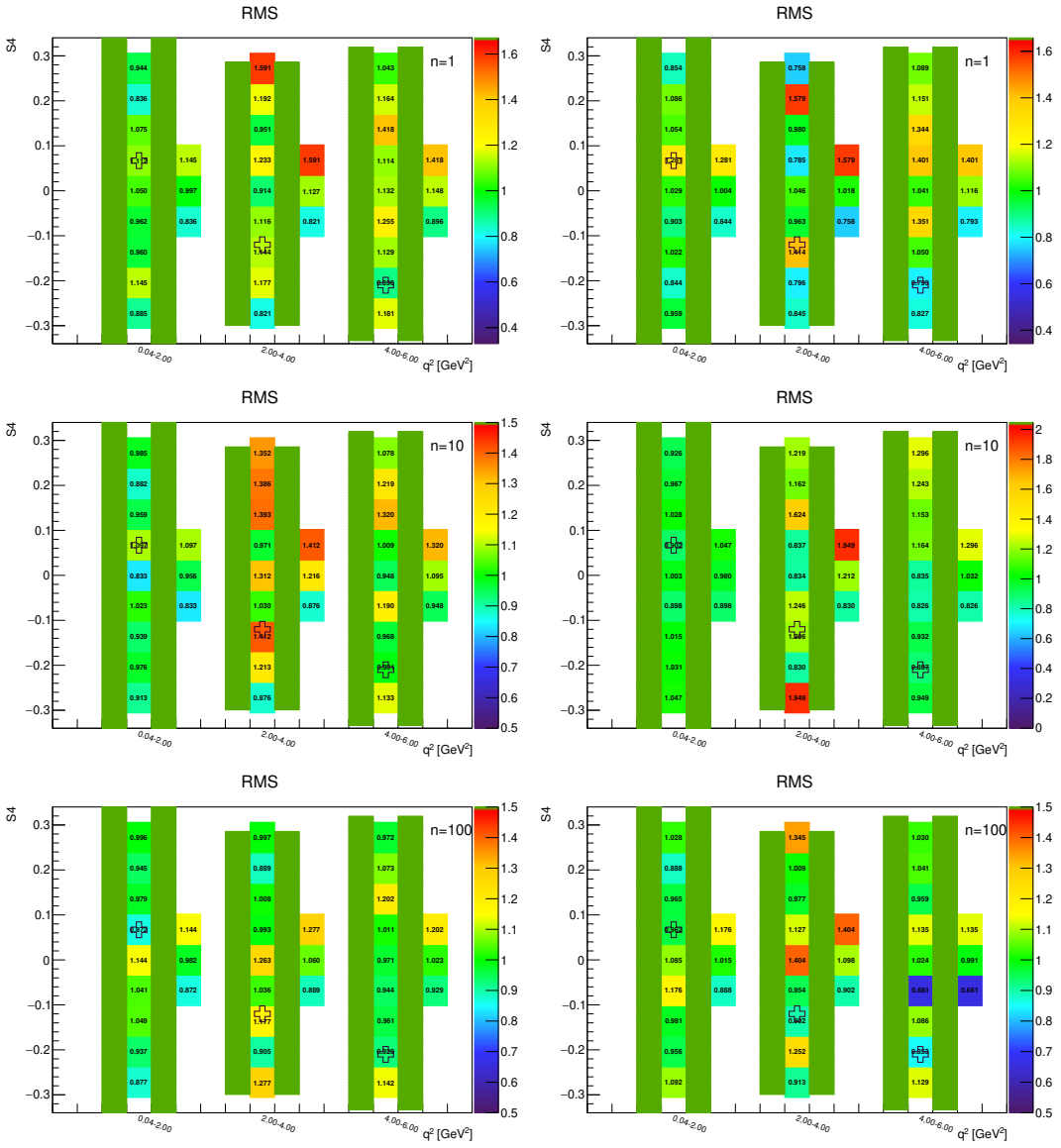

Figure A.116: Toy-MC studies of the S_4-fold, with $r = 1$. Figures show the pull RMS without (left) and with acceptance (right) on the parameter S_4. The green bands represent fit-p.d.f. positivity range. The top figures correspond to the Run-1 like number of events (n = 1), while the middle and the bottom to 10× and 100× larger simulated samples.

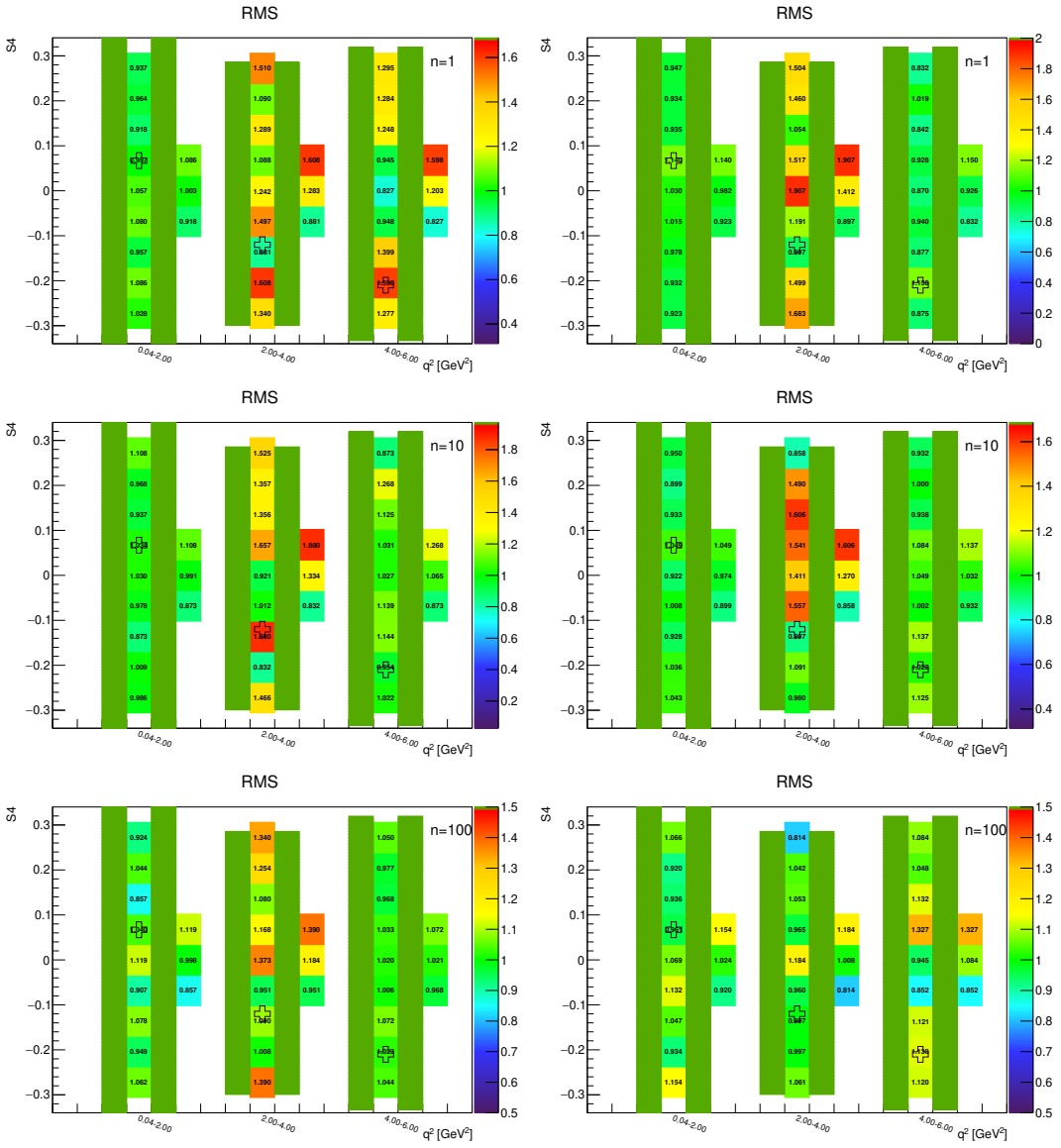

Figure A.117: Toy-MC studies of the S_4-fold, with $r = 2$. Figures show the pull RMS without (left) and with acceptance (right) on the parameter S_4. The green bands represent fit-p.d.f. positivity range. The top figures correspond to the Run-1 like number of events (n = 1), while the middle and the bottom to 10× and 100× larger simulated samples.

A.5.4 S_5-fold – parameter F_L

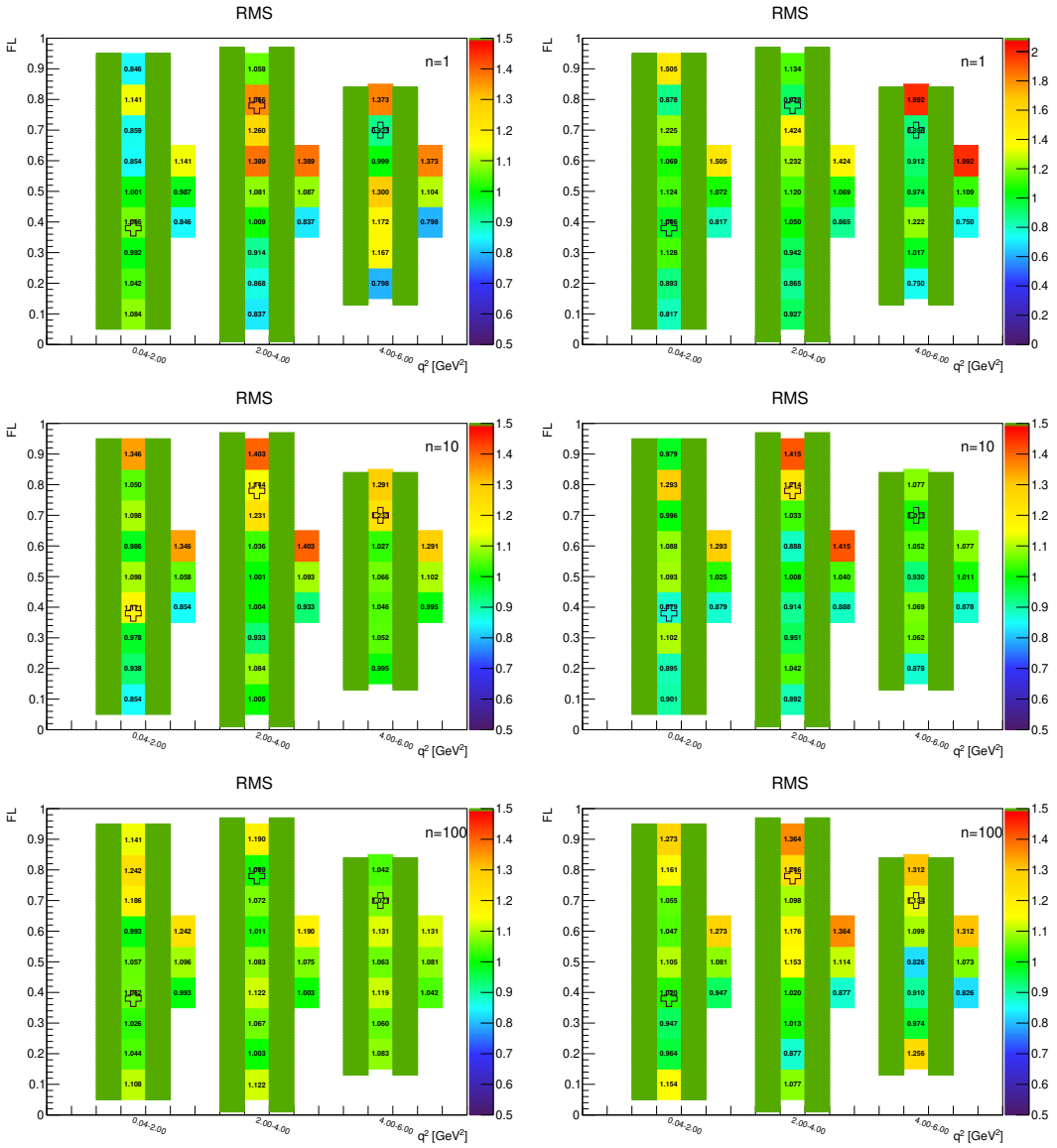

Figure A.118: Toy-MC studies of the S_5-fold, with $r = 0.5$. Figures show the pull RMS without (left) and with acceptance (right) on the parameter F_L. The green bands represent fit-p.d.f. positivity range. The top figures correspond to the Run-1 like number of events (n = 1), while the middle and the bottom to 10× and 100× larger simulated samples.

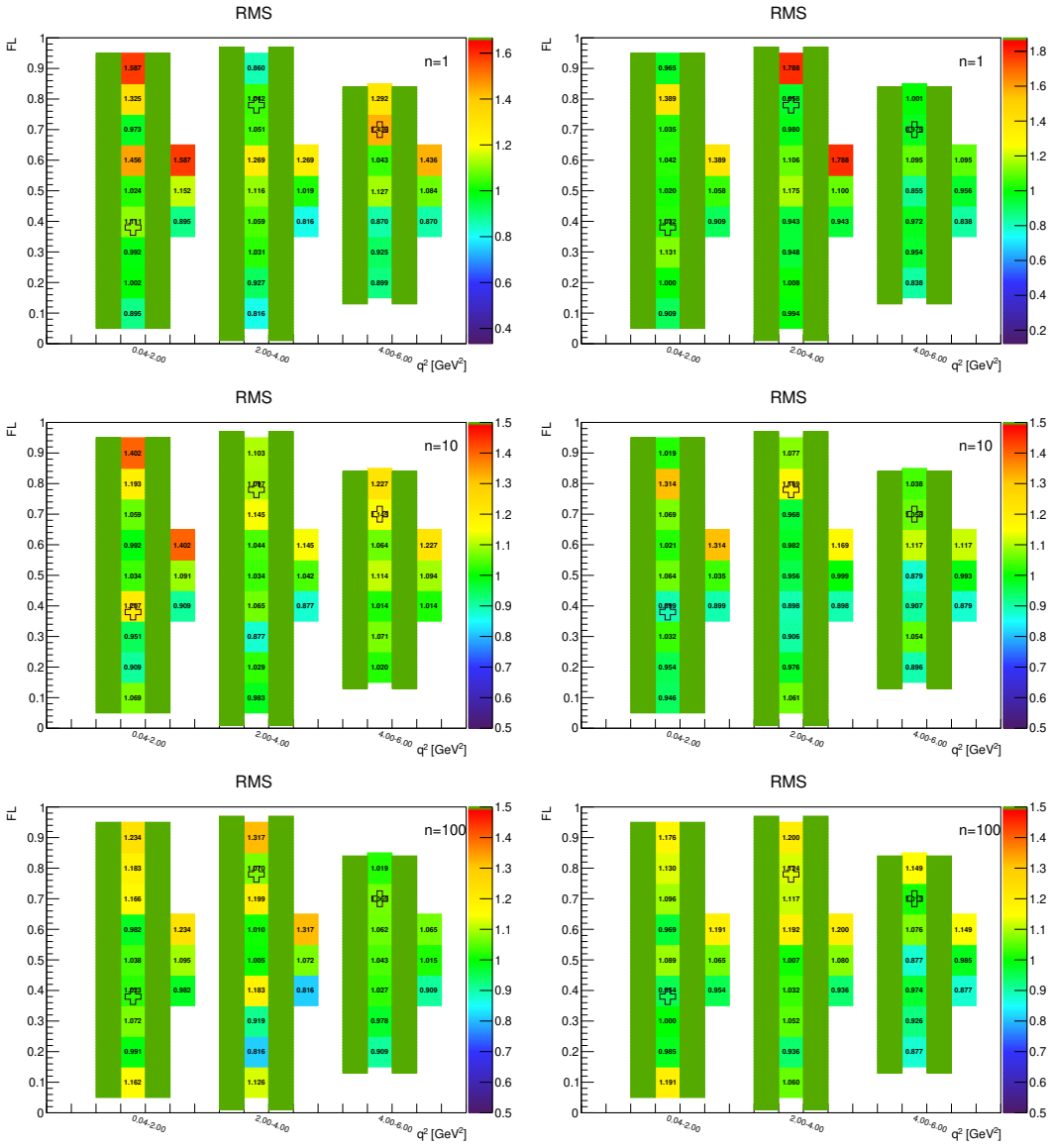

Figure A.119: Toy-MC studies of the S_5-fold, with $r = 1$. Figures show the pull RMS without (left) and with acceptance (right) on the parameter F_L. The green bands represent fit-p.d.f. positivity range. The top figures correspond to the Run-1 like number of events (n = 1), while the middle and the bottom to 10× and 100× larger simulated samples.

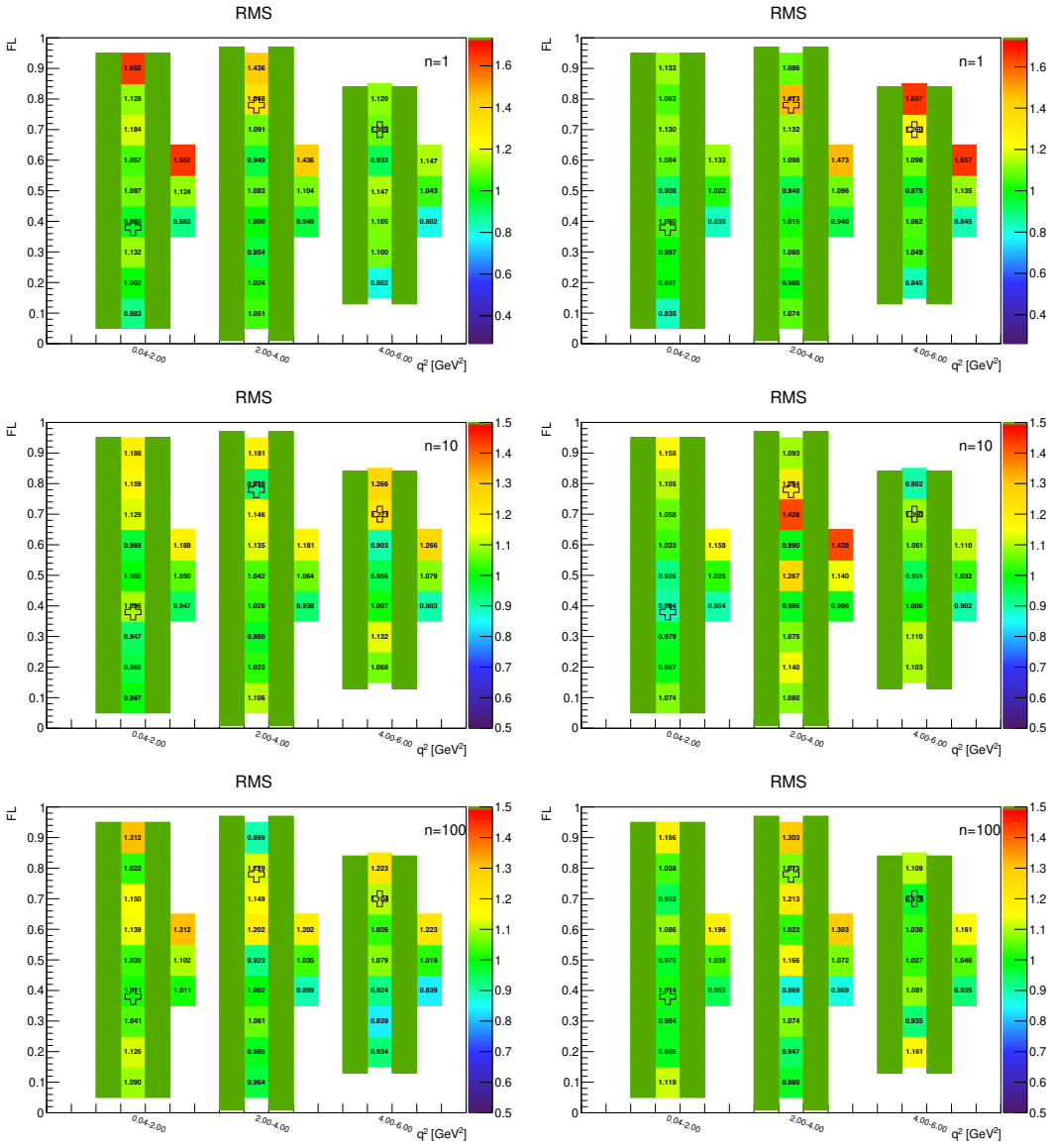

Figure A.120: Toy-MC studies of the S_5-fold, with $r = 2$. Figures show the pull RMS without (left) and with acceptance (right) on the parameter F_L. The green bands represent fit-p.d.f. positivity range. The top figures correspond to the Run-1 like number of events (n = 1), while the middle and the bottom to 10× and 100× larger simulated samples.

A.5.5 S_5-fold – parameter S_3

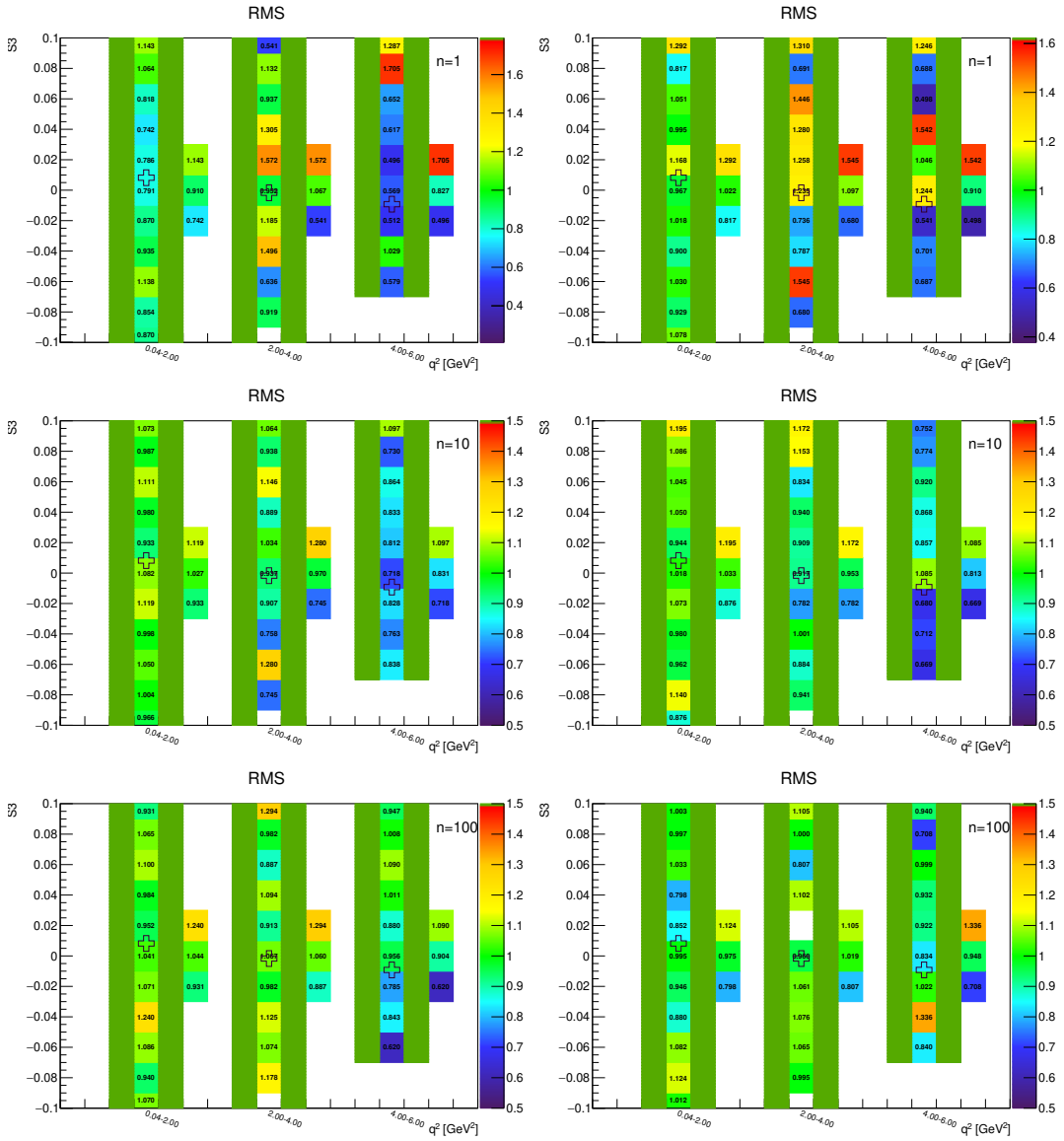

Figure A.121: Toy-MC studies of the S_5-fold, with $r = 0.5$. Figures show the pull RMS without (left) and with acceptance (right) on the parameter S_3. The green bands represent fit-p.d.f. positivity range. The top figures correspond to the Run-1 like number of events (n = 1), while the middle and the bottom to 10× and 100× larger simulated samples.

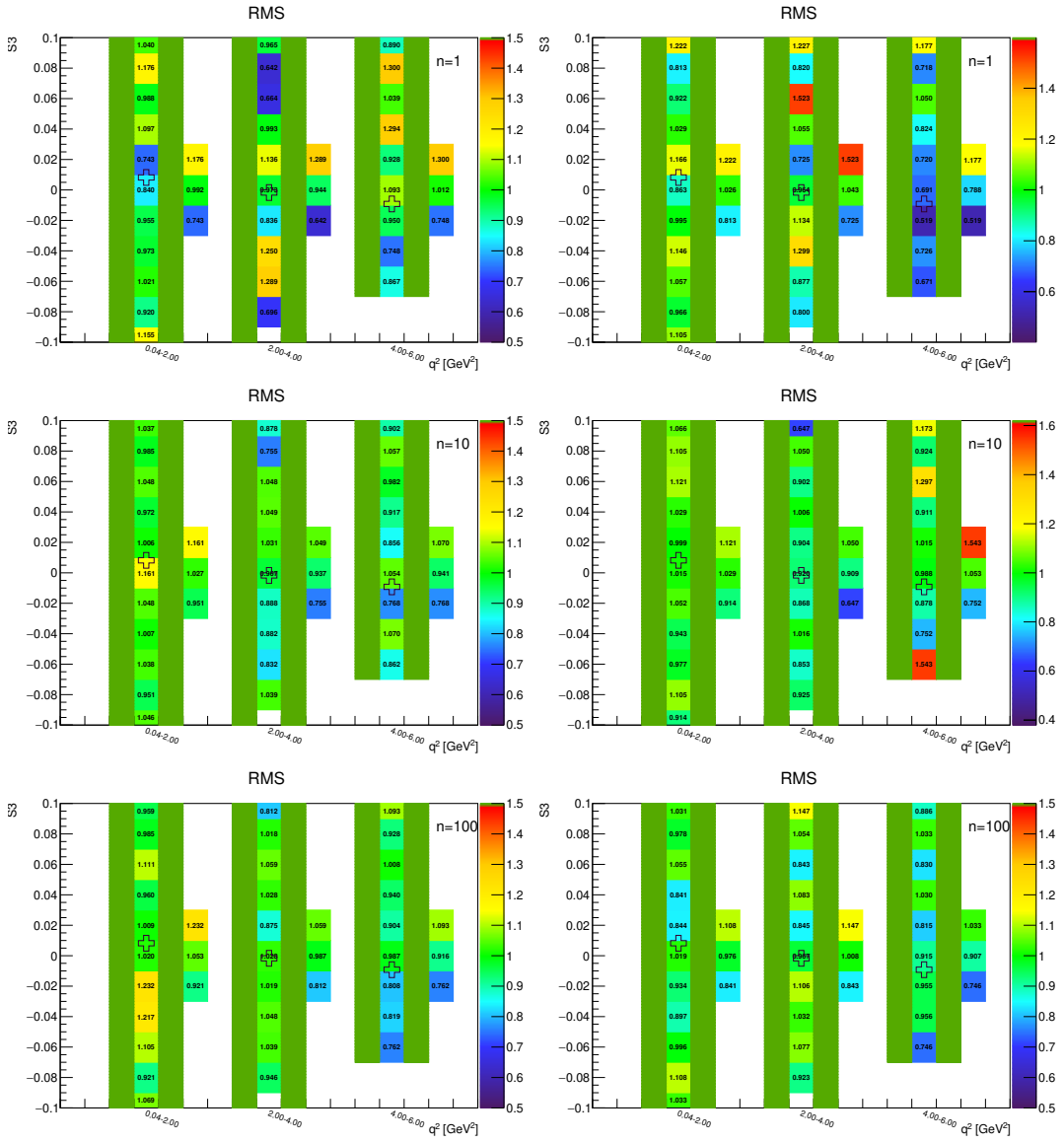

Figure A.122: Toy-MC studies of the S_5-fold, with $r = 1$. Figures show the pull RMS without (left) and with acceptance (right) on the parameter S_3. The green bands represent fit-p.d.f. positivity range. The top figures correspond to the Run-1 like number of events (n = 1), while the middle and the bottom to 10× and 100× larger simulated samples.

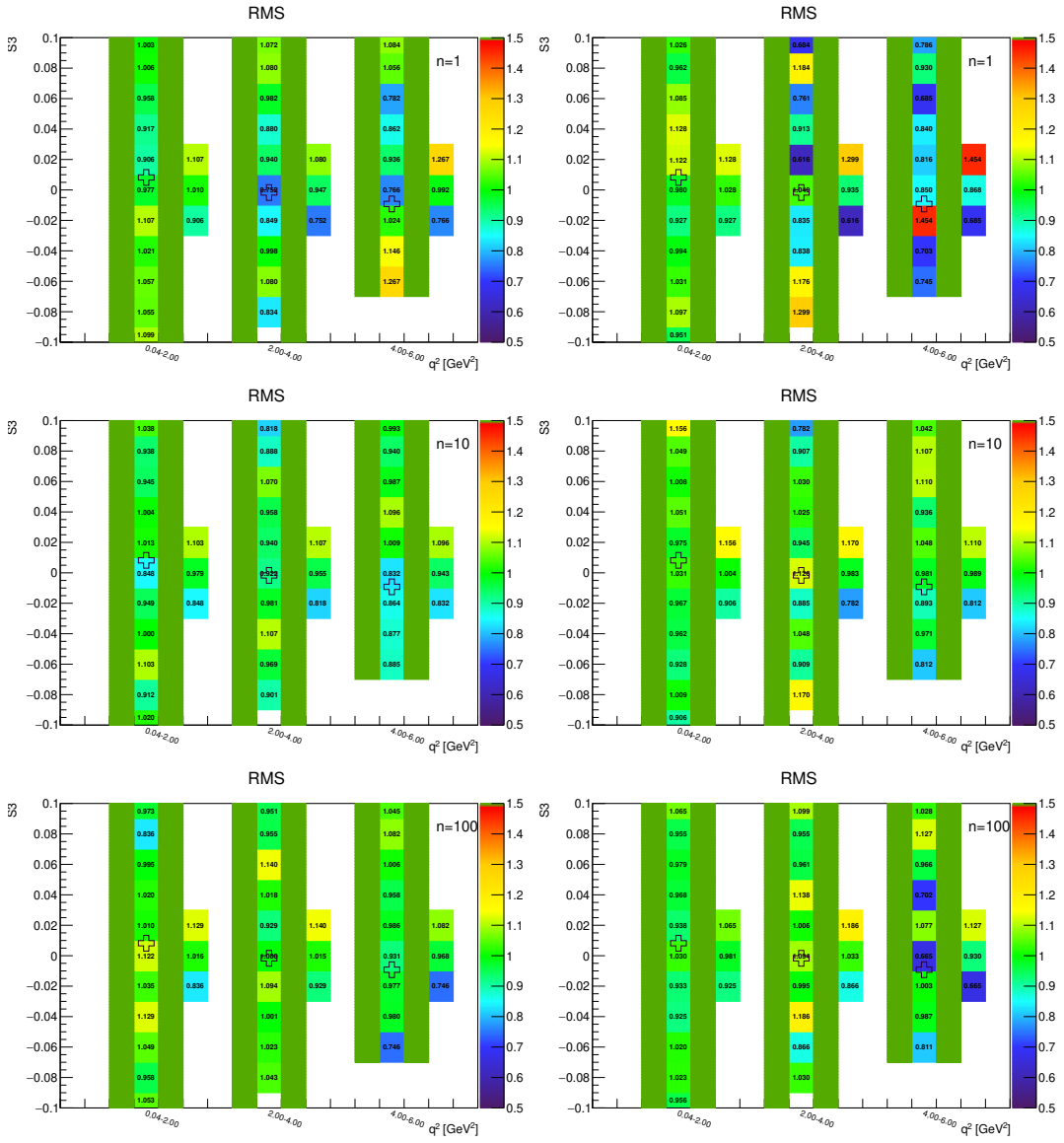

Figure A.123: Toy-MC studies of the S_5-fold, with $r = 2$. Figures show the pull RMS without (left) and with acceptance (right) on the parameter S_3. The green bands represent fit-p.d.f. positivity range. The top figures correspond to the Run-1 like number of events (n = 1), while the middle and the bottom to 10× and 100× larger simulated samples.

A.5.6 S_5-fold – parameter S_5

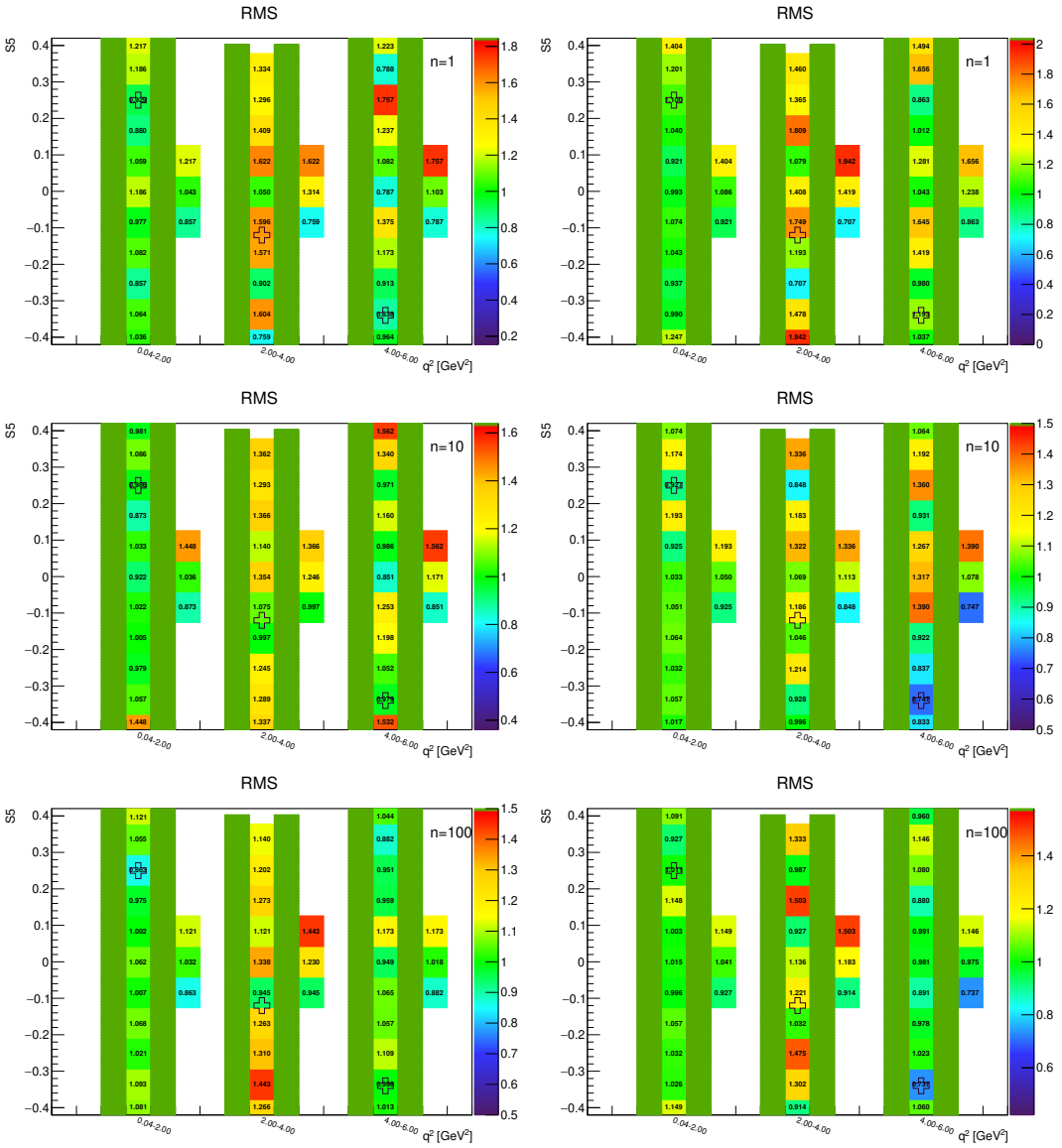

Figure A.124: Toy-MC studies of the S_5-fold, with $r = 0.5$. Figures show the pull RMS without (left) and with acceptance (right) on the parameter S_5. The green bands represent fit-p.d.f. positivity range. The top figures correspond to the Run-1 like number of events (n = 1), while the middle and the bottom to 10× and 100× larger simulated samples.

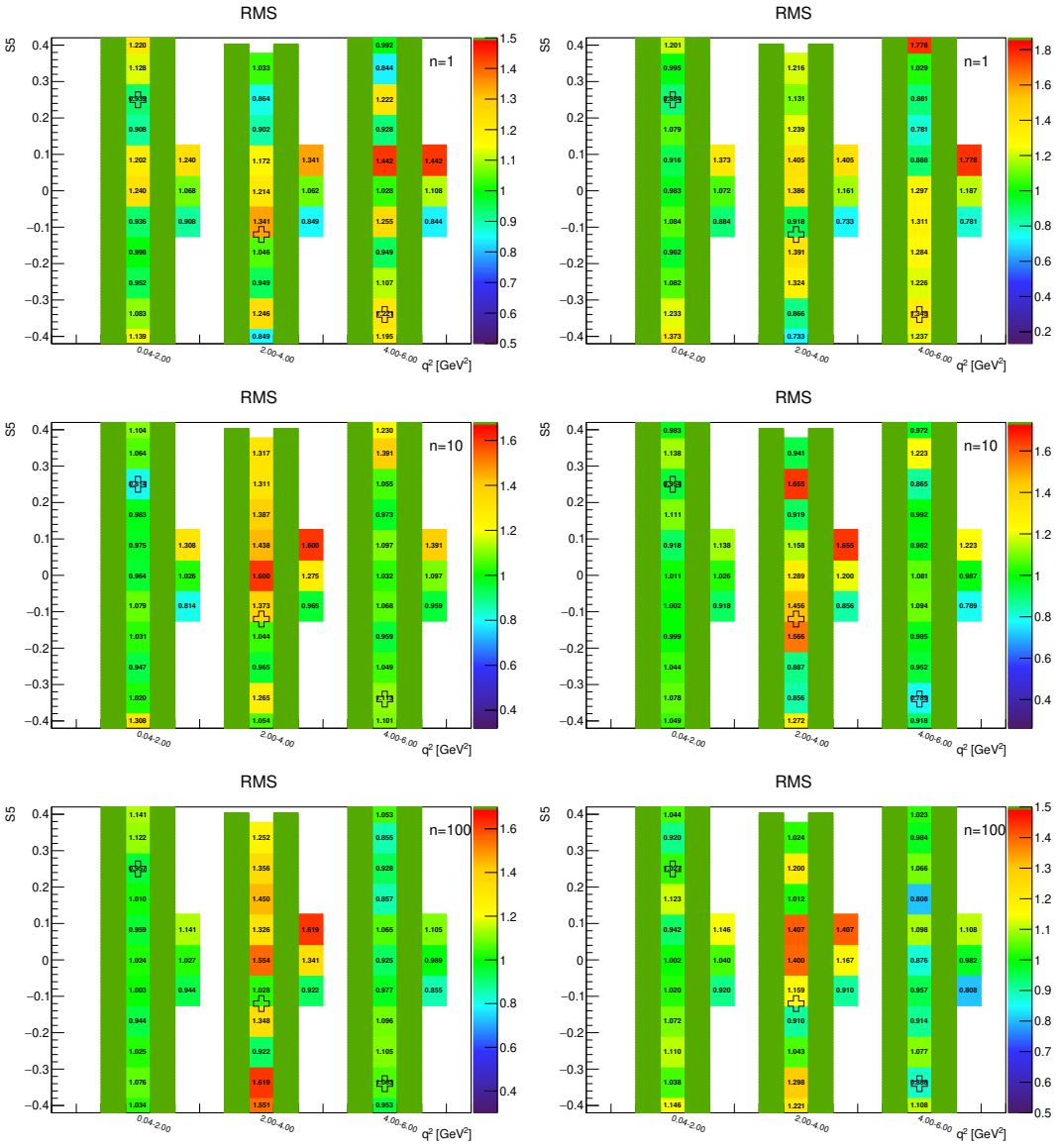

Figure A.125: Toy-MC studies of the S_5-fold, with $r = 1$. Figures show the pull RMS without (left) and with acceptance (right) on the parameter S_5. The green bands represent fit-p.d.f. positivity range. The top figures correspond to the Run-1 like number of events (n = 1), while the middle and the bottom to 10× and 100× larger simulated samples.

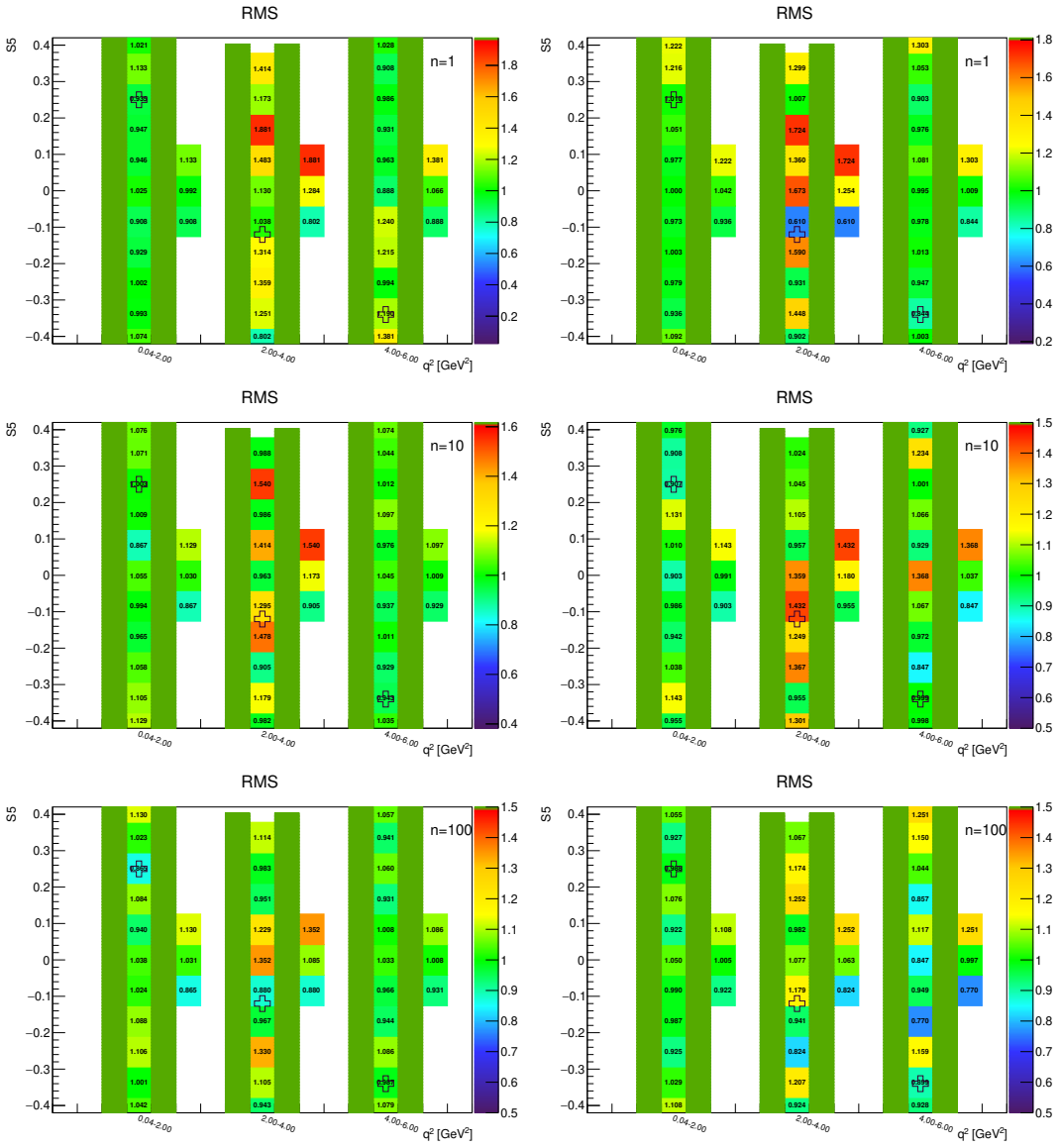

Figure A.126: Toy-MC studies of the S_5-fold, with $r = 2$. Figures show the pull RMS without (left) and with acceptance (right) on the parameter S_5. The green bands represent fit-p.d.f. positivity range. The top figures correspond to the Run-1 like number of events (n = 1), while the middle and the bottom to 10× and 100× larger simulated samples.

A.5.7 S_7-fold – parameter F_L

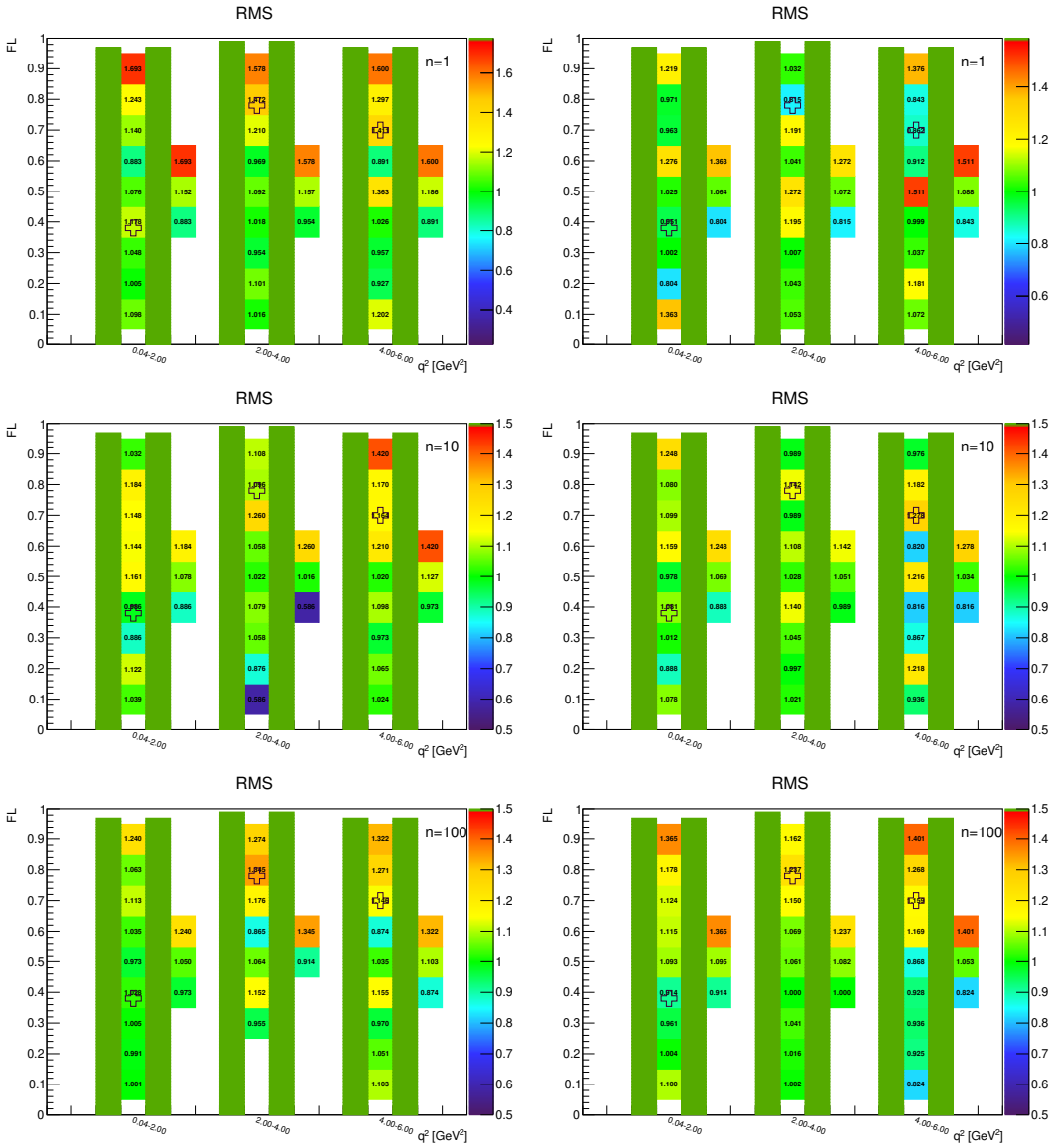

Figure A.127: Toy-MC studies of the S_7-fold, with $r = 0.5$. Figures show the pull RMS without (left) and with acceptance (right) on the parameter F_L. The green bands represent fit-p.d.f. positivity range. The top figures correspond to the Run-1 like number of events (n = 1), while the middle and the bottom to 10× and 100× larger simulated samples.

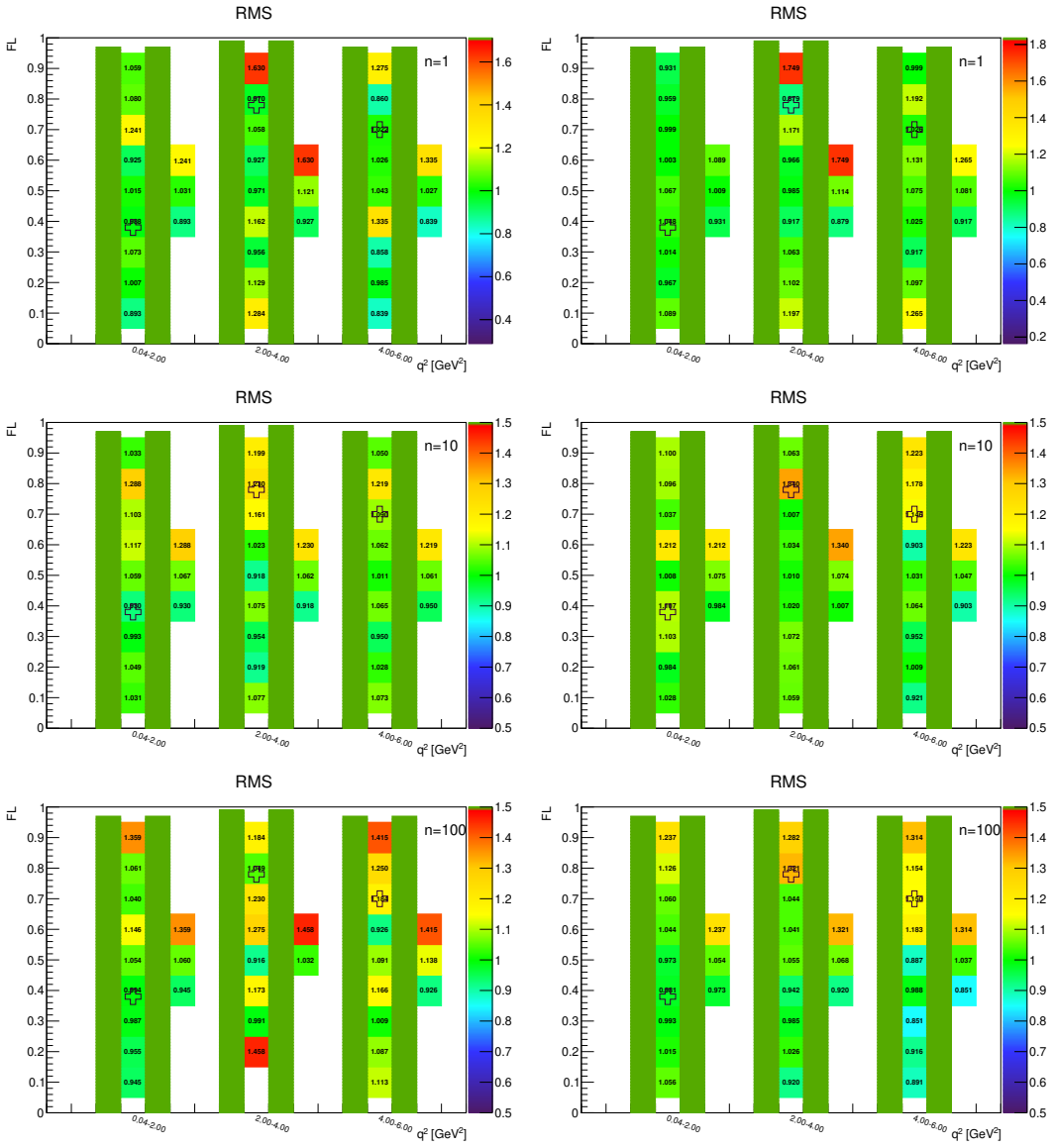

Figure A.128: Toy-MC studies of the S_7-fold, with $r = 1$. Figures show the pull RMS without (left) and with acceptance (right) on the parameter F_L. The green bands represent fit-p.d.f. positivity range. The top figures correspond to the Run-1 like number of events (n = 1), while the middle and the bottom to 10× and 100× larger simulated samples.

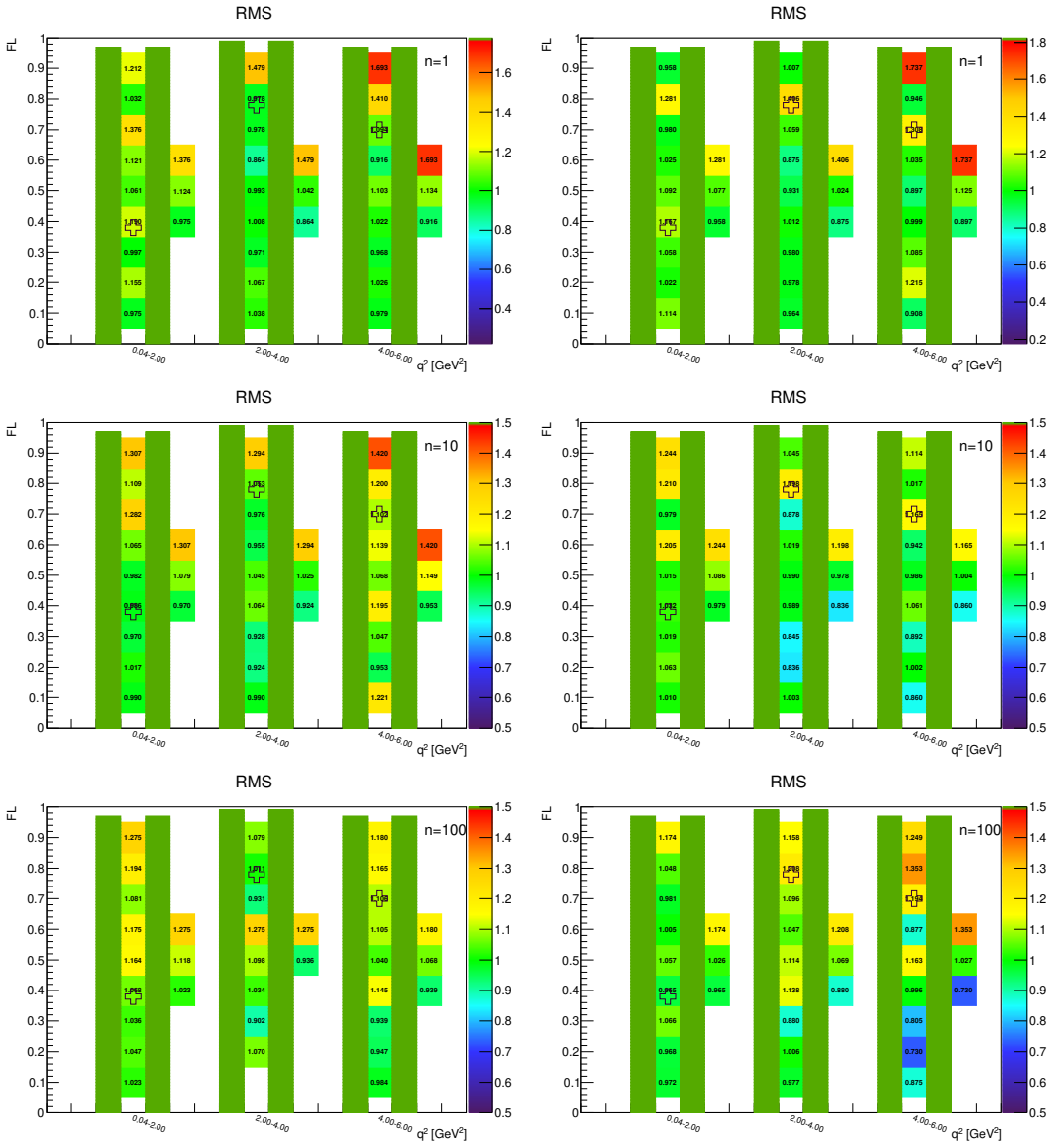

Figure A.129: Toy-MC studies of the S_7-fold, with $r = 2$. Figures show the pull RMS without (left) and with acceptance (right) on the parameter F_L. The green bands represent fit-p.d.f. positivity range. The top figures correspond to the Run-1 like number of events (n = 1), while the middle and the bottom to 10× and 100× larger simulated samples.

A.5.8 S_7-fold – parameter S_3

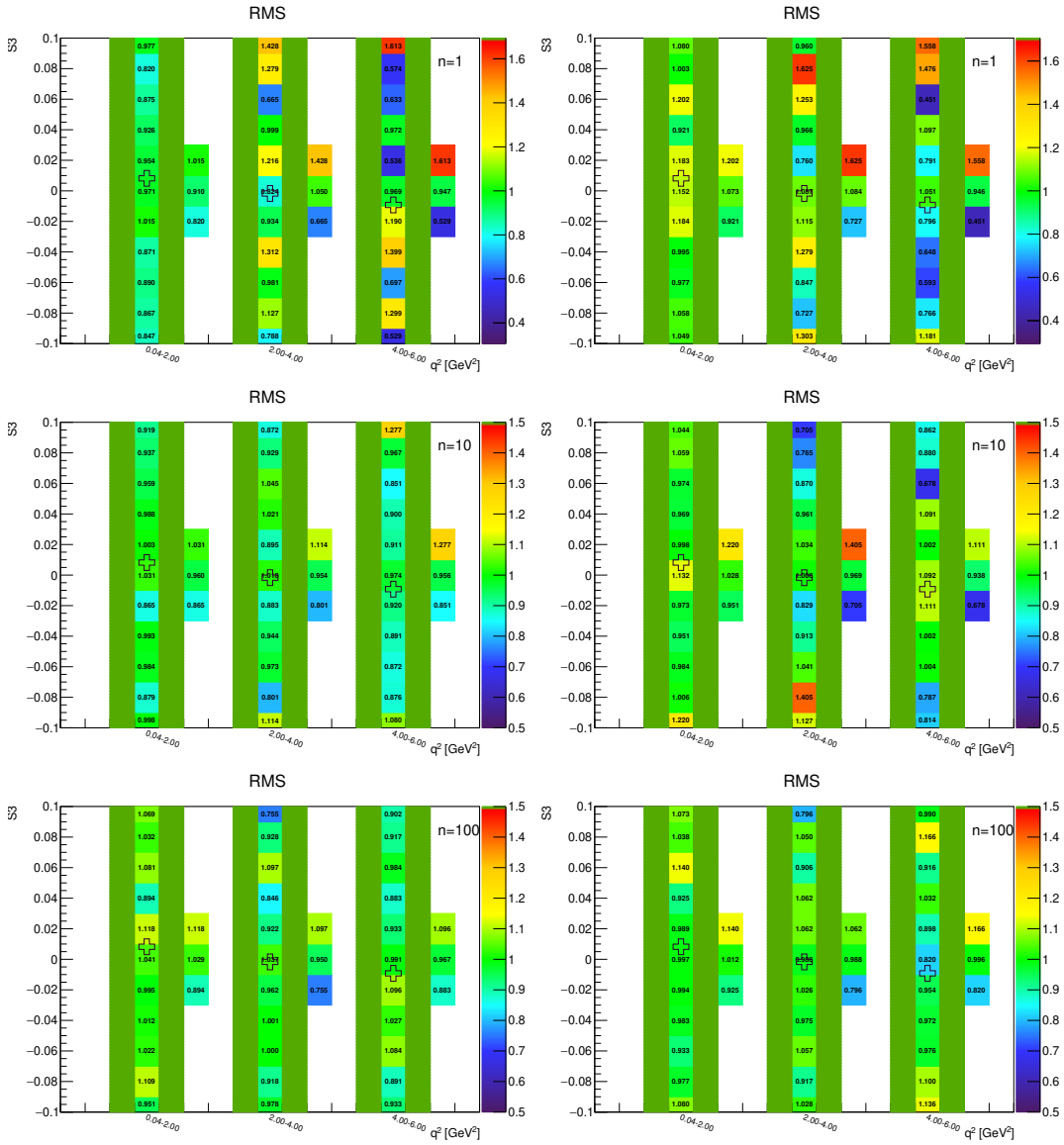

Figure A.130: Toy-MC studies of the S_7-fold, with $r = 0.5$. Figures show the pull RMS without (left) and with acceptance (right) on the parameter S_3. The green bands represent fit-p.d.f. positivity range. The top figures correspond to the Run-1 like number of events (n = 1), while the middle and the bottom to 10× and 100× larger simulated samples.

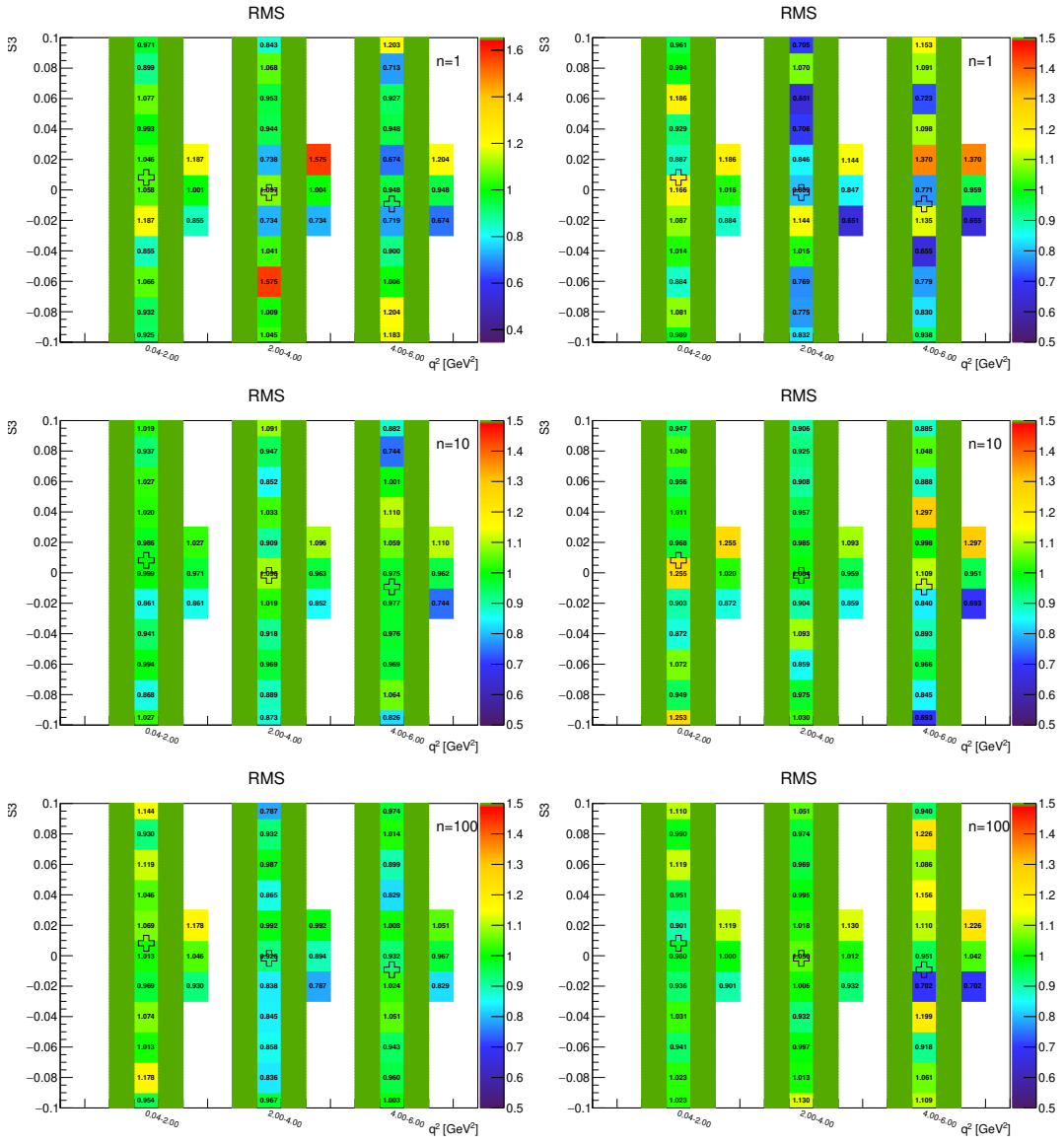

Figure A.131: Toy-MC studies of the S_7-fold, with $r = 1$. Figures show the pull RMS without (left) and with acceptance (right) on the parameter S_3. The green bands represent fit-p.d.f. positivity range. The top figures correspond to the Run-1 like number of events (n = 1), while the middle and the bottom to 10× and 100× larger simulated samples.

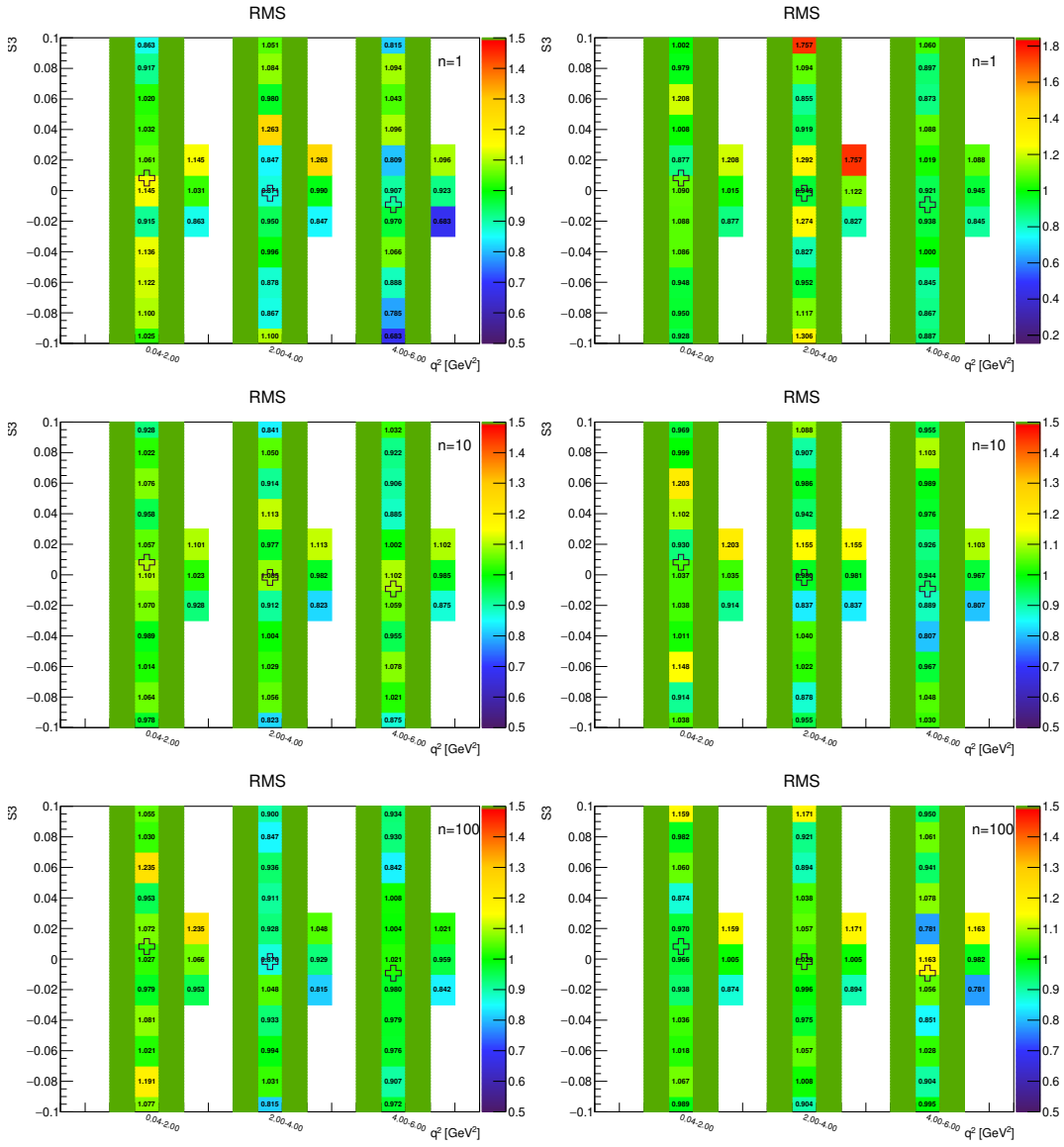

Figure A.132: Toy-MC studies of the S_7-fold, with $r = 2$. Figures show the pull RMS without (left) and with acceptance (right) on the parameter S_3. The green bands represent fit-p.d.f. positivity range. The top figures correspond to the Run-1 like number of events (n = 1), while the middle and the bottom to 10× and 100× larger simulated samples.

A.5.9 S_7-fold – parameter S_7

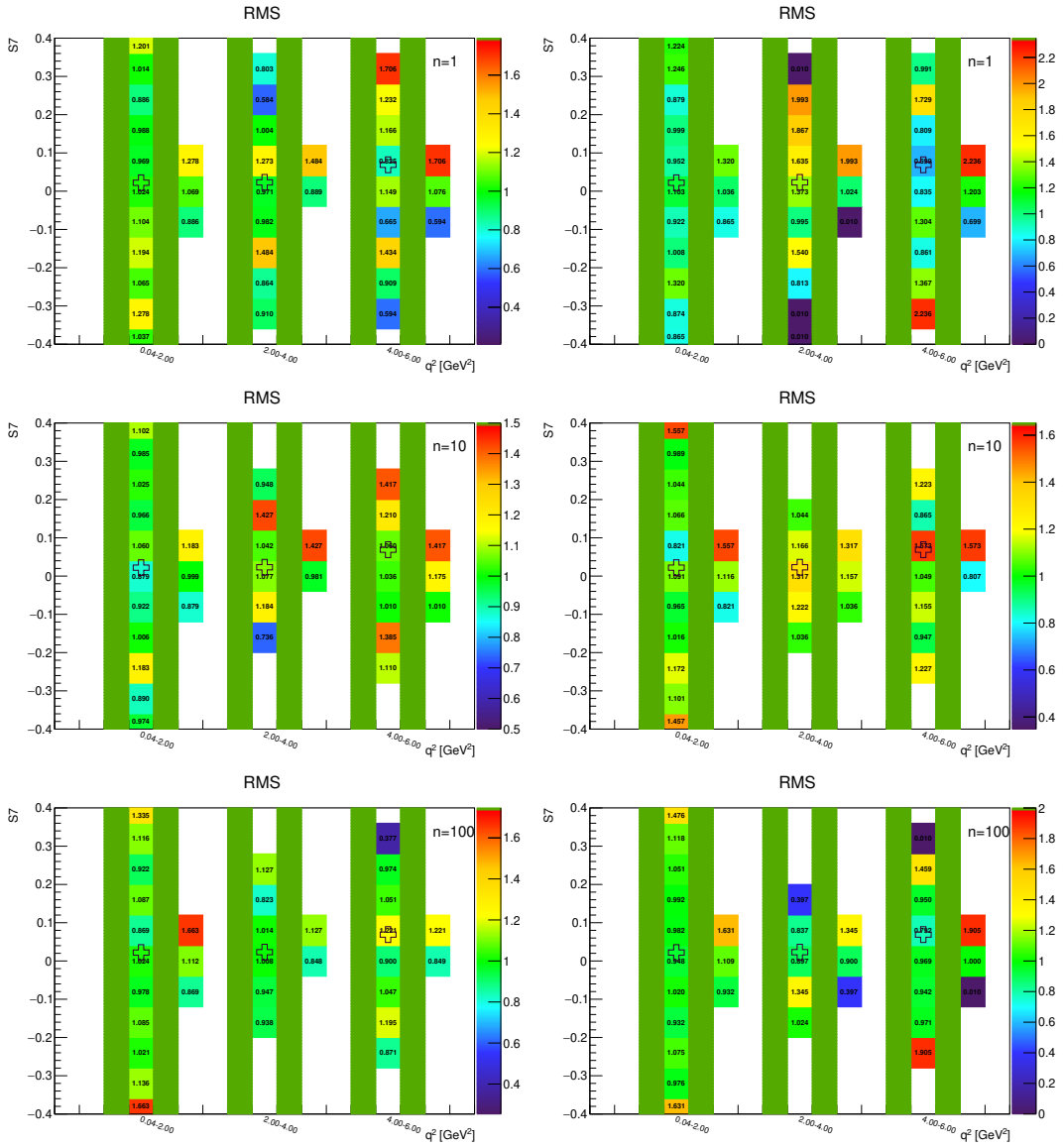

Figure A.133: Toy-MC studies of the S_7-fold, with $r = 0.5$. Figures show the pull RMS without (left) and with acceptance (right) on the parameter S_7. The green bands represent fit-p.d.f. positivity range. The top figures correspond to the Run-1 like number of events (n = 1), while the middle and the bottom to 10× and 100× larger simulated samples.

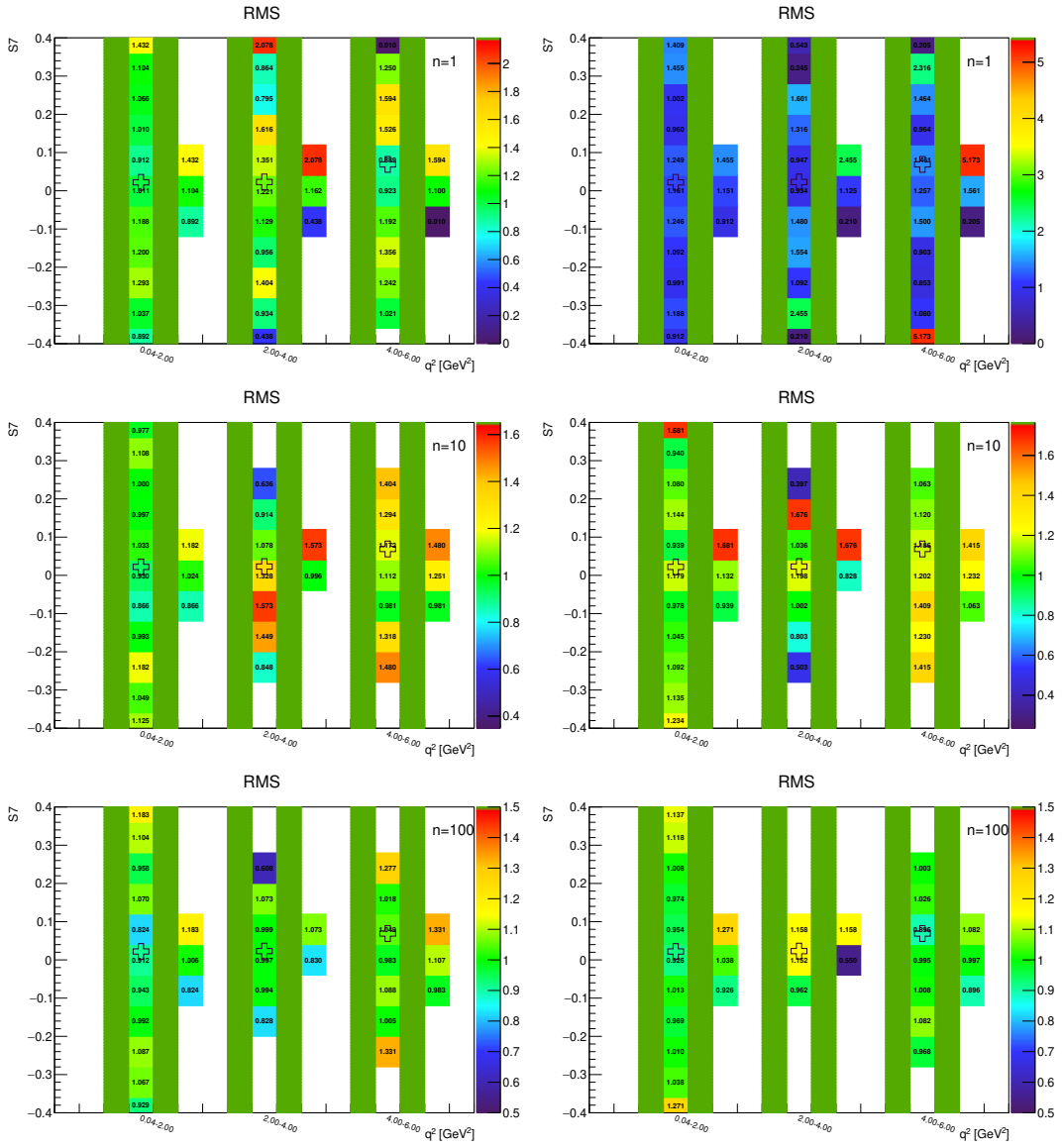

Figure A.134: Toy-MC studies of the S_7-fold, with $r = 1$. Figures show the pull RMS without (left) and with acceptance (right) on the parameter S_7. The green bands represent fit-p.d.f. positivity range. The top figures correspond to the Run-1 like number of events (n = 1), while the middle and the bottom to 10× and 100× larger simulated samples.

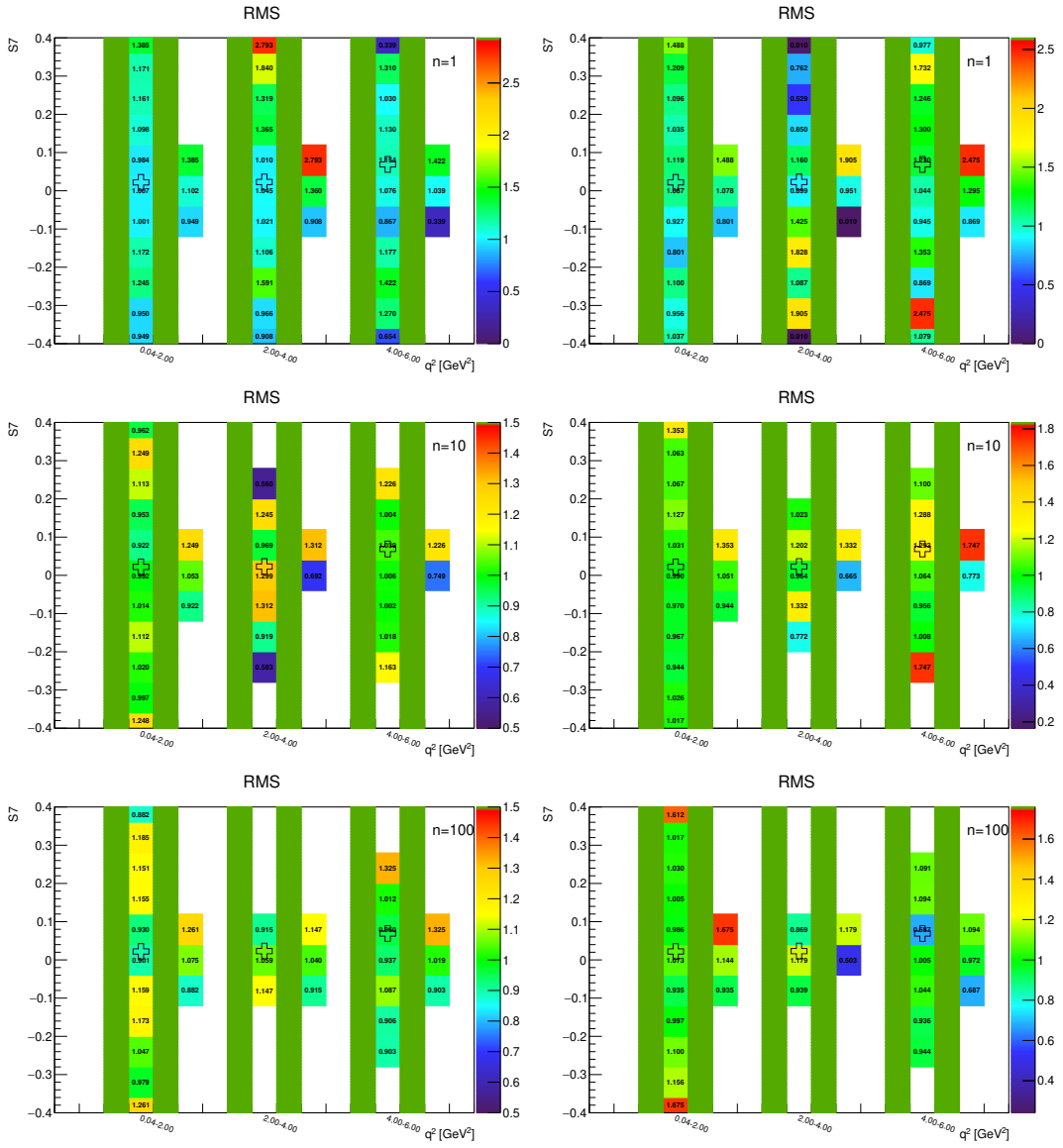

Figure A.135: Toy-MC studies of the S_7-fold, with $r = 2$. Figures show the pull RMS without (left) and with acceptance (right) on the parameter S_7. The green bands represent fit-p.d.f. positivity range. The top figures correspond to the Run-1 like number of events (n = 1), while the middle and the bottom to 10× and 100× larger simulated samples.

A.5.10 S_8-fold – parameter F_L

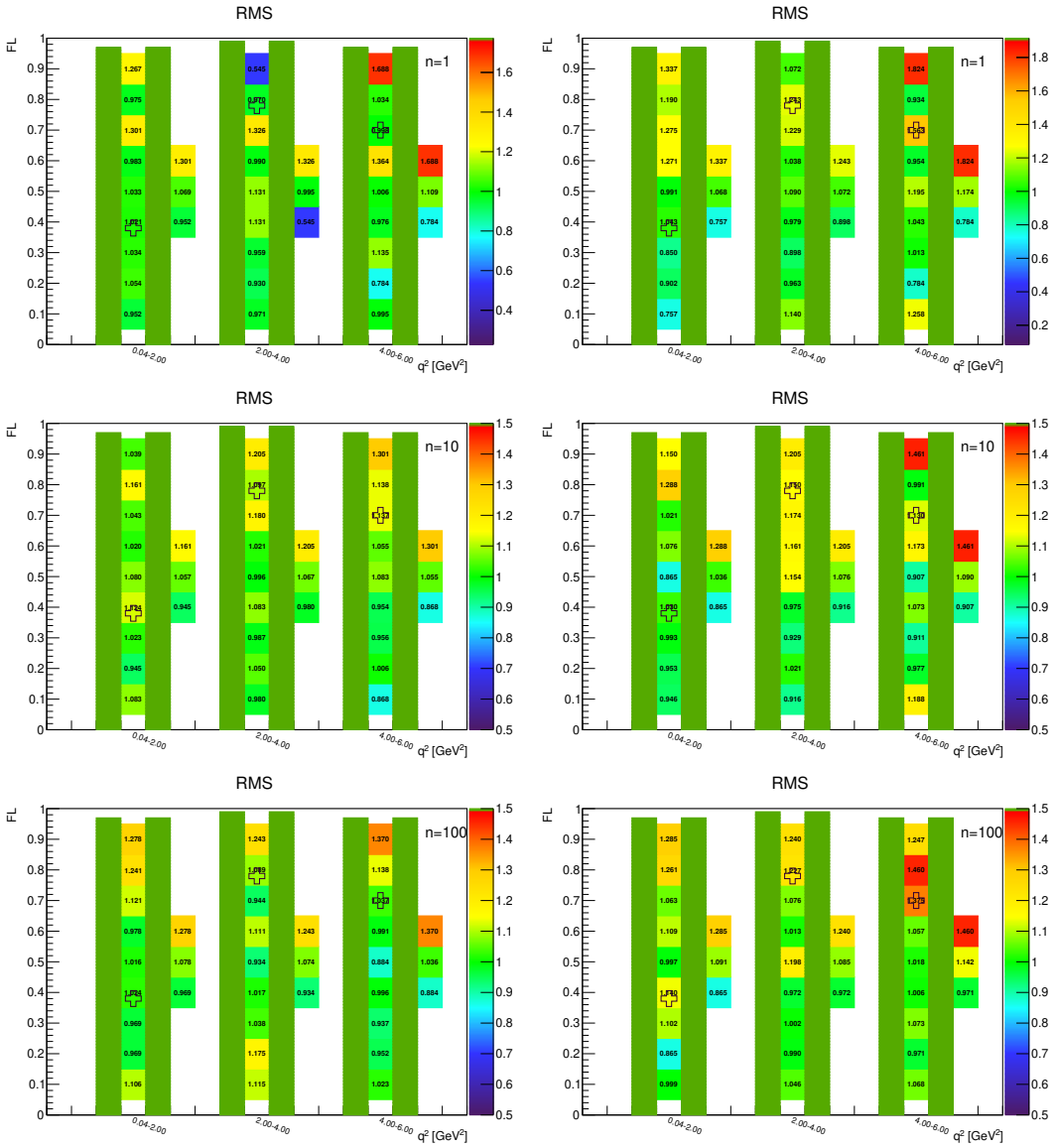

Figure A.136: Toy-MC studies of the S_8-fold, with $r = 0.5$. Figures show the pull RMS without (left) and with acceptance (right) on the parameter F_L. The green bands represent fit-p.d.f. positivity range. The top figures correspond to the Run-1 like number of events (n = 1), while the middle and the bottom to 10× and 100× larger simulated samples.

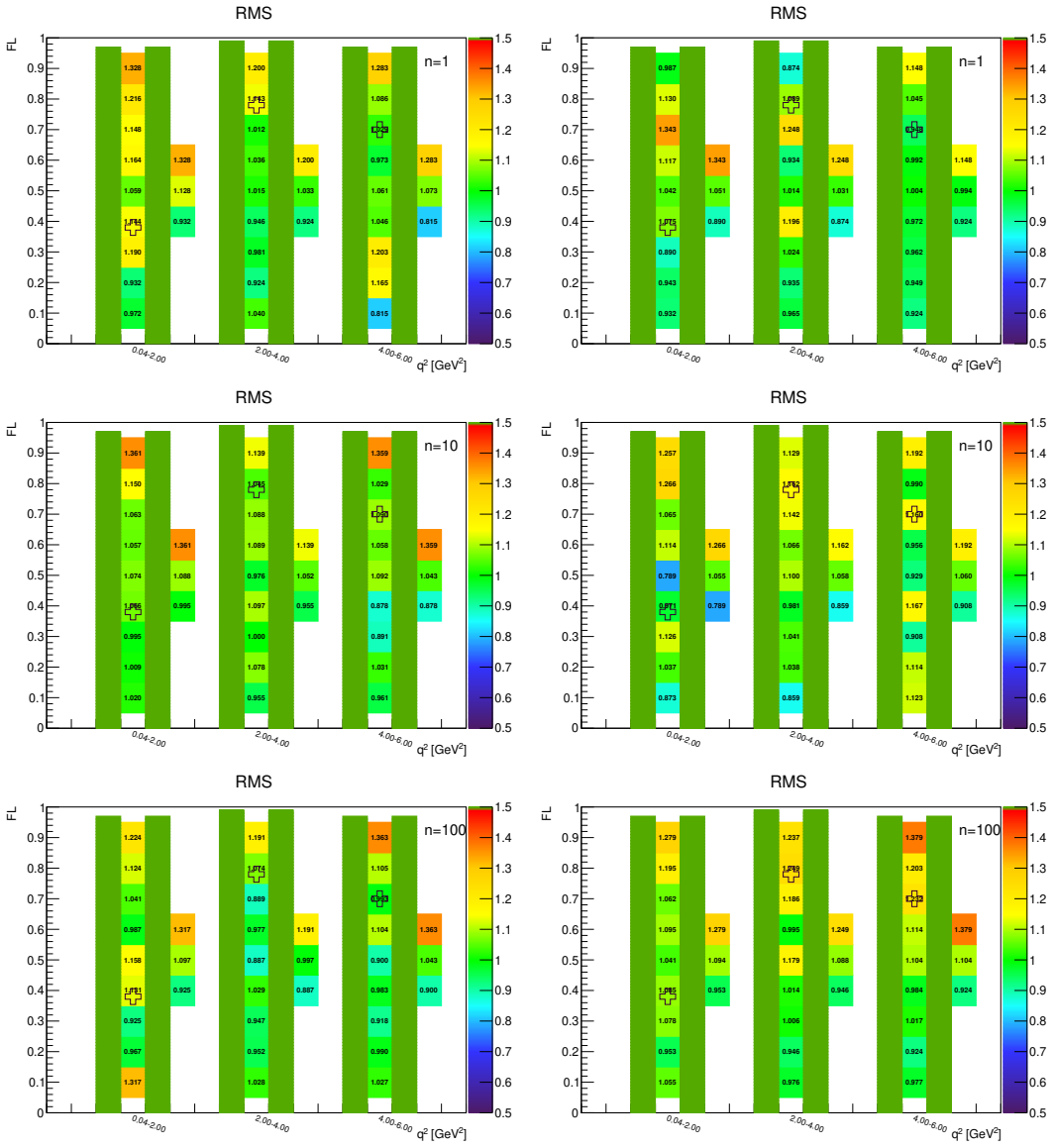

Figure A.137: Toy-MC studies of the S_8-fold, with $r = 1$. Figures show the pull RMS without (left) and with acceptance (right) on the parameter F_L. The green bands represent fit-p.d.f. positivity range. The top figures correspond to the Run-1 like number of events (n = 1), while the middle and the bottom to 10× and 100× larger simulated samples.

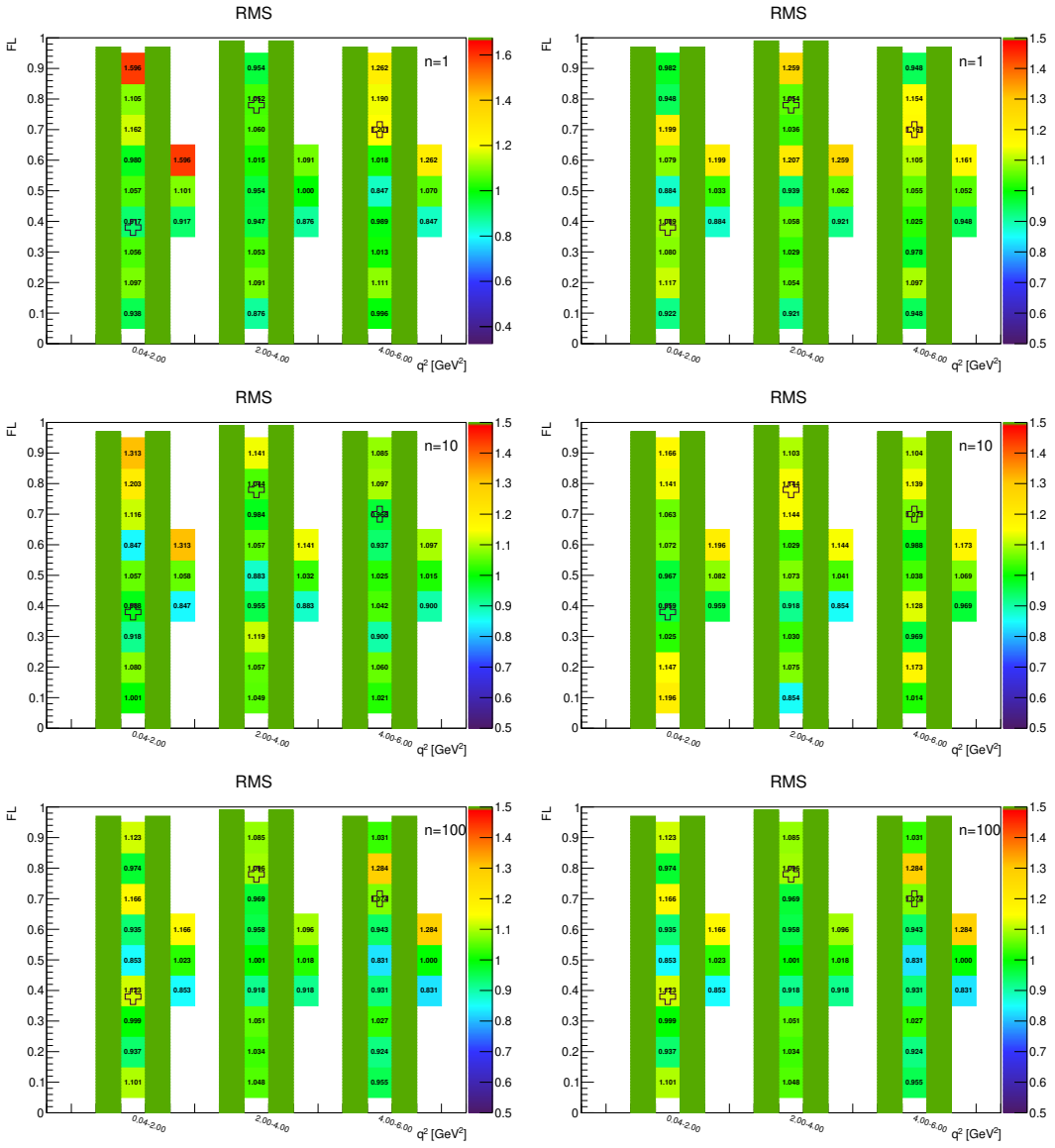

Figure A.138: Toy-MC studies of the S_8-fold, with $r = 2$. Figures show the pull RMS without (left) and with acceptance (right) on the parameter F_L. The green bands represent fit-p.d.f. positivity range. The top figures correspond to the Run-1 like number of events (n = 1), while the middle and the bottom to 10× and 100× larger simulated samples.

A.5.11 S_8-fold – parameter S_3

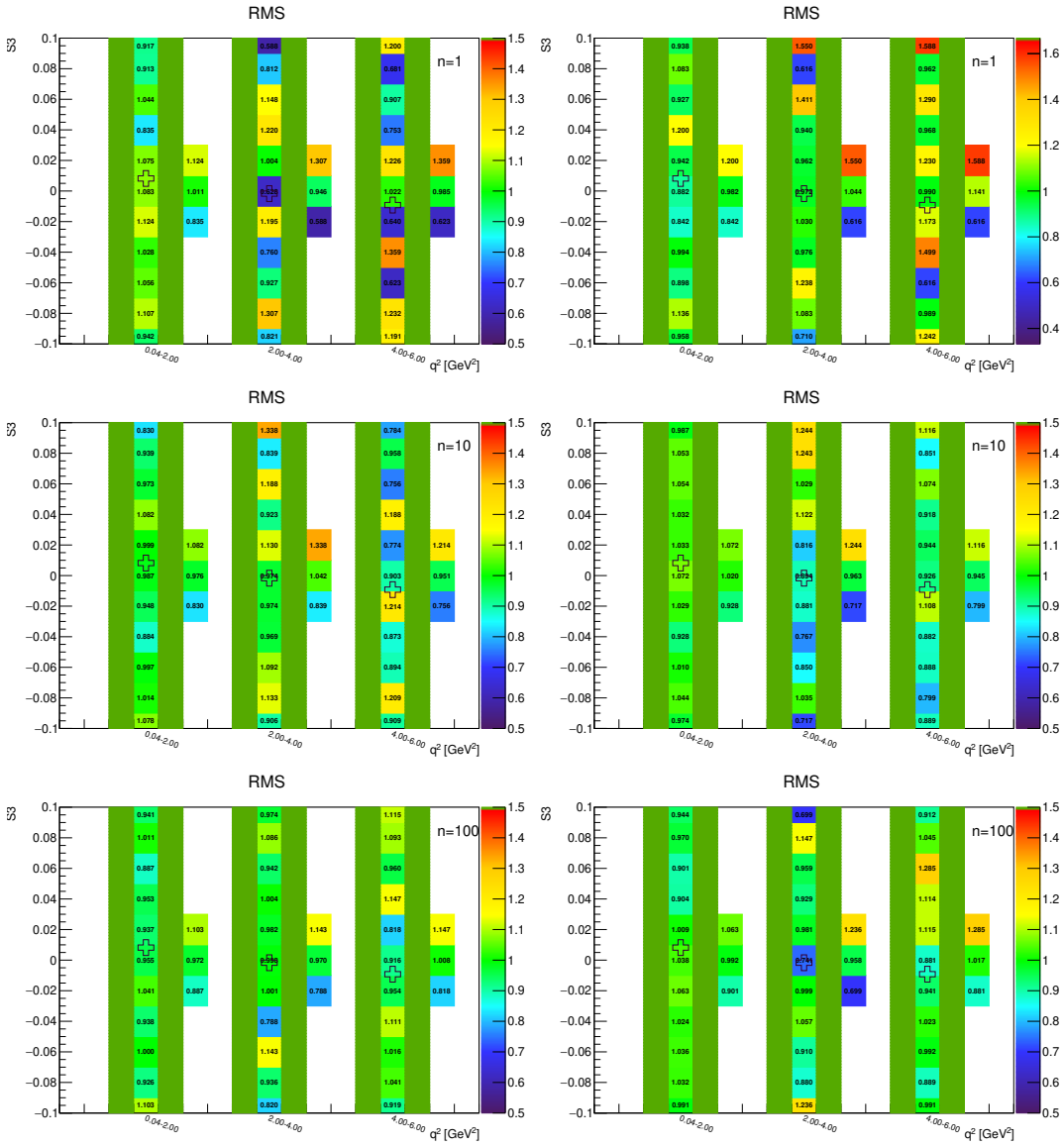

Figure A.139: Toy-MC studies of the S_8-fold, with $r = 0.5$. Figures show the pull RMS without (left) and with acceptance (right) on the parameter S_3. The green bands represent fit-p.d.f. positivity range. The top figures correspond to the Run-1 like number of events (n = 1), while the middle and the bottom to 10× and 100× larger simulated samples.

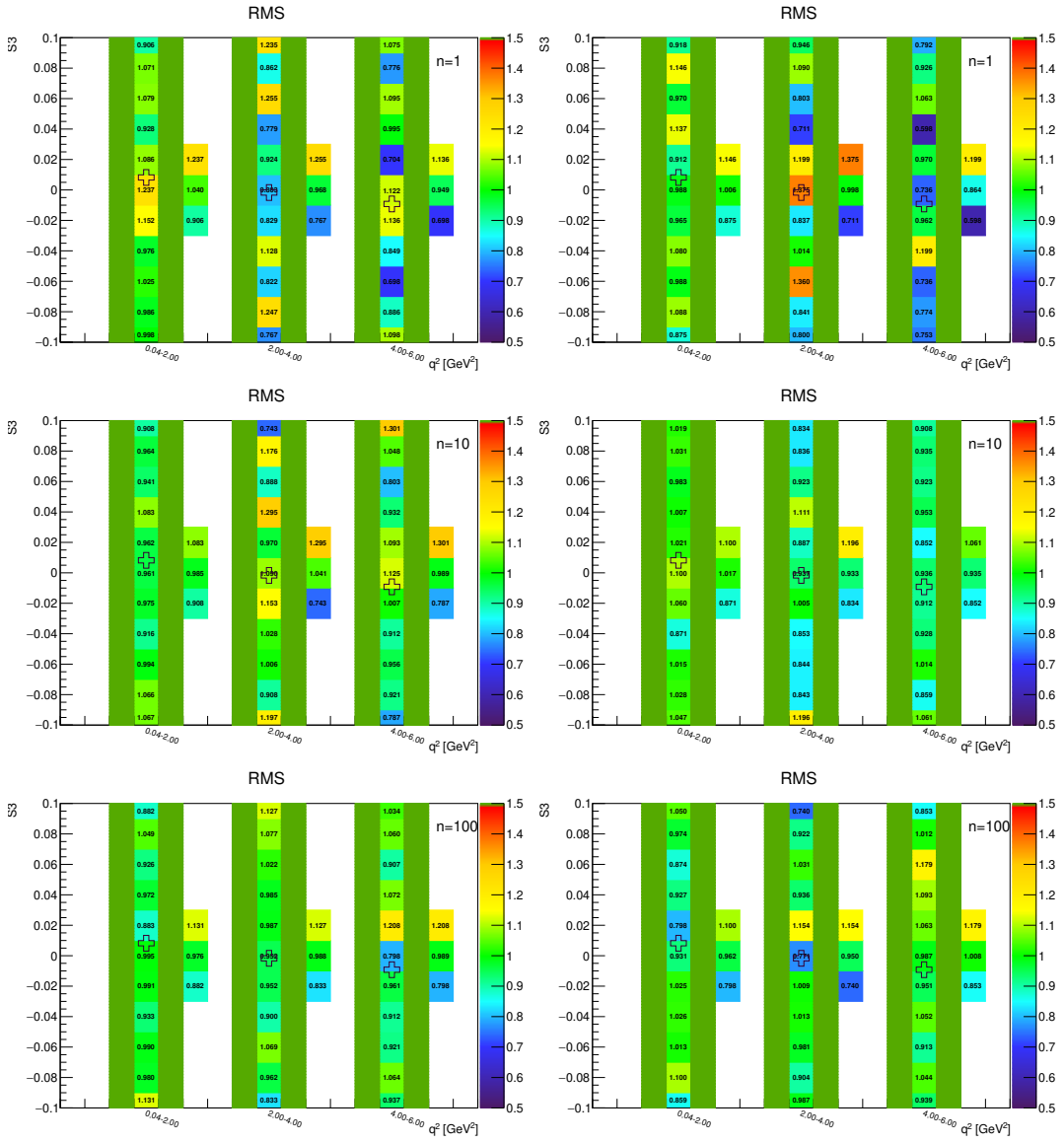

Figure A.140: Toy-MC studies of the S_8-fold, with $r = 1$. Figures show the pull RMS without (left) and with acceptance (right) on the parameter S_3. The green bands represent fit-p.d.f. positivity range. The top figures correspond to the Run-1 like number of events (n = 1), while the middle and the bottom to 10× and 100× larger simulated samples.

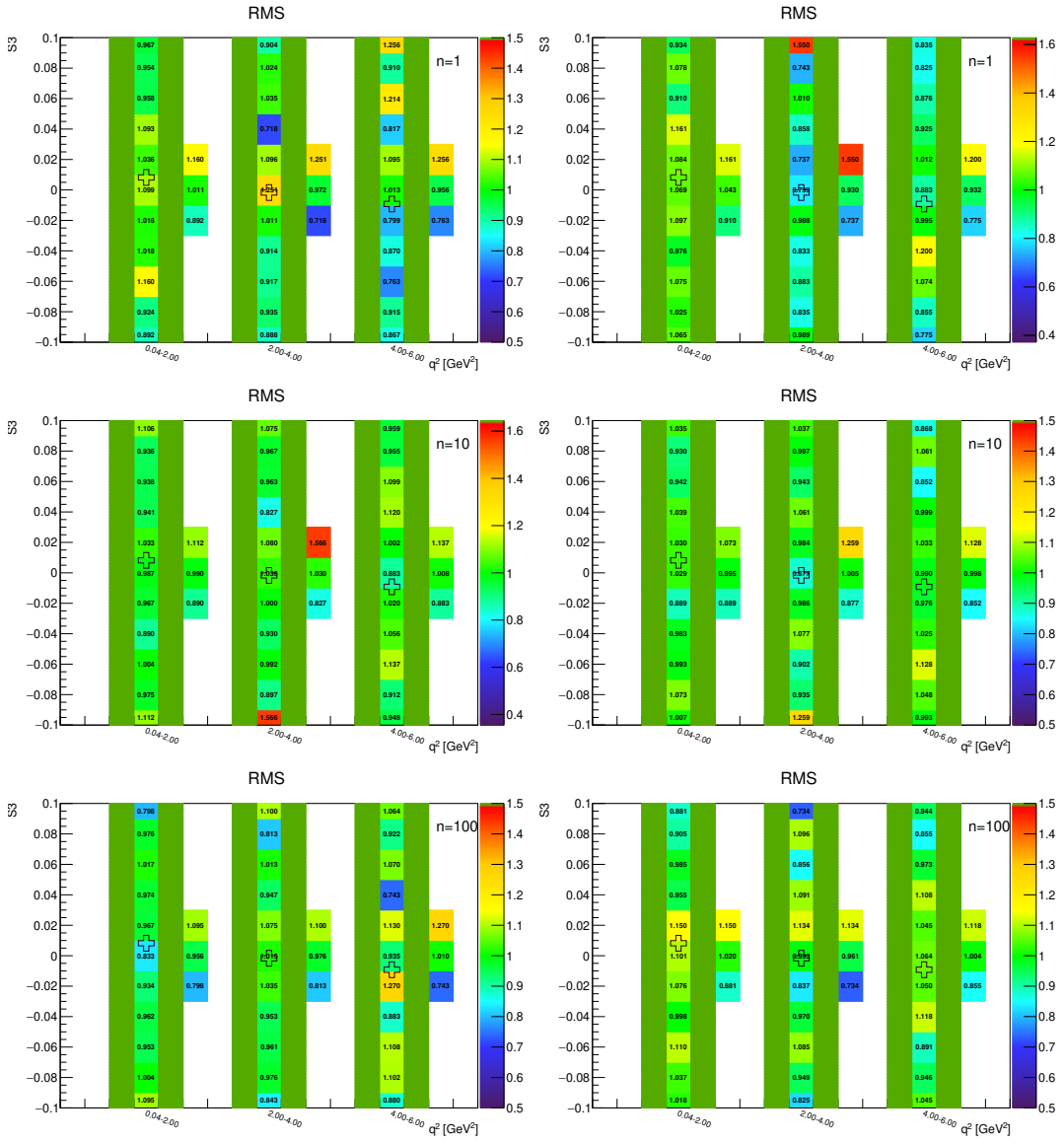

Figure A.141: Toy-MC studies of the S_8-fold, with $r = 2$. Figures show the pull RMS without (left) and with acceptance (right) on the parameter S_3. The green bands represent fit-p.d.f. positivity range. The top figures correspond to the Run-1 like number of events (n = 1), while the middle and the bottom to 10× and 100× larger simulated samples.

A.5.12 S_8-fold – parameter S_8

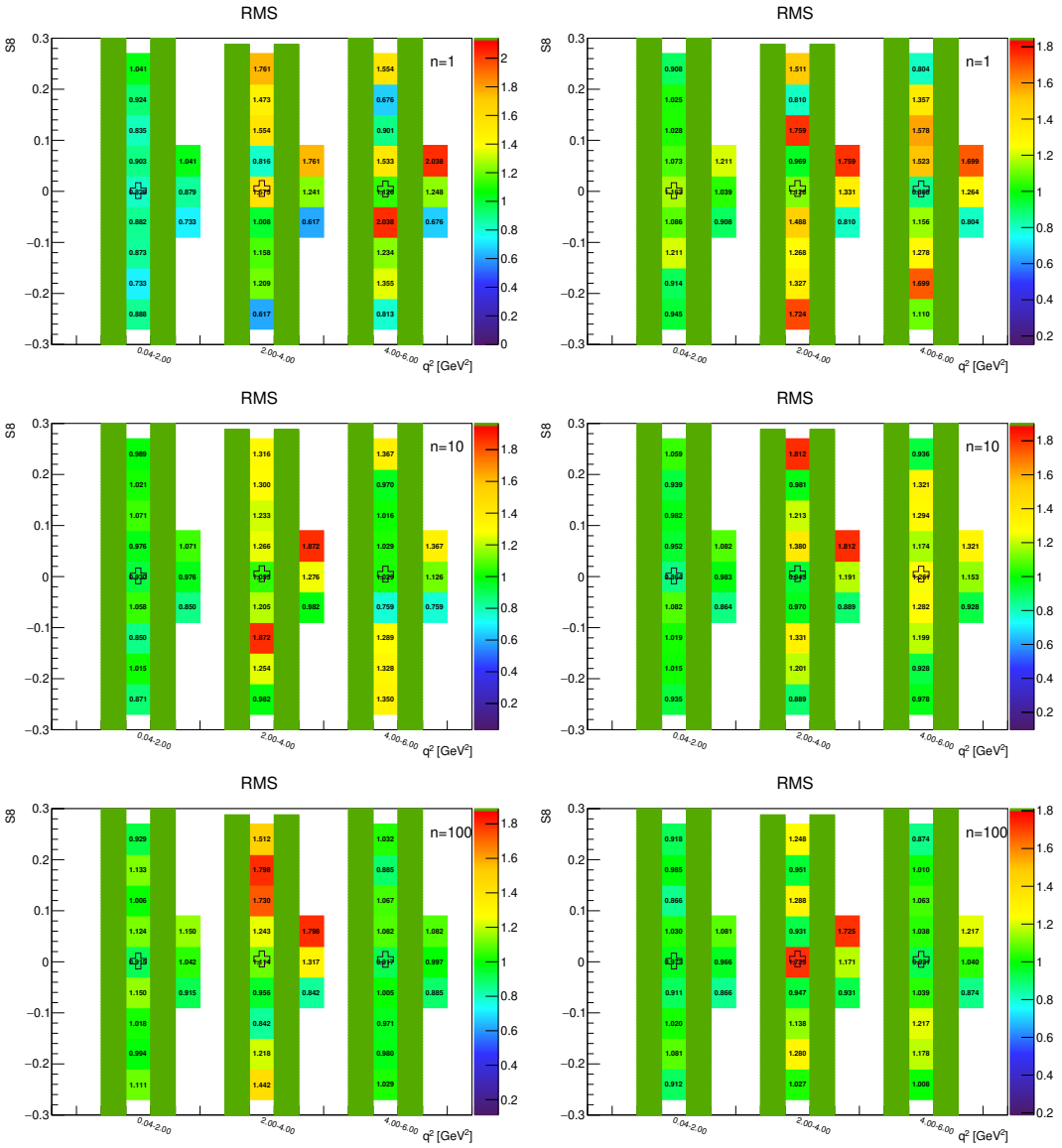

Figure A.142: Toy-MC studies of the S_8-fold, with $r = 0.5$. Figures show the pull RMS without (left) and with acceptance (right) on the parameter S_8. The green bands represent fit-p.d.f. positivity range. The top figures correspond to the Run-1 like number of events (n = 1), while the middle and the bottom to 10× and 100× larger simulated samples.

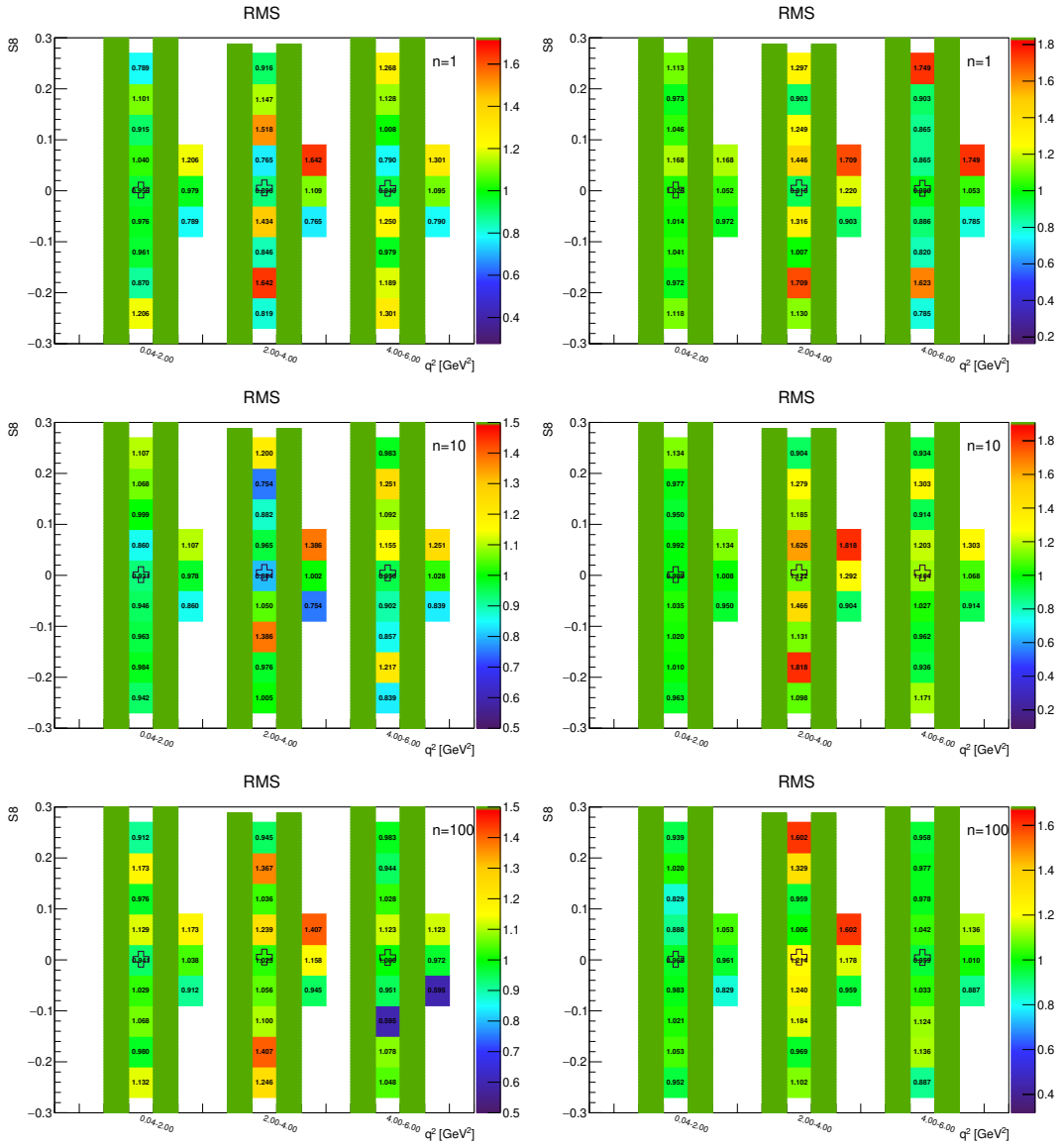

Figure A.143: Toy-MC studies of the S_8-fold, with $r = 1$. Figures show the pull RMS without (left) and with acceptance (right) on the parameter S_8. The green bands represent fit-p.d.f. positivity range. The top figures correspond to the Run-1 like number of events (n = 1), while the middle and the bottom to 10× and 100× larger simulated samples.

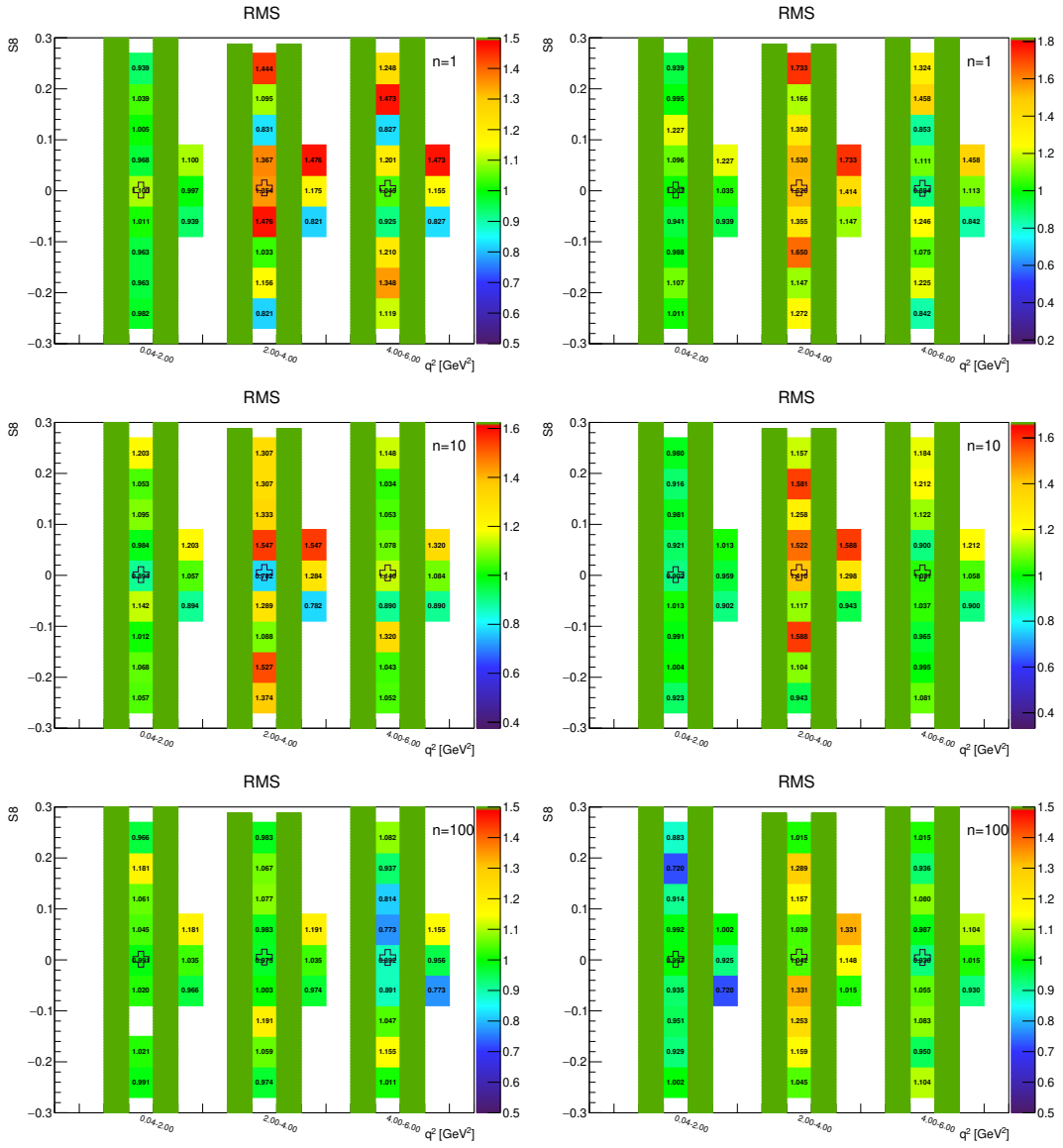

Figure A.144: Toy-MC studies of the S_8-fold, with $r = 2$. Figures show the pull RMS without (left) and with acceptance (right) on the parameter S_8. The green bands represent fit-p.d.f. positivity range. The top figures correspond to the Run-1 like number of events (n = 1), while the middle and the bottom to 10× and 100× larger simulated samples.